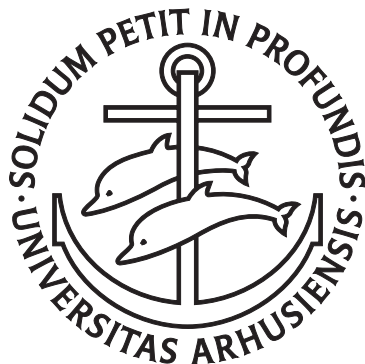

MASS SPECTROSCOPY
EXPERIMENTS ON
CHROMOPHORE IONS AND THE
EFFECT OF A SINGLE WATER
MOLECULE



JØRGEN H. HOUMØLLER
DEPARTMENT OF PHYSICS AND ASTRONOMY
FACULTY OF SCIENCE AND TECHNOLOGY
AARHUS UNIVERSITY, DENMARK

PHD THESIS
SEPTEMBER 2016

This document was typeset using the L^AT_EX document processing system originally developed by Leslie Lamport, based on T_EX typesetting system created by Donald Knuth.

This PhD thesis has been submitted to the Graduate School of Science and Technology at Aarhus University in order to fulfil the requirements for obtaining a PhD degree in Physics. The work presented has been carried out under supervision of Steen Brøndsted Nielsen at the Department of Physics and Astronomy.

Preface

This thesis is based on results from experiments conducted while in the group of Steen Brøndsted Nielsen at Aarhus University, between the years 2012 - 2016. Most of the results obtained during my PhD has already been described in detail in published peer-reviewed papers; these are included at the end of the thesis. The focus of this thesis has therefore mainly been on describing the technical aspects of the experimental work, and on drawing an overall conclusion based on the collected experimental results. I was recently involved in the design and construction of a new experimental setup for luminescence detection from gas phase ions. A detailed description of the experimental setup will be given, and a few experimental results will be discussed. During my PhD, I have spent a lot of time in the laboratory optimising the experimental workflow and furthered the development of the experimental hardware and software. In order to illustrate my involvement in the development of the different experimental setups, a small description highlighting certain aspects of my contributions can be found in the appendix. I have contributed to papers that do not touch upon the subject of ion-solvent interaction, these papers will therefore only be listed in my published work, and not touched upon further.

With all this being said, I hope you will enjoy reading my thesis and the learning experience that it aims to deliver.

Jørgen H. Houmøller

Acknowledgements

I would like to take the opportunity to thank my supervisor Steen Brøndsted Nielsen for his continued enthusiasm, passion and never diminishing positive attitude. Steen has fostered a welcoming attitude in the group, which has made me enjoy every day at work. Steen has always been willing to discuss new results and ideas, which has kept the motivation high. Furthermore, I would like to extend a special thanks to Kristian Støchkel for training me in all things laboratory related. Your determination to teach every little detail of the experimental setups kept me on my toes. In this respect, the mechanical workshop and the electronics department has been invaluable for the experimental developments in the laboratory, and their efforts has been greatly appreciated. A special thanks to Camilla Skinnerup Byskov for healthy discussions about everything work and non-work related. On this note, all the other office mates; Lisbeth, Lasse, Jeppe and Christina also deserved recognition for contributing to the positive attitude in the office. I thank Hjalte Kiefer, Annette Svendsen and our Swedish-American friend Mark Stockett for enlightening and always interesting discussions of experimental details, curiosities and problems. Mark has deserved special thanks for proofreading sections of this thesis. Our secretary Karin Vittrup who has helped in all things administration related also deserves recognition.

I would also like to thank my family who has always been supportive and interested in what I was doing, even though it could

be difficult to understand what it actually was that I was doing.

Last, but certainly not least, I would like to thank my wife and children; Helene, Arthur and Edith for helping me remember the life outside of work, and for your everlasting support.

List of Publications

This thesis is based upon the following papers. The listed papers can be found in Appendix B on page 121 in the order specified below. The papers will be referenced by their Roman numerals throughout the thesis.

- I.** M. Wanko, **J. Houmøller**, K. Støchkel, M.B.S. Kirketerp, M. Åxman, M. Brøndsted Nielsen, S. Brøndsted Nielsen and Angel Rubio,
Substitution effects on the absorption spectra of nitrophenolate isomers
Phys. Chem. Chem. Phys., **14**, (2012), 12905.
- II.** **J. Houmøller**, M. Wanko, K. Støchkel, A. Rubio, and S. Brøndsted Nielsen,
On the Effect of a Single Solvent Molecule on the Charge-Transfer Band of a Donor-Acceptor Anion
J. Am. Chem. Soc., **135**, (2013), 6818.
- III.** **J. Houmøller**, M. Wanko, A. Rubio, and S. Brøndsted Nielsen,
Effect of a Single Water Molecule on the Electronic Absorption by o and p-Nitrophenolate: A Shift to the Red or to the Blue?
J. Phys. Chem. A, **119**, (2015), 11498.

- IV.** K. Støchkel, C.N. Hansen, **J. Houmøller**, L.M. Nielsen, K. Anggara, M. Linares, P. Norman, F. Nogueira, O.V. Maltsev, L. Hintermann, S. Brøndsted Nielsen, P. Naumov and B.F. Milne,
On the Influence of Water on the Electronic Structure of Firefly Oxyluciferin Anions from Absorption Spectroscopy of Bare and Monohydrated Ions in Vacuo
J. Am. Chem. Soc., **135**, (2013), 6485.
- V.** **J. Houmøller**, S.H. Kaufman, K. Støchkel, L.C. Tribedi, S. Brøndsted Nielsen and J.M. Weber,
On the Photoabsorption by Permanganate Ions in Vacuo and the Role of a Single Water Molecule. New Experimental Benchmarks for Electronic Structure Theory
ChemPhysChem, **14**, (2013), 1133.
- VI.** M.H. Stockett, L. Musbat, C. Kjær, **J. Houmøller**, Y. Toker, A. Rubio, B.F. Milne and S. Brøndsted Nielsen,
The Soret absorption band of isolated chlorophyll a and b tagged with quaternary ammonium ions
Phys. Chem. Chem. Phys., **17**, (2015), 25793.
- VII.** B.F. Milne, C. Kjær, **J. Houmøller**, M.H. Stockett, Y. Toker, A. Rubio and S. Brøndsted Nielsen,
On the Exciton Coupling between Two Chlorophyll Pigments in the Absence of a Protein Environment: Intrinsic Effects Revealed by Theory and Experiment
Angew. Chem. Int. Ed., **55**, (2016), 6248.
- VIII.** M.H. Stockett, **J. Houmøller**, K. Støchkel, A. Svendsen, and S. Brøndsted Nielsen,
A cylindrical quadrupole ion trap in combination with an electrospray ion source for gas-phase luminescence and absorption spectroscopy
Rev. Sci. Instrum., **87**, (2016), 053103.
- IX.** M.H. Stockett, **J. Houmøller** and S. Brøndsted Nielsen,
Nile Blue shows its true colors in gas-phase absorption and luminescence ion spectroscopy
J. Chem. Phys., **145**, (2016), 104303.

I have further contributed to the following papers, which are not a part of the work presented in this thesis. Listed after publication date.

- M. A. Christensen, E.A.D. Pia, **J. Houmøller**, S. Thomsen, M. Wanko, A.D. Bond, Rubio, S. Brøndsted Nielsen and M. Brøndsted Nielsen,
Cross-Conjugation vs. Linear Conjugation in Donor Bridge Acceptor Nitrophenol Chromophores
Eur. J. Org. Chem., **10** (2014), 2044.
- J. Elm, M.H. Stockett, **J. Houmøller**, M. Åxman, K.V. Mikkelsen, M. Brøndsted Nielsen and S. Brøndsted Nielsen,
Gas-phase spectroscopy of a vinylheptafulvene chromophore
Eur. J. Mass Spectrom., **21**, (2015), 569.
- L. H. Andersen, A. V. Bochenkova, **J. Houmøller**, H.V. Kiefer, E. Lattoufa and M.H. Stockett,
A PYP chromophore acts as a 'photoacid' in an isolated hydrogen bonded complex
Phys. Chem. Chem. Phys., **18**, (2016), 9909.

Contents

Preface	i
Acknowledgements	iii
List of Publications	v
1 Introduction	1
2 Experimental Setup - SEP1	5
2.1 Overview	6
2.2 Ion source	6
2.3 Ion separation	9
2.4 Detection	10
2.5 Experimental scheme	15
2.6 Shortcomings of SEP1	17
3 Experimental Setup - LUNA	19
3.1 Overview	21
3.2 Ion Trap	24
3.3 Detection	25
3.4 Mass selection	27
3.5 Data acquisition	39
3.6 Control sequence	40
3.7 Control and analysis software	41

<i>Contents</i>	ix
3.8 Florescence spectra	43
4 Experimental Setup - Light Sources	47
4.1 Stimulated emission	47
4.2 Laser timing	50
4.3 Light manipulation	51
4.4 Sum frequency generator	55
5 Results on Nitrophenolates	59
5.1 Bare nitrophenolate ions	63
5.2 Micro solvated nitrophenolates	64
6 Other systems	73
6.1 Oxyluciferin	73
6.2 Permanganate	76
6.3 <i>p</i> -Benzoquinone	77
6.4 Tris(bipyridine)ruthenium(II)	81
6.5 Protonated nucleobases	82
6.6 Summary of experimental results	87
7 Outlook	91
8 Summary	93
9 Dansk Resumé	97
A Abbreviations	101
B Personal contributions	103
Bibliography	107
Publications	121

Introduction

Absorption of visible light by molecules plays a fundamental role for life on earth. Many molecules that absorb visible light are highly π -conjugated. π -conjugation means that the electron density is distributed across a relative large portion of the molecule *i.e.* over multiple sp^2 -hybridised atoms. The light absorbing parts of these molecules are called chromophores. Chromophores are found in many different biological systems, they are responsible for the green colour of leaves, the orange colour of carrots, the red colour of our blood and the green light emitted from insects like the firefly to name a few cases. Perhaps the most critical example of the importance of biochromophores is seen in photosynthesis. In photosynthesis solar energy is harvested by plants through the chlorophyll chromophore and the energy is used to produce sugar and oxygen from carbon dioxide and water. Another example of the importance of light absorption, is the shift from *cis* to *trans* configuration of the Retinal chromophore. This structural change is part of the visual cycle, that enables us to see. Biochromophores are in nature often part of bigger systems of multiple absorbers or in an interplay with specific surrounding molecules or proteins. The central role of the biochromophores in nature, has naturally inspired a lot of interest in the scientific community as a whole. The study of biochromophores is a highly multidisciplinary endeavour including both theoretical and experimental work from the fields of biology, chemistry and physics.

The study of the bare chromophores extracted from their natural environment reveals intrinsic properties of the individual chromophores. These studies are enabled by gas-phase spectroscopy techniques, that allow the study of the bare chromophores as both ionic and neutral species[1–4]. Isolated chromophores have been studied in great detail, both experimentally and theoretically[5–18]. In recent years computational power has increased, enabling the use of high accuracy quantum chemistry calculations on biological systems[19, 20]. Combining experimental results with quantum chemical calculations can give previously unknown insights into the actual mechanisms in play for the different systems. Comparing the studies of the unperturbed chromophores to the ones conducted on the chromophores in solution phase reveal information about the perturbing nature of the specific solution. Since many bio chromophores in nature exists in protein pockets[21–23], their actual natural environment might be some place in between gas phase and solution phase, where effectively only few interactions with the environment are of importance. Only a few studies have investigated the effects of single solvent molecules on the photophysical properties of biochromophores, and these studies has focused on specific chromophores and not the overall effect of a solvent molecule[24–28].

The aim of this PhD study has been to experimentally investigate the effect of micro solvation of ionic chromophores by single solvent molecules on the transition energies of the chromophores. Knowledge about the perturbing effects of single solvent molecules is an important piece in understanding the effects of the local environment on the biochromophore systems, where single water molecules or amino acid residues might interact with the chromophore in the protein pocket. More specifically a model system of nitrophenolates has been studied in order to limit the level of complexity of the system. The knowledge gained from the model system is then used to understand the specific perturbing effects of single solvent molecules on bigger biological chromophores.

Absorption spectroscopy is usually used to reveal the absorption energies of chromophores in solution. Here the fraction of incident light absorbed by the solution is used to calculate the absorbance of the system. This works well for chromophores in solution where

the concentration of absorbers is fairly high. Regrettably, the use of normal absorption spectroscopy, when dealing with molecular gas phase ions, is difficult due to the low ion densities achievable. Instead of normal absorption spectroscopy, a technique called *Action Spectroscopy* is utilized for obtaining the absorption spectra of the different chromophores presented in this study. Action spectroscopy is the correlation between some action and the wavelength of absorbed light by the gas phase chromophore ion. For the data presented in this thesis, the action monitored is mostly fragmentation. When the chromophore absorbs light a photoactive electron is excited. The system then returns to the electronic ground state by internal conversion, to a vibrational excited state. To release the excess energy the chromophore can fragment and thereby release the specific binding energy of the broken bonds. In some cases, the excited electron is detached as either direct emission or thermal emission from a vibrational hot ground state. In these cases the depletion of the parent signal is monitored as the action. A home-build sector mass spectrometer called separator 1 (SEP1) is used to measure the action spectra of the bare ionic chromophores and their solvent-complexes. The details of the SEP1 setup will be described in the following chapter.

In addition to fragmentation and electron emission, photon emission (luminescence) is another important relaxation mechanism for excited chromophores. An instrument like SEP1, which is based on charged particle detection, is "blind" to this channel. In order for action spectroscopy to reveal the total absorption of the chromophores, it is assumed that photon emission from the excited state is constant over the wavelength region of absorption, or not present at all. In order to measure the actual luminescent properties of biochromophores, a new experimental setup (LUminescence iNstrument in Aarhus, LUNA) has been build. As of writing this thesis, no results related to the effect of micro solvation has been achieved at LUNA, but a general description and motivation for the setup will be given in chapter 3 on page 19.

Experimental Setup - sep1

In this chapter the experimental setup SEP1 is described.

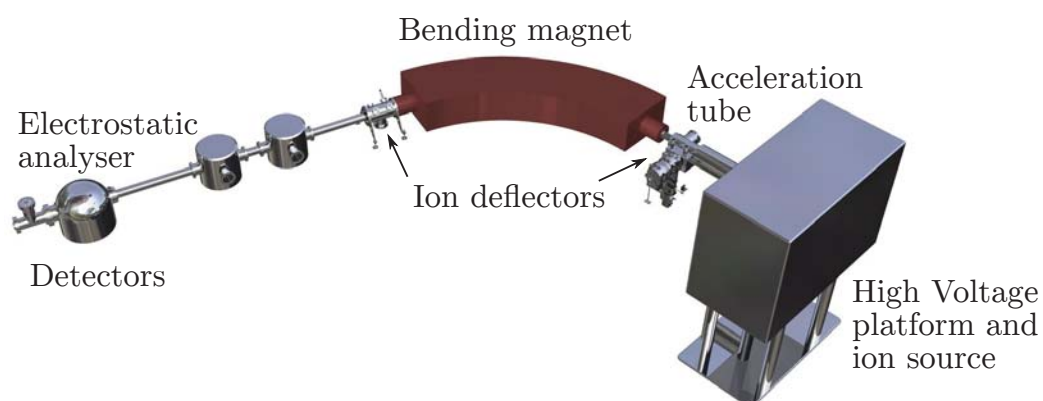


Figure 2.1: Illustration of the sector mass spectrometer named SEP1. Ions are produced in an electrospray ion source mounted on a high voltage platform, which is raised to 50 kV for ion acceleration. The parent ion is selected by its mass to charge ratio in an electromagnet. After laser excitation, the ions may dissociate and a channeltron detector detects the number of a specific of fragment ion selected by an electrostatic analyser.

2.1 Overview

SEP1 is an accelerator mass spectrometer (Figure 2.1 on the preceding page)[29–34]. Magnetic and electric fields are utilized to select and analyse ions and fragment ions. The first section of the instrument is the ion source. The ion source currently installed is an electrospray ion source. In the next section of SEP1, the ions are accelerated by an electric field gradient over the distance of approximately one meter. Normally the ions are accelerated to a kinetic energy of 50 keV per charge. The ions of interest are then separated according to their mass over charge ratio by an electromagnetic field. In the long straight path from the magnet to the electrostatic analyser (ESA), the ions can interact with a laser pulse. An electric field is utilized in the ESA for separating ions based on their kinetic energy to charge ratio. After the analyser, a channeltron detector is used to count the number of fragment ions. A new detector-section was added to SEP1 in April of 2016. The new section houses a detector that enables SEP1 to monitor the yield of neutral fragments, which are not effected by the electric fields in the ESA.

2.2 Ion source

As mentioned before, the ion source at SEP1 is an electrospray ion source[35]. Electrospray ionization was invented in the late 1980s as an effective way of transferring large fragile biomolecules into the gas phase[36]. A detailed description of the theory behind electrospray is outside the scope of this thesis, and only the resulting effects and an overall description will be given in the section below. A schematic representation of the ion source at SEP1 can be found in Figure 2.2 on the next page.

A syringe pump pushes solution through an electrospray needle at a constant flow of the order of $\mu\text{l min}^{-1}$. A high voltage is applied to the needle, which ensures that the droplets are highly charged when leaving the needle. The low pressure in the first chamber and the potential difference between the needle and the heated capillary, draws the droplets through the heated capillary, where the solvent

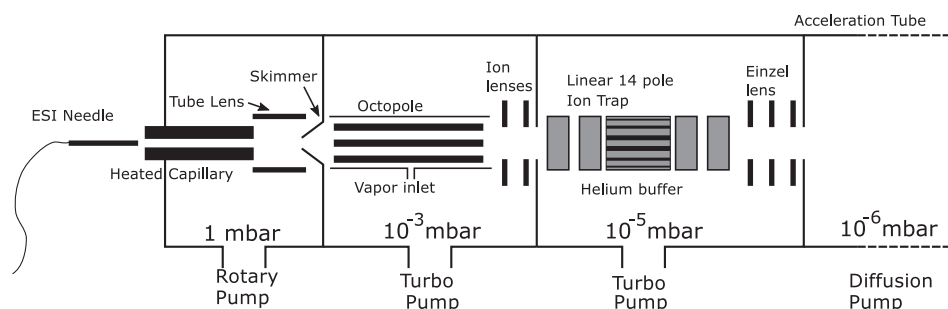


Figure 2.2: Illustration of the electrospray ion source. A needle with a high voltage applied, followed by a heated capillary transfers the ions into the gas phase. The generated ions are focused through a skimmer by a tube lens. The ions can be stored in the octopole or in the linear 14-pole ion trap before acceleration. When ions are stored in the linear ion trap, helium buffer gas is used to cool down the ions.

is evaporated. The surface charge makes the droplets coulomb explode when sufficient solvent has evaporated. After several cycles of evaporation and coulomb explosions bare ions are left.[37, 38] The output of the heated capillary is displaced a bit off center compared to the skimmer entrance. The off center shift minimizes the number of neutral solvent molecules entering the octopole. A tube lens focuses the ions through the skimmer and into an octopole. The octopole and the first lens package is used to guide the ions into the 14-pole trap. The octopole can additionally be used as a reaction chamber where ions undergo reactions with solvent molecules. A small tube is placed around the octopole, and a small nozzle directs the solvent vapour into the octopole (Figure 2.3). The ion picks up solvent molecules through collisions in the octopole. To maximize the number of ion-molecule reactions, the ions are trapped in the octopole with the first lens in the lens package acting as an end-electrode of a trap, effectively transforming the simple octopole into an ion trap. After passing the octopole and the first lens package, the ions enter a 14 pole ion trap (Figure 2.4 on the following page). Through collisions with helium buffer gas, the trap can store and cool the ions to room temperature. After the ion trap, the ions are accelerated to kinetic energies of 50 keV and then steered into the mass over charge selecting magnet.

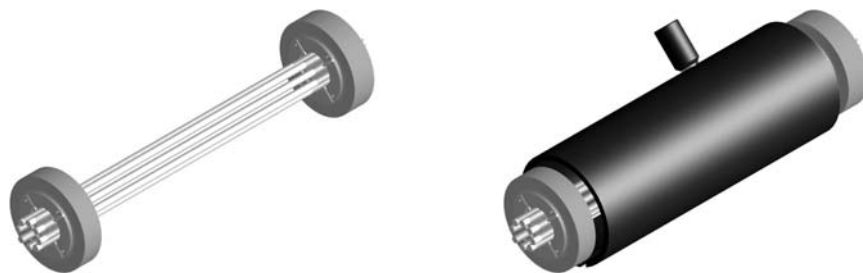


Figure 2.3: Illustration of the octopole used at SEP1. (a) Octopole. (b) Octopole with solvent vapor chamber.

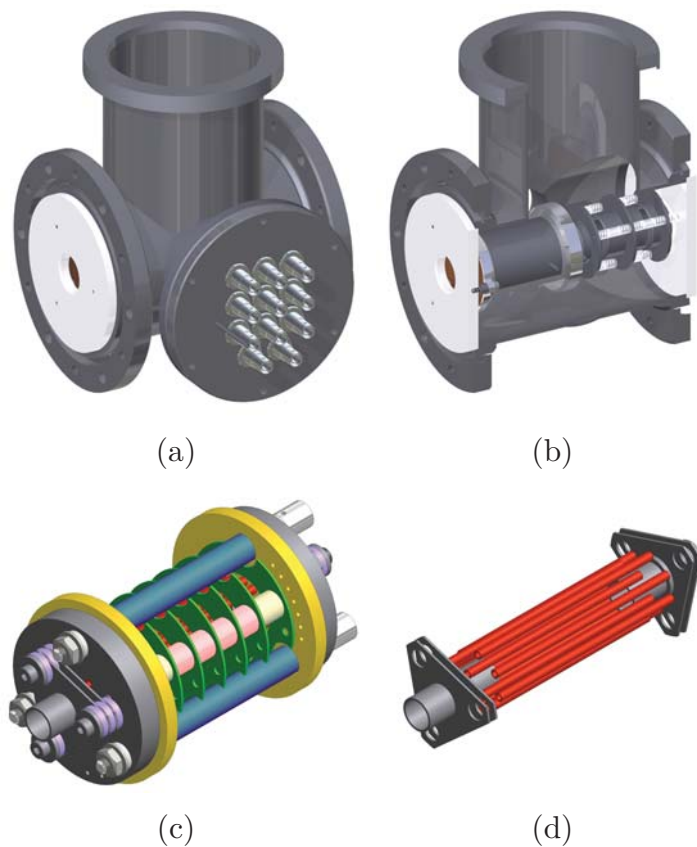


Figure 2.4: Illustration of the 14-pole trap installed at SEP1. (a) The trap chamber with BNC connectors and buffer gas inlet. (b) A side-cut view of the trap chamber, showing the einzel lens and ion trap. (c) Illustration of the actual ion trap. (d) The bare 14 pole ion trap.

2.3 Ion separation

The Lorentz force describes the acting force on an ion by electric and magnetic fields:

$$\mathbf{F} = q(\mathbf{E} + \mathbf{v} \times \mathbf{B}), \quad (2.1)$$

where q is the charge of the ion, \mathbf{E} is the applied electric field, \mathbf{v} is the velocity of the ion and \mathbf{B} is the magnetic field.

Only the $\mathbf{v} \times \mathbf{B}$ term is applicable in the electromagnetic field in the ion-separating magnet. The cross product in Equation 2.1 is always perpendicular to the velocity of the ions; hence, the kinetic energy of the ions remains unchanged. The equations for the kinetic energy, the centripetal force and the magnetic Lorentz force, can be equated to express the required mass over charge ratio for passing the magnet at a specific magnetic field strength:

$$\frac{m}{q} = \frac{B^2 r^2}{2V}, \quad (2.2)$$

where r is the radius of the bending magnet and V is the acceleration voltage. Equation 2.2 indicates that only ions with a specific mass over charge ratio follow the circular path of the magnet at a specific strength of the magnetic field, effectively removing all other ions from the ion beam.

In the ESA (Figure 2.5 on the next page), a perpendicular electric field bends the trajectory of the ions.

By equating the electric field part of the Lorentz force, with the centripetal force for the circular movement through the analyser, a measure for the required electric field strength is obtained:

$$E = \frac{2K}{qR}, \quad (2.3)$$

where K is the kinetic energy of the ions and R is the bending radius. The potential difference between the two analyser-plates (assumed parallel) can then be calculated.

$$V = E \cdot d = \frac{2Kd}{qR} \quad (2.4)$$

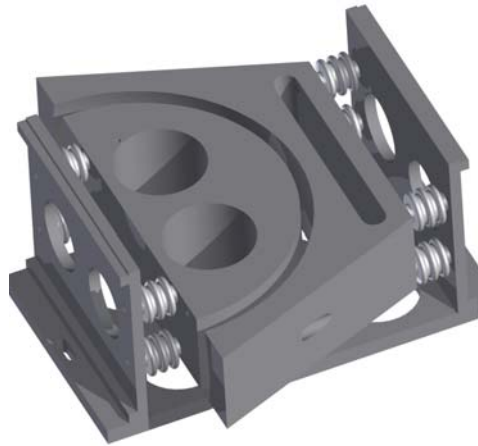


Figure 2.5: Illustration the electrostatic analyser used for fragment ion selection at SEP1.

where d is the distance between the two plates. At SEP1 the distance between the analyser plates is 16 mm and the center radius is 154.5 mm. This combined with a kinetic energy of the ions of 50 keV results in a potential difference of 10.4 kV. To acquire a zero-potential region between the plates, the applied voltages are ± 5.18 kV. The zero potential center of the analyser prohibits the high potentials on the analyser plates from accelerating or decelerating the ions, and thus changing the kinetic energy when entering the analyser.

2.4 Detection

As mentioned at the beginning of this chapter two detectors are currently installed at SEP1. Detector 1 is the channeltron detector sitting in the electrostatic analyser and Detector 2 is the SED detector after the electrostatic analyser, see Figure 2.6 on the facing page.

2.4.1 Detector 1

Detector 1 is a single channeltron detector, also known as a Channeltron Electron Multiplier (CEM). An illustration of the installed CEM can be seen in Figure 2.7 on page 12. The CEM has a high

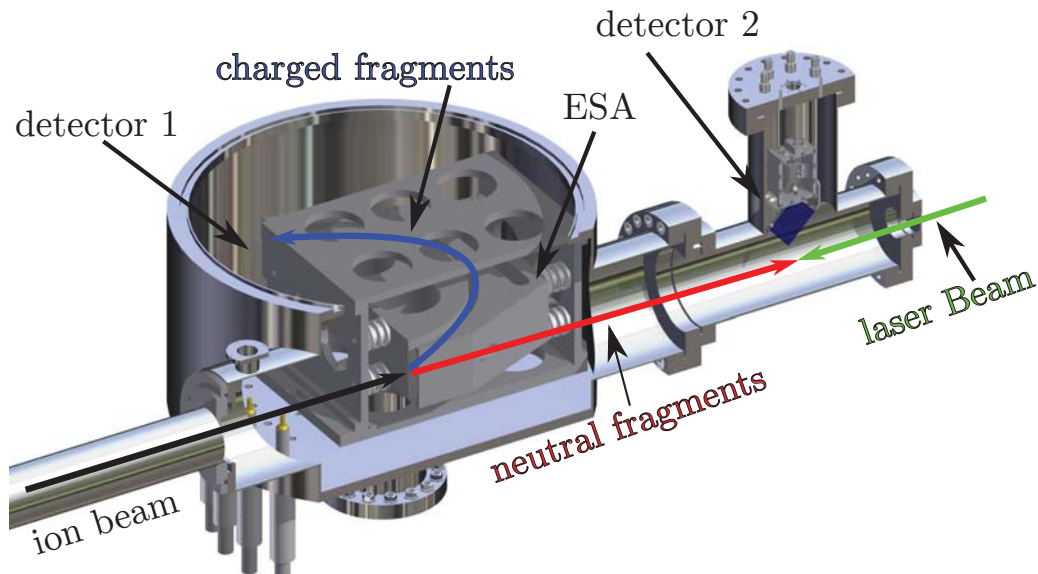


Figure 2.6: Visualising the detector placements at SEP1. (The illustration uses an old design of the SED detector.)

surface resistance, so that when a high positive potential is applied between the front and the back of the CEM, a continuous dynode is formed through the detector. This dynode acts as an electron multiplier, since secondary electrons are emitted, when primary particles with sufficient kinetic energy collide with the surface. The applied positive potential forces the electrons to travel down the tube and thereby collide multiple times with the surface of the CEM. This process results in an avalanche of electrons, which gives rise to an output current pulse of a few mA. In order to measure this current pulse on the anode of the detector, which has a high voltage potential applied, a small high voltage capacitor circuit is added, see Figure 2.8 on the following page. The capacitor ensures that the high voltage potential is not superimposed on the signal generated by the current pulse on the capacitor. The capacitor further transforms the current pulse to a potential pulse, which is then measurable by other electronics.

The output from the CEM is reshaped and amplified in a timing filter amplifier. The signal from the timing filter amplifier is then

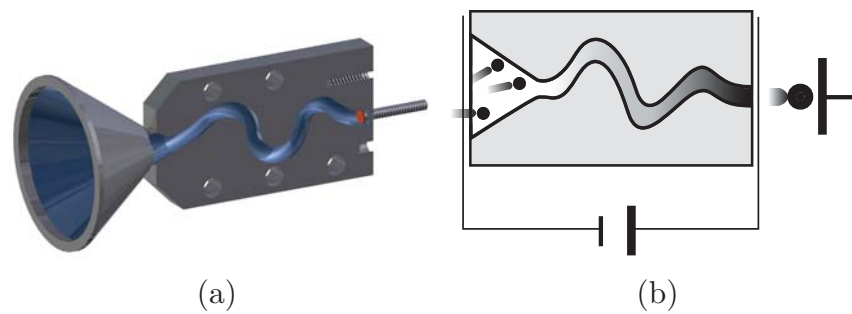


Figure 2.7: (a) Illustration of the CEM at SEP1. (b) Illustration of the working principle of the CEM. The grading through the channel illustrates the cascade of secondary electrons created. The potential difference over the CEM is 2.5 kV. [Illustrations are based on figures from the CEM user manual]

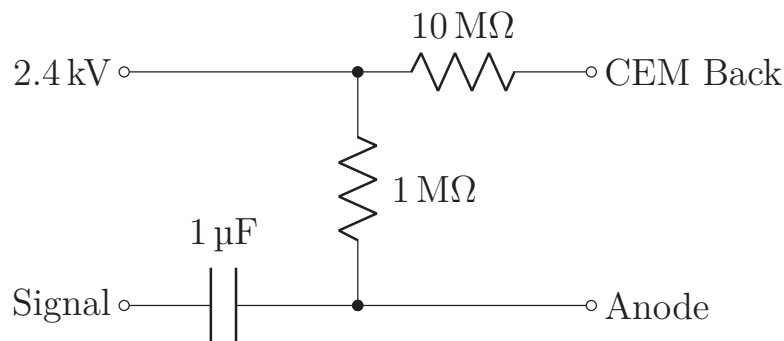


Figure 2.8: Circuit used for potential control and signal extraction for Detector 1. The 2.4 kV is applied to the back of the CEM, in addition to -100 V applied to the front (not shown here). This small negative potential prohibits low kinetic energy electrons from entering the detector.

transferred to a discriminator, which outputs a NIM or TTL pulse when triggered. At the end a computer basically counts the number of output pulses from the discriminator. The signal at all three stages can be seen in Figure 2.9 on the next page.

There are two main types of discriminators, the leading-edge discriminator and the constant fraction discriminator (CFD). The leading edge discriminator is the simplest. It outputs a signal when the input signal reaches a defined threshold (Figure 2.10(a) on the facing page). If the height of the input signal varies, the leading-edge discriminator will introduce a time walk. When using

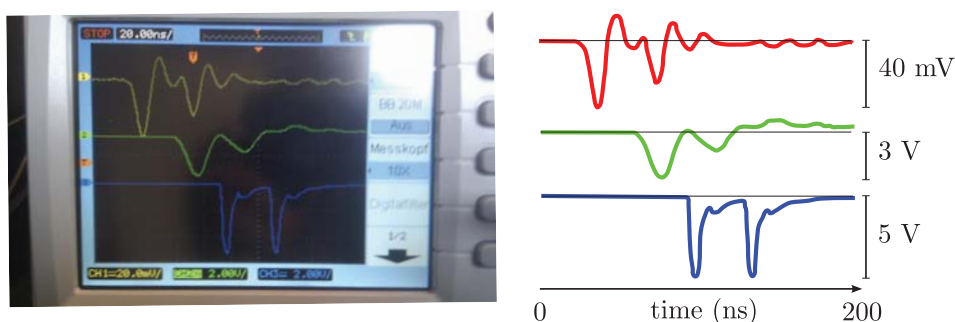


Figure 2.9: Illustrating process for signal preparation for counting at SEP1. Three signals are shown. The top signal is the output from the capacitor circuit shown in Figure 2.8 on the preceding page. The center signal is after the timing filter amplifier and the bottom signal is the output of the CFD to be counted.

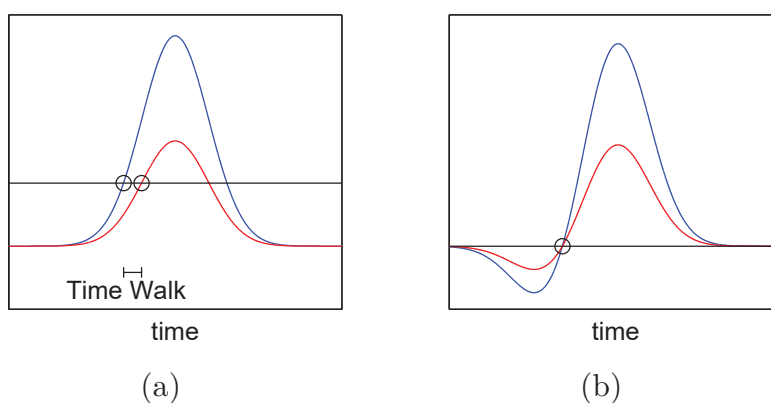


Figure 2.10: Illustrating the time of triggering from two peaks with different peak heights by the use of a (a) leading edge discriminator and (b) a constant fraction discriminator. The time of triggering is indicated by circles.

a CFD, the input is split into two identical pulses. One of the pulses is attenuated, delayed and inverted. The sum of the altered and the unaltered pulses gives rise to a zero-crossing at the same time, regardless of the input peak height (Figure 2.10(b)). This zero-time walk property can be important for time-of-flight measurements, where high time resolution is required. Since high accuracy on the timing information is of no importance for the experiments carried

out at SEP1, the CFD is used as a simple leading edge discriminator. The output from the CFD used at at SEP1 is a fast NIM pulse with a rise time of 2 ns.

2.4.2 Detector 2

It is only possible to monitor the yield of individual charged fragments using the ESA and detector 1. In the special cases where electron emission is one of the dominant deexcitation channels, one needs to measure a depletion of the parent ion beam, when using the ESA and detector 1. Depletion signals are often very difficult to measure, since the depletion signal is usually on the same order as the fluctuations in the parent beam. When a singly charged ion fragments or an anion detaches an electron, a neutral species always remain. This neutral is not affected by the electrostatic potential of the ESA, and will pass right through the analyser, with a high kinetic energy. This high kinetic energy neutral molecule can be detected by what is called a secondary electron detector (SED).

The SED at SEP1 (Figure 2.11 on the facing page)[39] is composed of a glass plate, coated with indium tin oxide. Indium tin oxide has a work function of approximately 4.5 eV[40], is highly conductive and transparent. These properties make indium tin oxide a good coating for secondary electron generation for this detector. The coating needs to be conductive since applying a negative potential on the glass plate can help in guiding the generated electrons. The coating furthermore needs to be transparent for laser light to pass through it. When a particle with high kinetic energy is indent on the coated glass plate, an electron can be emitted from the surface. This secondary electron is guided towards a channeltron detector by the applied electric field. The output pulses of the channeltron detector are counted as previously described.

In principal this detector can detect the full action spectra (disregarding photo emission) in one go. In the current configuration however, it is mostly useful for ion-current stability measurements, and special cases where electron detachment plays a significant role. Since the detector sits directly in the path of the neutrals from the parent beam, a fast channeltron is needed for high accuracy measurements. The SED was first tested on the *p*-benzoquinone anion,

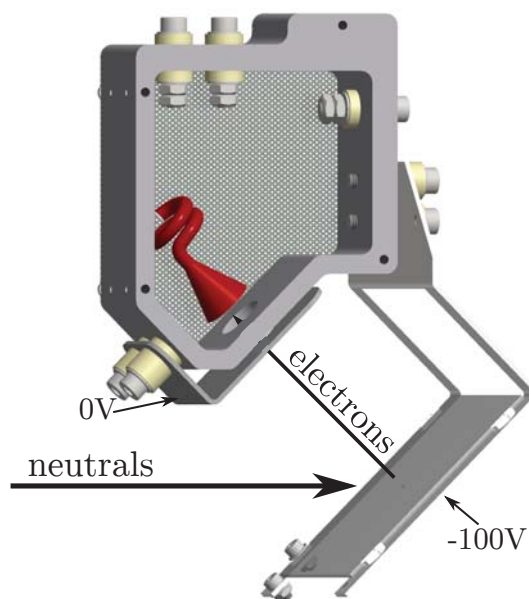


Figure 2.11: Illustration of the secondary electron detector at SEP1. The electron emitter is a coated glass plate, and the detector is a channeltron detector. High energy molecules hit the glass plate which releases electrons. These electrons are guided by a perpendicular electric field (Glass plate potential approximately -100 V) and focused by the small aperture (grounded) towards the channeltron detector.

which predominately deexcite by electron emission. The result of the SED measurement compared to the depletion measurement can be seen in Figure 2.12 on the next page. From these data it is clear that for certain experiments, the SED has some clear advantages.

2.5 Experimental scheme

The ion injection rate at SEP1 is 40 Hz while the repetition rate of the lasers are 20 Hz. This difference between the injection rate and laser repetition rate, makes it possible to continuously measure the "laser on" minus "laser off" signal *i.e.* the actual laser-induced signal. The laser-induced signal is normalized to the ion beam intensity (when possible) and the number of photons at the specific wavelength. The number of photons is proportional to the laser power multiplied by the laser wavelength. The relative cross section

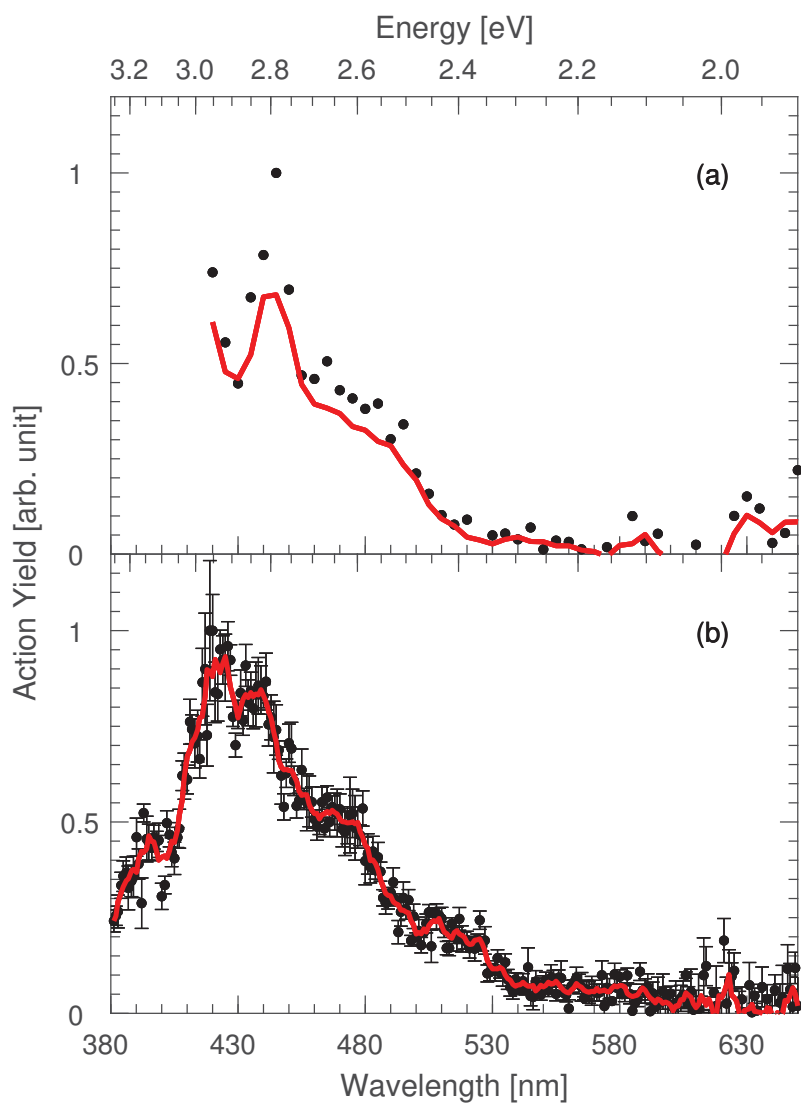


Figure 2.12: Action spectra from the first test of the SED on the *p*-benzoquinone anion. (a) Depletion measurement. (b) SED measurement. For both measurements the running average is superimposed as the red solid line.

for photon absorption is calculated by the use of

$$\frac{S - B}{B \cdot (P_{\text{laser}} \cdot \lambda)^n}, \quad (2.5)$$

where S is the "Laser on" signal, B is the "Laser off" signal, P_{laser} is the laser power measured at wavelength λ and n is the photon order *i.e.* the number of photons required to be absorbed before the ion fragments. Equation 2.5 assumes that the absorption cross section is a constant after absorption of the first photon. This assumption is clearly only an approximation, which is why two-photon processes are inherently difficult to analyse.

The full action spectrum is the weighted sum of the action spectra of the different fragmentation channels. To find the fragments of interest, a scan of the analyser voltage is performed. The power-dependence (fragmentation as a function of laser power) is measured for all significant fragments to determine the photon order. If the yield of fragmentation increases linearly with laser power, the photon order is one, and so on.

2.6 Shortcomings of SEP1

There are two major disadvantages of SEP1. The first disadvantage is the lack of luminescence detection, which we have taken care of by building a stand-alone luminescence setup LUNA. The second disadvantage is time frame for fragmentation detection. The short μs time frame can lead to what is known as a kinetic shift. Kinetic shifts occur when the dissociation time changes with wavelength, and the time window for measurements is too short to measure all fragmentations illustrated in Figure 2.13 on the following page. This can be understood on the basis of a fragmentation process with an activation energy E_a . If the Arrhenius expression is applicable for calculating the rate constant[41], then the rate constant for dissociation can be described as:

$$k_n = A \cdot \exp(-E_a/k_b T_n^*), \quad (2.6)$$

where A is a pre-exponential factor and T_n^* is the effective temperature of the molecule after absorption of n photons. The effective

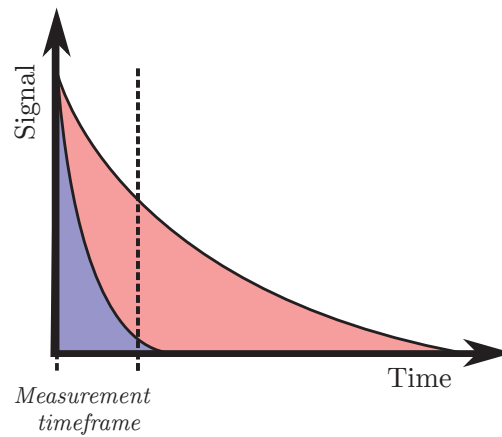


Figure 2.13: Kinetic shift illustrated. This plot shows the dissociation as a function of time, after absorbing a red photon (long decay time) and a blue photon (short decay time). The measurement time frame captures nearly all the dissociation after absorbing a blue photon, but only detects a fraction of the dissociation after absorbing a red photon.

temperature is dependent on the absorbed photon energy[42]. Absorbing a red photon results in a "cold" ion with a long lifetime and absorbing a blue photon results in a "hot" ion with a short lifetime. At SEP1, the dissociation time window is limited to a few μs , which could result in a discrimination towards high energies, as absorption of a high-energy photon results in faster dissociation, . In order to avoid misinterpreting the data due to kinetic shifts, one could measure the dissociation at a storage ring facility or from a trap, where the experimental time windows is much longer.

Experimental Setup - luna

Luminescence is relaxation by light emission. Luminescence is categorised in two categories: fluorescence and phosphorescence. Fluorescence is a fast processes, where the deexcitation happens between two levels of equal multiplicity. Fluorescence happens on the time scale of 1 ns to 100 ns. Phosphorescence happens when the levels has different multiplicities e.g. between a singlet and a triplet state. The classically forbidden transition results in a slow process on the time scale of milliseconds to multiple seconds. When a molecule is excited into an S_n state, internal conversion to the S_1 state is very fast, few hundred fs to ns. Consequently the excited molecule has ended up in the first electronically excited state, before it has hat time to emit a photon. This effect was formulated by Michael Kasha in 1950 and formally known as Kasha's rule[43]: *The emitting electronic level of a given multiplicity is the lowest excited level of that multiplicity*, meaning that the emission spectra of a molecule is independent on the excitation energy. Subsequently, the emitted photon from luminescence is often shifted to a lower energy relative to the absorbed photon, this is known as the Stokes shift.

As described in the last section of the previous chapter, one of the shortcomings of SEP1, is the lack of luminescence detection. This particular deexcitation pathway has some very interesting properties in addition to being another piece in the Action-Spectra puzzle. Since luminescence basically only takes place from the

lowest electronic excitation, it is possible to study the energy spacing between three electronic states in one go. This is nicely illustrated by looking at the potential results from a future experiment done on chlorophyll dimers.

Chlorophyll is the chromophore responsible for light absorption by green leaves in the photo synthesis mechanism. The light absorption and subsequent energy transfer in photosynthesis has a conversion efficiency of 95 % [44]. This efficiency is clearly much higher than current state of the art solar cells, which have efficiencies of approximately 40 % [45]. The absorption spectra of bare chlorophyll ion (ref [46] and paper **VI**) has been blue shifted almost 50 nm compared to chlorophyll in a variety of natural protein complexes [47–50]. It has been argued that the observed blue shift in transition energy could be an effect of an excitonic coupling between two or more pigments [51]. An exciton coupling is due to the interaction between two or more transition dipole moments. The interaction results in the formation of two new energy levels, exemplified by the interaction between two chlorophyll molecules in Figure 3.1 on the next page, where the two unperturbed levels $\psi_1^1\psi_2^0$ and $\psi_1^0\psi_2^1$, corresponding to an excitation to either the first chlorophyll molecule or the second, are split into two exciton states labelled Ψ^+ and Ψ^- . The exciton coupling results in both a blue shifted and a red shifted level compared to the unperturbed levels.

The absorption of light by bare chlorophyll molecules and by clusters of two chlorophyll molecules and a charge tag has been studied in the papers **VI** and **VII**. The resultant action spectra can be seen in Figure 3.2 on page 22. The data shows that the chlorophyll dimer is red shifted by 23 nm (0.07 eV) compared to the monomer. Aside from the shift in transition energy, the double-maximum character of the monomer spectrum is not present for the dimer, the origin of this effect is unknown. The second band in the dimer spectrum, around 610 nm, might originate from the higher-lying exciton state, but this needs further investigation.

In a fluorescence experiment it might be possible to excite the dimer with a single $E + \Delta E$ photon and then monitor the fluorescence of $E - \Delta E$ photons. If the system fluoresces at $E - \Delta E$ then the presence of an exciton coupling has been established. Studying the chlorophyll dimer by a fluorescence experiment is a

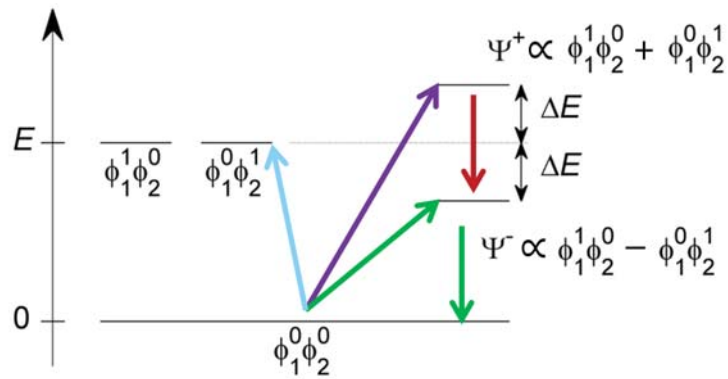


Figure 3.1: Simple level diagram illustrating an exciton coupling. The states on the left are the unperturbed states, and the states on the right are the shifted exciton states. The exciton splitting ΔE is shown. The exciton structure can be probed by fluorescence experiments, where the system is excited by a $E + \Delta E$ photon and fluorescence is monitored for $E - \Delta E$ photons. For further explanation see text.

long term goal. To reach this goal, a new fluorescence setup has been built. Since the experimental setup is new, it will be described in some detail in the following sections. Some experimental results will be shown, but not discussed in great detail. The details regarding the individual results can be found in the papers **VIII** and **IX**.

3.1 Overview

Even though the fluorescence quantum yields for special laser dye molecules are near unity[52], it has not been possible to detect any fluorescent light at SEP1. It is nearly impossible to detect photons emitted by ions that are moving perpendicular to the photon-detection at kinetic energies of 50 keV. So in order to study photon emission, it was necessary to build a dedicated setup for luminescence experiments called LUMinescence iNstrument in Aarhus, in short LUNA. The overall framework of LUNA is based upon the setups described in ref [53] and [54]. The overall setup is illustrated in Figure 3.3 on page 23. The ion source is in principle the same as is SEP1. The only difference is that instead of a linear ion trap and an acceleration region as present at SEP1, LUNA utilizes a simple Paul trap[55] to store the ions. Since the ions need to be

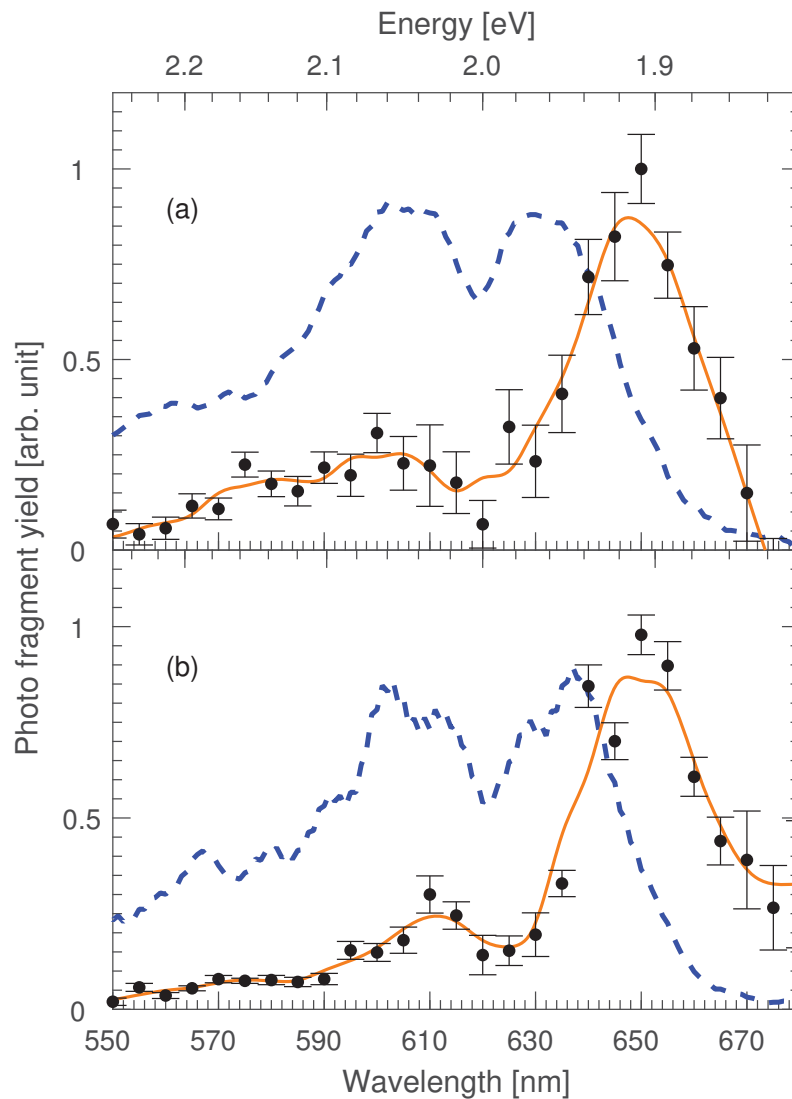
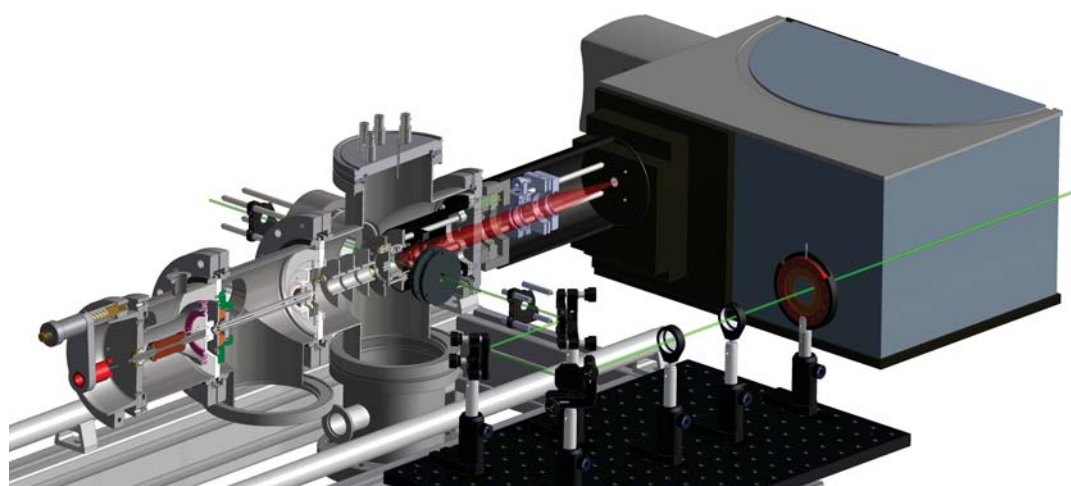
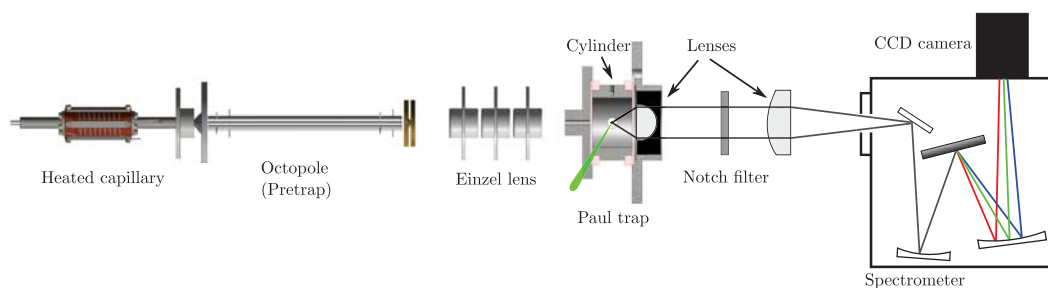


Figure 3.2: Action spectra of Chlorophyll monomers (blue broken line) and dimers (black points and red running average) for two different charge tags (a) tetramethylammonium cation, (b) acetylcholine cation. A clear red shift is seen for both charge tags, but it is difficult to determine if the shift is a result of exciton coupling or some other effect. [papers VI and VII]



(a)



(b)

Figure 3.3: (a) 3D illustration and (b) schematic overview of LUNA. Light emission from the laser excited ions in the Paul trap is collected and focused into the spectrometer. The schematic overview is not drawn to scale.

stationary during the experiment there is no acceleration region in this setup. The ions will be stored in the trap during laser excitation and light emission. Laser light will enter the trap from the side of the setup, and either a photo multiplier or a spectrometer can detect fluorescence through a mesh-grid which acts as an end cap of the trap. Since most of the ion source was described in the previous chapter, only the ion trap and detection setup will be described below.

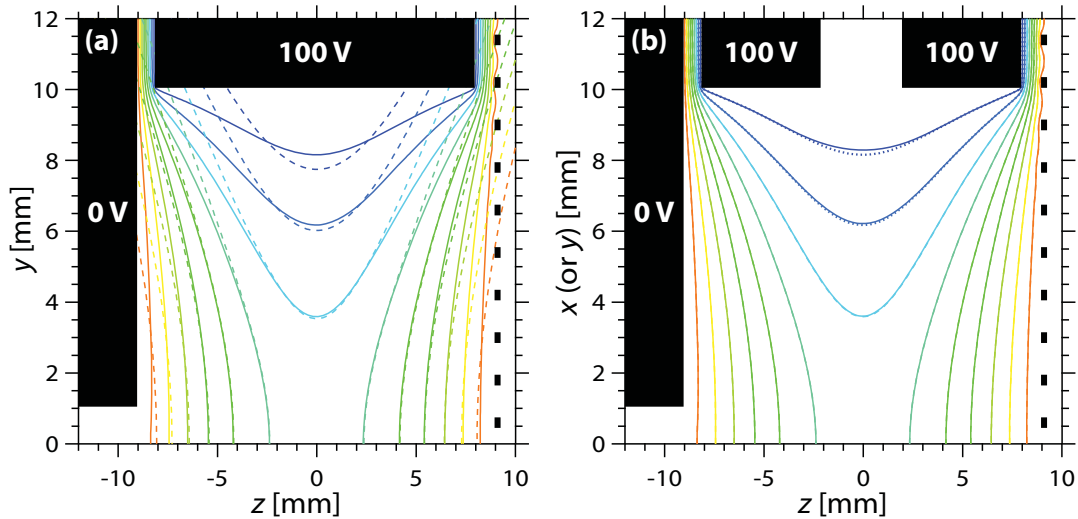


Figure 3.4: Shows calculated electric field gradients using an ideal quadrupole field (Dotted lines) and the simplified design (Full lines) for two different cross-sections of the trap. The two figures show the trap cut in two different planes.

3.2 Ion Trap

As mentioned earlier, the ion trap in this setup is a simplified version of the Paul trap. In a Paul trap (3D quadrupole), an RF field creates a rotating saddle point potential, that keeps the ions centred in the trap. The original Paul trap uses hyperbolic geometries to optimize the electric field gradients for ion trapping. The simplified version of the Paul trap used at LUNA uses a much simpler cylindrical geometry with planar end caps. This simplification results in minor changes to the field gradient, but as evidenced by the numerical calculations shown in Figure 3.4, the effect is only visible close to the edges of the trap. The simplified design is much easier to manufacture and the difference in trapping efficiency should be minimal for our setup, since the ions are entering the trap along z axis in figure 3.4. In the LUNA setup, one of the end caps has been replaced by a wire grid. This grid lets the emitted light be collected at a much larger solid angle than in other fluorescence setups[56–58]. The solid angle for light detection at LUNA is approximately ten percent.

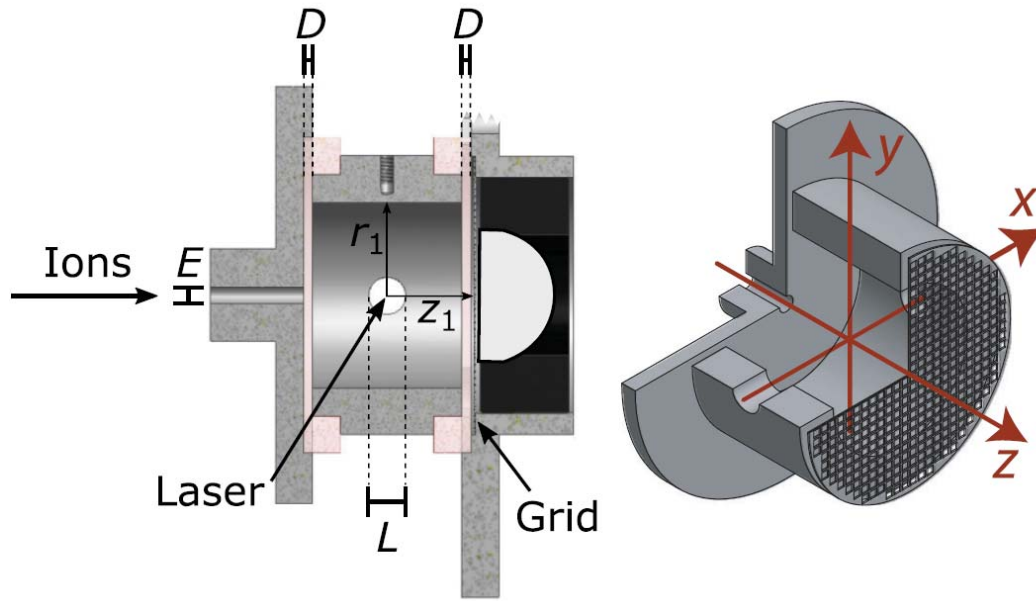


Figure 3.5: Crosssection view of the simplified Paul trap used at LUNA. A wire mesh grid acts as end electrode of the trap, allowing photons to pass through for subsequent detection. The pump laser is focused through the hole in the trap cylinder ($L = 4$ mm). The ion entrance is marked by E (2 mm). The trap dimensions $r_1 = 10$ mm, $z_1 = 9$ mm, the gap between the cylinder and end-cap electrodes $D = 1$ mm and the axes used for the numerical simulations are defined in the right-hand view, where the lens and its mounting system have been removed to reveal the grid.

3.3 Detection

The detection scheme at LUNA is a little different from SEP1, since we are now detecting photons and not ions. An illustration of the optical system for light collecting at LUNA can be seen in Figure 3.6 on the next page. The light emitted from the trapped ions is emitted in all directions. To detect as much light as possible, the collection lens (an aspheric condenser lens) is placed up against the grid electrode. The small distance between the lens and the ions results in a collection solid angle of approximately ten percent. After the condenser lens the light is collimated and directed through the vacuum window and a notch filter. This notch filter is a filter that prohibits transmission (transmits only 10^{-6}) of basically a single wavelength. This filter is used to filter out the scattered light

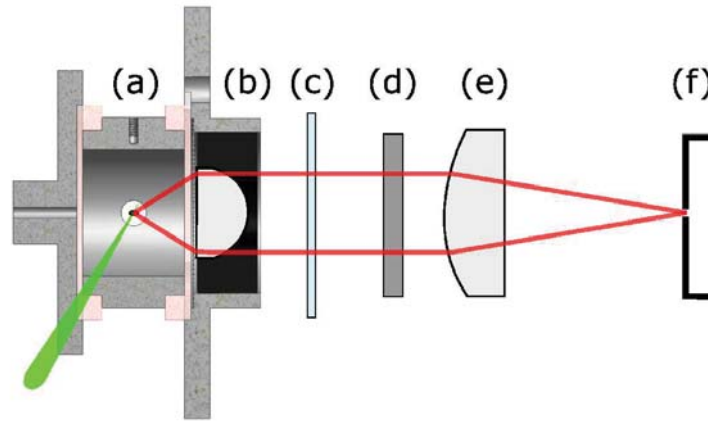


Figure 3.6: Illustrating the light collection in the LUNA setup. (a) simplified Paul Trap (b) collector lens (c) vacuum window (d) notch filter (e) focusing doublet lens (f) photon detector.

from the pump laser. The notch filter is composed of dielectric coatings which through destructive interference effectively blocks light at a specific wavelength. The destructive interference is most effective when light is normally incident on the filter. This is another advantage of using the condenser lens to collimate the light coming out of the trap. After the scattered light has been removed, the light is focused by a 100 mm focus length lens into the photon detector, which could be either a photo multiplier tube (PMT) or a spectrometer.

For measuring lifetimes of the excited states by fluorescence, a PMT can be used in much the same way as the channeltron at SEP1. A PMT consists of a thin photocatode that releases electrons when hit by a photon. This electron is then multiplied in a cascade effect as in the channeltron detector. The output current pulse is then measured through the same scheme as for the channeltron. A PMT does not give any information about the color of the photon. To be able to detect the color of the emitted photon, a spectrometer is needed.

The spectrometer used at LUNA is an Andor Shamrock SR-303i spectrometer. The working principal of the spectrometer is illustrated in Figure 3.7 on the facing page. Photons that enter the entrance slit are collimated by a mirror onto a diffraction grating. This grating separates the different colors in space. The

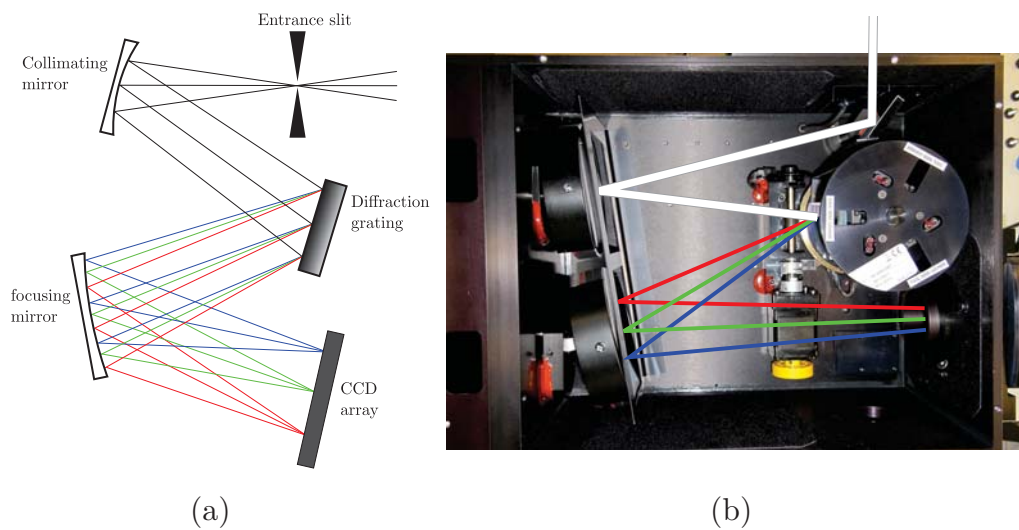


Figure 3.7: Illustrating the principle behind the spectrometer used at LUNA. (a) is a simple illustration of the working principle and (b) is an overlay of a picture of the actual spectrometer used at LUNA.

isolated colors are then focused onto a CCD array for detection by the refocusing mirror. The charge build up on the CCD array is measured and the intensity of light as a function of placement on the CCD *i.e.* the color of the light, can then be extracted. The angle of the mirrors and the line density of the grating can be controlled by the control software for the spectrometer, which makes it possible to control the resolution and optical range for the measurement. Likewise it is possible to adjust the speed and method of which charge is read from the CCD in order to maximise the reading speed, while still keeping the electric readout noise at a minimum.

3.4 Mass selection

3.4.1 Mathieu stability diagram

The behaviour of ions in a quadrupole ion trap can be described by the second order linear differential equation known as the Mathieu equation [59, 60]. When written for ion motion in an ideal quadrupole field, the Mathieu equation is given by

$$\frac{d^2u}{d\xi^2} + [a_u - 2q_u \cos(2\xi)]u = 0, \quad (3.1)$$

where, $\xi = \Omega t/2$ is a dimensionless parameter, with Ω being the radial frequency of the ring electrode potential, u represents the x , y and z coordinates and a and q are dimensionless trapping parameters (when cylindrical coordinates are used)

$$a_z = \frac{-16qeU_0}{m(r^2 + 2z_0^2)\Omega^2}, \quad (3.2)$$

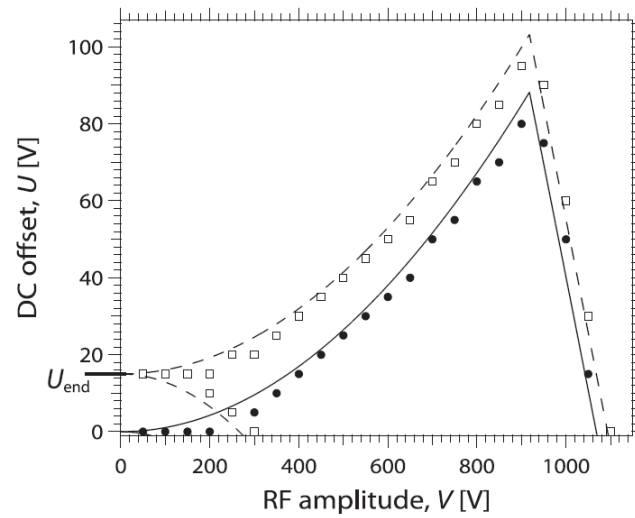
$$q_z = \frac{8qeV}{m(r^2 + 2z_0^2)\Omega^2}, \quad (3.3)$$

where m and qe are the mass and charge of the ion, Ω and V are the angular frequency and amplitude of the RF potential, $U_0 = U - U_{\text{end}}$ is the difference between the offset potential on the ring electrode and the potential on the end cap. The trapping parameters for r is given by $a_r = -a_z/2$ and $q_r = -q_z/2$

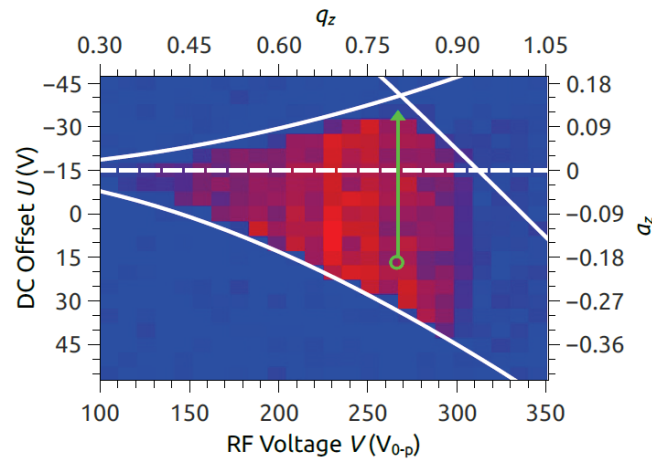
The parameters r_0 (the inner radius of the cylinder electrode) and z_0 (the distance from the center of the trap to the end-cap) are defined for the quadrupole ion trap, with hyperbolic electrodes. Numerical modelling of the simplified cylindrical geometry of our trap found effective values of $r_0 = 9.2$ mm and $z_0 = 8.8$ mm to be appropriate (the physical dimensions of the trap are $r_1 = 10$ mm and $z_1 = 9$ mm). Using Newton's law of motion it can be shown that only ions with certain values of a and q have stable trajectories inside the trap. Mass selection is achieved by adjusting U and V such that only ions of the desired m/z have a and q parameters within the stability region, *i.e.* at the peak of the stability region. In Figure 3.8 on the next page a numerical calculation and an experimentally obtained stability diagram are shown.

To maximise the number of ions stored in the ion trap, ions are loaded into the trap at a high-acceptance point of the Mathieu diagram. When all the ions are trapped (at low mass selectivity) the RF-DC offset is moved into the mass selecting point, this is illustrated by the green arrow in Figure 3.8(b) on the facing page.

Due to limitations on the RF amplitude two power supplies are used for mass selection. A 770 kHz RF supply is used for trapping



(a)



(b)

Figure 3.8: (a) Simulated stability region for an ion of 163 amu ion. The filled circles and open squares represent the simulated stability region with the end cap electrodes kept at ground potential and at 15 V, respectively. Also shown are the two theoretical stability regions, one for grounded end-caps (solid) and one for 15 V potential on the end cap (hollow). (b) Experimentally determined stability region for Rhodamine B cations ($m/z = 404$ amu). This is, to my knowledge the first published stability diagram measured by luminescence. The white lines are the stability boundaries for an ideal quadrupole potential. The green arrow shows the optimal DC pulse for ion accumulation and subsequently mass selection.

ion masses below approximately 200 amu, and a 250 kHz RF supply is used for ion masses above 200 amu.

3.4.2 Numerical simulations

Numerical simulations were carried out to estimate the ion cloud size and position, and to assist in the selection of trapping parameters. The numerical simulations were performed using the SIMION 8.0 software. All calculations were performed by former Postdoc. Annette Svendsen. SIMION calculates the electric fields of a given geometry and uses these fields to simulate how ions with a certain distribution of kinetic energies, masses and charge will be effected by the electric fields for given starting conditions. The full details of the simulations will not be covered in this thesis, and only the main parameters and results will be presented. Figure 3.9 on the next page shows the simulated ion density for ions with mass 163 amu and 479 amu. The dotted lines in Figure 3.9 shows the dimension of the laser-entrance hole. From the size of the hole, it is clear that it is possible to irradiate the whole ion cloud by the pump laser. Early experiments showed that it was possible to deplete more than half of the stored ion population with a single laser pulse.

3.4.3 Fundamental frequencies

The trajectory of a single trapped ion with no initial velocity is a planar motion in the x-y plane, illustrated by the figure of eight motion depicted in Figure 3.10(a) on page 32. When the trapped ion has an initial velocity in the x direction, the motion becomes the well know saddle point motion, illustrated by the trap potential in Figure 3.10(b).

The motions of the ions in the trap, are 3D figures of eight, composed of two secular frequencies ω_r and ω_z . The following equations hold for both the r and z components, with $q_r = -q_z/2$ and $a_r = -a_z/2$, where a_z and q_z are given by Equation 3.2 on page 28.

$$\omega_{u,n} = \left(n + \frac{1}{2}\beta_u \right) \Omega \quad \text{for } 0 \leq n < \infty, \quad (3.4)$$

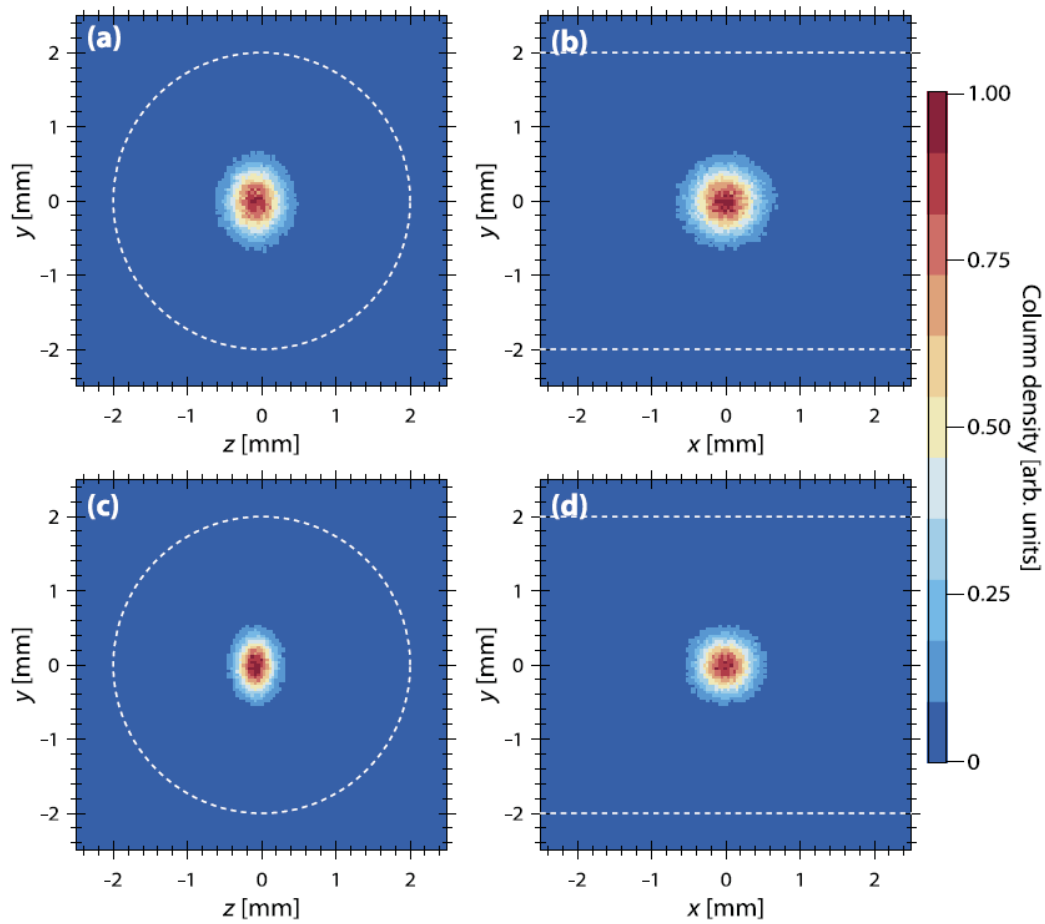


Figure 3.9: Panels (a) and (b) show calculated ion densities for 163 amu single charged anions trapped at an RF amplitude of 450 V, RF frequency of 770 kHz and with end-cap potentials of 15 V. Panels (c) and (d) show calculated ion densities for 479 amu single charged cations trapped at an RF amplitude of 1000 V, RF frequency of 770 kHz and with end-cap potentials of -15 V. The ion clouds are viewed along the x (a and c) and z (b and d) axes. The white dashed lines indicate size of the laser entry hole.

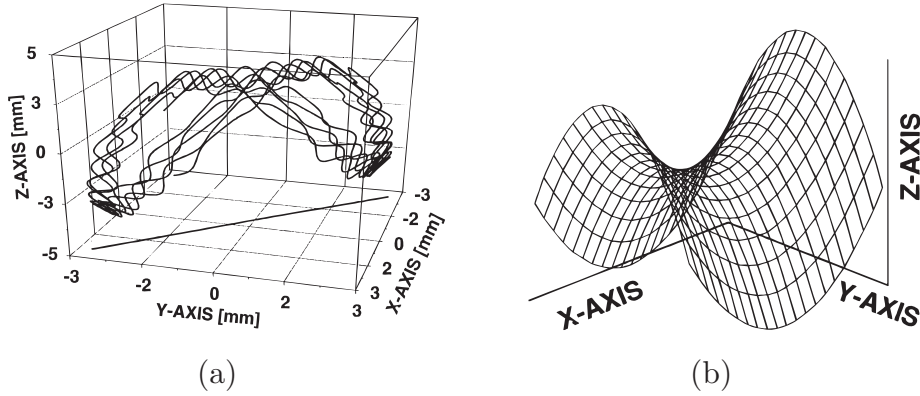


Figure 3.10: (a) Trajectory of a single trapped ion with initial position randomly selected and with no initial velocity. Taken from ref [61]. (b) Pure quadrupole potential surface for quadrupole ion trap. Taken from ref. [60].

where Ω is the RF angular frequency and β_u is a number between 0 and 1, and is given by the simple formula

$$\beta_u = \left[a_u + \frac{q_u^2}{2} \right]^{1/2}, \quad (3.5)$$

when $q_r < 0.2$ and $q_z < 0.4$. If this is not the case, β has to be calculated by a continued fraction expansion[60].

$$\begin{aligned} \beta_u^2 = a_u + & \frac{q_u^2}{(\beta_u + 2)^2 - a_u - \frac{q_u^2}{(\beta_u + 4)^2 - a_u - \frac{q_u^2}{(\beta_u + 6)^2 - a_u - \dots}}} \\ + & \frac{q_u^2}{(\beta_u - 2)^2 - a_u - \frac{q_u^2}{(\beta_u - 4)^2 - a_u - \frac{q_u^2}{(\beta_u - 6)^2 - a_u - \dots}}} \end{aligned} \quad (3.6)$$

This expansion can be approximated[62] by

$$\beta_u = \left[a_u - \frac{(a_u - 1)q_u^2}{2(a_u - 1)^2 - q_u^2} - \frac{(5a_u + 7)q_u^4}{32(a_u - 1)^3(a - 4)} - \frac{(9a_u^2 + 58a_u + 29)q_u^6}{64(a_u - 1)^5(a_u - 4)(a_u - 9)} \right]^{1/2}. \quad (3.7)$$

Using the equations above, it is possible to calculate the fundamental ($n = 0$) frequencies for the ion motion in both the radial and axial dimension for a specific mass to charge ratio. By applying a small RF potential, of frequency $\omega_{z,0}$ on the end caps of the ion trap, it is possible to resonantly excite a specific ion mass, and thereby eject it out of the trap. This resonant excitation can be used for single ion excitation, time dependent single ion excitation using a chirp pulse (a single sine function with increasing frequency), multiple ion excitation using a custom potential time series and much more. An interesting option regarding mass selection, is the excitation of multiple frequencies at once. This can be done by applying the inverse Fourier transform of a specific frequency structure, which then results in a potential time series containing all the wanted frequencies. This method is called stored waveform inverse Fourier transform (SWIFT) ion excitation.

3.4.4 SWIFT

I recently designed and built a SWIFT excitation add-on for the Paul trap at LUNA. For the sake of reference, a simple guide to SWIFT calculations for the hardware used at LUNA is given below. Details regarding the understanding of fast Fourier and fast inverse Fourier transform as well as general DAC systems are outside the scope of this thesis, and only the simple steps for calculating the SWIFT pulse will be given below. For graphical illustration of the SWIFT pulse generation, see Figure 3.11 on the following page.

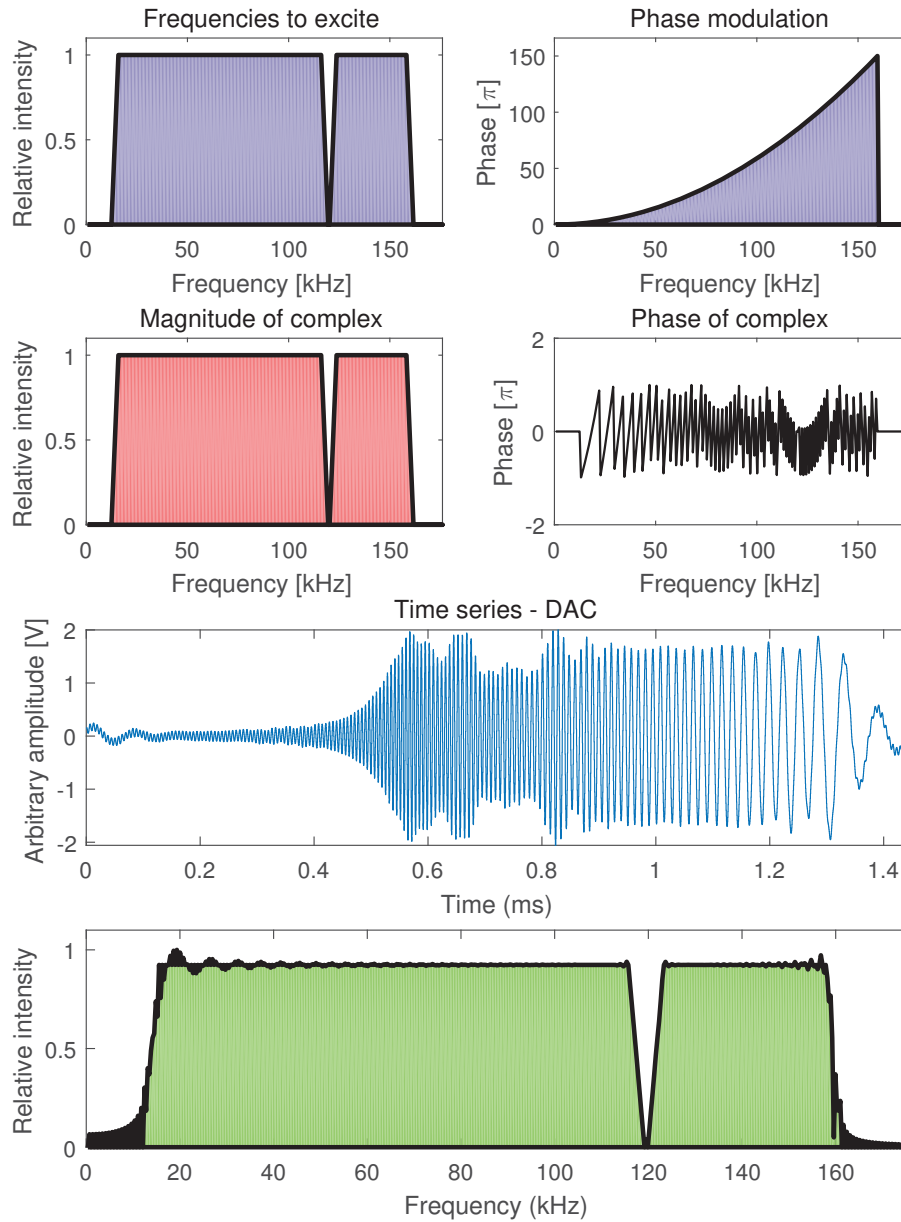


Figure 3.11: Illustration of a calculated SWIFT pulse. For calculation details, see text. First row: Specified frequency magnitude and phase for which to calculate the inverse Fourier transform. Second row: Corresponding magnitude and phase of the complex frequencies. Third row: Inverse Fourier transform of the frequency spectrum. Here matlab's inverse fast Fourier transform algorithm has been used. Fourth row: Fourier transform of time series zero padded on both sides to represent the actual output pulse. This illustrates the actual frequency spectrum of the SWIFT pulse.

1. Create frequency and time arrays that fit in resolution and length to the DAC hardware update rate and buffer. In this case, the onboard buffer of the DAC card (NI USB-6351 from National Instruments) has a length of $l = 4095$ and an analog output rate of $f = 2.86$ MS/s. The arrays can maximum be l long. The time resolution is $1/f$ and the frequency resolution is f/l .
2. Next, the frequency structure has to be defined. This can be done in a number of different ways, in this example, a smoothed step function has been used. It can be seen that a specific frequency is missing in this example (Figure 3.11 on the preceding page), this corresponds to the frequency of the specific ion that we want isolated in the trap.
3. A phase modulation needs to be applied to the frequency spectrum to produce a SWIFT pulse that is not a sharp peak at time zero. Here a simple quadratic phase modulation relation is used. For a more rigorous investigation of magnitude smoothing and phase modulation the reader is referred to ref. [63] and [64].
4. Create a complex array formed by the magnitude array and phase array. The complex number should be on the form ae^{-ib} where a is the magnitude and b is the phase.
5. When the complex frequency spectrum has been obtained, use you favourite software to calculate the inverse Fourier transform, which along with the time array generated in step 1, is the potential time series that needs to be applied to the end caps of the trap.

When a SWIFT pulse is used for excitation with mass spectrometry in mind, there are many different smaller corrections to the simple step-by-step above[65]. But for our use, this simple way of doing it should work just fine. For an overview of the applications and calculations of the SWIFT pulses the review article by Shenhen Guan and Alan G. Marshall is highly recommended[66].

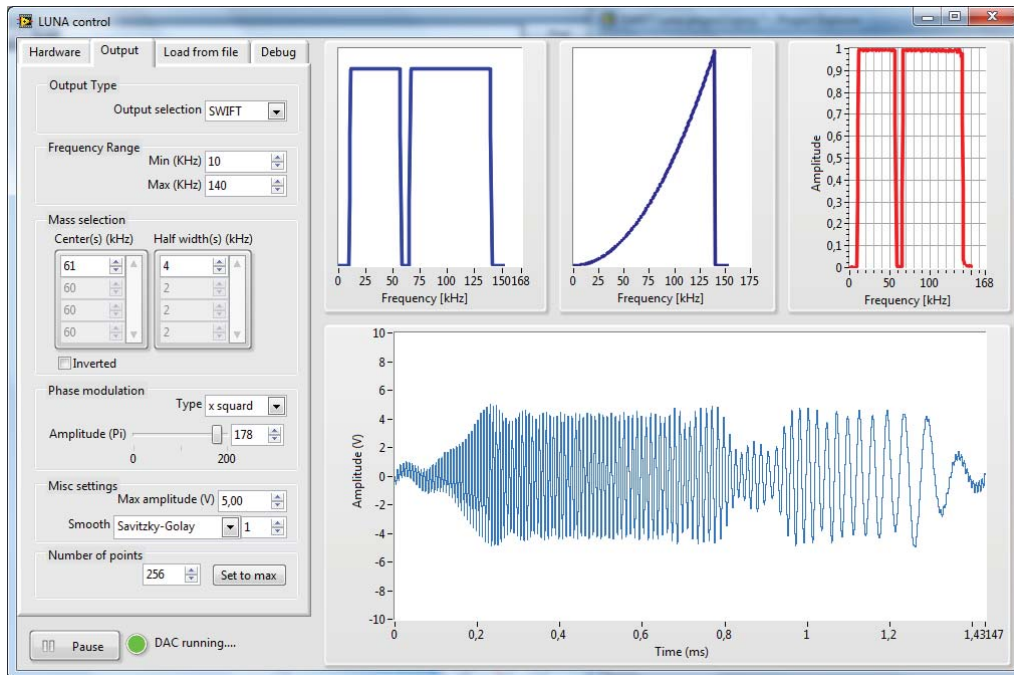


Figure 3.12: User interface of SWIFT generation software in SWIFT pulse mode. The software has the additional ability to create a SWIFT pulse with multiple "holes", and to create an *inverse* SWIFT pulse, where you kick out ions in multiple ranges.

The SWIFT method is a new method in our lab (first tried implemented in July 2016) and the effectiveness of the setup has yet to be determined.

The software used for SWIFT generation and hardware control is written in LabVIEW. The software user interface is shown in Figure 3.12 for SWIFT generation and in Figure 3.13 on the next page for single sine and chirp pulse generation. The current setup uses a standard DAC for generating the potential waveform, this is a cheap way of building an arbitrary waveform generator. The downside of not using a dedicated arbitrary waveform generator is the update rate. With the current setup, a maximum frequency of approximately 300 kHz can be generated before the trace starts to look distorted. With a dedicated arbitrary waveform generator, with update rates of 400 MS/s this limit is two orders of magnitude higher. The maximum needed frequency is determined by the RF frequency of the trap. The maximum frequency to apply in order to excite the lowest trapped mass is $\Omega/2$. When working at the

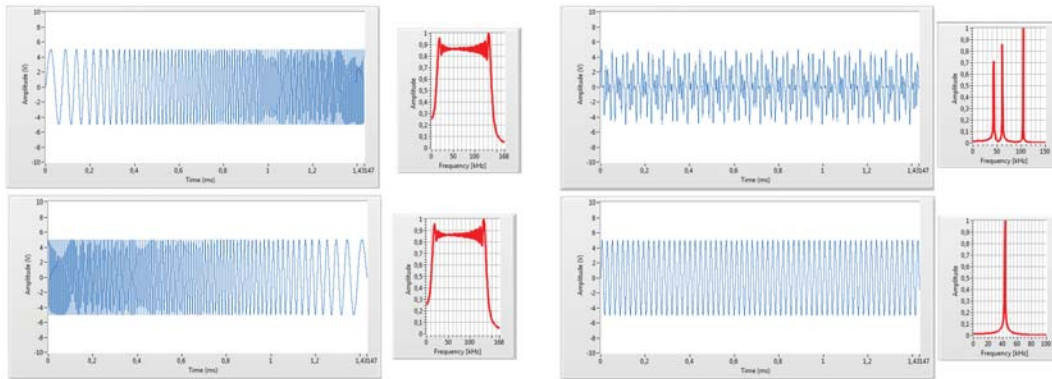


Figure 3.13: Other modes of operation: Chirp and reversed chirp pulse mode used for ion ejection TOF. Single and multiple single frequency sine functions for single ion ejection.

limit of the frequency range, my concern is that the limitations in generating a smooth waveform can introduce unwanted frequency components in the SWIFT pulse, and thereby limit the effect. This potential effect has yet to be tested in detail.

Since the SWIFT-technique has only just been implemented as of writing this thesis, only preliminary tests have been performed. A simple scan of the center frequency of a SWIFT pulse ranging from 10 kHz to 150 kHz, and with a center half-width of 5 kHz can be seen in Figure 3.14 on the following page. The sample probed is Rhodamine 6G with tap water added, which should result in a small shift of the emission wavelength due to Rhodamine 6G + salt complexes. The figure shows the measured emission spectra for each SWIFT center frequency. The data is presented in a contour view, where the data is projected onto the wavelength and SWIFT center frequency axis. The data clearly shows that SWIFT pulses can be used to excite ions out of the ion trap, while keeping a specified mass over change stored. Further more, it can be used to identify the fluorescent species stored in the ion trap. By the use of Equation 3.2 on page 28, Equation 3.4 on page 30 and Equation 3.7 on page 33, it is possible to calculate the ion mass corresponding to each SWIFT center frequency. This is shown in Figure 3.15 on page 39. According to the simple gaussian fit, the fluorescent ion has an mass of 506 amu. This ion mass could be a result of adding a single copper ion to the Rhodamine dye. The shift in

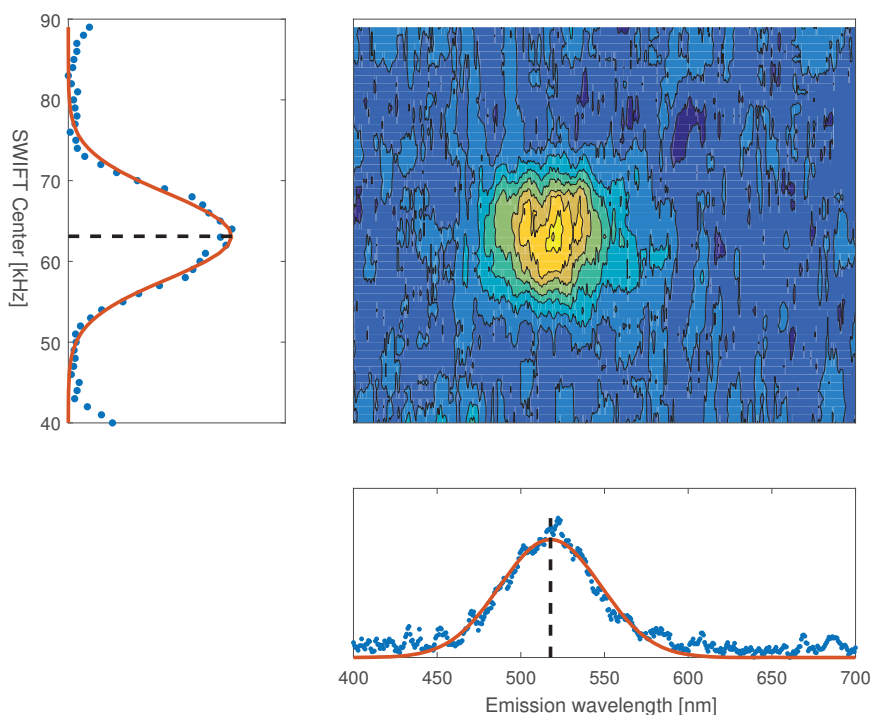


Figure 3.14: A scan of center frequency of a SWIFT pulse (for further description, see tekst). Projections are made onto the wavelength axis and center frequency axis.

emission wavelength (518 nm) compared to the bare Rhodamine 6G (504 nm)[67] is 0.07 eV, which is also what is seen when adding copper to Rhodamine 6G in solution phase[68]. The interpretation of the experimental results above clearly requires more work before drawing an actual conclusion, so the simple observations above should not be taken as from a well conducted scientific experiment, but more as a curious observation. It is clear that the mass band, see Figure 3.15 on the next page, is very broad, even when taking into account the convolution of the width of the SWIFT band center frequency, the FWHM is still on the order of 80 amu. The mass resolution can be further enhanced by adjusting the number of SWIFT pulses, the peak-peak voltage of the SWIFT pulse, and so on. Overall the SWIFT technique brings some very interesting options for the LUNA setup. Unfortunately it has not yet been used for any real experiments, so the true value of the technique and its

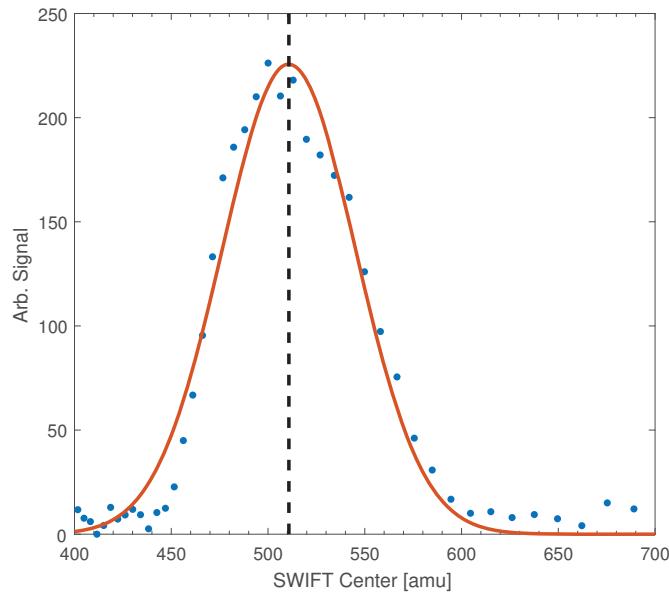


Figure 3.15: Showing the data from Figure 3.14 on the preceding page projected onto the SWIFT center axis, where the SWIFT center frequency has been transformed to the corresponding ion mass over charge. For further details, see text.

possibilities for the LUNA setup has yet to be discovered.

3.5 Data acquisition

As mentioned earlier, one of the greatest advantages of using light emission to probe the electronic structure of ions, is the simplification of the data analysis and interpretation. When analysing data from SEP1, one has to take into account: the PID fragments and their relative yield - which often can be difficult to determined correctly; the power dependence for each fragment ion; ion beam fluctuations, which often are difficult to monitor; the possibility of having kinetic shifts and the difficulty in modelling non-coherent multi photon absorption. At LUNA many of these challenges are inherently avoided.

Kasha's rule states that photo emission predominately happens from the lowest lying electronic state. This means that light emission

probes the first excited state, while the pump beam absorption can probe overlying states. This also means, that if the ion absorbs multiple photons and subsequently dissociate, the signal is not recorded by the spectrometer since no light is emitted. The number of ions in the ion trap does not matter, since all emission wavelengths are measured at once. Furthermore, effects like kinetic shifts are clearly not an issue when dealing with light emission from ions stored in a trap. The only aspect one needs to be aware of, is the transmission coefficients of the optical system, and the detection efficiency of the CCD camera or PMT as a function of photon energy. The transmission coefficient of the optical system and the efficiency if the CCD only varies by a small amount across the visible spectrum, but the non-reflective coating on the optical elements can begin to have an actual effect on the detection efficiency of the system when the emitted light is in the IR range. A correction to the non-perfect transmission efficiency is easily applied on the basis of the transmission coefficients for the different optical coatings.

3.6 Control sequence

The trigger timings at SEP1, is used to make sure the laser and ions overlap in time. At LUNA however, the trigger timings are a little more delicate. The mass selection mechanism at LUNA can first be applied when the ions are in the trap, otherwise the DC potential of the cylinder or the RF on the end caps will affect the efficiency with which ions are transferred into the ion trap. This means that we can not continually feed ions into the trap. To overcome this problem, we have developed a custom control sequence for the LUNA experiment, shown in Figure 3.16 on the facing page. Ions are continually filled into the pretrap octopole. The octopole pretrap empties at T_1 , where the ions are transferred into the Paul trap. When the ions have all been trapped, mass selection methods can be applied at $T_2 = T_1 + 1$ ms. The duration of the mass selecting step can be varied, it is usually approximately 2 ms for DC mass selection and approximately 30 ms for SWIFT mass selection. The laser is fired after mass selection at T_3 and the camera is triggered. The minimum exposure time of the camera is approximately 2 ms.

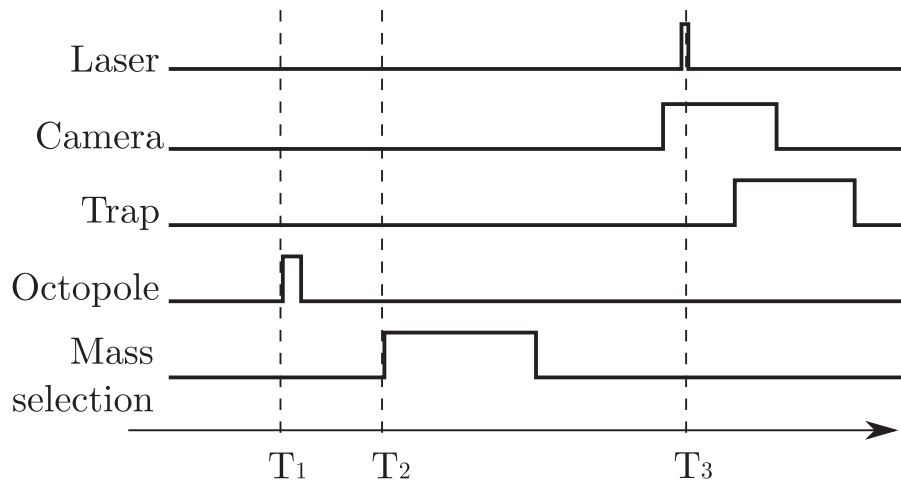


Figure 3.16: Timing scheme for the LUNA experiment. See text for more detail.

After the picture is acquired, the trap is triggered and emptied. When triggering the trap, the RF is turned off and the polarity of the end caps are inverted, which empties the trap of ions. After this step, the whole sequence starts over. At LUNA, the CCD camera controls when the ions should be off for background measurements. This guarantees that the data collection is synchronized with the trapping sequence, and that light emission always gives rise to a positive difference signal measurements. In the camera control program, we set a number of frames that we want taken for both background and signal. When the camera acquires a background frame, it sets a *Shutter* output low. This low output is inverted to a high output that continuously triggers the ion trap power supply and no ions are trapped. The software is written to automatically subtract the background from the actual signal. To make sure that the trap is triggered normally when taking the actual signal, the trap-trigger from LabVIEW and the shutter-trigger from the camera are added as illustrated in Figure 3.17 on the next page.

3.7 Control and analysis software

The control software for LUNA is much simpler than the one for SEP1, simply due to the fact that, as described before, the fluorescence

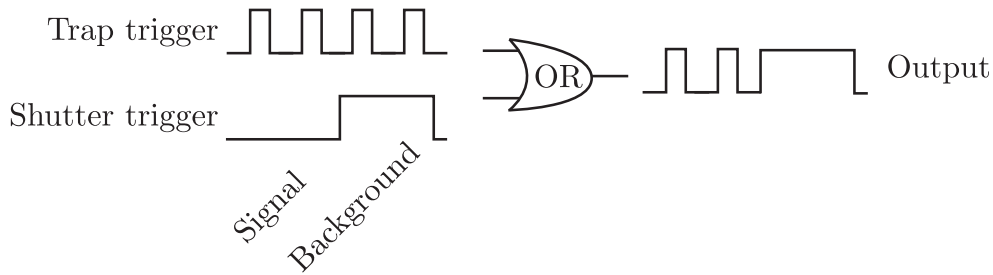


Figure 3.17: Output from LUNA-timing control and shutter output from camera combined to a single signal for triggering the ion trap at LUNA.

experiment is much simpler. Aside from CONSYS, there are two additional critical software components to the to the LUNA control software. A LabVIEW program controls timing trigger and an *Andor Basic* script controls the data acquisition. The triggering control software controls a *PCI-6602* counter card from National Instruments. The *PCI-6602* card has eight internal counters. These counters are used to create trigger signals of a given length and at a given delay compared to a so called *Master Trigger*. The *Master Trigger* is set to run at 20 Hz to match the rate of the lasers used. The other seven counters are used to create triggers for everything else. The UI of the program can be seen in Figure 3.18 on the facing page.

The *Andor Basic* scripted control sequence is structured in the following way: The basic setup requires the user to input the number of frames per acquisition x , and the total number of acquisitions n . After the initial setup the camera takes x frames with the trap triggered, *i.e.* a background measurements and x signal frames with ions in the trap. When this is done, the software updates the total accumulated signal, and saves the current acquisition to a file for use in other programs. This sequence is run n times, or until terminated by the user. When the data acquisition is complete, another program can be used to generate the final datafile. The final datafile contains information about the current ion, excitation wavelength, filter type, CONSYS info, trigger settings and more.

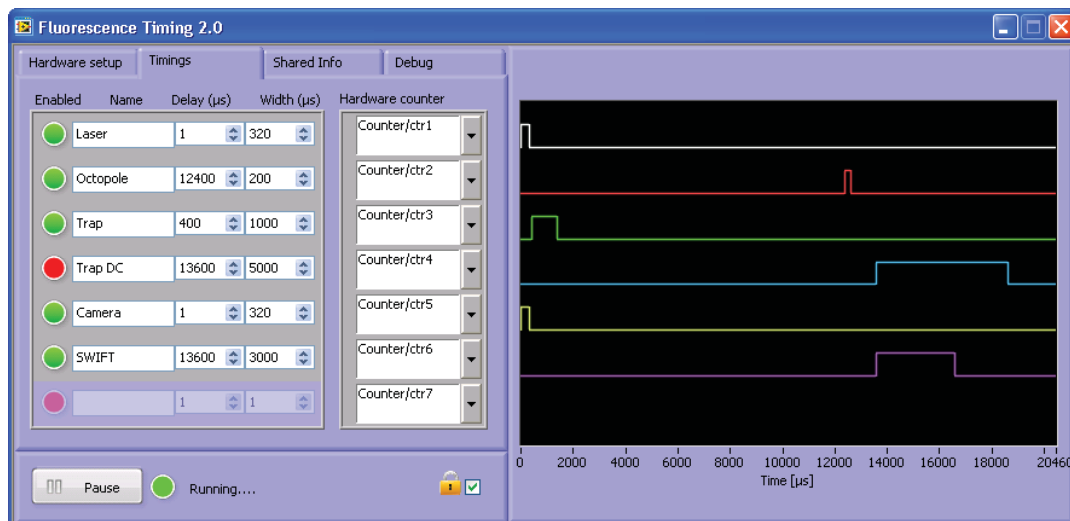


Figure 3.18: User interface of the trigger software used at LUNA. The individual triggers can be enabled, disabled and renamed as needed.

3.8 Florescence spectra

The major downside of luminescence experiments on ions in the gas phase, is the usually low quantum yield for light emission. Luminescence has to compete with internal conversion vibrational relaxation and dissociation which for most ions are much faster than luminescence. The first fluorescence spectra taken at LUNA, was of laser dyes in the Rhodamine family in December 2015 (paper **VIII** [69]). The fluorescence yield is close to 100 % for these ions, which makes them optimal systems for testing purposes. The quality of the spectra seen in Figure 3.19(a) on page 45 obtained at LUNA, is comparable to those reported by others[67], which confirm that the experimental setup is working.

As of July 2016 the ion with the lowest quantum efficiency for light emission that we have measured at LUNA, is Nile Blue (NB) (paper **IX** [70]) with a quantum efficiency of maybe approximately 10 % [71, 72]. NB has been used as a bio marker in biological systems [73, 74], and as a benchmark for quantum chemical calculations [75, 76]. The colour of NB in solution varies greatly depending on the solvent used, However, the colour does not have a simple dependence on the polarity of the solvent [76, 77]. The NB action spectra and emission spectra measured at SEP1 and

LUNA are shown in Figure 3.19 on the facing page. The spectra clearly show the beauty of the fluorescence experiment compared to the photo-dissociation action spectroscopy experiment conducted at SEP1. The emission spectrum is much more smooth than the absorption spectrum, and much simpler to analyse.

There are a couple of reasons why we are able to acquire emission spectra of low quantum yield gas phase bio molecular ions. The first, and perhaps most important, is that the solid angle for light detection in LUNA is an order of magnitude higher compared to other systems[53, 58, 67]. Due to the high detection efficiency at LUNA, it is possible to use low repetition rate lasers. Low repetition rate lasers (Hz to kHz) are often tunable over a large wavelength region. 20 Hz tunable nanosecond lasers are currently used at LUNA, but the setup would work equally good with a high repetition rate or even a continuous wave laser. The lasers currently used at LUNA can output from UV to IR, enabling us to probe excitations over a broad range. The notch filters used at LUNA are positioned outside of the vacuum chamber, making it easy to change the filter to accommodate the specific experiment. Looking to the future, the modular design on LUNA enables the addition of a new cooling section, which would make it possible to study light absorption of cold ions. Furthermore, adding a drift tube for ion mobility mass selection would enable us to study light emission from structure selected ions.

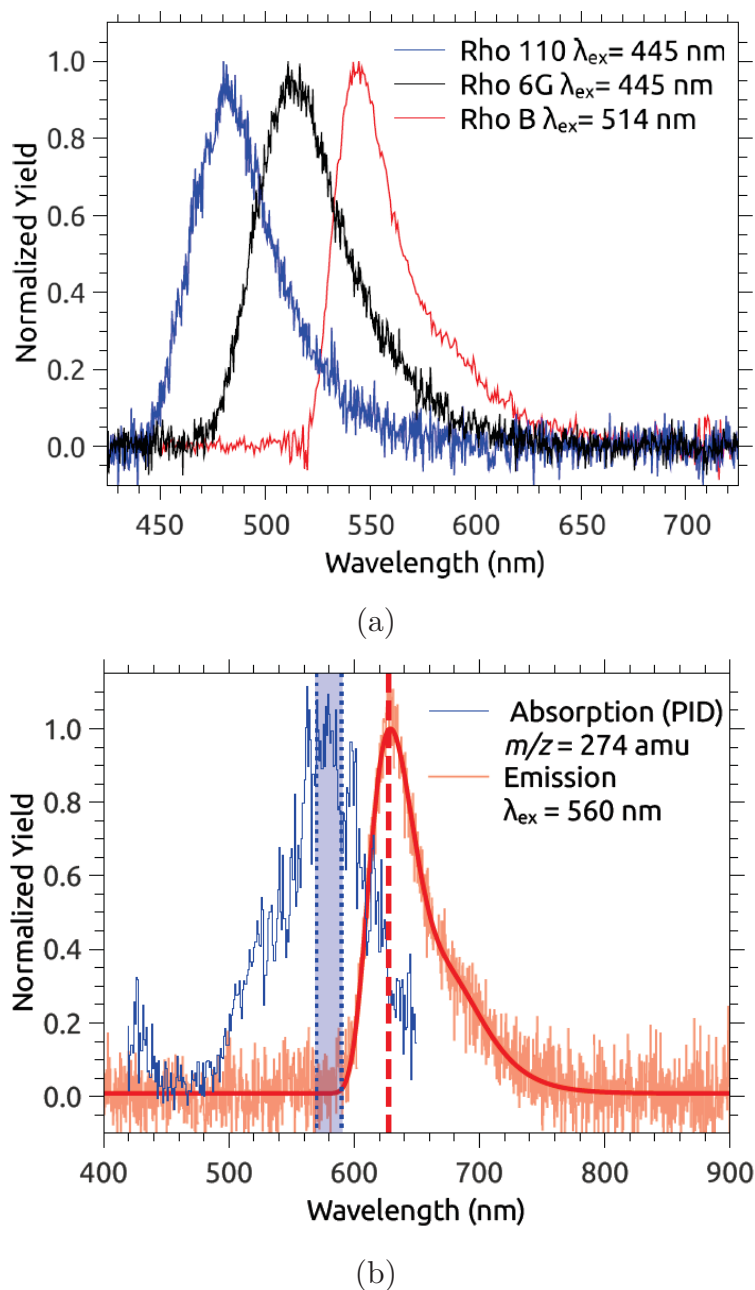


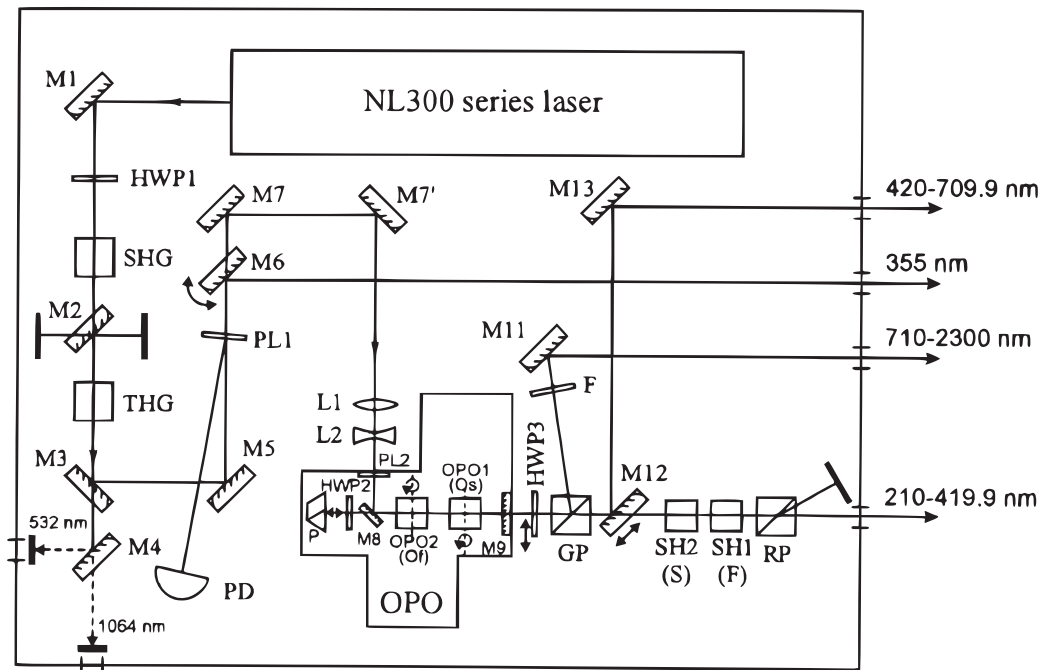
Figure 3.19: (a) Emission spectra of Rhodamine 110, Rhodamine 6G, and Rhodamine B cations excited at the indicated wavelengths. Figure from VIII. (b) Absorption (blue) and emission (red) spectra of Nile Blue in vacuo. The solid red line is a fit to the emission data. The vertical lines indicate the absorption and emission band maxima and their uncertainties. Figure from IX.

Experimental Setup - Light Sources

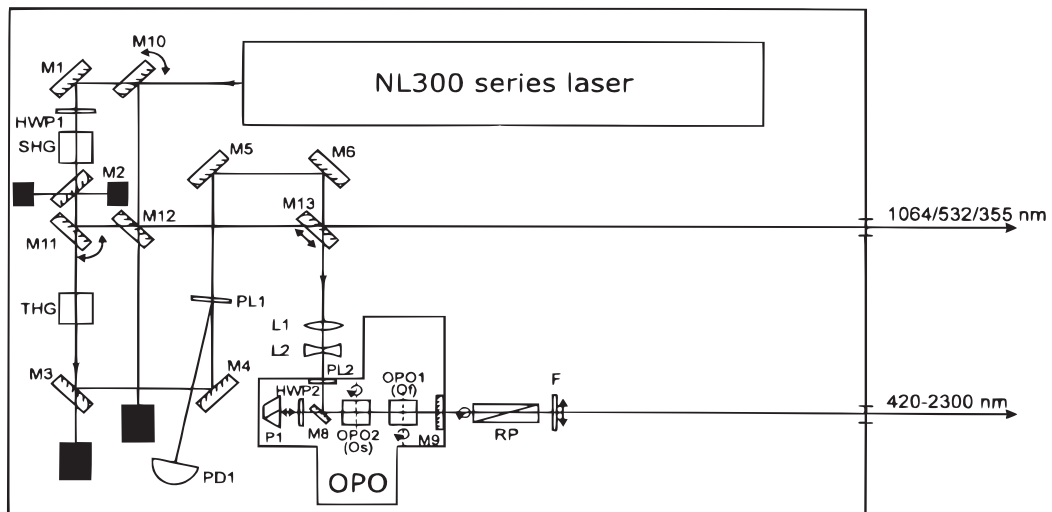
Since lasers are an essential part of the current experimental setups in our lab, the laser systems will be described in some detail here. In addition to the actual lasers, a description of a sum-frequency generating laser add-on will be described. Currently two laser systems are installed in the lab. The two lasers are both EKSPLA Q-switched nanosecond pulsed lasers, where the laser medium is a Nd:YAG crystal. Together the two lasers span a wavelength region from 210 nm (UV) to 2300 nm (IR). The two lasers are shown schematically in Figure 4.1 on the next page. The full details of laser operation are outside the scope of this thesis, and therefore only a brief description of the working principal will be given[78].

4.1 Stimulated emission

The laser medium used for the two lasers is Nd:YAG (neodymium-doped yttrium aluminium garnet) crystals. A simplified energy diagram of neodymium is illustrated in Figure 4.2. The neodymium is an effective four level system, where the transitions from the pumped E_4 level to the E_3 level and from the E_2 level to the E_1 are fast and non-radiative, but the transition from E_3 to E_2 is slow in comparison. The difference in the lifetimes of the different



(a)



(b)

Figure 4.1: (a): Laser 1. (b): Laser 2. Both lasers are Q-switched nanosecond pulsed lasers. They both utilize an OPO for wavelength tuning. The main difference between the two lasers is that Laser 1 has two extra second harmonic generating crystals (SH1 and SH2) used to generate photons in the UV. [Illustrations copied from laser manual]

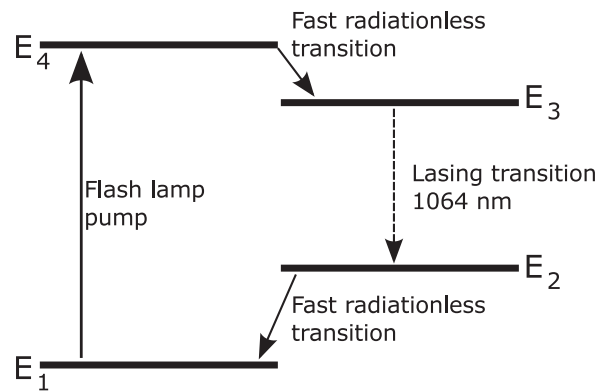


Figure 4.2: Schematic view of the energy levels of neodymium atoms used for population inversion.

energy levels ensures that when the system is excited by the use of flash lamps, the excited systems accumulate in the E_3 state. When the E_2 state is depleted, population inversion is obtained between E_3 and E_2 . An incoming photon with the right energy can then stimulate emission of a second photon from the laser medium. When population inversion is achieved, stimulated emission of a new photon is far more likely than absorption of the incoming photon. The stimulated photon has the same energy and phase as the photon that triggered the emission. If two highly reflective mirrors are placed on either side of the laser medium, a laser cavity is created (Figure 4.3 on the following page), where light can bounce back and forth giving rise to a cascade of stimulated photons. In order to get the light out of the cavity one of the mirrors transmits a small percentage of light. This mirror then acts as an output coupler for the cavity.

The mechanism described above will give rise to a continuous wave (CW) laser. When an intense laser pulse is needed, the laser must be driven in pulsed mode. When a laser is pulsed, the average CW power is concentrated to a pulse length of for instance 5 ns, which dramatically increasing the peak intensity. The EKSPLA lasers at SEP1 are Q-switched lasers. Q-switching is the switching of the quality of the laser cavity *i.e.* the ability to keep the photons inside the cavity. In the particular laser systems used at SEP1, a Pockels Cell and a polariser do the Q-switching, see Figure 4.3 on

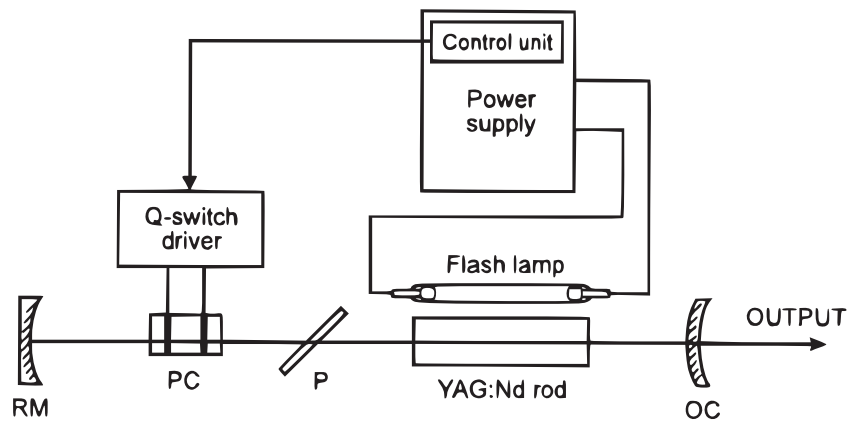


Figure 4.3: Illustration of the laser cavity in the two lasers at SEP1.
[Illustration copied from laser manual]

the next page. When the quality of the cavity is low, the Pockels Cell acts as a Quarter-wave plate, and the phase of the linearly polarized light, is changed by $\pi/2$ during one round trip. Since the polarization of the light is turned ninety degrees, the polariser will now absorb most of the light, and no lasing is achieved. During the time of low quality, the gain *i.e.* population inversion, of the system increases, only limited by spontaneous emission. This high gain is transferred into a very intense laser pulse when the cavity quality is raised. This is done by applying a high voltage (approximately 3 kV) to the Pockels Cell, which then acts as a half wave plate, switching the polarization of the photons by π per cavity round trip. A change in polarization of π results in an effectively unchanged polarization, which is then transmitted through the polariser and reflected of the end mirror. When the photons stay in the cavity, a cascade of stimulated emitted photons are created after a few cavity round trips, and a laser pulse is emitted.

4.2 Laser timing

The laser timing needs to be controllable, for the laser to be of use in a pulsed experiment. The triggering mechanism, for the specific lasers at SEP1, is illustrated in Figure 4.4 on the facing page. The input trigger pulse is shown in the top frame. When

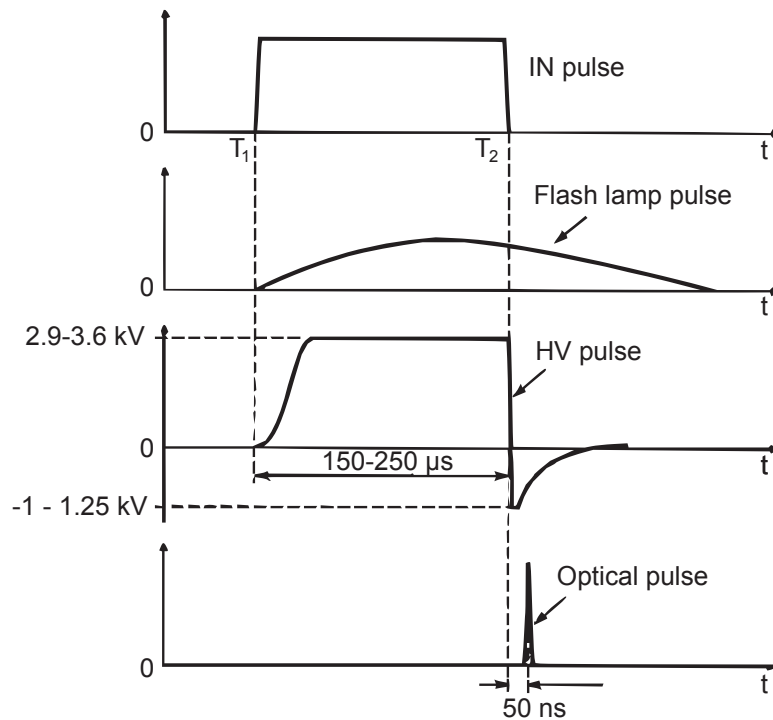


Figure 4.4: Laser timing scheme [Illustration from laser manual].

the input trigger voltage is raised, the power supply capacitors discharge through the flash lamps and closes the Q-switch. When the input trigger goes low, the Q-switch is opened and a laser pulse is generated. The length of the trigger pulse determines the amount of population inversion reached, and thereby influences the output laser pulse power. By adjusting the width of the trigger signal, the laser pulse intensity can be varied, but beyond certain values, the output of the laser becomes unstable. A typical pump duration is approximately 300 μs .

4.3 Light manipulation

The Nd:YAG fundamental 1064 nm laser pulse is frequency doubled (1064 nm+1064 nm) and tripled (1064 nm+532 nm) in two non-linear Deuterated potassium dihydrogen phosphate (KD_2PO_4 , DKDP) crystals resulting in a 355 nm laser pulse. This pulse pumps an optical parametric oscillator (OPO)[79] to generate tunable light

in the visible and UV range. Since light manipulations by non-linear effects is of great importance for all the laser systems used at SEP1 and LUNA, an overall explanation is given here.

In our first year physics courses, we learn that polarization in the dielectric material is linearly proportional to the applied electric field. This is only true as an approximation. In reality the polarization is composed of many terms both linear and non-linear, which comes into play at high electric fields strengths:

$$P(t) = \varepsilon_0(\chi^{(1)}\mathbf{E}(t) + \chi^{(2)}\mathbf{E}^2(t) + \chi^{(3)}\mathbf{E}^3(t) + \dots), \quad (4.1)$$

where ε_0 is the vacuum permittivity, $\chi^{(n)}$ is the n th order non-linear susceptibility for the medium. Without going into the details of the derivation, the non-linear terms in the polarisation leads to the standard non-linear wave equation:

$$\nabla^2\mathbf{E} - \frac{n^2}{c^2}\frac{\partial^2}{\partial t^2}\mathbf{E} = \frac{1}{\varepsilon_0 c^2}\frac{\partial^2}{\partial t^2}\mathbf{P}^{\text{NL}}, \quad (4.2)$$

where n is the refractive index of the medium, c is the speed of light, \mathbf{E} is the electric field and \mathbf{P}^{NL} is the non-linear part of what is called the polarisation density. This equation show the non-linear term as a driving force for the electromagnetic waves. One of the consequences of this is that energy mixing between different frequencies can occur. By the use of second order non-linearity

$$\mathbf{P}^{\text{NL}} = \varepsilon_0\chi^{(2)}\mathbf{E}^2(t), \quad (4.3)$$

and an electric field composed of two frequencies ω_1 and ω_2 , the non-linear polarisation will equate to

$$\begin{aligned} \mathbf{P}^{\text{NL}} = \varepsilon_0\chi^{(2)}\mathbf{E}^2(t) = \frac{\varepsilon_0}{4}\chi^{(2)}\left[& |E_1|^2 e^{-i2\omega_1 t} + |E_2|^2 e^{-i2\omega_2 t} \right. \\ & + 2E_1 E_2 e^{-i(\omega_1 + \omega_2)t} \\ & + 2E_1 E_2^* e^{-i(\omega_1 - \omega_2)t} \\ & \left. + (|E_1|^2 + |E_2|^2) e^0 + \text{c.c.} \right], \end{aligned} \quad (4.4)$$

where c.c is the complex conjugate. By inserting an electric field of two frequencies into the second order non-linear term of the polarisation, frequency components of $2\omega_1$, $2\omega_2$, $\omega_1 + \omega_2$ and $\omega_1 - \omega_2$ arise.

These frequencies are referred to as second harmonics generation, sum-frequency generation and difference-frequency generation. The discussion above illustrates the possibility of mixing different frequencies using non-linear optics, if the applied electric field is strong enough. The above discussion totally ignores the position and time overlap of the two components in the electrical field. Taking the spatial overlap into account, one can realise that in order to have efficient generation of e.g. frequency $\omega_3 = \omega_1 + \omega_2$, the wave vectors ($|k_i| = n(\omega_i)\omega_i/c$, where $n(\omega_i)$ is the refractive index at frequency ω_i) need to match in such a way as to minimize the phase mismatch

$$\Delta k = k_{\omega_3} - k_{\omega_1} - k_{\omega_2} = 2\pi \left(\frac{n_{\omega_3}}{\lambda_{\omega_3}} - \frac{n_{\omega_1}}{\lambda_{\omega_1}} - \frac{n_{\omega_2}}{\lambda_{\omega_2}} \right). \quad (4.5)$$

The relationship between the efficiency of e.g. sum-frequency generation and the phase mismatch is proportional to

$$\eta \propto \text{sinc}^2(\Delta k L), \quad (4.6)$$

where L is the length of the crystal. η is sharply peaked at $\Delta k = 0$. It is impossible to get phase-matching ($\Delta k = 0$) in a 'normal' medium, since the refractive index continuously drops as the wavelength of light increases. Birefringent crystals are crystals where the refractive index depends not only on the wavelength, but also on the polarisation of the light. The crystals used for obtaining phase matching are usually uniaxial crystals. These crystals have a special direction named the optic axis. Light with polarisation perpendicular to the optic axis has the "ordinary" refractive index n_o , and light polarised parallel to the optic axis has the "extraordinary" refractive index n_e . The ordinary ray will always experience the refractive index n_o , but depending on the direction of the extraordinary ray it will experience a refractive index somewhere between n_o and n_e . The effective refractive index for the extraordinary ray is given by

$$n_e(\omega_i, \theta)^2 = \frac{n(\omega_i)_{e,0}^2 n(\omega_i)_o^2}{n(\omega_i)_{e,0}^2 \cos^2 \theta + n(\omega_i)_o^2 \sin^2 \theta} \quad (4.7)$$

where $n_{e,0}$ and $n_{o,0}$ is the refractive index of the extra ordinary and ordinary axes in the crystal and θ is the angle relative to the

optic axis. Based on the discussion above, by choosing the right non-linear crystal and calculating the angle for phase matching, it is possible to generate light of new frequencies.

As mentioned in the begin of this section, the third harmonic (355 nm) of the fundamental Nd:YAG 1064 nm light is used to pump an OPO. The specific design of the OPO is based upon the *image-rotating optical parametric oscillator*[80], where a high reflecting 355 nm mirror and a image-rotating 180° prism acts as a cavity for the pump pulse. This technique has been shown to improve the overall beam quality of the generated signal. The visible light is generated in two Barium Borate (BBO) crystals. Besides the obvious doubling of conversion length by using two crystals, it also eliminates the spatial walk off of only passing a single angled crystal. The BBO's generate the effective reverse of sum-frequency generation, where a single pump frequency is used to generate two new frequencies, for historic reasons called the signal and the idler. The signal and the idler is generated with different resulting polarisations. The signal beam is horizontally polarised and ranges from 420 nm to 709 nm and the idler beam is vertically polarised and ranges from 710 nm to 2300 nm, the wanted output is selected on the basis of their polarisation by rotating a Rochon prism (named after its inventor Abbé Alexis Marie Rochon 1741-1817). This prism consists of two birefringent crystal prisms, where the ordinary and extraordinary rays remain collinear through the first prism, but upon entering the second prism the extraordinary rays experience a change in refractive index and is therefore refracted at the interface. In order to generate UV photons, the signal or the idler can be frequency doubled again, to generate UV photons in the range 210 nm to 354 nm and 355 nm to 419 nm. The output power in the different wavelength regions can be seen in Figure 4.5 on the next page as the red curve. From this curve it is clear that the low power around 700 nm is going to translate into even less power around the frequency doubled 355 nm range, which is also evident by the dip in output power in the figure. In order to circumvent the use of doubling the low power idler beam to generate UV photons sum-frequency generation is used yet again in a home build laser add on, where the visible light from the OPO signal is mixed with the fundamental YAG frequency to generate UV photons in the

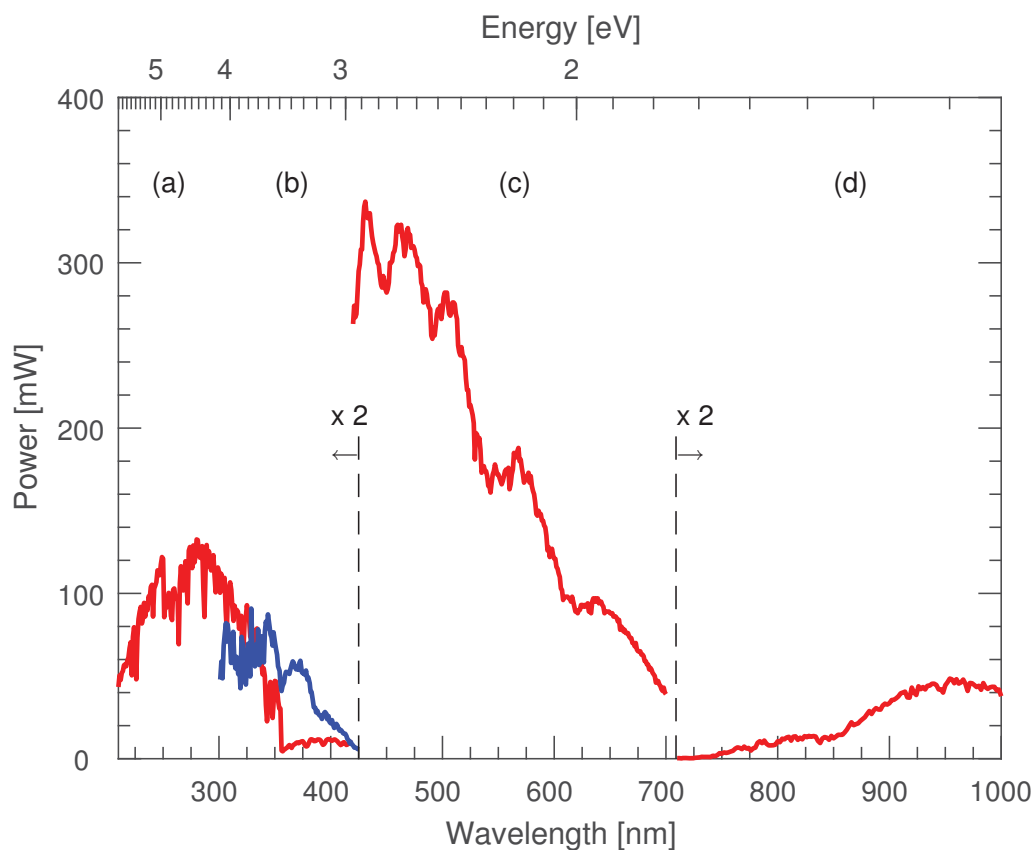


Figure 4.5: (a,c,d) Output power of the EKSPLA lasers. The third harmonic 355 nm of the Nd:YAG laser 1064 nm pumps an OPO to generate visible (c) signal beam and IR (d) idler beam. (a) The light from the OPO is frequency doubled to produce light in the UV range. (b) (Blue) The visible light and the fundamental YAG pumps a BBO crystal to generate the sum-frequency.

range of 301 nm to 425 nm, depicted as the blue line in Figure 4.5.

4.4 Sum frequency generator

The outline of the sum-frequency add on can be seen in Figure 4.6 on the following page. In this add-on a BBO crystal is used for sum-frequency generation. When the UV light has been generated, a Pellin Broca prism[81] separates the three different wavelengths in space. The Pellin Broca prism is cut in a way that transmits a specific wavelength perpendicular to the incoming direction when

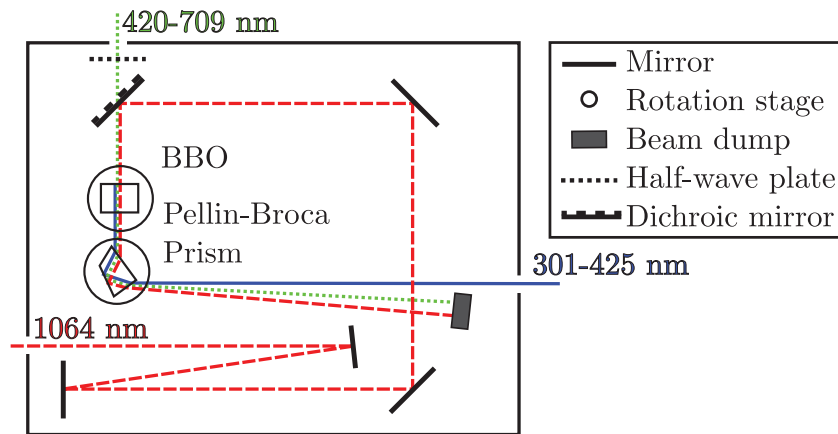


Figure 4.6: Illustration of the setup for sum frequency generation between the Nd:YAG fundamental wavelength and visible light from the OPO. A BBO crystal generates the sum frequency photon, and a prism selects the generated UV photon.

the specific wavelength is incident in the Brewster angle. The calculated phase matching angles and prism angles for each input wavelength can be seen in Figure 4.7 on the next page. The overall output of the sum frequency generation is shown in Figure 4.5 on the preceding page as the blue curve.

A LabVIEW program controls the stepper motors on the motorized rotational stages that hold the BBO and prism. The program has a look-up-table with all the wavelength-step value pairs for both the BBO and prism. The control program keeps track of which position the two stages are currently at, and changes them as needed. There are no reset switches on the stepper motors, so if there is a sudden loss of power for the computer running the control software it might forget where the two rotation stages currently are. To limit the possibility of this happening, the control software writes the current position to a local file. As a further safety measure, the stepper motor control and the host computer is running on a UPS (Uninterruptible Power Supply - a backup battery).

Without this sum-frequency add on, some of the fundamental results presented in this thesis would not have been possible.

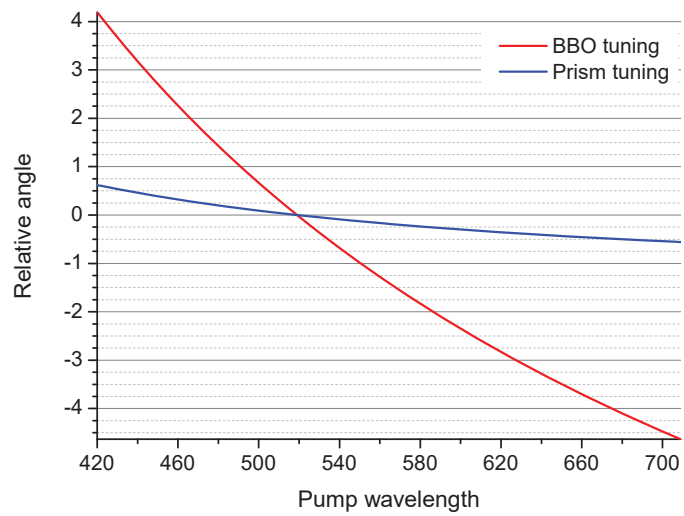


Figure 4.7: Calculated phase matching angle for the BBO, and tuning angle for the wavelength selecting prism, both measured in degrees. Angles are relative to the angles at 519 nm, which is the cut angle of the BBO.

Results on Nitrophenolates

This chapter summarises the study of the nitrophenolate anions, published in papers **I**, **II** and **III**. Since the specific information of the experiments has already been published, only specific topics and results will be discussed below. Furthermore, the data presented in this and the following chapter has no error bars. These are removed to make the figures easier to read. For more detailed information, the reader is referred to the previously mentioned papers.

The structure of the three isomers of nitrophenolate are shown in Figure 5.1. The nitrophenolates are composed of a hydroxy group and nitro group, separated by a spacer - in this case a benzene ring. The three different isomers have some very distinct differences, which will be apparent later. Nitrophenolates are good model

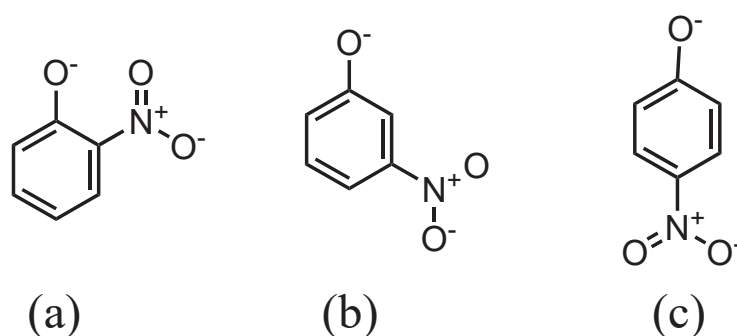


Figure 5.1: Illustrating the structure of (a) *ortho*, (b) *meta* and (c) *para*-nitrophenolate

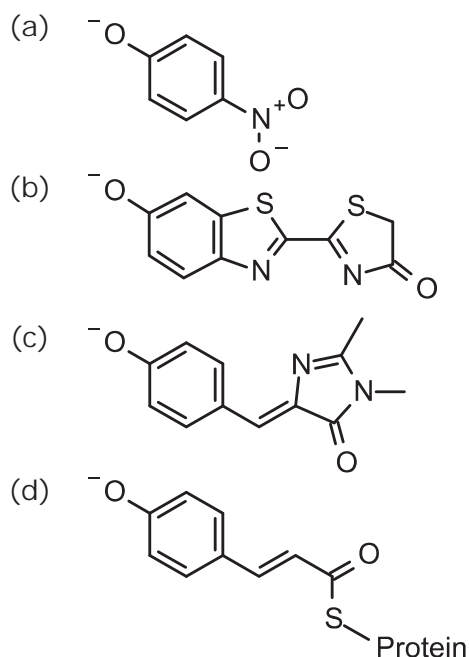


Figure 5.2: Illustrating the likeness between the (a) *para*-nitrophenolate and the three bio chromophores (b) oxyluciferin, (c) Green Fluorescent Protein and (d) Photoactive yellow Protein.

systems for larger biomolecules, such as oxyluciferin[82, 83]; the luminophore responsible for light emission from fireflies, the Green Fluorescent Protein (GFP) chromophore [6] and the Photoactive yellow Protein (PYP) chromophore [84]. These three highly interesting chromophores all share the same phenolate motif as the nitrophenolate isomers, illustrated in Figure 5.2. The overall goal of studying the nitrophenolates is to gain a fundamental understanding of the photo physical properties of this simple model system, and how local perturbations from micro solvation effects these properties. The knowledge gained from this system can then be used to understand the photo physical properties of more complex bio chromophores.

Many biochromophores, e.g. oxyluciferin, undergo charge-transfer (CT) transitions upon excitation. In order for a chromophore to have a charge-transfer transition, one of its components must have electron donating properties, and another must have electron

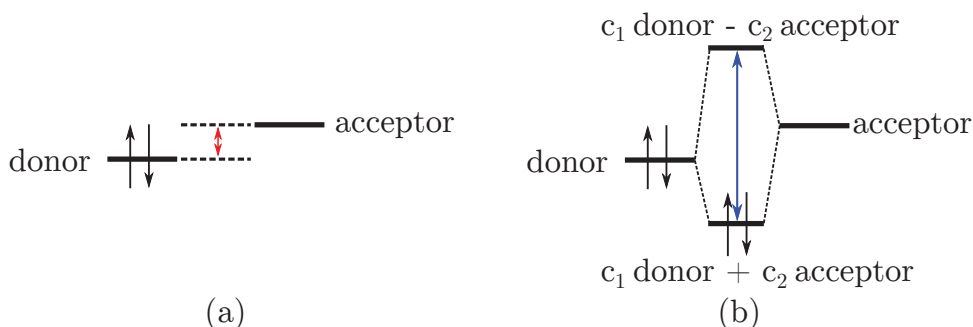


Figure 5.3: (a) Energy spacing between two non-interaction molecular orbitals, (b) Energy spacing between two highly mixed molecular orbitals

acceptor properties. This results in charge being moved from a donor-orbital of the chromophore to a acceptor-orbital upon excitation. This type of transition usually has a relative low oscillator strength due to the separation of the donor and acceptor-orbitals, and the transition is usually found at lower energies than "normal" transitions[7]. This lower transition energy can be illustrated on the basis of the energy spacing between two coupled orbitals. The transition energy between two non-interaction molecular orbitals, *i.e.* a charge-transfer like transition, is just the energy difference between the two non-interacting orbitals. As soon as the molecular orbitals start to mix, the spacing between the two new orbitals becomes larger. This is illustrated in Figure 5.3.

In order to effectively model the charge-transfer transition of larger bio molecules by our model system, the spacer between the hydroxy and nitro groups must act to block mixing. As evident from the resonance structures and calculated HOMO (highest occupied molecular orbital) and LUMO (lowest unoccupied molecular orbital) in Figure 5.4 on the following page, the *ortho* and *para*-nitrophenolates exhibit a high degree of coupling, *i.e.* a high degree of electron delocalisation, between the donor and acceptor groups of the ions. For the *ortho* and *para* isomers, it does not strictly make sense to talk about donor and acceptor groups since the whole

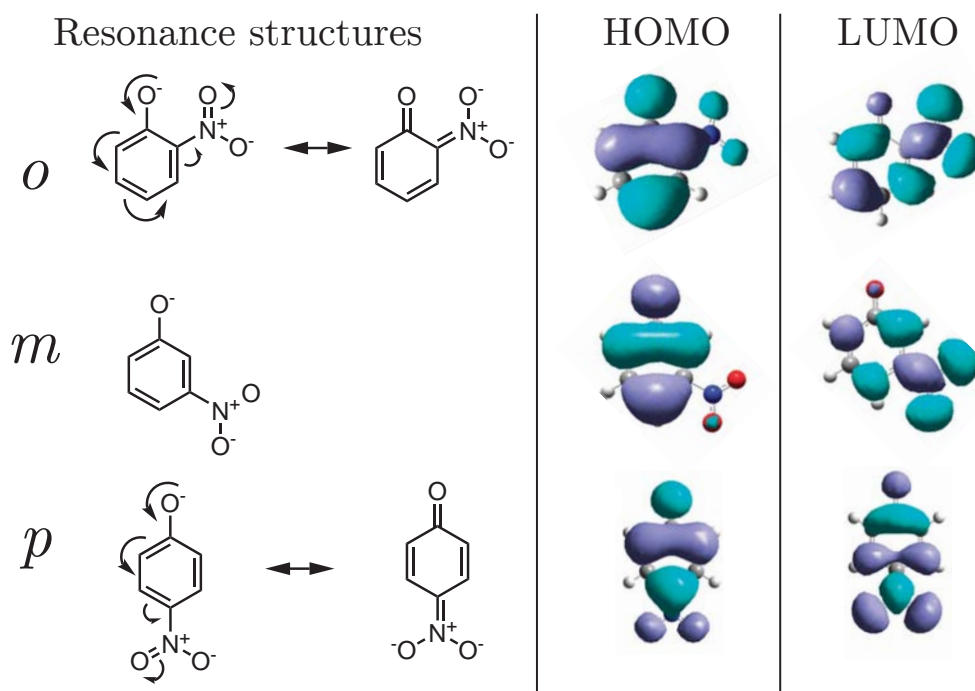


Figure 5.4: Illustrating resonance structures for *ortho*, *meta* and *para*-nitrophenolate anions. In the case of the *ortho* and *para* isomers, two resonance structures exist illustrating the high degree of electron delocalisation in these two isomers. Whereas no such resonance structures can be drawn for the *meta* isomer, illustrating the localised conjugation. The calculated highest occupied molecular orbital (HOMO) and lowest unoccupied molecular orbital (LUMO) are shown, which show the same conclusion.

molecule acts as both charge donor and acceptor. For the sake of consistency, I am still going to use the term *donor* for the phenolate group, and *acceptor* for the nitro group. The *meta*-nitrophenolate isomer exhibits a much more localised electron density in the HOMO and LUMO, *i.e.* the charge is not delocalised between the donor and acceptor groups. The transition in the *meta* isomer is a CT transition. This is one of the strengths in using the nitrophenolates as a model system, the type of transition can be controlled, by choosing the right isomer.

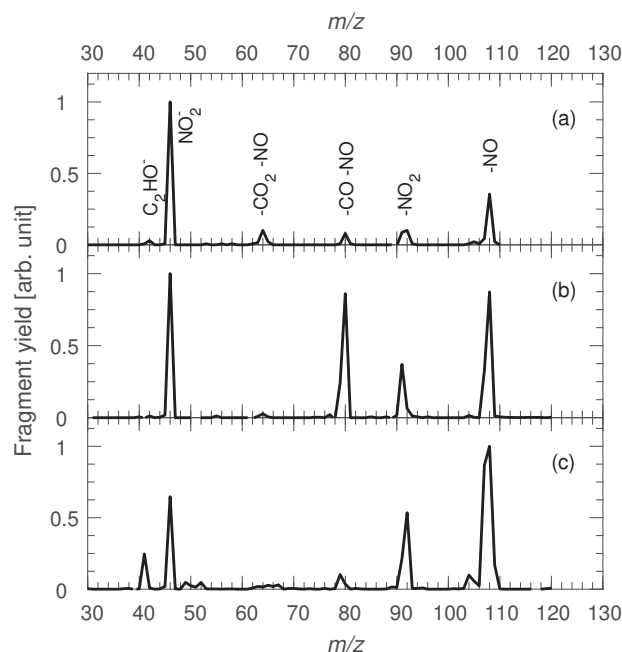


Figure 5.5: Fragmentation pattern of (a) *ortho*-nitrophenolate, (b) *meta*-nitrophenolate and (c) *para*-nitrophenolate, excited at a laser wavelength of 450 nm, 520 nm and 420 nm, respectively. The fragments are denoted in the top frame, as either the fragment ion or what neutral species has been lost from the parent ion.

5.1 Bare nitrophenolate ions

To understand the effects of a perturbation environment, it is crucial to know how the bare system behaves. As described earlier, a number of different measurements has to be done, in order to get the action spectra. In this chapter, action spectra refer to the fragmentation action spectra. One needs to know the fragmentation pattern of the ion, the action spectra associated with the formation of each fragment and the number of photons required for fragmentation. In the following, *meta*-nitrophenolate is used to illustrate the different aspects of the analysis of the experimental data.

The fragmentation pattern of all the bare nitrophenolate anions can be seen in Figure 5.5. The fragmentation pattern is quite rich compared to the small size of the nitrophenolates. To get the total action spectrum, the action spectra for each fragmentation channel has to be acquired. In order to do that, the power dependence of

fragmentation has to be obtained. The power dependence for the three most dominant fragments of *m*-nitrophenolate ($m/z = 46$ amu, $m/z = 80$ amu and $m/z = 108$ amu) can be seen in Figure 5.6 on the facing page. The individual power fits ($yield = laser\ power^{order}$) reveal orders between 1.6 and 2.3, but it is difficult to say exactly what the order should be. All that with certainty can be concluded is that fragmentation of the bare ions, on the time scale of the SEP1 experiments, is a multi photon process. In the following action spectra a two-photon process has been assumed. The weighted sum of the individual action spectra, weighed relative to their yield in the fragmentation spectra, results in the total action spectra. The action spectra for each fragment of *m*-nitrophenolate can be seen in Figure 5.7 on page 66. The total action spectra for all three isomers can be seen in Figure 5.8 on page 67. It is quite clear from the total action spectra that the *meta* isomer absorbs much further to the red than the *ortho* and *para* isomers. In conclusion, if we assume that the *ortho* and *para*-nitrophenolates are completely coupled, and that the *meta*-nitrophenolate is completely decoupled (pure CT transition), the study of these nitrophenolates has taught us that by decoupling the donor and acceptor states in this model system, a lowering of the transition energy by 0.82 eV can be achieved (band maximum for *para* 3.15 eV minus band maximum for *meta* 2.33 eV).

5.2 Micro solvated nitrophenolates

Since we now understand the properties of the bare nitrophenolate isomers, it is time to add a single water molecule to the ions, to form ion-solvent complexes which mimic the local environment in e.g. a protein pocket. Based on the calculations in papers **II** and **III**, the single water molecule binds to the phenolate group in all three isomers (see Figure 5.9 on page 67). In the case of *ortho*-nitrophenolate, the water molecule binds to both the phenolate and the nitro group, but more strongly to the former. The binding energy of the *para*-nitrophenolate complex is less than that of the *meta*-nitrophenolate complex, indicating that some of the negative charge for the *para* isomer is still on the nitro group, which means that the phenolate and nitro group are still somewhat coupled in

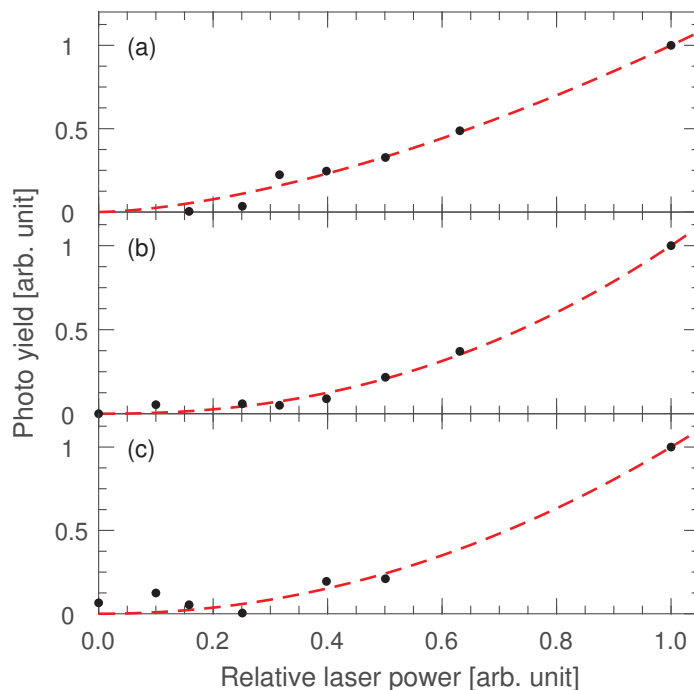


Figure 5.6: Power dependence measurements for the three most dominant fragments of *meta*-nitrophenolate. (a) fragment $m/z = 46$ amu, (b) fragment $m/z = 80$ amu and (c) fragment $m/z = 108$ amu, measured at laser wavelengths of 510 nm, 520 nm and 550 nm, respectively.

the *para* isomer.

As before, with the bare ions, the first experiment to do is to look at the fragmentation pattern of the water complexes. The fragmentation patterns can be seen in Figure 5.10 on page 68. The fragmentation pattern has been reduced to a single fragment: loss of the water molecule. This and the linear power dependence seen in Figure 5.11 on page 69 greatly simplifies the analysis of the experimental data. The binding energy of the water molecule is on the order of 0.5 eV so after absorbing a 2.5 eV photon, there is enough excess energy left to ensure a fast dissociation. The fast dissociation ensures that no kinetic shift is present in the SEP1 data. The resulting action spectra can be seen superimposed on the action spectra for the bare ion in Figure 5.12 on page 70. It is clearly seen that a single water molecule shifts the absorption band for all three isomers, but the direction is not constant. In the

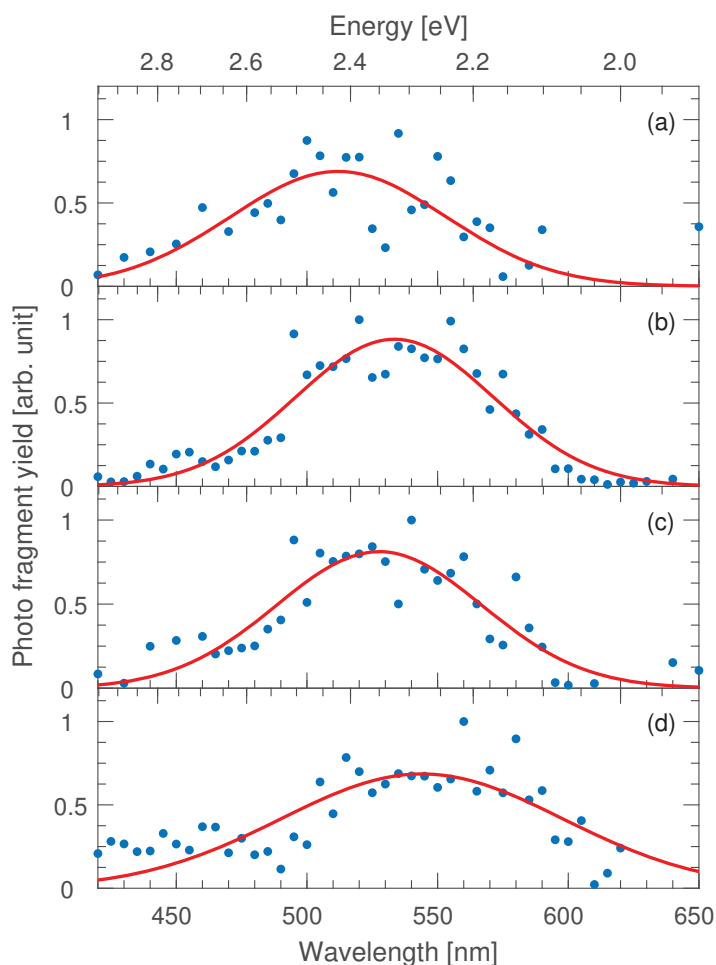


Figure 5.7: Action spectra for each fragmentation channel of the bare *meta*-nitrophenolate anion. (a) $m/z = 46$ amu, (b) $m/z = 80$ amu, (c) $m/z = 91$ amu and (d) $m/z = 108$ amu. Gaussian fits (red) are superimposed to help guide the eye.

meta isomer case, where the transition is a 'pure' CT transition, we see a blue shift. The blue shift is due to a simple electrostatic effect. When the charge is moved from the donor to the acceptor group, the interaction energy between the dipole of the solvent, and the charge on the ion is reduced. This now less favourable interaction increases the transition energy. This electrostatic effect shifts the absorption band more for stronger binding solvents as can be seen in paper **II** and in Figure 5.14 on page 72. In the case of the *ortho* and *para* isomers, a small redshift is seen in the action spectra. This is due to the fact that binding a single water molecule

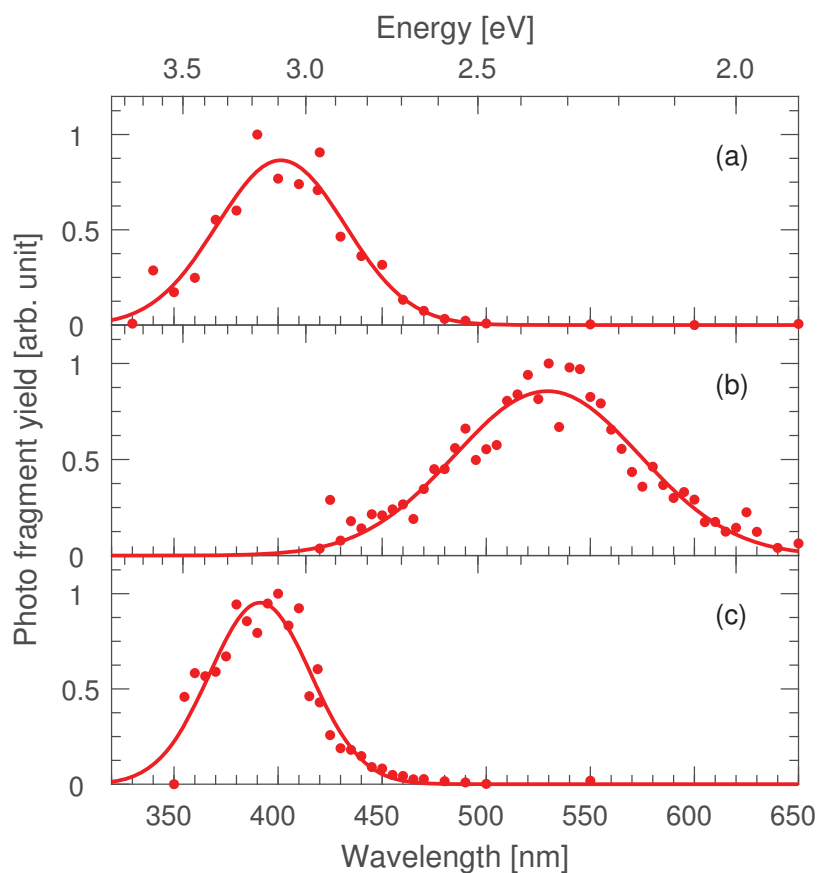


Figure 5.8: Action spectra of the bare nitrophenolate anions. (a) *ortho*-nitrophenolate, (b) *meta*-nitrophenolate and (c) *para*-nitrophenolate. The data for *ortho* and *para*-nitrophenolate were obtained at the ELISA storage ring facility in Aarhus[85, 86]. Gaussian fits are superimposed to help guide the eye.

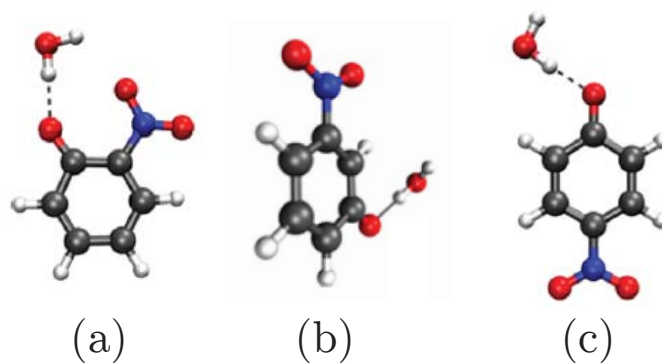


Figure 5.9: Calculated structures of the micro solvated nitrophenolate isomers (a) *ortho*, (b) *meta* and (c) *para*. For all isomers, the water molecule binds to the phenolate group.[87]

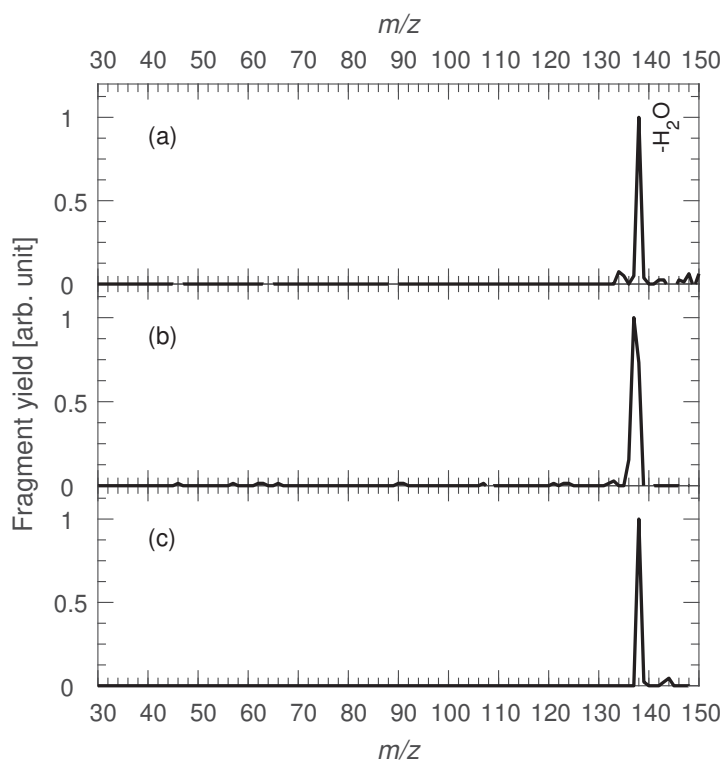


Figure 5.10: Fragmentation pattern of (a) *ortho*-nitrophenolate water complex, (b) *meta*-nitrophenolate water complex and (c) *para*-nitrophenolate water complex, excited at laser wavelengths of 415 nm, 475 nm and 415 nm, respectively. The only fragmentation channel available is the loss of the solvent molecule.

pulls the charge towards the water, lowering the conjugation. This effect is illustrated in Figure 5.13 on page 71. The binding of a solvent molecule effectively makes the electronic transition more CT like. The now CT-like transition will, as for the *meta* isomer, weaken the interaction between the solvent dipole and the ion charge upon excitation. This weakening will then result in a blue shift in the transition energy. The relative small red shifts of 0.10 eV and 0.15 eV for the *ortho* and *para* isomers respectively, is a result of both the red and blue shift in transition energy. A summary of the experimental data on the nitrophenolates can be seen in Table 5.1 on the next page.

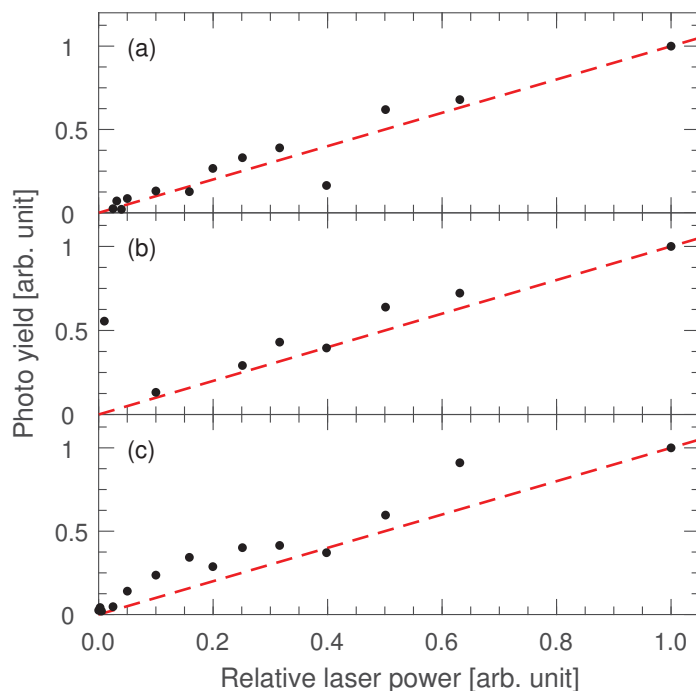


Figure 5.11: Power dependence measurements for the three nitrophenolate water complexes. (a) *ortho*-nitrophenolate water complex, (b) *meta*-nitrophenolate water complex and (c) *para*-nitrophenolate water complex, measured at laser wavelengths of 415 nm, 475 nm and 415 nm respectively. All isomers exhibit one photon dependence on the loss of water.

Table 5.1: Absorption band maximum in nm and eV, and shifts from the bare ions in ΔeV . A negative ΔeV value corresponds to a red shifted absorption.

Ion	<i>Bare</i>		<i>Solvent</i>		ΔeV
	nm	eV	nm	eV	
<i>o</i> -nitrophenolate	399	3.11	^a 412	3.01	-0.10
<i>m</i> -nitrophenolate	530	2.38	^a 485	2.56	0.22
	-	-	^b 485	2.56	0.22
	-	-	^c 505	2.46	0.12
<i>p</i> -nitrophenolate	393	3.15	^a 413	3.00	-0.15

^awater, ^bmethanol, ^cacetonitrile

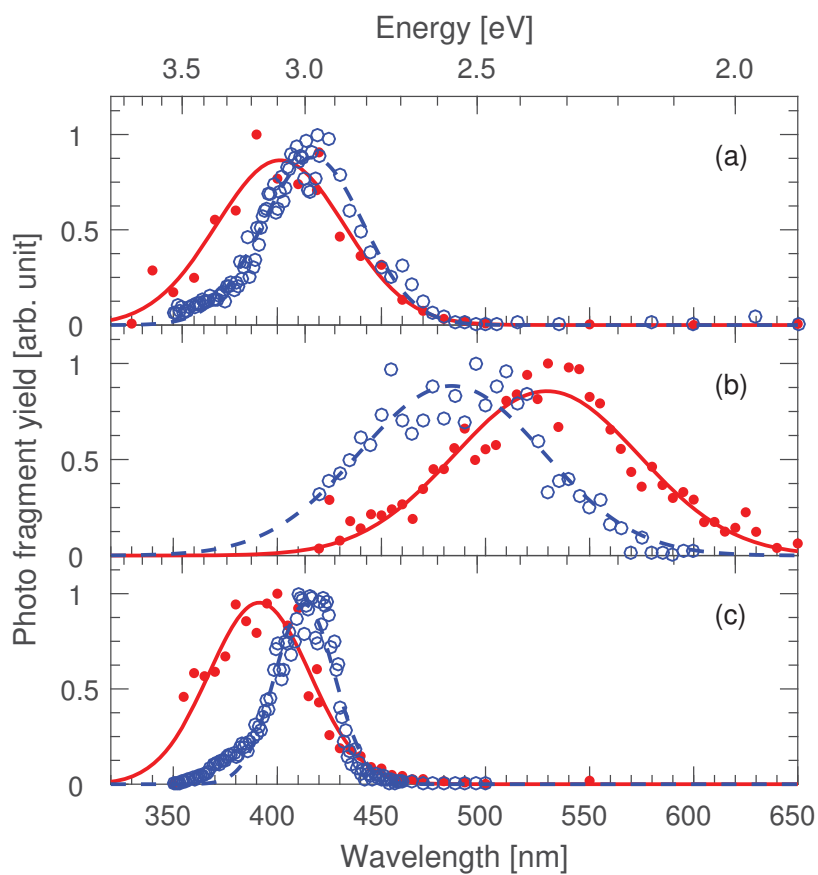


Figure 5.12: Action spectra for the water complexes (blue hollow circles, and broken line) of (a) *ortho*-nitrophenolate, (b) *meta*-nitrophenolate and (c) *para*-nitrophenolate. The action spectra of the bare isomers are superimposed (red full circles, full line). Gaussian fits are likewise superimposed to help guide the eye.

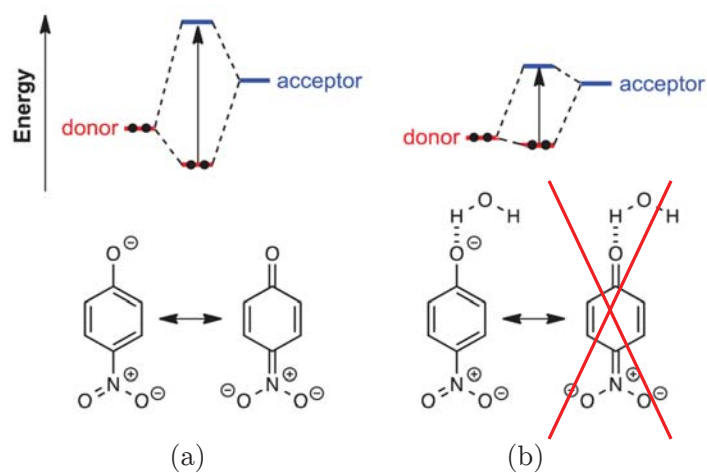


Figure 5.13: Illustrating the effect of micro solvation on the conjugation on *para*-nitrophenolate. (a) When no water molecule is present, the conjugation is spread over the whole ion. (b) The conjugation is lowered upon binding a single water molecule, effectively creating a more CT-like transition and lowering the transition energy.

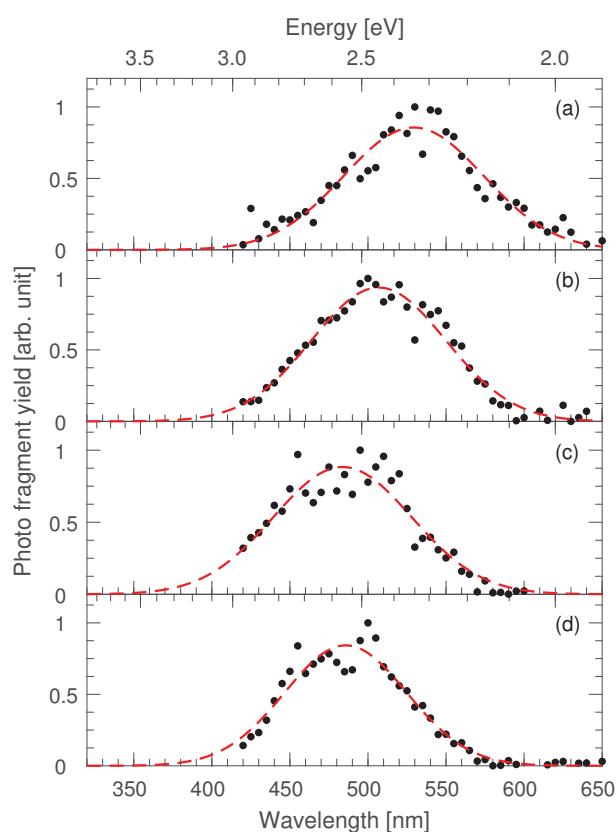


Figure 5.14: Action spectra for the (a) bare *meta*-nitrophenolate, and complexes with a single (b) acetonitrile, (c) water and (d) methanol molecule. The calculated binding energies increase downward. The binding energies are 0.50 eV, 0.54 eV and 0.65 eV for the acetonitrile, water and methanol complexes respectively. Gaussian fits are superimposed to help guide the eye.

Other systems

In this chapter I will use the results from the previous chapter, and illustrate how these can be used to interpret the experimental results for other, more complex, systems. The systems that will be covered are oxyluciferin, permanganate, *p*-benzoquinone anion, $\text{Ru}(\text{bipy})_3^{2+}$ and protonated adenine, protonated thymine and protonated uracil. The structures of said ions, and the nitrophenolates, can be seen in Figure 6.1 on the following page. The details of each individual study can be found in the corresponding papers cited for each experiment, and only brief introductions and discussions will be presented here.

6.1 Oxyluciferin

Oxyluciferin is the luminophore responsible for light emission from fireflies. Oxyluciferin is furthermore also the luminophore responsible for light emission from various forms of click beetles and railroad worms, but here the light emitted is of different colors than seen in the fireflies. In nature, oxyluciferin is chemically excited[88, 89] into the first excited state. Light is then emitted by returning to the ground state. The transition has been calculated to be a charge-transfer like transition[90, 91]. An interesting question is how is the color of the emitted light from oxyluciferin tuned? It has been proposed[92] that a single water molecule inside the luciferase protein could have a profound effect on the photophysical proper-

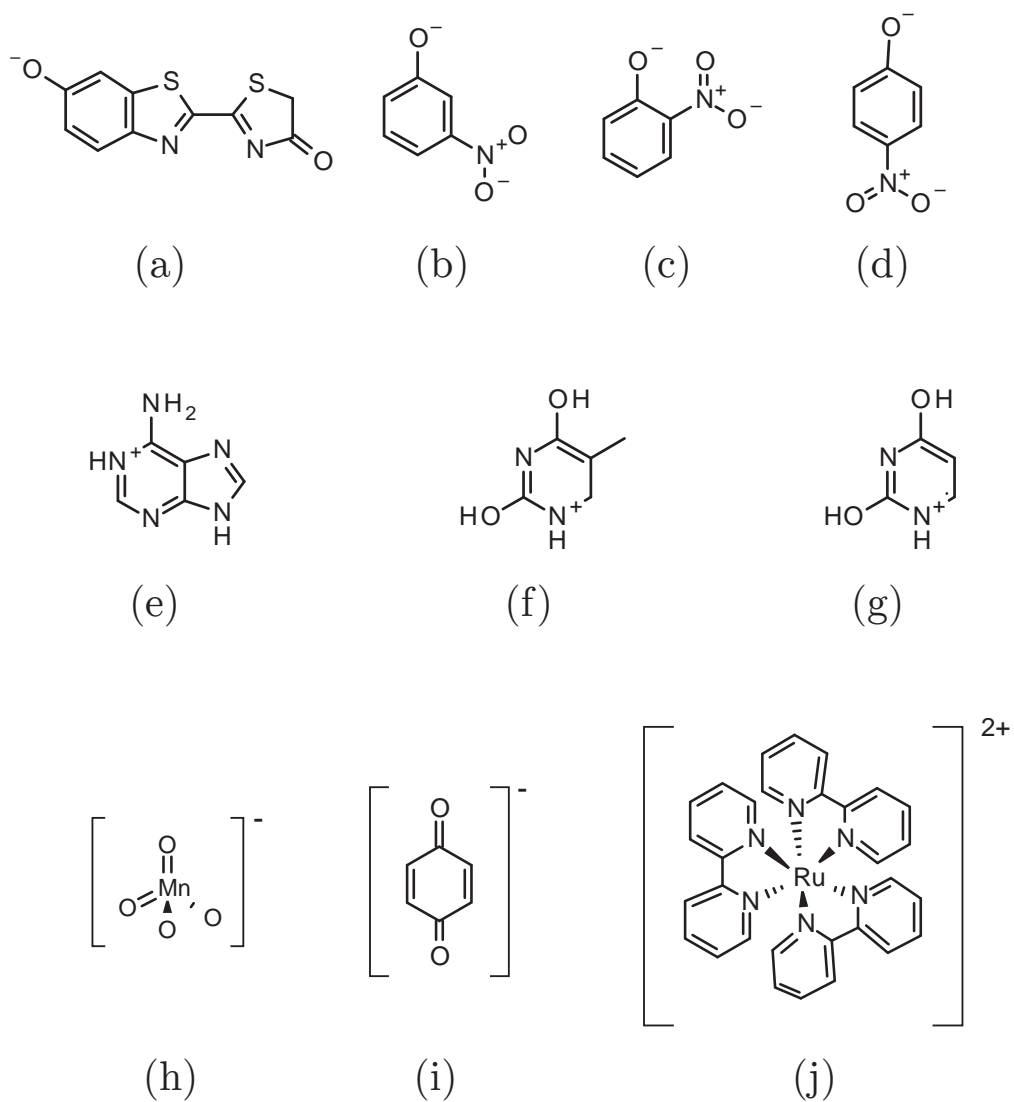


Figure 6.1: Molecular structures of the ions represented in this chapter. (a) oxyluciferin, (b) *m*-nitrophenolate, (c) *o*-nitrophenolate, (d) *p*-nitrophenolate, (e) protonated adenine, (f) protonated thymine, (g) protonated uracil, (h) permanganate, (i) *p*-benzoquinone anion and (j) $\text{Ru}(\text{bipy})_3^{2+}$.

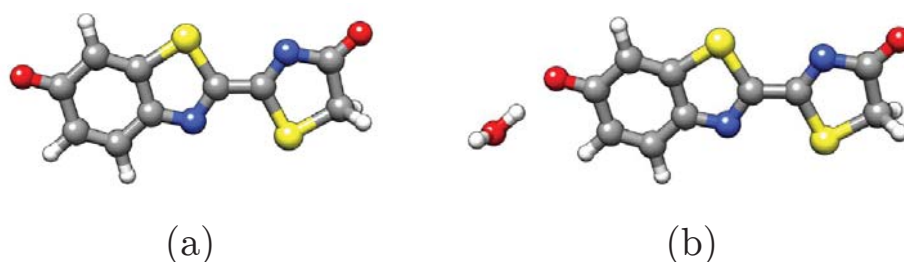


Figure 6.2: Structure of (a) oxyluciferin and (b) oxyluciferin-water complex. The water molecule binds to the phenolate group. Carbon atoms are grey, oxygen red, sulfur yellow, nitrogen blue and hydrogen white.[96]

ties of the oxyluciferin chromophore. In order to investigate this proposal, the effect of the local environment has been the focus of a few theoretical studies, where micro solvation was found to give a small red or blue shift, dependent on the solvent location[93–95]. However, the calculated shifts has only been on the order of 5 nm, which is not nearly enough to explain the diverse colors found in nature. In order to establish the actual effect of micro solvation, we have studied the intrinsic light absorbing properties of the bare oxyluciferin anion and the properties of the oxyluciferin-water complex (paper IV [96]). The calculated structures of both the bare ion and the solvent complex can be seen in Figure 6.2.

The experimental approach is exactly the same as for the nitrophenolate isomers, described in the previous chapter. The action spectra for the bare ion and water complex can be seen in Figure 6.3 on the following page. A very clear blue shift in the absorption spectra is seen upon micro solvation. The shift is 0.23 eV, which is approximately the same shift seen in the *meta*-nitrophenolate case, and much the same conclusions can be drawn. The water molecule binds to the phenolate-group, and when change is moved away from this group upon excitation, the ion-dipole interaction is weakened. This weakening of the ion-dipole interaction increased the transition energy and a blue shift is observed. This strong shift due to micro solvation indicates that the transition is indeed a CT-like transition. And that the local environment can have a huge effect on the transition energies of oxyluciferin.

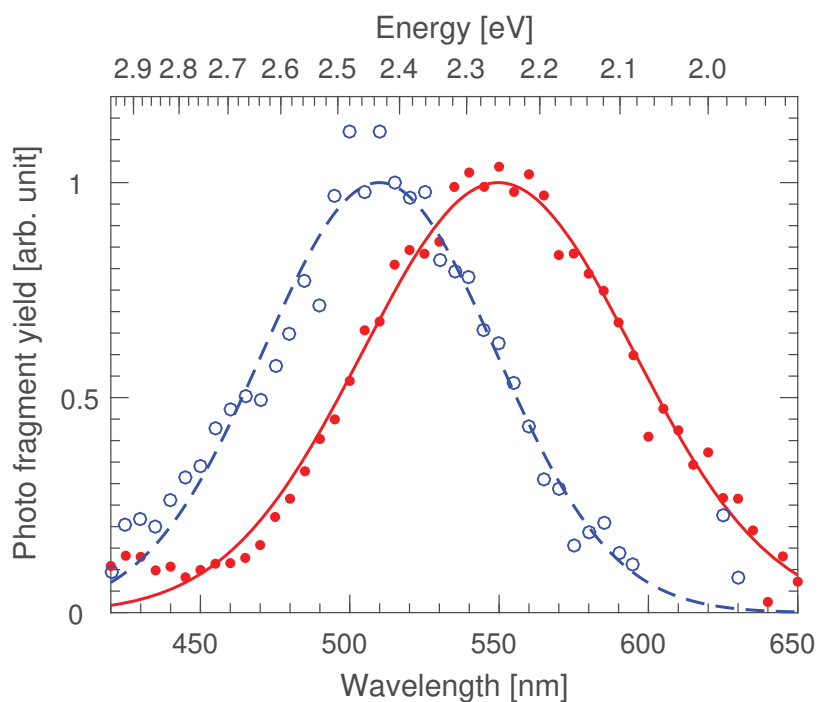


Figure 6.3: Action spectra of (red solid) oxyluciferin and (blue hollow) oxyluciferin-water complex. Gaussian fits are superimposed to help guide the eye.

The data presented here provide information on the absorption by the ions, and not light emission which is the actual interesting property. But given the fact that a single water molecule can shift the color of the light absorbed by 50 nm, it is clear that perturbations from the local environment should be able to change the wavelength of emitted light also. The ideal experiment for looking at shifts in light emission is clearly to study the actual light emitted from this ion, but that has not yet been accomplished in the gas phase.

6.2 Permanganate

Permanganate is not a biomolecule, but it is still an interesting ion to study, due to its popularity as a oxidising agent. The absorption spectrum was first measured in detail by Holt and Ballhausen in 1967[97]. Since then permanganate has been used as a benchmark

system for theoretical models[98–101]. Permanganate is very different from the previously mentioned ions, simply due to the fact that permanganate does not have a dipole moment, it is highly symmetrical. One of the interesting properties of the electronic structure of permanganate, is that upon electronic excitation, the geometry changes to a lower symmetry due to Jahn-Teller distortion[102, 103]. But what is of most interest for the work presented in this thesis is the investigation of the effect on the electronic structure of binding a solvent molecule to a completely symmetrical charge distribution. It is clear that the electron delocalisation must be greatly affected by binding a solvent molecule. This is going to localise the charge, wherever the binding occurs. Drawing upon the conclusions from the nitrophenolate study, a couple of things can happen. The fact that the charge is going to be more localised, would result in a more CT like transition, which would result in a red shift of the absorption band. The now CT like transition is going to be effected by the electrostatic cost of moving charge away from the solvent molecule, which would result in a blue shift in the absorption band. The question then is, which effect is going to impact the electronic energy levels the most? The absorption data are shown in Figure 6.4 on the next page. A small blue shift, of 12 meV is observed, which must be the result of the two perturbing effects almost cancelling each other. It is very peculiar that, what must be a big effect on the electronic structure has such a small effect on the electronic energy spacing.

6.3 *p*-Benzoquinone

Quinones are a central component of the transfer of charge in the photosynthesis system [104]. In the photosynthesis system, the quinones transfer electrons in a near resonant electron transfer transition, it is therefore important that the electronic levels of the quinone are constant for the transfer to be efficient[105]. *p*-benzoquinone is a central moiety that accounts for the electron-accepting part of the quinones found in the photosynthesis-system, and has therefore been of great interest[106–111]. The effect of micro solvation was studied by Mark H. Stockett and Steen

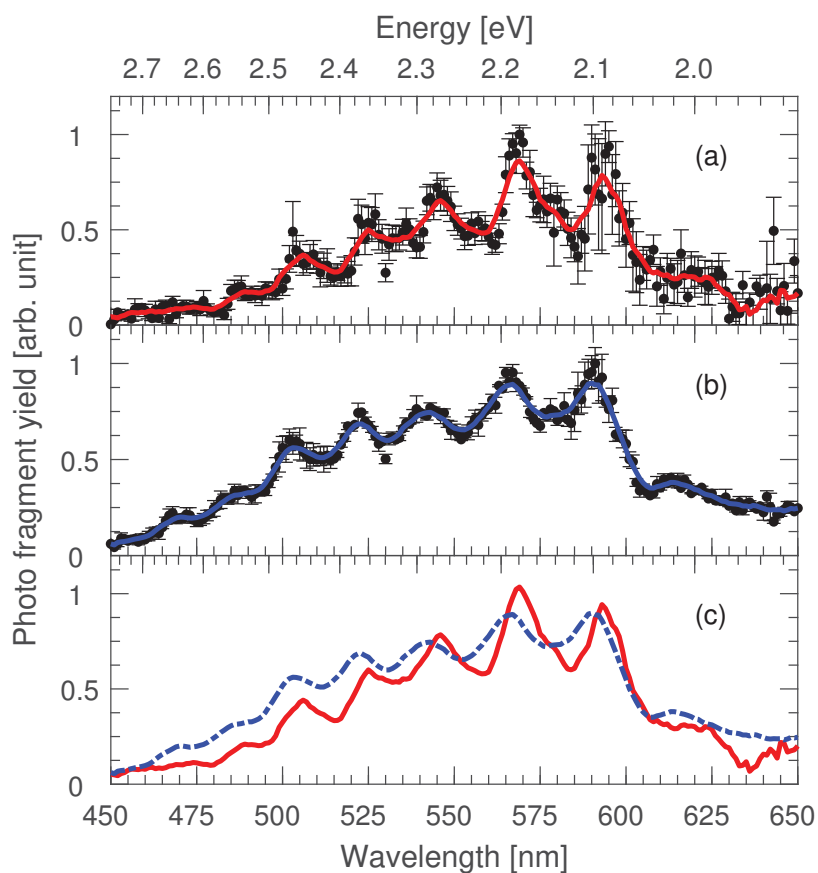
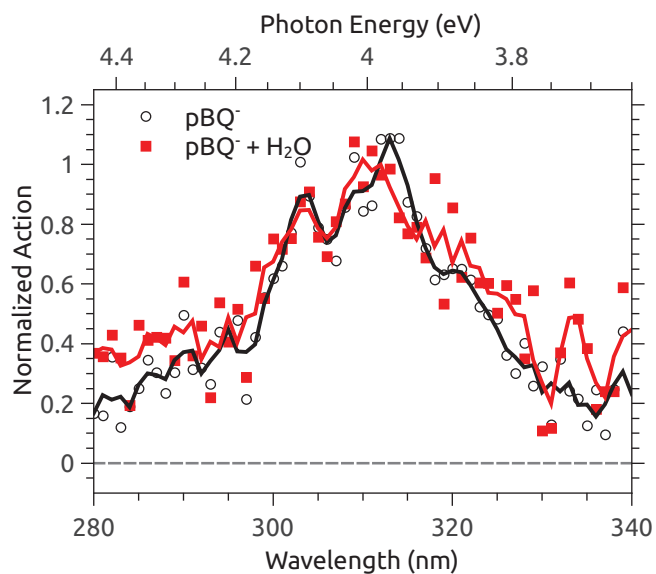


Figure 6.4: Action spectra of (a) bare permanganate anion, (b) permanganate-water complex and (c) a replot of the two superimposed ten point averages, where the red solid line is the bare ion and the blue broken line is the water complex. The peaks in the action spectra corresponds to vibrational fine structure due to a vibronic coupling to the Mn–O stretching mode of 740 cm^{-1} and 725 cm^{-1} for the bare ion and water complex, respectively.

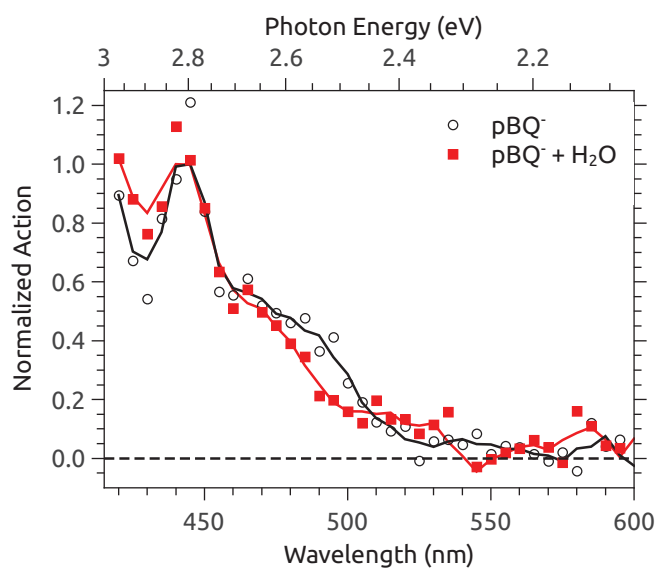
Brøndsted Nielsen [112], by looking at the action spectra of the bare *p*-benzoquinone and the *p*-benzoquinone-water complex. Like permanganate, *p*-benzoquinone has no permanent dipole moment and has a very high degree of symmetry. Like permanganate, the symmetry of the electronic conjugation must be lowered by attaching a water molecule.

Unlike the other ions presented in this thesis, *p*-benzoquinone does not fragment after laser excitation. After photo excitation an electron is emitted, either as direct photodetachment or delayed thermionic emission from a hot ground state. It is not possible to measure electrons at SEP1, and at the time of the *p*-benzoquinone experiment it was only possible to measure charged fragments. In order to measure the action spectrum of *p*-benzoquinone, the depletion signal was monitored as a function of wavelength. This is done by monitoring the depletion of the parent ion signal after photo excitation. In the case of the water complex, it was possible to monitor the water loss channel, but these data are not shown here since the water loss only corresponds to approximately one percent of the overall action. The depletion spectra for two transitions in *p*-benzoquinone and the water complex can be seen in Figure 6.5 on the following page. After the installation of the new detector at SEP1, it has been possible to measure the neutrals formed after electron detachment. This has made it possible to measure the action spectra on the UV side of the lowest transition. These data are shown in Figure 6.6 on page 81 from 380 nm to 600 nm.

Just as was seen for permanganate, the effect of a single water molecule on the separation of the electronic levels is minimum. For *p*-benzoquinone there actually seems to be no measurable shift between the absorption spectra of the bare ion and of the water complex. Again, as for permanganate, the two opposing effects must cancel each other. The robustness of the transition energies of *p*-benzoquinone under perturbations from the local environment makes the quinone an ideal electron acceptor - which is just what is needed in the nature.



(a)



(b)

Figure 6.5: Depletion spectra of *p*-benzoquinone (open black circles) and the water complex (filled red squares) for two different transitions. (a) First transition, solid line is a 5 point moving average, (b) Second transition, solid line is 3 point moving average. For further details see text and ref [112].

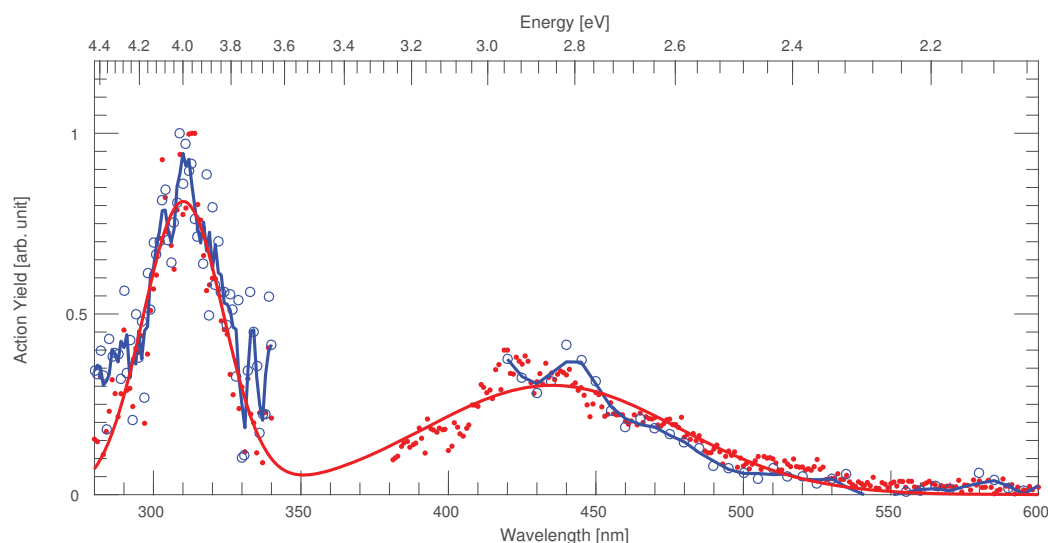


Figure 6.6: Action spectra of the bare *p*-benzoquinone anion (red solid) and *p*-benzoquinone water complex (blue hollow). The high energy transition is depletion data from [112], the low energy transition is new data acquired using the SED detector at SEP1. A gaussian fit is shown for both transitions in the bare ion to help guide the eye. 4 point moving averages are superimposed on the water complex data. The two transitions are normalised to the data measured in an Ar matrix by Piech *et al.* [113] (not shown).

6.4 Tris(bipyridine)ruthenium(II)

The transition in Tris(bipyridine)ruthenium(II), $(\text{Ru}(\text{bipy})_3^{2+})$, is a textbook example of a metal-to-ligand charge transfer transition [114–116]. The ground state of the dication is a singlet with the HOMO located on the center rubidium, while the LUMO is located on the ligands [117]. The transition of the $\text{Ru}(\text{bipy})_3^{2+}$ lies in the visible range, and has made the ion interesting in regards to light-harvesting for artificial photosynthesis [118, 119]. In the study by Mark H. Stockett and Steen Brøndsted Nielsen [120], the shift in transition energy when going from the bare $\text{Ru}(\text{bipy})_3^{2+}$ ion to the $\text{Ru}(\text{bipy})_3^{2+} + \text{acetonitrile}$ complex was investigated using action spectroscopy. $\text{Ru}(\text{bipy})_3^{2+}$, like permanganate and *p*-benzoquinone, is highly symmetrical and has no permanent dipole. The absorption spectra (Figure 6.7 on the following page) show, just like for permanganate and *p*-benzoquinone, no significant shift in transition

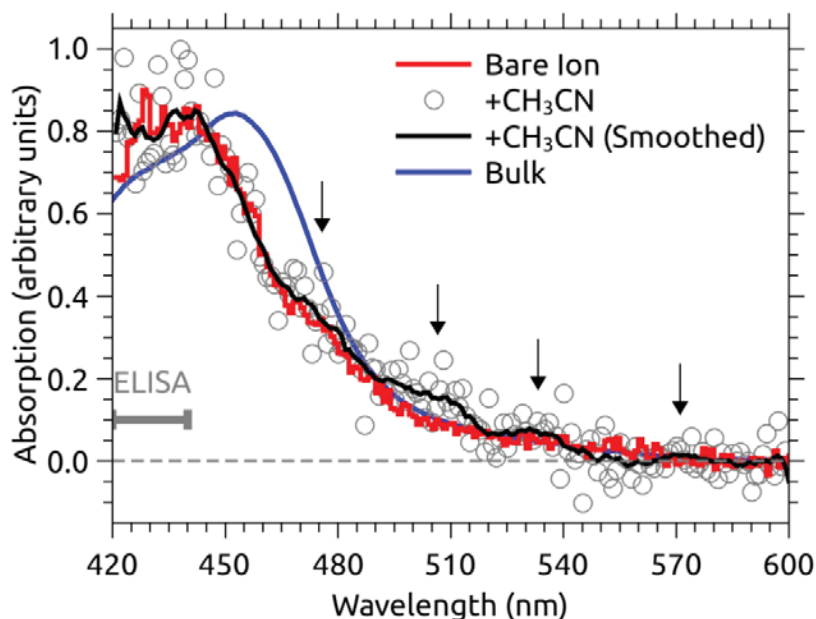


Figure 6.7: Action spectra of $\text{Ru}(\text{bipy})_3^{2+}$. The red line is dissociation action spectra for the bare ion, the open circles and the solid black line is data and 10-point running average of the acetonitrile complex. The black arrows indicate maxima in the low energy tail corresponding to $1250 \pm 250 \text{ cm}^{-1}$. Absorption band maximum measured at the electronic storage ring ELISA is added as the light gray bar. The blue line is the absorption by $\text{Ru}(\text{bipy})_3^{2+}$ in bulk acetonitrile solution. Figure from [120].

energy upon micro solvation. In order to really establish the band maxima it would be relevant to measure the action below 420 nm.

6.5 Protonated nucleobases

In order for life to have evolved beyond the prebiotic era (4 billion years ago[121]), where no protective stratospheric ozone layer was present, the photo stability of DNA and RNA was crucial. It is the nucleobases (adenine, thymine, cytosine, guanine and uracil) that are responsible for UV light absorption, so the general interest in the photo physical properties of the nucleobases is no surprise[122–129]. In the two papers by Sara Øvad Pedersen *et al.* [130, 131] protonated thymine, protonated Adenine and protonated uracil bare ions and single-water complexes were studied using action

spectroscopy. The action spectra of protonated adenine (Figure 6.8 on the next page) shows no shift in transition energy upon micro solvation. This would indicate that the positive charge is delocalised over the whole ion. Surprisingly, no shift in transition energy is seen between the bare nucleobase and the fully solvated one either, which again shows that the transition is not at all affected by the surrounding micro environment. In the case of protonated thymine and protonated uracil, the action spectra become a little more complicated. Based on calculations, two tautomers are present in the ion beam. For both protonated thymine and protonated uracil, the two tautomers present are called 138^+ and 178^+ , where the nomenclature indicates the protonation on the ring position and oxygen atom and was first introduced in ref. [132] and kept here for the sake of consistency. The tautomers can be seen in Figure 6.9 on the following page, along with their calculated percentage in the ion beam and calculated absorption band maximums. According to calculations the two tautomers are responsible for light absorption at two different wavelengths. The 138^+ tautomer absorbs light at approximately 300 nm and the 178^+ tautomer absorbs light at approximately 250 nm.

In the protonated thymine spectrum, Figure 6.10(a) on page 85, only one absorption band (178^+ tautomer) is seen for the bare nucleobase, which fits nicely with the calculated percentage of the 138^+ tautomer of only up to 4%. This band is not affected by the addition of a single water molecule, indicating a fully delocalised charge distribution on this tautomer. By adding a water molecule, the relative importance of the 138^+ tautomer seems to be enhanced, based on the small absorption band seen for the water complex at 305 nm. It is unfortunately not possible to measure a shift in this transition due to the low signal for the bare ion at this wavelength. It would be interesting to go back and do the Thymine experiment again, this time with focus on measuring the 138^+ tautomer signal for the bare ion.

In protonated uracil, two bands are seen in the absorption spectrum, Figure 6.10(b) on page 85. These two bands corresponds to both tautomers being present in the ion beam. Again, as for protonated thymine, the addition of a water molecule does not shift the absorption band for the 178^+ tautomer. Again this indicates a

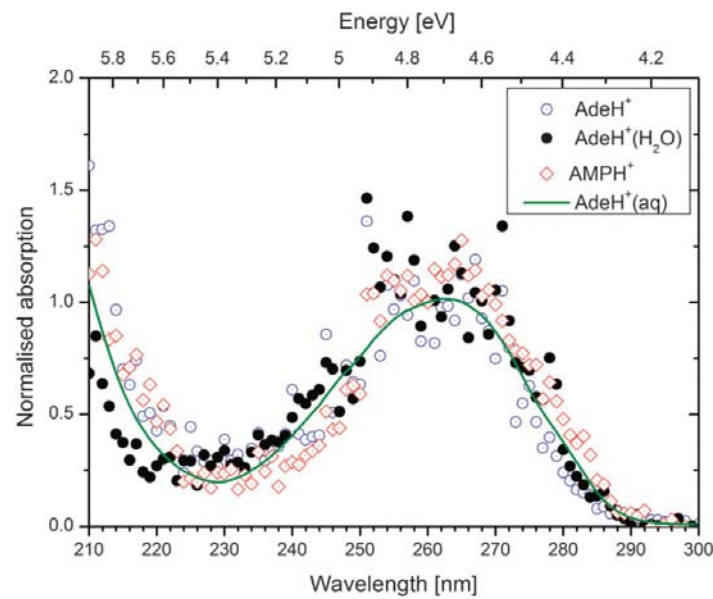


Figure 6.8: Action spectra of the protonated adenine (hollow blue circles) and water complex (full black circles). The absorption spectra for fully solvated Adenine is superimposed as the solid green line. Furthermore the action spectra of protonated AMP is added (hollow red diamonds), but has no interest for the study presented in this thesis. Figure from [131].

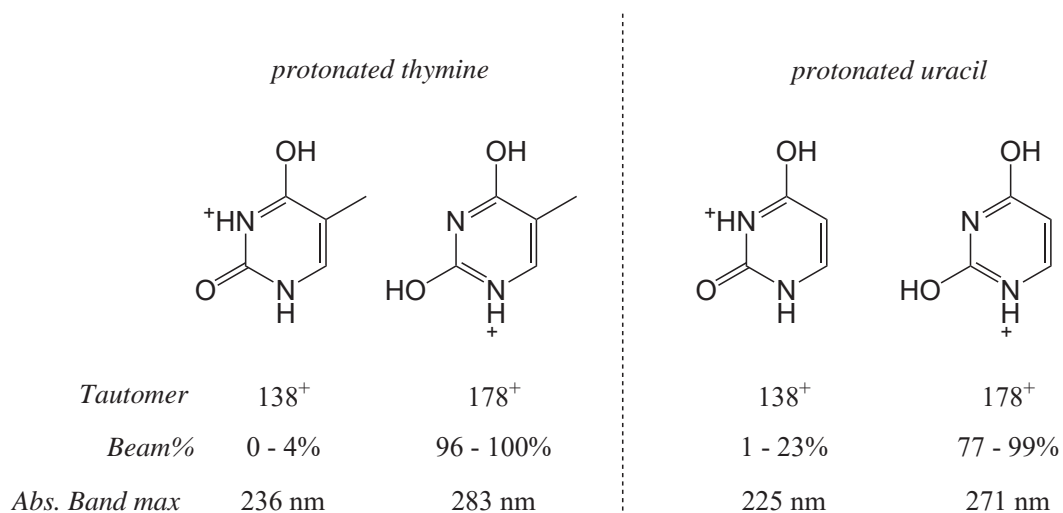
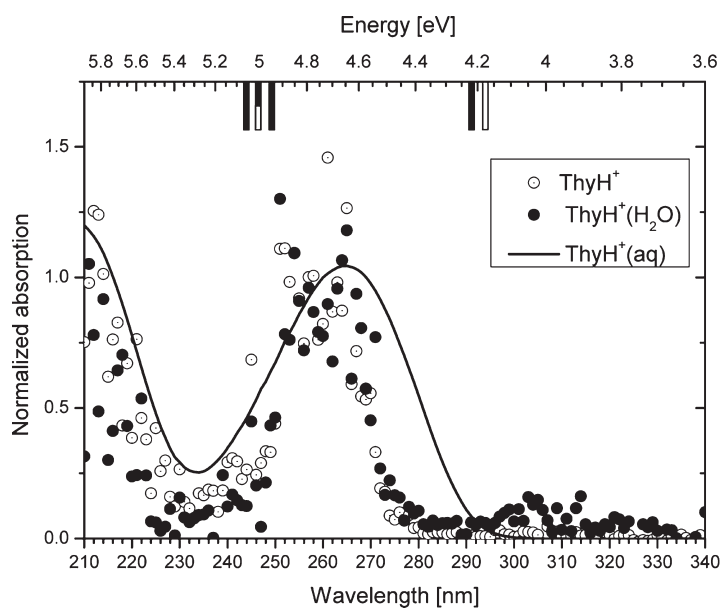
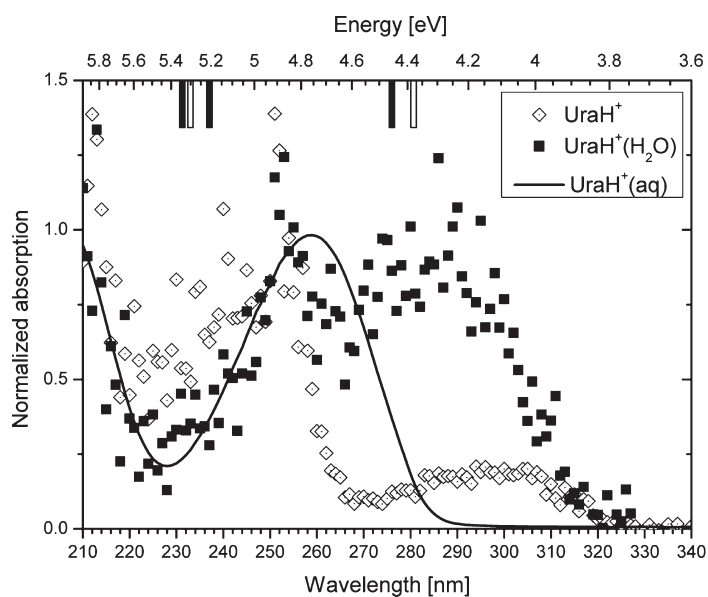


Figure 6.9: Illustrating the two tautomers of Thymine and Uracil, and their calculated percentage of the ion beam at SEP1 and calculated mean absorption band maximum. All values from [130].



(a)



(b)

Figure 6.10: Action spectra of (a) protonated thymine and (b) protonated uracil bare ions (hollow) and water complexes (solid). The absorption spectra for fully solvated species are superimposed as the solid black lines. The bars on top illustrate the TD-DFT calculated vertical excitation energies. Figures from ref [130].

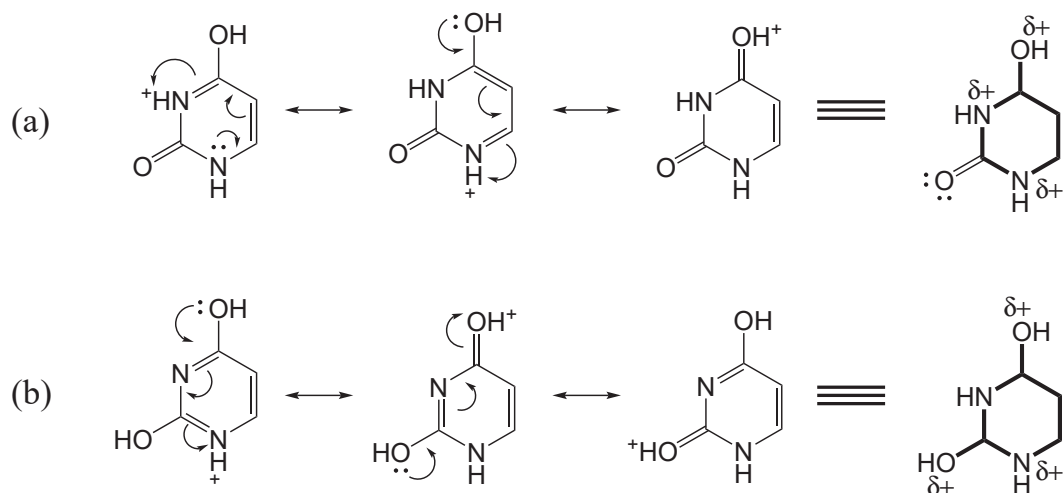


Figure 6.11: Resonance structures of protonated uracil tautomers. (a) 138^+ tautomer, (b) 178^+ tautomer. Based on the resonance structures, the 138^+ tautomer exhibit a CT-like transition, where the lone pairs on the oxygen can be transferred into the ring structure upon excitation. Whereas the charge on the 178^+ tautomer is delocalised over the whole molecule. The charge delocalisation on both tautomers is illustrated by the bold lines.

completely delocalised charge distribution. Furthermore, as seen for protonated thymine, the percentage of the 138^+ tautomer increased upon binding a water molecule, as seen by the relative height in the absorption data. On top of the increase in tautomer 138^+ percentage, a clear blue shift is seen in the absorption band maximum. The shift in energy is 0.14 eV. This, and the fact that the absorption band is broader and much more red shifted compared to the absorption from the 178^+ tautomer, indicates that this transition could have a CT transition.

The conclusion that the 138^+ tautomer has CT character, and the 178^+ tautomer is fully delocalised, is further established by looking at the simple resonance structures in Figure 6.11. The resonance structures illustrates the complete conjugation on the 178^+ tautomers (just as for permanganate, *p*-benzoquinone and $\text{Ru}(\text{bipy})_3^{2+}$), and a somewhat localised conjugation for the 138^+ tautomers.

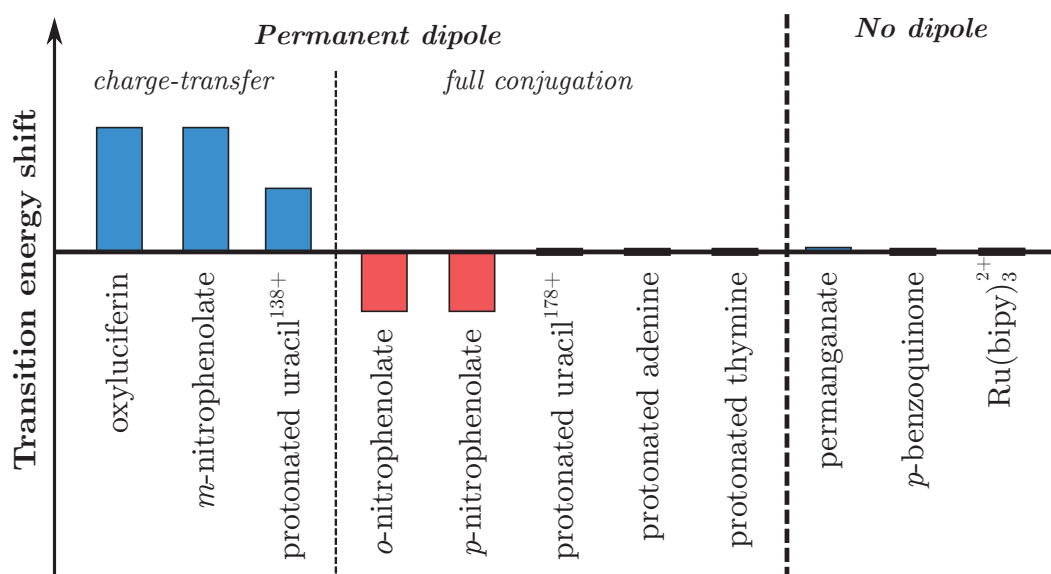


Figure 6.12: Summarising the experimental results of micro solvation experiments. Oxyluciferin, *meta*-nitrophenolate and the 138⁺ tautomer of protonated uracil has a transition with a high degree of charge-transfer, resulting in a blue shift upon micro solvation. *ortho*-nitrophenolate and *para*-nitrophenolate show a red shift, due to superposition of a more CT-like transition and hence also electrostatic effect upon micro solvation. Protonated adenine, protonated thymine and the 178⁺ tautomer of protonated uracil show no shift in transition energy upon micro solvation. No shift is seen for any of the ions with no permanent dipole: *p*-benzoquinone or Ru(bipy)₃²⁺, and only a very small blue shift is seen for permanganate.

6.6 Summary of experimental results

All the experimental data currently available on the effect of micro solvation on the electronic transitions studied at SEP1 are summarised in Table 6.1 and Figure 6.12.

Judging from the data, micro solvation has almost no effect on the highly symmetrical no permanent dipole ions. These ions have shown to be very robust in terms of electronic transition energies regardless of perturbations from the local environment. This category of ions could be used in molecular electronics if robustness of the electronic transition energy is desired[133], as in the case of e.g. the quinones in photosynthesis. In contrast, if color modulation by the perturbations from the local environment is

Table 6.1: Absorption band maximum in nm and eV, and shifts from the bare ions in ΔeV . A negative ΔeV value corresponds to a red shifted absorption.

Ion	<i>Bare</i>		<i>Solvent</i>		
	nm	eV	nm	eV	ΔeV
oxyluciferin	548	2.26	^a 498	2.49	0.23
<i>m</i> -nitrophenolate	530	2.38	^a 485	2.56	0.22
	-	-	^b 485	2.56	0.22
	-	-	^c 505	2.46	0.12
<i>o</i> -nitrophenolate	399	3.11	^a 412	3.01	-0.10
<i>p</i> -nitrophenolate	393	3.15	^a 413	3.00	-0.15
protonated uracil ¹³⁸	298	4.16	^a 288	4.31	0.14
protonated uracil ¹⁷⁸	254	4.88	^a 254	4.88	0
protonated thymine ¹³⁸	?	?	^a 305	4.06	?
protonated thymine ¹⁷⁸	260	4.77	^a 260	4.77	0
protonated adenine	264	4.97	^a 264	4.97	0
permanganate	564	2.20	^a 561	2.21	0.01
<i>p</i> -benzoquinone ¹	435	2.85	^a 435	2.85	0
<i>p</i> -benzoquinone ²	312	3.97	^a 312	3.97	0
Ru(bipy) ₃ ²⁺	260	4.77	^c 260	4.77	0

^awater, ^bmethanol, ^cacetonitrile, ^{138/178}tautomer
^{1/2}transition number

desirable, an ion with high degree of charge-transfer transition like *meta*-nitrophenolate or oxyluciferin should be chosen. In the case of the protonated nucleobases, the transition energies of protonated adenine and protonated thymine showed no effect from the local environment and in the case of protonated uracil, only the tautomer with CT like transition showed a blue shift. These two extreme types of transitions are easily interpreted:

- The transition energy, of a no-permanent dipole moment ion, is not affected by the local micro environment.
- The transition energy of a charge-transfer transition is blue shifted due to simple electrostatic effects.

For the *ortho* and *para*-nitrophenolate, a small red shift was seen in the transition energies. This red shift is most likely due to a superposition of de-coupling (more CT like transition) and electrostatic cost of the transition in a non-trivial way. In order to fully understand the perturbing effects on intermediate systems more data is needed.

In conclusion, it is not trivial to predict the effect of the local micro environment on a transition energy, unless the molecule is totally symmetric or has a transition with a high degree of charge transfer. In the case of a very symmetric ion the effects of micro solvation cancels out to a near net zero effect. In the case of a transition with high degree of charge transfer, a blue shift of up to approximately 0.2 eV can be expected, due to electrostatic effects. This conclusion is drawn upon a very limited dataset, and future experiments should be conducted in order to verify the conclusion presented here.

Outlook

The data presented in this thesis for the study of the effect on the transition energy by micro solvation, has come about due to many different projects on many vastly different ions. In order to pinpoint e.g. the potential maximum effect of micro solvation on a charge-transfer transition, or the effect of a much stronger binding solvent on a fully symmetrical charge distribution, a more rigorous approach could be taken than the one presented here. The more controlled approach would be to have some model systems, like the ones shown in this thesis, and have them subjected to a larger range of solvent molecules, with varying polarisability and dipole moment. In order to get any meaningful observations from such a study, the complexes might need to be cooled down in order to pinpoint the absorption band maximum with high accuracy[134, 135]. This cooling of the ion-complexes would enable the detection of much smaller shifts in transition energy. Cooling of the ions might also make it possible to study the effect of two or more solvent molecules attached. This has not previously been possible at SEP1, which may be due to the place of complex formation. At SEP1 the solvent complexes are formed in an octopole. If the complexes were instead formed in the multipole ion trap, the potential of the trapping field would be more flat near the center. This flat trapping potential would result in fewer accelerated collisions, and might lead to formation of larger solvated ions. This would shed light upon not only the first step in ion solvation, but also the steps in between bare ion and fully

solvated. On that note, for the *meta*-nitrophenolate-acetonitrile and protonated uracil-water complexes, a single solvent molecule was seen to shift the absorption almost half the way to the fully solvated species. This observation naturally raises the question of how many solvent molecules are actually needed for a species to be fully solvated? Another curious result presented in this thesis is the fact that there is no shift in absorption band maximum upon micro solvation for the symmetrical ions *p*-benzoquinone and $\text{Ru}(\text{bipy})_3^{2+}$. It would be interesting to study this result on a wider variety of solvent molecules to see, if the two opposing effects always will result in a zero shift.

In the case of oxyluciferin, it would be very exciting to study the fluorescence instead of the absorption. This experiment has already begun by the building of the LUNA setup. To be able to see fluorescence from oxyluciferin, the ion needs to be cooled down in order for fluorescence to compete with internal conversion. This requires modifications to the current LUNA setup, as cooling has not yet been implemented. There are a few ways such a cooling could be implemented. The simple, fastest and cheapest way is to modify the current setup and add a small liquid nitrogen reservoir, which either touch the Paul trap, or cool the helium buffer gas[136]. This would, if mounted and screened correctly result in ion temperatures of around 100 K. Another, more expensive but also more effective cooling mechanism is cryo cooling, where ions can reach temperatures of a few kelvin[137]. This setup requires a whole new vacuum section at LUNA, with multiple turbo pumps and ion transmission components. No matter which method is used, the ability to study fluorescence from cold molecular ions would open up new exciting experiments. These experiments will be based on luminescence from cold ions, which will remove many of the experimental uncertainties. In addition to cooling the ions at LUNA, the possibility of selecting individual isomers based on their 3D structure by the use of Ion Mobility Mass Spectrometry[138–140] would open up whole new world of exciting projects, where we would have total control over the isomers in the ion beam.

In short, the future seems bright and cold!

Summary

In the course of my PhD studies, I have investigated the intrinsic photophysical properties of a wide range of molecular ions important in the contexts of biophysics, nanotechnology, and fundamental chemical physics. My molecular case studies have included permanganate, oxyluciferin, chlorophyll complexes, the chromophore of the Photoactive Yellow Protein (PYP), vinylheptafulvene derivatives, and several nitrophenolates. The latter are good model systems for larger biochromophores that contain the phenolate moiety and that undergo charge-transfer transitions. Experiments on bare ions with a single solvent molecule attached revealed the fundamental perturbing effects of a nearby dipole: One water molecule blueshifts the absorption by the *meta*-nitrophenolate isomer by 0.22 eV. This isomer undergoes a charge-transfer transition, where charge density moves from the donor phenolate group to the accepting nitro group. The weakening of the electrostatic interaction between the ion charge and the solvent dipole upon excitation results in the higher transition energy for the complex. In contrast, the effect of a single water molecule on the fully conjugated *ortho* and *para* isomers results in red shifts of 0.10 eV and 0.15 eV, respectively. In these cases, the solvent molecule localises the negative charge at one end and as a result the delocalisation is lowered (*i.e.* donor and acceptor states are decoupled), which results in a more charge-transfer like transition, which gives rise to a red-shifted transition energy. This effect is larger than the loss of interaction energy between

the phenolate oxygen and the water dipole. For the oxyluciferin anion, which is responsible for light emission from fireflies and other insects, I measured a similar blue shift as for *meta*-nitrophenolate. Oxyluciferin is one example of a biochromophore (*i.e.* a molecule responsible for the photo-activity of a biological protein or enzyme) that contains the phenolate moiety. Our results indicate that the nature of the transition in the oxyluciferin case is also charge transfer and lend support to the idea that the large colour differences (from yellow-green to red) seen between different insects such as fireflies, click beetles and railroad worms are due to microenvironmental effects within the luciferase enzyme. In other experiments, it was found that a single solvent molecule attached to a symmetric ion with no permanent dipole moment (permanganate, *p*-benzoquinone and $\text{Ru}(\text{bipy})_3^{2+}$) does not affect the electronic transition energy much, despite a significant perturbation of the charge distribution within the ion. The explanation is the same as that for *ortho* and *para* nitrophenolates: there are two opposing shifts that almost balance each other. Finally, a study of protonated nucleobases (uracil, thymine and adenine) showed the same effects as described above, where only tautomers that undergo a charge-transfer like transition showed a (blue) shift in transition energy. Other transitions were affected very little by the presence of a nearby water molecule. These experiments were all conducted on a home-built sector mass spectrometer equipped with an electrospray ion source, where action spectroscopy was performed using wavelength-tunable, nanosecond-pulsed lasers. I wrote the control software for most of the experimental setup using LabVIEW. The software has automated many aspects of the experimental work, resulting in better and faster experimental results. The previously mentioned laser systems, which generate visible light by pumping an optical parametric oscillator (OPO) with the third harmonic of a Nd:YAG laser, lack power in the output region between 350 nm to 420 nm. In order to circumvent this limitation I have built a laser add-on that uses sum-frequency generation to generate light in the colour region between 301 nm to 425 nm. This is done using a non-linear BBO crystal. The fundamental Nd:YAG 1064 nm photons are mixed with the photons in the visible region generated by the OPO to generate the UV photons. This sum-frequency add-on was crucial in obtaining

the absorption band maximum for the *ortho* and *para* nitrophenolate ions and the chlorophyll complexes in the Soret band region. Furthermore, the sum-frequency add-on has been used to obtain data for the oxyluciferin and dimethylated oxyluciferin cation (yet unpublished), and the photo yellow protein (PYP) chromophore. Gas-phase action spectroscopy uses photo-induced dissociation or electron emission (the action) as an indirect measure of an ion's absorption spectrum. This technique is not optimal for large ions which have many degrees of freedom over which to distribute the excitation energy and may thus require the absorption of multiple optical photons to induce a measurable action signal. In such cases, measurement of laser-induced fluorescence (which requires only a single photon) may be an attractive alternative. Recently, I was also involved in the design and construction of a new setup for luminescence experiments on ions in vacuo. This setup also uses electrospray ionisation to bring the ions into the gas phase. The heart of this setup is a cylindrical Paul trap where ions are stored and photoexcited. I designed and constructed the optical setup for the input laser, which utilizes Fresnell diffraction to optimise the spatial profile of the laser. I have also designed the optical setup for light collection from the Paul trap. As a way to improve the mass-selectivity of the Paul trap, I also designed and implemented an axial excitation scheme to selectively eject unwanted ions from the Paul trap. I have written the software used for controlling the axial excitation, trigger timings, the spectrometer and the CCD camera.

Dansk Resumé

I løbet af min PhD har jeg undersøgt de fotofysiske egenskaber af en bred vifte af molekulære ioner der har relevans indenfor biofysik, nanoteknologi, og fundamental kemisk fysik. De ioner jeg har undersøgt er permanganat, oxyluciferin, klorofyl komplekser, kromoforen af Photoactive Yellow Protein (PYP), ioner fra vinylheptafulvene familien, og flere nitrophenolater. Sidstnævnte er gode modelsystemer for større biochromophorer der indeholder en phenolatgruppe og som har en *charge-transfer* overgang. Forsøg med nøgne ioner med et enkelt vandmolekyle bundet afslørede effekten af en nærliggende dipol: Et vandmolekyle blåskifter *meta*-nitrophenolat-isomerens absorption med 0.22 eV. Denne isomer undergår en charge-transfer overgang, hvor ladningstæthed flyttes fra donor phenolatgruppen til den accepterende nitrogruppe. Svækkelsen af den elektrostatiske vekselvirkning mellem ionens ladningen og vandmolekylets dipol ved excitation resulterer i en højere excitationensenergi for komplekset. I modsætning hertil rødforskyder et enkelt vandmolekyle bundet til de fuldt konjugerede *ortho* og *para* isomerer overgangsenergien med hhv. 0.10 eV og 0.15 eV. I disse tilfælde lokaliserer vandmolekylets dipol den negative ladning i den ene ende af ionen, hvilket medfører at konjugationen mindskes (dvs. donor- og acceptor-tilstandene afkobles), hvilket resulterer i en mere charge-transfer lignende overgang, der giver anledning til en rødforskydning af overgangsenergien. Denne effekt er større end tabet af vekselvirkningsenergien mellem phenolatetoxygenet og vandets dipol. For oxyluciferinanio-

nen, som er ansvarlig for lysudsendelse fra ildfluer og andre insekter, målte jeg et lignende blåskift som for *meta*-nitrophenolaten. Oxy-luciferin er et eksempel på en biochromophor (dvs. et molekyle der er ansvarlig for foto-aktiviteten af et biologisk protein eller enzym), der indeholder en phenolatgruppe. Vores resultater understøtter hypotesen om at farveforskellene (fra gul-grøn til rød) der ses udsendt af forskellige insekter som ildfluer, klik biller og "railroad" orme skyldes mikromiljøets påvirkninger af kromoforen i luciferase-enzymet. I andre forsøg blev det konstateret, at et enkelt vandmolekyle bundet til en symmetrisk ion uden permanent dipolmoment (permanganat, *p*-benzoquinon og $\text{Ru}(\text{bipy})_3^{2+}$) ikke påvirker den elektroniske overgang meget, på trods af en væsentlig forstyrrelse af det konjugerede system. Forklaringen er den samme som for *ortho* og *para* nitrophenolaterne: Der er to modsatrettede forskydninger, som næsten balancerer hinanden. Endelig viste en undersøgelse af protoniserede nukleobaser (uracil, thymin og adenin) de samme tendenser som beskrevet ovenfor, hvor kun tautomerene, der har en *charge-transfer* overgang gav anledning til et (blå)skift i overgangsenergien. Andre overgange blev meget lidt påvirket af tilstedeværelsen af et nærliggende vandmolekyle. Alle disse eksperimenter blev udført på et hjemmebygget sektor massespektrometer udstyret med en elektrospay ionkilde, hvor action spektroskopi blev udført ved hjælp af tunebare nanosekund-pulserede lasere. Jeg skrev kontrolsoftwaren til styring af det meste af forsøgsopstillingen i LabVIEW. Dette program har automatiseret mange aspekter af det eksperimentelle arbejde, hvilket har resulteret i bedre og hurtigere resultater. De tidligere nævnte lasersystemer, der genererer synligt lys ved at pumpe en optisk parametriske oscillator (OPO) med den tredje harmoniske fra en Nd:YAG-laser, har lille lysintensitet i området mellem 350 nm og 420 nm. For at omgå denne begrænsning har jeg bygget et lasermodul, der bruger sum-frekvens generering til at lave lys i området mellem 301 nm og 425 nm. Dette sker ved hjælp af en ikke-lineær BBO krystal. Den fundamentale Nd:YAG 1064 nm foton mikser med fotonerne i det synlige område fra OPO'en for derved at generere UV fotoner. Denne sum-frekvens tilføjelse var afgørende for at bestemme absorptionsbåndmaksimummet for *ortho* og *para*-nitrophenolat ionerne og klorofyl komplekserne i Soret båndet. Desuden er sum-frekvens til-

føjelsen blevet anvendt til at opsamle data for oxyluciferinkationen og den dimethylerede oxyluciferinkationen (endnu ikke publiceret), og PYP kromoforen. Gas-fase action spektroskopi bruger foto-fragmentering eller elektron emission (action) som et indirekte mål for ionens absorptionsspektrum. Denne teknik er ikke optimal for store ioner, der har mange frihedsgrader over hvilke det er muligt at fordele excitationsenergien. Således kan absorption af flere fotoner være nødvendigt for at inducere et målbart action signal inden for instrumentets måletid (i vores eksperimenter mikrosekunder). I sådanne tilfælde kan måling af laser-induceret fluorescens (som kun kræver en enkelt foton) være et attraktivt alternativ. Jeg har været involveret i opbygningen af et nyt luminescens instrument for ioner i vakuum. Denne opstilling anvender også elektropray ionisering til at bringe ionerne på gasform. Hjertet er en cylindrisk Paul fælde, hvor ionerne fanges og fotoexciteres. Jeg har designet og bygget den optiske opstilling for input laseren, som anvender Fresnell diffraktion til at optimere den rumlige laserprofil. Jeg har ligeledes designet det optiske setup for lysopsamling fra Paul fælden. Som en måde at forbedre masse-selektiviteten i Paul fælden, har jeg bygget en opstilling der selektivt kan excitere ioner aksialt og derved skubbe uønskede ioner ud af Paul-fælden. Jeg har skrevet den software der anvendes til styring af denne opstilling, tidsstyringen, spektrometret og CCD-kameraet.

Abbreviations

ADC	Analog to Digital Converter
CEM	Channeltron Electron Multiplier
CFD	Constant Fraction Discriminator
CID	Collision Induced Dissociation
CT	Charge-Transfer
DAC	Digital to Analog Converter
ELISA	Electrostatic Storage Ring for Ions in Aarhus
ESA	Electrostatic Analyser
ESI	Electrospray Ionisations
FPGA	Field-Programmable Gate Array
FWHM	Full width half maximum
HOMO	Highest occupied molecular orbital
IC	Internal Conversion
IVR	Intramolecular Vibrational energy Redistribution
LED	Leading Edge Discriminator
LUMO	Lowest unoccupied molecular orbital
LUNA	Luminescence Instrument in Aarhus
OPO	Optical Parametric Oscillator
PCL	Programmable Logic Controller
PID	Photo Induced Dissociation
PMT	Photo Multiplier Tube
SEP1	Seperator 1
TDC	Time to Digital Converter
TOF	Time of Flight

Personal contributions

This chapter has no explicit scientific value other than to highlight my contributions to the experimental setups used during my PhD.

SEP1

Control software

At SEP1 I have been one of two contributors to the data acquisition software, and I have been responsible for the continued development since April of 2015. The software has helped automate nearly every aspect of the data acquisition, and has been running smoothly and consistently. The ease of use has helped new members of the group quickly to be able to run experiments by themselves. The control software automates the scanning of the ESA potential, laser wavelengths (both for the EKSPLA lasers and for the sum-frequency add-on), the automated filter wheel and the magnet current. The program uses a National Instruments FPGA (field programmable gate array) to control the timings and to count the signals from the detectors at a time resolution of 4 ns.

Heated capillary

I have contributed to the design of the heated capillaries used at SEP1 and LUNA, and I have been responsible for the assembly of

both. I was deeply involved in the development of the heated capillary and the electrospray ion source that was built for a group in Rome (paola.bolognesi@cnr.it).

SED

I have contributed to the design of the newly installed secondary electron detector at SEP1. I have designed and implemented the required electronic circuits and components and I have assembled and tested the unit. Furthermore, I have adjusted the control software to enable both detector 1 and detector 2.

LUNA

I have contributed to the overall design of LUNA. I have assembled the whole setup in collaboration with Postdoc. Mark H. Stockett. I have designed the optical system for light detection and laser beam clean up.

Software

In addition to the CONSYS software, I have designed and created the control software for LUNA. This includes the control script for the spectrometer and CCD camera, and the control software and hardware (PC trigger card and logic circuits) for the different timing aspects of the setup. In addition to this, I have written a program that lets you scan a parameter (laser wavelength, filter wheel, CONSYS parameter etc.) while recording the luminescence.

SWIFT

I have designed and implemented the stored waveform inverse Fourier transform (SWIFT) mass-selecting method at LUNA. This includes both the software for generating the different potential time series (SWIFT pulse and single and multiple sine and chirp pulses) and hardware. I have made the electronic circuit for coupling the SWIFT pulse to the end cap DC potentials of the Paul trap.

Sum-frequency add-on

I have designed and assembled the sum-frequency generating laser add-on, in addition to adapting the EKSPLA laser for use with the add-on. I have calculated and measured the different angles for the BBO (the non-linear crystal) to generate the sum-frequency signal. Furthermore, I have written the control software for easy control of the input/output wavelengths.

Data analysis software

In order to make the data analysis fast and consistent I have written a data analysis program that supports all data files from SEP1 and LUNA. This program makes it easy and fast to analyse and compare different data files. In addition, it is also possible to add and scale data from different data files in order to get the averaged data and standard deviations. The analysis program can add data files to a shared database. This database is searchable from the analysis software, making it fast and easy to find specific data files.

Miscellaneous software and overall maintenance

In addition to the control software for SEP1 and LUNA, I have developed the communication scheme between the different programs and computers. This scheme makes the reading and writing of different parameters (filter wheel, laser wavelength, CONSYS information etc.) easy and consistent.

I have been responsible for the day-to-day maintenance of the laboratory for the last year and a half. This includes cooling water, pressurised air, oil-, scroll- and turbo pumps, adjustments of detection electronics, debugging of faulty hardware/software, cabling and so on.

Bibliography

- [1] V. Yatsyna, D. J. Bakker, P. Salén, R. Feifel, A. M. Rijs, and V. Zhaunerchyk. *Infrared Action Spectroscopy of Low-Temperature Neutral Gas-Phase Molecules of Arbitrary Structure*. Phys. Rev. Lett., **117**: 118101 (2016).
- [2] M. S. de Vries and P. Hobza. *Gas-Phase Spectroscopy of Biomolecular Building Blocks*. Annu. Rev. Phys. Chem., **58**: 585–612 (2007).
- [3] R. Weinkauff, J.-P. Schermann, M. de Vries, and K. Kleinermanns. *Molecular physics of building blocks of life under isolated or defined conditions*. EPJ D, **20**: 309–316 (2002).
- [4] T. W. Robinson, H. G. Kjaergaard, S.-I. Ishiuchi, M. Shinozaki, and M. Fujii. *Vibrational Overtone Spectroscopy of Jet-Cooled Aminophenols as a Probe for Rotational Isomers*. J. Phys. Chem. A, **108**: 4420–4427 (2004).
- [5] S. Boye, H. Krogh, I. B. Nielsen, S. Brøndsted Nielsen, S. U. Pedersen, U. V. Pedersen, L. H. Andersen, A. F. Bell, X. He, and P. J. Tonge. *Vibrationally resolved photoabsorption spectroscopy of red fluorescent protein chromophore anions*. Phys. Rev. Lett., **90**: 118103 (2003).
- [6] S. Boye, I. B. Nielsen, S. Brøndsted Nielsen, H. Krogh, A. Lapierre, H. B. Pedersen, S. U. Pedersen, U. V. Pedersen, and L. H. Andersen. *Gas-phase absorption properties of a green fluorescent protein-mutant chromophore: The W7 clone*. J. Chem. Phys., **119**: 338–345 (2003).
- [7] I. Alata, C. Dedonder, M. Broquier, E. Marceca, and C. Jouvet. *Role of the Charge-Transfer State in the Electronic Absorption of Protonated Hydrocarbon Molecules*. J. Am. Chem. Soc., **132**: 17483–17489 (2010).

- [8] K. Lincke, T. Sølling, L. H. Andersen, B. Klærke, D. B. Rahbek, J. Rajput, C. B. Oehlenschläger, M. Å. Petersen, and M. Brøndsted Nielsen. *On the absorption of the phenolate chromophore in the green fluorescent protein-role of individual interactions*. Chem. Commun., **46**: 734–736 (2010).
- [9] M. A. Christensen, E. A. Della Pia, J. Houmøller, S. Thomsen, M. Wanko, A. D. Bond, A. Rubio, S. Brøndsted Nielsen, and M. Brøndsted Nielsen. *Cross-Conjugation vs. Linear Conjugation in Donor-Bridge-Acceptor Nitrophenol Chromophores*. Eur. J. Org. Chem., **2014**: 2044–2052 (2014).
- [10] M. W. Forbes and R. A. Jockusch. *Deactivation Pathways of an Isolated Green Fluorescent Protein Model Chromophore Studied by Electronic Action Spectroscopy*. J. Am. Chem. Soc., **131**: 17038–17039 (2009).
- [11] P. Markush, P. Bolognesi, A. Cartoni, P. Rousseau, S. Maclot, R. Delaunay, A. Domaracka, J. Kocisek, M. C. Castrovilli, B. A. Huber, and L. Avaldi. *The role of the environment in the ion induced fragmentation of uracil*. Phys. Chem. Chem. Phys., **18**: 16721–16729 (2016).
- [12] K. Chingin, R. M. Balabin, V. Frankevich, K. Barylyuk, R. Nieckarz, P. Sagulenko, and R. Zenobi. *Absorption of the green fluorescent protein chromophore anion in the gas phase studied by a combination of FTICR mass spectrometry with laser-induced photodissociation spectroscopy*. Int. J. Mass Spectrom., **306**: 241 – 245 (2011).
- [13] M. Wanko, P. García-Risueño, and A. Rubio. *Excited states of the green fluorescent protein chromophore: Performance of ab initio and semi-empirical methods*. Phys. Status Solidi B, **249**: 392–400 (2012).
- [14] L. H. Andersen, I. B. Nielsen, M. B. Kristensen, M. O. A. El Ghazaly, S. Haacke, M. Brøndsted Nielsen, and M. Å. Petersen. *Absorption of Schiff-Base Retinal Chromophores in Vacuo*. J. Am. Chem. Soc., **127**: 12347–12350 (2005).
- [15] O. Valsson and C. Filippi. *Gas-Phase Retinal Spectroscopy: Temperature Effects Are But a Mirage*. J. Phys. Chem. Lett., **3**: 908–912 (2012).
- [16] M. Goto, J. Matsumoto, H. Shiromaru, Y. Achiba, T. Majima, H. Tanuma, and T. Azuma. *Laser-induced thermal detachment of hot, large molecular ions under multiphoton-absorption conditions*. Phys. Rev. A, **87**: 033406 (2013).
- [17] E. Epifanovsky, K. Kowalski, P.-D. Fan, M. Valiev, S. Matsika, and A. I. Krylov. *On the electronically excited states of uracil*. J. Phys. Chem. A, **112**: 9983–9992 (2008).

- [18] E. Epifanovsky, I. Polyakov, B. Grigorenko, A. Nemukhin, and A. I. Krylov. *Quantum Chemical Benchmark Studies of the Electronic Properties of the Green Fluorescent Protein Chromophore. 1. Electronically Excited and Ionized States of the Anionic Chromophore in the Gas Phase*. J. Chem. Theory Comput., **5**: 1895–1906 (2009).
- [19] Y. Shao, L. F. Molnar, Y. Jung, J. Kussmann, C. Ochsenfeld, S. T. Brown, A. T. B. Gilbert, L. V. Slipchenko, S. V. Levchenko, D. P. O’Neill, R. A. DiStasio, Jr., R. C. Lochan, T. Wang, G. J. O. Beran, N. A. Besley, J. M. Herbert, C. Y. Lin, T. Van Voorhis, S. H. Chien, A. Sodt, R. P. Steele, V. A. Rassolov, P. E. Maslen, P. P. Korambath, R. D. Adamson, B. Austin, J. Baker, E. F. C. Byrd, H. Dachsel, R. J. Doerksen, A. Dreuw, B. D. Dunietz, A. D. Dutoi, T. R. Furlani, S. R. Gwaltney, A. Heyden, S. Hirata, C.-P. Hsu, G. Kedziora, R. Z. Khalliulin, P. Klunzinger, A. M. Lee, M. S. Lee, W. Liang, I. Lotan, N. Nair, B. Peters, E. I. Proynov, P. A. Pieniazek, Y. M. Rhee, J. Ritchie, E. Rosta, C. D. Sherrill, A. C. Simmonett, J. E. Subotnik, H. L. Woodcock, III, W. Zhang, A. T. Bell, A. K. Chakraborty, D. M. Chipman, F. J. Keil, A. Warshel, W. J. Hehre, H. F. Schaefer, III, J. Kong, A. I. Krylov, P. M. W. Gill, and M. Head-Gordon. *Advances in methods and algorithms in a modern quantum chemistry program package*. Phys. Chem. Chem. Phys., **8**: 3172–3191 (2006).
- [20] C. M. Oana and A. I. Krylov. *Cross sections and photoelectron angular distributions in photodetachment from negative ions using equation-of-motion coupled-cluster Dyson orbitals*. J. Chem. Phys., **131** (2009).
- [21] F. Yang, L. G. Moss, and G. N. Phillips. *The molecular structure of green fluorescent protein*. Nat. Biotechnol., **10**: 1246–1251 (1996).
- [22] J. Petersen, P. G. Wilmann, T. Beddoe, A. J. Oakley, R. J. Devenish, M. Prescott, and J. Rossjohn. *The 2.0-Å Crystal Structure of eqFP611, a Far Red Fluorescent Protein from the Sea Anemone Entacmaea quadricolor*. J. Biol. Chem., **278**: 44626–44631 (2003).
- [23] I. Nielsen, S. Boyé-Péronne, M. El Ghazaly, M. Kristensen, S. Brøndsted Nielsen, and L. Andersen. *Absorption Spectra of Photoactive Yellow Protein Chromophores in Vacuum*. Biophys. J., **89**: 2597 – 2604 (2005).
- [24] D. Zuev, K. B. Bravaya, M. V. Makarova, and A. I. Krylov. *Effect of microhydration on the electronic structure of the chromophores of the photoactive yellow and green fluorescent proteins*. J. Chem. Phys., **135**: 194304 (2011).
- [25] A. Sinicropi, T. Andruniow, N. Ferré, R. Basosi, and M. Olivucci. *Properties of the Emitting State of the Green Fluorescent Protein Resolved at the CASPT2//CASSCF/CHARMM Level*. J. Am. Chem. Soc., **127**: 11534–11535 (2005).

- [26] K. B. Bravaya, M. G. Khrenova, B. L. Grigorenko, A. V. Nemukhin, and A. I. Krylov. *Effect of Protein Environment on Electronically Excited and Ionized States of the Green Fluorescent Protein Chromophore*. J. Phys. Chem. B, **115**: 8296–8303 (2011).
- [27] A. R. Milosavljević, V. Z. Cerovski, F. Canon, M. L. Ranković, N. Škoro, L. Nahon, and A. Giuliani. *Energy-Dependent UV Photodissociation of Gas-Phase Adenosine Monophosphate Nucleotide Ions: The Role of a Single Solvent Molecule*. J. Phys. Chem. Lett., **5**: 1994–1999 (2014).
- [28] E. G. Buchanan, J. R. Gord, and T. S. Zwier. *Solvent Effects on Vibronic Coupling in a Flexible Bichromophore: Electronic Localization and Energy Transfer induced by a Single Water Molecule*. J. Phys. Chem. Lett., **4**: 1644–1648 (2013).
- [29] M.-B. S. Kirketerp, T. Ryhding, K. Støchkel, M. Brøndsted Nielsen, and S. Brøndsted Nielsen. *Role of Nearby Charges on the Electronic Structure of π -Conjugated Molecules: Symmetric versus Asymmetric Charge Distributions in Oligo(*p*-phenyleneethynylene)*. J. Phys. Chem. A, **115**: 1222–1227 (2011).
- [30] K. Støchkel, B. F. Milne, and S. Brøndsted Nielsen. *Absorption Spectrum of the Firefly Luciferin Anion Isolated in Vacuo*. J. Phys. Chem. A, **115**: 2155–2159 (2011).
- [31] J. A. Wyer and S. Brøndsted Nielsen. *Absorption by Isolated Ferric Heme Nitrosyl Cations In Vacuo*. Angew. Chem. Int. Ed., **51**: 10256–10260 (2012).
- [32] S. Tomita, J. Forster, P. Hvelplund, A. Jensen, and S. Brøndsted Nielsen. *High energy collisions of protonated water clusters*. EPJ D, **16**: 119–122 (2001).
- [33] H. Shen, P. Hvelplund, D. Mathur, A. Barany, H. Cederquist, N. Selberg, and D. Lorents. *Fullerene-fullerene collisions - fragmentation and electron-capture*. Phys. Rev. A, **52**: 3847–3851 (1995).
- [34] P. Hvelplund, L. Andersen, C. Brink, D. Yu, D. Lorents, and R. Ruoff. *Charge-transfer in collisions involving multiply-charged *c*-60 molecules*. Z. Phys. D, **30**: 323–326 (1994).
- [35] O. Boltalina, P. Hvelplund, T. Jorgensen, M. Larsen, M. Larsson, and D. Sharoitchenko. *Electron capture by fluorinated fullerene anions in collisions with Xe atoms*. Phys. Rev. A, **62**: 023202 (2000).
- [36] J. B. Fenn, M. Mann, C. K. Meng, S. F. Wong, and C. M. Whitehouse. *Electrospray ionization for mass spectrometry of large biomolecules*. Science, **246**: 64–71 (1989).

- [37] S. Nguyen and J. B. Fenn. *Gas-phase ions of solute species from charged droplets of solutions*. Proc. Natl. Acad. Sci. U.S.A., **104**: 1111–1117 (2007).
- [38] J. Fernandez de la Mora. *Electrospray ionization of large multiply charged species proceeds via Dole’s charged residue mechanism*. Anal. Chim. Acta, **406**: 93 – 104 (2000).
- [39] J. Sandström, P. Andersson, K. Fritioff, D. Hanstorp, R. Thomas, D. Pegg, and K. Wendt. *Laser photodetachment mass spectrometry*. Nucl. Instr. Meth. Phys. Res. B, **217**: 513 – 520 (2004).
- [40] Y. Park, V. Choong, Y. Gao, B. R. Hsieh, and C. W. Tang. *Work function of indium tin oxide transparent conductor measured by photoelectron spectroscopy*. Appl. Phys. Lett., **68**: 2699–2701 (1996).
- [41] J. U. Andersen, E. Bonderup, and K. Hansen. *On the concept of temperature for a small isolated system*. J. Chem. Phys., **114**: 6518–6525 (2001).
- [42] L. H. Andersen, H. Bluhme, S. Boye, T. J. D. Jørgensen, H. Krogh, I. B. Nielsen, S. Brøndsted Nielsen, and A. Svendsen. *Experimental studies of the photophysics of gas-phase fluorescent protein chromophores*. Phys. Chem. Chem. Phys., **6**: 2617–2627 (2004).
- [43] M. Kasha. *Characterization of electronic transitions in complex molecules*. Discuss. Faraday Soc., **9**: 14–19 (1950).
- [44] Y.-C. Cheng and G. R. Fleming. *Dynamics of Light Harvesting in Photosynthesis*. Annu. Rev. Phys. Chem., **60**: 241–262 (2009).
- [45] M. A. Green, K. Emery, Y. Hishikawa, W. Warta, and E. D. Dunlop. *Solar cell efficiency tables (Version 45)*. Prog. photovolt., **23**: 1–9 (2015).
- [46] B. F. Milne, Y. Toker, A. Rubio, and S. Brøndsted Nielsen. *Unraveling the Intrinsic Color of Chlorophyll*. Angew. Chem., **127**: 2198–2201 (2015).
- [47] E. L. Smith. *The Chlorophyll-protein Compound Of The Green Leaf*. J. Gen. Physiol., **24**: 565–582 (1941).
- [48] N. W. Withers, R. S. Alberte, R. A. Lewin, J. P. Thornber, G. Britton, and T. W. Goodwin. *Photosynthetic unit size, carotenoids, and chlorophyll—protein composition of Prochloron sp., a prokaryotic green alga*. Proc. Natl. Acad. Sci. U.S.A., **75**: 2301–2305 (1978).
- [49] J. A. Guikema and L. A. Sherman. *Chlorophyll-protein organization of membranes from the cyanobacterium Anacystis nidulans*. Arch. Biochem. Biophys., **220**: 155 – 166 (1983).

- [50] J. C. Waldron and J. M. Anderson. *Chlorophyll-Protein Complexes from Thylakoids of a Mutant Barley Lacking Chlorophyll b*. Eur. J. Biochem., **102**: 357–362 (1979).
- [51] B. F. Milne, C. Kjær, J. Houmøller, M. H. Stockett, Y. Toker, A. Rubio, and S. Brøndsted Nielsen. *On the Exciton Coupling between Two Chlorophyll Pigments in the Absence of a Protein Environment: Intrinsic Effects Revealed by Theory and Experiment*. Angew. Chem. Int. Ed., **55**: 6248–6251 (2016).
- [52] R. Kubin and A. Fletcher. *Fluorescence quantum yields of some rhodamine dyes*. J. Lumin., **27**: 455 – 462 (1983).
- [53] J. T. Khoury, S. E. Rodriguez-Cruz, and J. H. Parks. *Pulsed fluorescence measurements of trapped molecular ions with zero background detection*. J. Am. Soc. Mass Spectrom., **13**: 696 – 708 (2002).
- [54] J. Mitchell Wells, E. R. Badman, and R. Graham Cooks. *A Quadrupole Ion Trap with Cylindrical Geometry Operated in the Mass-Selective Instability Mode*. Anal. Chem., **70**: 438–444 (1998).
- [55] W. Paul and H. Steinwedel. *Ein neues Massenspektrometer ohne Magnetfeld*. Z. Naturforsch. A, **8**: 448–450 (1953).
- [56] Q. Bian, M. W. Forbes, F. O. Talbot, and R. A. Jockusch. *Gas-phase fluorescence excitation and emission spectroscopy of mass-selected trapped molecular ions*. Phys. Chem. Chem. Phys., **12**: 2590–2598 (2010).
- [57] M. Kordel, D. Schooss, C. Neiss, L. Walter, and M. M. Kappes. *Laser-Induced Fluorescence of Rhodamine 6G Cations in the Gas Phase: A Lower Bound to the Lifetime of the First Triplet State*. J. Phys. Chem. A, **114**: 5509–5514 (2010).
- [58] K. Chingin, H. Chen, G. Gamez, and R. Zenobi. *Exploring Fluorescence and Fragmentation of Ions Produced by Electrospray Ionization in Ultrahigh Vacuum*. J. Am. Soc. Mass Spectrom., **20**: 1731 – 1738 (2009).
- [59] E. Mathieu. *Mémoire sur le mouvement vibratoire d’une membrane de forme elliptique*. J. Math. Pures Appl., **13**: 137–203 (1868).
- [60] R. E. March. *An Introduction to Quadrupole Ion Trap Mass Spectrometry*. J. Mass Spectrom., **32**: 351–369 (1997).
- [61] M. Nappi, C. Weil, C. Cleven, L. Horn, H. Wollnik, and R. Graham Cooks. *Visual representations of simulated three-dimensional ion trajectories in an ion trap mass spectrometer*. Int. J. Mass Spectrom. Ion Processes, **161**: 77 – 85 (1997).

- [62] R. March, R. Hughes, and J. Todd. *Quadrupole Storage Mass Spectrometry*. A Wiley-Interscience publication. Wiley (1989). Pp. 200.
- [63] S. Guan and R. T. McIver. *Optimal phase modulation in stored wave form inverse Fourier transform excitation for Fourier transform mass spectrometry. I. Basic algorithm*. J. Chem. Phys., **92**: 5841–5846 (1990).
- [64] S. Guan. *Optimal phase modulation in stored waveform inverse Fourier transform excitation for Fourier transform mass spectrometry. II. Magnitude spectrum smoothing*. J. Chem. Phys., **93**: 8442–8445 (1990).
- [65] L. Jing, C. Li, R. L. Wong, D. A. Kaplan, and I. J. Amster. *Improved Mass Accuracy for Higher Mass Peptides by Using SWIFT Excitation for MALDI-FTICR Mass Spectrometry*. J. Am. Soc. Mass Spectrom., **19**: 76 – 81 (2008).
- [66] S. Guan and A. G. Marshall. *Stored waveform inverse Fourier transform (SWIFT) ion excitation in trapped-ion mass spectrometry: Theory and applications*. Int. J. Mass Spectrom. Ion Processes, **157**: 5 – 37 (1996).
- [67] M. W. Forbes and R. A. Jockusch. *Gas-Phase Fluorescence Excitation and Emission Spectroscopy of Three Xanthene Dyes (Rhodamine 575, Rhodamine 590 and Rhodamine 6G) in a Quadrupole Ion Trap Mass Spectrometer*. J. Am. Soc. Mass Spectrom., **22**: 93–109 (2011).
- [68] M. Zhao, X.-F. Yang, S. He, and L. Wang. *A rhodamine-based chromogenic and fluorescent chemosensor for copper ion in aqueous media*. Sens. Actuators, B, **135**: 625 – 631 (2009).
- [69] M. H. Stockett, J. Houmøller, K. Støchkel, A. Svendsen, and S. Brøndsted Nielsen. *A cylindrical quadrupole ion trap in combination with an electrospray ion source for gas-phase luminescence and absorption spectroscopy*. Rev. Sci. Instrum., **87**: 053103 (2016).
- [70] M. H. Stockett, J. Houmøller, and S. Brøndsted Nielsen. *Nile blue shows its true colors in gas-phase absorption and luminescence ion spectroscopy*. J. Chem. Phys., **145**: 104303 (2016).
- [71] H. Oliveira, A. Camargo, L. Macedo, M. Gehlen, and A. da Silva. *Synthesis, structure, electronic and vibrational spectra of 9-(Diethylamino)-benzo(a)phenoxazin-7-ium-5-N-methacrylamide*. Spectrochim. Acta, Part A, **58**: 3103 – 3111 (2002).
- [72] R. Sens and K. H. Drexhage. *Fluorescence quantum yield of oxazine and carbazine laser dyes*. Journal of Luminescence, **24**: 709 – 712 (1981).
- [73] C. W. Lin, J. R. Shulok, S. D. Kirley, L. Cincotta, and J. W. Foley. *Lyosomal localization and mechanism of uptake of nile blue photosensitizers in tumor-cells*. Cancer Res., **51**: 2710–2719 (1991).

- [74] H. J. Van Staveren, O. C. Speelman, M. J. H. Witjes, L. Cincotta, and W. M. Star. *Fluorescence Imaging and Spectroscopy of Ethyl Nile Blue A in Animal Models of (Pre)malignancies*. Photochem. Photobiol., **73**: 32–38 (2001).
- [75] M. Marazzi, H. Gattuso, and A. Monari. *Nile blue and Nile red optical properties predicted by TD-DFT and CASPT2 methods: static and dynamic solvent effects*. Theor. Chem. Acc., **135**: 1–11 (2016).
- [76] S. Fleming, A. Mills, and T. Tuttle. *Predicting the UV-vis spectra of oxazine dyes*. Beilstein J. Org. Chem., **7**: 432–441 (2011).
- [77] A. G. Gilani, S. Hosseini, M. Moghadam, and E. Alizadeh. *Excited state electric dipole moment of nile blue and brilliant cresyl blue: A comparative study*. Spectrochim. Acta, Part A, **89**: 231 – 237 (2012).
- [78] P. W. Milloni and J. H. Eberly. *Lasers*. Wiley-Interscience (1988).
- [79] J. A. Giordmaine and R. C. Miller. *Tunable Coherent Parametric Oscillation in LiNbO₃ at Optical Frequencies*. Phys. Rev. Lett., **14**: 973–976 (1965).
- [80] A. V. Smith and M. S. Bowers. *Image-rotating cavity designs for improved beam quality in nanosecond optical parametric oscillators*. J. Opt. Soc. Am. B, **18**: 706–713 (2001).
- [81] P. Pellin and A. Broca. *A Spectroscope of Fixed Deviation*. Astrophys. J., **10**: 337 (1899).
- [82] K. Gomi and N. Kajiyama. *Oxyluciferin, a Luminescence Product of Firefly Luciferase, Is Enzymatically Regenerated into Luciferin*. J. Biol. Chem., **276**: 36508–36513 (2001).
- [83] L. Zhong-wei, A. min Ren, J. fu Guo, T. Yang, J. D. Goddard, and J. kang Feng. *Color-Tuning Mechanism in Firefly Luminescence: Theoretical Studies on Fluorescence of Oxyluciferin in Aqueous Solution Using Time Dependent Density Functional Theory*. J. Phys. Chem. A, **112**: 9796–9800 (2008).
- [84] W. L. Ryan, D. J. Gordon, and D. H. Levy. *Gas-Phase Photochemistry of the Photoactive Yellow Protein Chromophore trans-p-Coumaric Acid*. J. Am. Chem. Soc., **124**: 6194–6201 (2002).
- [85] J. U. Andersen, P. Hvelplund, S. Brøndsted Nielsen, S. Tomita, H. Wahlgreen, S. P. Møller, U. V. Pedersen, J. S. Forster, and T. J. D. Jørgensen. *The combination of an electrospray ion source and an electrostatic storage ring for lifetime and spectroscopy experiments on biomolecules*. Rev. Sci. Instrum., **73**: 1284–1287 (2002).

- [86] S. P. Møller. *ELISA, and electrostatic storage ring for atomic physics*. Nucl. Instr. Meth. Phys. Res. A, **394**: 281 – 286 (1997).
- [87] M. Wanko, J. Houmøller, K. Støchkel, M.-B. Suhr Kirketerp, M. Å. Petersen, M. Brøndsted Nielsen, S. Brøndsted Nielsen, and A. Rubio. *Substitution effects on the absorption spectra of nitrophenolate isomers*. Phys. Chem. Chem. Phys., **14**: 12905–12911 (2012).
- [88] F. Liu, Y. Liu, L. D. Vico, and R. Lindh. *Theoretical Study of the Chemiluminescent Decomposition of Dioxetanone*. J. Am. Chem. Soc., **131**: 6181–6188 (2009).
- [89] Y. Ando, K. Niwa, N. Yamada, T. Enomoto, T. Irie, H. Kubota, Y. Ohmiya, and H. Akiyama. *Firefly bioluminescence quantum yield and colour change by pH-sensitive green emission*. Nat. Photonics, **2**: 1749–4885 (2008).
- [90] I. Navizet, Y.-J. Liu, N. Ferré, H.-Y. Xiao, W.-H. Fang, and R. Lindh. *Color-Tuning Mechanism of Firefly Investigated by Multi-Configurational Perturbation Method*. J. Am. Chem. Soc., **132**: 706–712 (2010).
- [91] D. Cai, M. A. L. Marques, B. F. Milne, and F. Nogueira. *Bioheterojunction Effect on Fluorescence Origin and Efficiency Improvement of Firefly Chromophores*. J. Phys. Chem. Lett., **1**: 2781–2787 (2010).
- [92] P. Naumov, Y. Ozawa, K. Ohkubo, and S. Fukuzumi. *Structure and Spectroscopy of Oxyluciferin, the Light Emitter of the Firefly Bioluminescence*. J. Am. Chem. Soc., **131**: 11590–11605 (2009).
- [93] G. Orlova, J. D. Goddard, and L. Y. Brovko. *Theoretical Study of the Amazing Firefly Bioluminescence: The Formation and Structures of the Light Emitters*. J. Am. Chem. Soc., **125**: 6962–6971 (2003).
- [94] N. Nakatani, J.-y. Hasegawa, and H. Nakatsuji. *Red Light in Chemiluminescence and Yellow-Green Light in Bioluminescence: Color-Tuning Mechanism of Firefly, Photinus pyralis, Studied by the Symmetry-Adapted Cluster-Configuration Interaction Method*. J. Am. Chem. Soc., **129**: 8756–8765 (2007).
- [95] C.-I. Song and Y. M. Rhee. *Development of force field parameters for oxyluciferin on its electronic ground and excited states*. Int. J. Quantum Chem., **111**: 4091–4105 (2011).
- [96] K. Støchkel, C. N. Hansen, J. Houmøller, L. M. Nielsen, K. Anggara, M. Linares, P. Norman, F. Nogueira, O. V. Maltsev, L. Hintermann, S. Brøndsted Nielsen, P. Naumov, and B. F. Milne. *On the Influence of Water on the Electronic Structure of Firefly Oxyluciferin Anions from*

- Absorption Spectroscopy of Bare and Monohydrated Ions in Vacuo.* J. Am. Chem. Soc., **135**: 6485–6493 (2013).
- [97] S. L. Holt and C. J. Ballhausen. *Low temperature absorption spectra of $KMnO_4$ in $KClO_4$.* Theor. Chim. Acta, **7**: 313–320 (1967).
- [98] H. Hsu, C. Peterson, and R. M. Pitzer. *Calculations on the permanganate ion in the ground and excited states.* J. Chem. Phys., **64**: 791–795 (1976).
- [99] M. Nooijen. *Combining coupled cluster and perturbation theory.* J. Chem. Phys., **111**: 10815–10826 (1999).
- [100] R. M. Dickson and T. Ziegler. *A density functional study of the electronic spectrum of permanganate.* Int. J. Quantum Chem., **58**: 681–687 (1996).
- [101] M. Seth, T. Ziegler, A. Banerjee, J. Autschbach, S. J. A. van Gisbergen, and E. J. Baerends. *Calculation of the A term of magnetic circular dichroism based on time dependent-density functional theory I. Formulation and implementation.* J. Chem. Phys., **120**: 10942–10954 (2004).
- [102] L. Jose, M. Seth, and T. Ziegler. *Molecular and Vibrational Structure of Tetroxo d0 Metal Complexes in their Excited States. A Study Based on Time-Dependent Density Functional Calculations and Franck–Condon Theory.* J. Phys. Chem. A, **116**: 1864–1876 (2012).
- [103] J. Neugebauer, E. J. Baerends, and M. Nooijen. *Vibronic Structure of the Permanganate Absorption Spectrum from Time-Dependent Density Functional Calculations.* J. Phys. Chem. A, **109**: 1168–1179 (2005).
- [104] J. M. Berg, J. L. Tymoczko, and L. Stryer. *Biochemistry.* New York: W H Freeman, 6 edition (2006). Chapter 19.
- [105] G. L. Closs and J. R. Miller. *Intramolecular Long-Distance Electron Transfer in Organic Molecules.* Science, **240**: 440–447 (1988).
- [106] M. Marianski, A. Oliva, and J. J. Dannenberg. *A Reinvestigation of the Dimer of para-Benzoquinone and Pyrimidine with MP2, CCSD(T), and DFT Using Functionals Including Those Designed to Describe Dispersion.* J. Phys. Chem. A, **116**: 8100–8105 (2012).
- [107] M. Zamadar, A. R. Cook, A. Lewandowska-Andralojc, R. Holroyd, Y. Jiang, J. Bikalis, and J. R. Miller. *Electron Transfer by Excited Benzoquinone Anions: Slow Rates for Two-Electron Transitions.* J. Phys. Chem. A, **117**: 8360–8367 (2013).
- [108] V. Barone, R. Improta, G. Morelli, and F. Santoro. *UV-vis spectra of p-benzoquinone anion radical in solution by a TD-DFT/PCM approach.* Theor. Chem. Acc., **118**: 143–148 (2007).

- [109] D. A. Horke, Q. Li, L. Blancafort, and J. R. R. Verlet. *Ultrafast above-threshold dynamics of the radical anion of a prototypical quinone electron-acceptor*. Nat. Chem., **5**: 711–717 (2013).
- [110] R. Lahtinen, D. J. Fermin, K. Kontturi, and H. H. Girault. *Artificial photosynthesis at liquid / liquid interfaces: photoreduction of benzoquinone by water soluble porphyrin species*. J. Electroanal. Chem., **483**: 81 – 87 (2000).
- [111] A. M. Weyers, R. Chatterjee, S. Milikisiyants, and K. V. Lakshmi. *Structure and Function of Quinones in Biological Solar Energy Transduction: A Differential Pulse Voltammetry, EPR, and Hyperfine Sublevel Correlation (HYSCORE) Spectroscopy Study of Model Benzoquinones*. J. Phys. Chem. B, **113**: 15409–15418 (2009).
- [112] M. H. Stockett and S. Brøndsted Nielsen. *Transition energies of benzoquinone anions are immune to symmetry breaking by a single water molecule*. Phys. Chem. Chem. Phys., **18**: 6996–7000 (2016).
- [113] K. Piech, T. Bally, T. Ichino, and J. Stanton. *Vibronic spectra of the p-benzoquinone radical anion and cation: a matrix isolation and computational study*. Phys. Chem. Chem. Phys., **16**: 2011–2019 (2014).
- [114] A. Juris, V. Balzani, F. Barigelletti, S. Campagna, P. Belser, and A. von Zelewsky. *Ru(II) polypyridine complexes: photophysics, photochemistry, electrochemistry, and chemiluminescence*. Coord. Chem. Rev., **84**: 85 – 277 (1988).
- [115] N. H. Damrauer, G. Cerullo, A. Yeh, T. R. Boussie, C. V. Shank, and J. K. McCusker. *Femtosecond Dynamics of Excited-State Evolution in Ru(bpy)₃²⁺*. Science, **275**: 54–57 (1997).
- [116] K. Kalyanasundaram. *Photophysics, photochemistry and solar energy conversion with tris(bipyridyl)ruthenium(II) and its analogues*. Coord. Chem. Rev., **46**: 159 – 244 (1982).
- [117] S. R. Stoyanov, J. M. Villegas, and D. P. Rillema. *Density Functional Theory Calculations of Selected Ru(II) Two Ring Diimine Complex Dications*. Inorg. Chem., **41**: 2941–2945 (2002).
- [118] J. H. Alstrum-Acevedo, M. K. Brennaman, and T. J. Meyer. *Chemical approaches to artificial photosynthesis. 2*. Inorg. Chem., **44**: 6802–6827 (2005).
- [119] B. D. Koivisto, K. C. D. Robson, and C. P. Berlinguette. *Systematic Manipulation of the Light-Harvesting Properties for Tridentate Cyclometalated Ruthenium(II) Complexes*. Inorg. Chem., **48**: 9644–9652 (2009).

- [120] M. H. Stockett and S. Brøndsted Nielsen. *Does a single CH_3CN molecule attached to $Ru(bipy)_3^{2+}$ affect its absorption spectrum?* J. Chem. Phys., **142** (2015).
- [121] E. A. Bell, P. Boehnke, T. M. Harrison, and W. L. Mao. *Potentially biogenic carbon preserved in a 4.1 billion-year-old zircon.* Proc. Natl. Acad. Sci. U.S.A., **112**: 14518–14521 (2015).
- [122] A. S. Chatterley, C. W. West, G. M. Roberts, V. G. Stavros, and J. R. R. Verlet. *Mapping the Ultrafast Dynamics of Adenine onto Its Nucleotide and Oligonucleotides by Time-Resolved Photoelectron Imaging.* J. Phys. Chem. Lett., **5**: 843–848 (2014).
- [123] R. Improta, F. Santoro, and L. Blancafort. *Quantum Mechanical Studies on the Photophysics and the Photochemistry of Nucleic Acids and Nucleobases.* Chem. Rev., **116**: 3540–3593 (2016).
- [124] D. Ghosh, D. Kosenkov, V. Vanovschi, C. F. Williams, J. M. Herbert, M. S. Gordon, M. W. Schmidt, L. V. Slipchenko, and A. I. Krylov. *Noncovalent Interactions in Extended Systems Described by the Effective Fragment Potential Method: Theory and Application to Nucleobase Oligomers.* J. Phys. Chem. A, **114**: 12739–12754 (2010).
- [125] K. B. Bravaya, O. Kostko, M. Ahmed, and A. I. Krylov. *The effect of π -stacking, H-bonding, and electrostatic interactions on the ionization energies of nucleic acid bases: adenine-adenine, thymine-thymine and adenine-thymine dimers.* Phys. Chem. Chem. Phys., **12**: 2292–2307 (2010).
- [126] L. M. Nielsen, S. V. Hoffmann, and S. Brøndsted Nielsen. *Electronic coupling between photo-excited stacked bases in DNA and RNA strands with emphasis on the bright states initially populated.* Photochem. Photobiol. Sci., **12**: 1273–1285 (2013).
- [127] J. C. Marcum, A. Halevi, and J. M. Weber. *Photodamage to isolated mononucleotides-photodissociation spectra and fragment channels.* Phys. Chem. Chem. Phys., **11**: 1740–1751 (2009).
- [128] C. E. Crespo-Hernández, B. Cohen, P. M. Hare, and B. Kohler. *Ultrafast Excited-State Dynamics in Nucleic Acids.* Chem. Rev., **104**: 1977–2020 (2004).
- [129] M. Barbatti, A. J. A. Aquino, and H. Lischka. *The UV absorption of nucleobases: semi-classical ab initio spectra simulations.* Phys. Chem. Chem. Phys., **12**: 4959–4967 (2010).

- [130] S. Ø. Pedersen, C. S. Byskov, F. Turecek, and S. Brøndsted Nielsen. *Structures of protonated thymine and uracil and their monohydrated gas-phase ions from ultraviolet action spectroscopy and theory*. J. Phys. Chem. A, **118**: 4256–4265 (2014).
- [131] S. Ø. Pedersen, K. Støchkel, C. S. Byskov, L. M. Nielsen, and S. Brøndsted Nielsen. *Gas-phase spectroscopy of protonated adenine, adenosine 5'-monophosphate and monohydrated ions*. Phys. Chem. Chem. Phys., **15**: 19748–19752 (2013).
- [132] J. K. Wolken and F. Turecek. *Proton affinity of uracil. A computational study of protonation sites*. J. Am. Soc. Mass Spectrom., **11**: 1065 – 1071 (2000).
- [133] P. Petrangolini, A. Alessandrini, and P. Facci. *Hydroquinone-Benzoquinone Redox Couple as a Versatile Element for Molecular Electronics*. J. Phys. Chem. C, **117**: 17451–17461 (2013).
- [134] O. V. Boyarkin, S. R. Mercier, A. Kamariotis, and T. R. Rizzo. *Electronic Spectroscopy of Cold, Protonated Tryptophan and Tyrosine*. J. Am. Chem. Soc., **128**: 2816–2817 (2006).
- [135] S. R. Mercier, O. V. Boyarkin, A. Kamariotis, M. Guglielmi, I. Tavernelli, M. Cascella, U. Rothlisberger, and T. R. Rizzo. *Microsolvation Effects on the Excited-State Dynamics of Protonated Tryptophan*. J. Am. Chem. Soc., **128**: 16938–16943 (2006).
- [136] D. Gerlich. *Ion-neutral collisions in a 22-pole trap at very-low energies*. Phys. Scr., **T59**: 256–263 (1995).
- [137] X.-B. Wang and L.-S. Wang. *Development of a low-temperature photoelectron spectroscopy instrument using an electrospray ion source and a cryogenically controlled ion trap*. Rev. Sci. Instrum., **79**: 073108 (2008).
- [138] A. B. Kanu, P. Dwivedi, M. Tam, L. Matz, and H. H. Hill. *Ion mobility-mass spectrometry*. J. Mass Spectrom., **43**: 1–22 (2008).
- [139] B. D. Adamson, N. J. A. Coughlan, R. E. Continetti, and E. J. Bieske. *Changing the shape of molecular ions: photoisomerization action spectroscopy in the gas phase*. Phys. Chem. Chem. Phys., **15**: 9540–9548 (2013).
- [140] B. D. Adamson, N. J. A. Coughlan, G. da Silva, and E. J. Bieske. *Photoisomerization Action Spectroscopy of the Carbocyanine Dye DTC+ in the Gas Phase*. J. Phys. Chem. A, **117**: 13319–13325 (2013).

Publications

Cite this: *Phys. Chem. Chem. Phys.*, 2012, **14**, 12905–12911

www.rsc.org/pccp

PAPER

Substitution effects on the absorption spectra of nitrophenolate isomers†

Marius Wanko,^a Jørgen Houmøller,^b Kristian Støchkel,^b
Maj-Britt Suhr Kirketerp,^b Michael Åxman Petersen,^c Mogens Brøndsted Nielsen,^c
Steen Brøndsted Nielsen*^b and Angel Rubio*^a

Received 20th May 2012, Accepted 17th July 2012

DOI: 10.1039/c2cp41636k

Charge-transfer excitations highly depend on the electronic coupling between the donor and acceptor groups. Nitrophenolates are simple examples of charge-transfer systems where the degree of coupling differs between *ortho*, *meta* and *para* isomers. Here we report the absorption spectra of the isolated anions *in vacuo* to avoid the complications of solvent effects. Gas-phase action spectroscopy was done with two different setups, an electrostatic ion storage ring and an accelerator mass spectrometer. The results are interpreted on the basis of CC2 quantum chemical calculations. We identified absorption maxima at 393, 532, and 399 nm for the *para*, *meta*, and *ortho* isomer, respectively, with the charge-transfer transition into the lowest excited singlet state. In the *meta* isomer, this π – π^* transition is strongly redshifted and its oscillator strength reduced, which is related to the pronounced charge-transfer character, as a consequence of the topology of the conjugated π -system. Each isomer's different charge distribution in the ground state leads to a very different solvent shift, which in acetonitrile is bathochromic for the *para* and *ortho*, but hypsochromic for the *meta* isomer.

1 Introduction

We have recently investigated the intrinsic optical properties and solvatochromism of a series of extended *p*-nitrophenolates by state-of-the-art gas-phase action spectroscopy and quantum chemical calculations.² These compounds are text book examples of donor–acceptor chromophores with the phenolate oxygen as a donor group and the nitro as an acceptor group. The position of the charge-transfer (CT) excitation in the absorption spectrum was found to depend strongly on the π -conjugated spacer between the donor and acceptor groups. Thus, extending the spacer resulted in a bathochromically shifted CT excitation, which we ascribe to an increased conjugation at both ends of the molecule—the donor and acceptor groups—along with a decreased electronic coupling between them. Moreover, we found that one has to be very careful in relating solution absorption characteristics of these

anionic chromophores to their intrinsic absorption properties. Thus, chromophores may show a different progression of absorption maxima in solution relative to that observed in the gas phase. In the monodisperse oligomer approach, the optical properties of a series of conjugated oligomers are usually investigated in solution and from extrapolation of these data, the properties of an infinite polymer are predicted.^{3–7} For charged compounds, such as phenolates, solution experiments may provide misleading results.

As a continuation of our work on nitrophenolates, we have now turned to the three possible substitution motifs, *p*-, *m*-, and *o*-nitrophenolate. The new fundamental questions we seek to answer in this work are how substitution determines the donor–acceptor coupling, *i.e.*, mixing of donor HOMO with acceptor LUMO, and how this coupling affects the intrinsic absorption characteristics and the sensitivity to solvent effects.

2 Experimental

We used two different experimental setups for our action spectroscopy measurements, which are complementary in the covered range of wavelengths, the kind of fragments that are detected, and the fragmentation time window. Compounds for both experiments were purchased from Sigma-Aldrich.

2.1 ELISA experiments

These were carried out at the electrostatic ion storage ring in Aarhus (ELISA).^{8,9} Electrospray ionization was used to produce

^a Nano-Bio Spectroscopy Group and ETSF Scientific Development Centre, Departamento de Física de Materiales, UPV/EHU, Centro de Física de Materiales CSIC-UPV/EHU-MPC and DIPC, Av. Tolosa 72, E-20018 San Sebastián, Spain.
E-mail: angel.rubio@ehu.es

^b Department of Physics and Astronomy, Aarhus University, Ny Munkegade, DK-8000 Aarhus C, Denmark. E-mail: sbn@phys.au.dk

^c Department of Chemistry, University of Copenhagen, Universitetsparken 5, DK-2100 Copenhagen Ø, Denmark

† Electronic supplementary information (ESI) available: Experimental setups, time, mass, and power spectra, spectra of individual ion yields, absorption spectra and geometries from different QM methods, complete ref. 1. See DOI: 10.1039/c2cp41636k

the ions that were subsequently accumulated in a 22-pole ion trap and thermally equilibrated by collisions with a helium buffer gas therein. The ions were accelerated in a bunch to kinetic energies of 22 keV, and a bending magnet was used to select the appropriate ions according to their mass-to-charge ratio. The revolution time of the ions in the ring is *ca.* 50 μ s. Following injection into the ring, the ions were stored for about 40 ms before being irradiated by a nanosecond light pulse from a tunable EKSPLA laser. This is an Nd:YAG laser where the third harmonic (355 nm) pumps an optical parametric oscillator (OPO). The visible output from this OPO is frequency doubled in a crystal, providing UV light. The repetition rate of the experiment was 10 Hz. Lifetimes were obtained from measurements of the yield of neutrals hitting a microchannel plate (MCP) detector located at the end of the straight section opposite to the side where photoexcitation was performed. From fits to the time spectra, it is possible to extrapolate back to time zero, defined as the time when the laser was fired, to obtain the total number of photoexcited ions for each wavelength used (relative, not absolute, number) and subsequently deduce the absorption from this information by normalizing to both the average number of photons in the laser pulses and the neutrals yield prior to photoexcitation.

2.2 Sep1 experiments

In this setup, operating at a repetition rate of 40 Hz, the yield of fragment ions was monitored as a function of excitation wavelength, up to 10 μ s after photoexcitation in a single pass experiment. Ions were again produced by electrospray ionization and accumulated in a 14-pole ion trap. An ion bunch was accelerated to 50 keV energies and appropriate ions were selected by a magnet. These were photoexcited by light from a similar laser system as that used at ELISA, again in a merged beam configuration. The laser was operated at 20 Hz, irradiating every second ion bunch, so that the difference signal—"laser on" minus "laser off"—could continuously be measured. The shortest wavelength that the laser provides is 420 nm. An electrostatic analyzer allowed NO_2^- or ions that had lost NO to reach a channeltron detector where they were counted. The yields of these two ion fragments were summed to obtain the action spectra.

It is important to keep the differences between the two setups in mind. In the ELISA experiment, slow delayed dissociation is monitored after one-photon absorption, whereas in the Sep1 setup, fast dissociation is monitored after non-coherent absorption of two photons (see Section 5.1). Also the photo-induced signal (the action) is measured in different ways: in the ring experiment, the sum of neutrals formed from all the dissociation channels is sampled, whereas in the other setup, a single dissociation channel, involving one ionic fragment with a particular mass-to-charge ratio, is sampled in one experiment.

3 Computational details

Ground-state geometries were optimized using the MP2 level of theory and the TZVPP basis set.^{10,11} Excited-state properties were calculated using the linear-response CC2 coupled-cluster model¹² and the aug-cc-pVDZ basis set,¹³ if not denoted otherwise. These calculations were done with turbomole code.¹⁴

CC2 has been successfully applied to *p*-nitrophenolates of different sizes before.² To validate the CC2 results for the *meta* isomer and study solvent shifts, the *ab initio* multi-reference method SORCI¹⁵ was used in combination with the aug-cc-pVDZ basis set and the SV(P) basis set^{10,11,13} augmented with diffuse functions of the aug-cc-pVDZ set, as implemented in the ORCA program package.¹⁶ The MR-DDCI2 calculation that produces the average natural orbitals employed a CAS(6,4) reference of the frontier π orbitals, truncated with $T_{\text{pre}} = 10^{-3}$. In the final MR-DDCI3 + Q calculation, the entire π -electron system is included in a RAS(12: 5 2 /2/ 3 2) reference. Thresholds T_{nat} and T_{sel} were both set to 10^{-6} . For calculations of solvent shifts, geometries were optimized in the presence of the COSMO reaction field, using the PBE0 hybrid functional¹⁷ and the TZVP basis set.^{10,11} Electron vertical detachment energies (VDE) at the CCSD(T) level of theory were calculated using the aug-cc-pVDZ basis set and the ORCA code.¹⁶

TDDFT absorption energies can be found in the ESI†, but will not be discussed, as both pure and hybrid functionals are not applicable due to the varying CT character of the relevant states.

For natural population analysis of the RHF wave function, Gaussian03 was used.¹

4 Results

4.1 Gas-phase spectra

Fig. 1 shows the absorption spectra of the three nitrophenolate isomers *in vacuo*, as obtained from the two experimental setups, together with the results of theoretical calculations at the CC2 level. The two experiments resolve different features of the absorption spectrum, each of which would lead to different conclusions when considered alone. The ELISA spectra of the three isomers show one broad band that peaks at 393 nm (3.15 eV, *para*), 363 nm (3.42 eV, *meta*), and 399 nm (3.11 eV, *ortho*), respectively. The spectra obtained from the combined fragment ion yields in the Sep1 experiment differ in several aspects. The *para*- and *ortho*-isomer spectra show bands peaking at 434 nm (2.86 eV) and 453 nm (2.74 eV), respectively, hence are significantly red-shifted compared to the ELISA spectra. The *meta*-isomer spectrum shows a very broad band peaking at 532 nm (2.33 eV), which is not resolved in the ELISA spectrum and is strongly red-shifted compared to the bands of *para* and *ortho* isomers. This is in contrast to the blue-shifted feature visible in the ELISA spectrum of the *meta* isomer. The neutral and fragment ion yields are arbitrarily scaled, hence the relative intensities of the features are unknown.

In the ELISA data for the *meta* isomer, the 532 nm (2.33 eV) band cannot be distinguished from the background counts. In the case of the *para* and *ortho* isomers, neither experiment detects absorption for wavelengths longer than 500 nm (2.48 eV). The lowest band in these two isomers shows the same onset in both experiments, but is broadened and/or red-shifted in the Sep1 experiment, which does not cover the entire band due to the wavelength limitation.

Theoretical calculations at the CC2 level find only one low-lying dipole-allowed transition for the *para* and the *ortho* isomer. Its energy reproduces the absorption maximum of the ELISA spectrum with great accuracy. This allows a safe assignment of

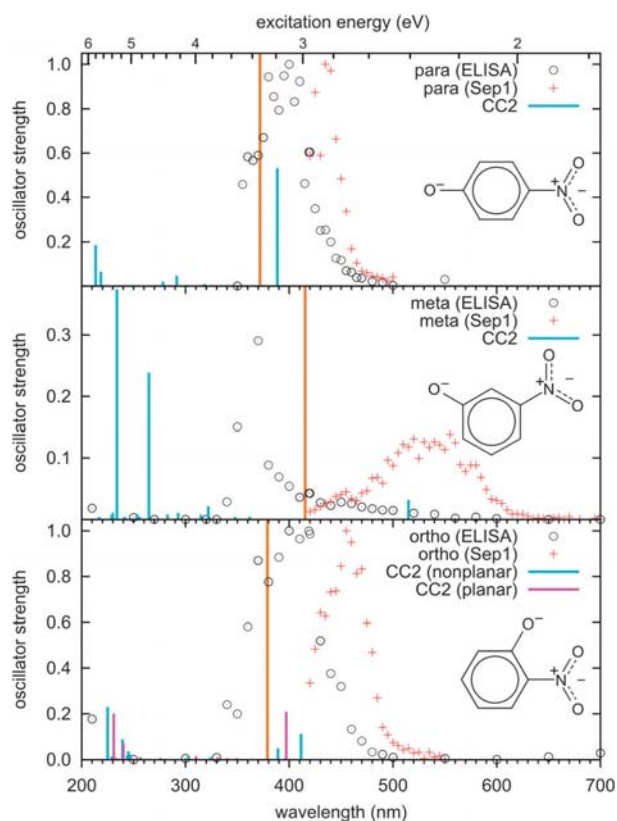


Fig. 1 Measured and calculated absorption spectra of the nitrophenolate isomers *in vacuo*. Neutral yields from the ELISA experiment are compared with joined fragment ion yields from the Sep1 experiment and theoretical excitation energies. Theoretical vertical detachment energies from Table 2 are indicated by orange lines.

the experimental band to the S_0 – S_1 transition. The S_1 state is dominated by the π – π^* singly-excited configuration involving the frontier π orbitals. The oscillator strength is smaller for the *ortho* isomer by a factor of three.

The theoretical spectrum of *m*-nitrophenolate agrees perfectly with the Sep1 spectrum, but does not reproduce the feature that dominates the ELISA spectrum. Vertical excitation into the S_1 state, which is the lowest π – π^* excited state, like in the other two isomers, is predicted at 515 nm (2.41 eV), with an oscillator strength (0.03) smaller by a factor of 5–7 compared to the *ortho* isomer. Hence, the S_0 – S_1 excitation in *m*-nitrophenolate is predicted to be weak and significantly red-shifted. The reason for this redshift and the differences in the experimental data will be discussed below.

Theoretical calculations at the DFT and MP2 level yield planar *para* and *meta* isomers. For *ortho*, MP2/TZVPP finds a non-planar minimum 0.4 kcal mol^{−1} below the planar transition state. Due to the flatness of the potential energy surface, the O–N–C–C dihedral angle depends strongly on the method (HF: 4°, PBE0: 13°, PBE: 18°, MP2/aug-cc-pVTZ: 26°). In the MP2/TZVPP geometry, used for the spectra calculations, the dihedral is 31° and thus somewhat larger than that at the basis set limit of MP2. The effect of non-planarity on the spectrum, however, is limited. As shown in Fig. 1, the S_1 excitation is red-shifted by 0.11 eV (14 nm) and an energetically close n – π^* transition, which is dipole forbidden in the planar geometry, borrows some oscillator strength from the π – π^* state.

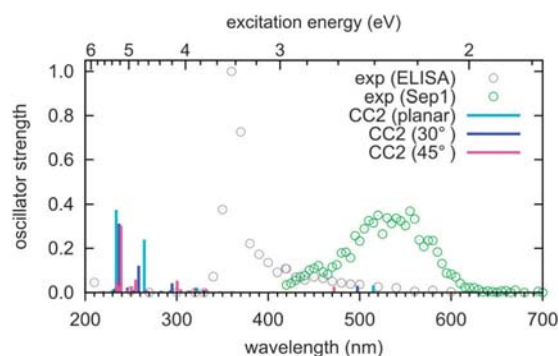


Fig. 2 Absorption spectrum of *m*-nitrophenolate *in vacuo*. The CC2/aug-cc-pVDZ results are based on geometries with varying twist angle of the nitro group.

The theoretical spectra also show two strong transitions to resonant states above the ionization threshold (see Table 2 for VDE's), which are missing in the ELISA spectra. In all three systems, there is a dipole-forbidden n – π^* state below the VDE.

To test whether non-planarity affects states in the region of the experimental absorption spectra of *m*-nitrophenolate, we performed CC2 calculations on geometries with varying O–N–C–C dihedral (Fig. 2). With increasing twist, the S_0 – S_1 transition is blue-shifted, reaching 472 nm (2.63 eV) at 45°, which is still far lower in energy than the prominent feature in the ELISA spectrum. Further twist is energetically prohibitive and has little effect on the excitation energies. Note that the oscillator strength of the S_0 – S_1 transition does not change with non-planarity and that the n – π^* transition is still not visible. Therefore, we exclude the possibility of a strongly blue-shifted S_1 state due to non-planarity at room temperature. The latter rather leads to a broadening of the spectrum, as can be seen in the solution spectrum (see below).

4.2 Solution spectra

Absorption spectra of the three isomers in acetonitrile solution are shown in Fig. 3, together with the computed gas-phase line spectra. The lowest band maxima are located at 430 nm (2.88 eV, *para*), 473 nm (2.62 eV, *meta*), and 443 nm (2.80 eV, *ortho*), respectively. Furthermore, three bands are visible in the near-UV, which are not observed in the gas-phase experiment.

Apart from the expected solvent shifts, the experimental solution spectra agree surprisingly well with the theoretical gas-phase spectra, including the *meta* isomer. Both energies and oscillator strengths are reproduced for the S_1 state as well as for the states in the near-UV region (experimental absorptivities are arbitrarily scaled). In particular, the *m*-nitrophenolate solution spectrum confirms the red-shifted and weak S_1 transition, which is visible in the Sep1 spectrum and predicted by theory. Note that the S_1 band and the second peak in the near-UV band are red-shifted compared to the theoretical excitation energies for the *ortho* and *para* isomers. For *m*-nitrophenolate, a small blueshift occurs.

4.3 Theoretical solvent models for *m*-nitrophenolate

To further elucidate the discrepancies for the *meta* isomer between the ELISA data on the one hand and the theoretical gas-phase and experimental solvent and Sep1 gas-phase spectra

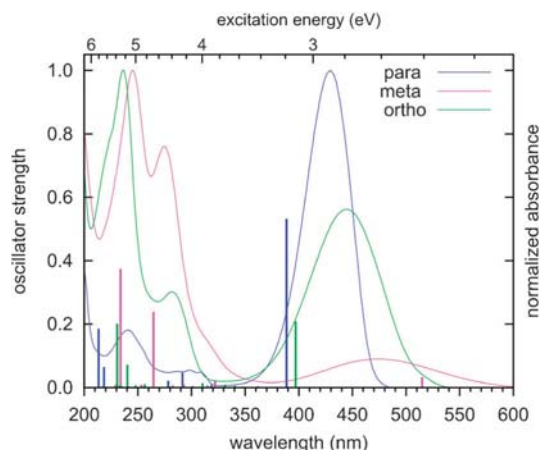


Fig. 3 Experimental absorption spectra of nitrophenolate isomers in acetonitrile (sodium salts; obtained using sodium *tert*-butoxide as base). Theoretical line spectra (gas phase) are superimposed, for comparison.

on the other hand, we theoretically modeled the solvent effect on the S_0 – S_1 absorption energy using a series of solvent models. For a number of 1–7 explicit solvent molecules, the lowest energy complex was determined using molecular dynamics and geometry optimization techniques. The bulk solvent was represented by the conductor-like screening model (COSMO). Table 1 shows the S_1 excitation energies with and without the COSMO reaction field. It also shows the total binding energy $E_{\text{bind}}^{\text{QM}}$ of the acetonitrile molecules to the complex within the COSMO medium. $E_{\text{bind}}^{\text{QM}}$ accounts for effects missing in the COSMO model, like H-bond formation and QM effects. For 1–3 solvent molecules, the binding energies are largest for salt bridges to the phenolate group, which accepts up to 4 direct hydrogen bonds. Salt bridges to the nitro group are weak (O–H distance of 2.4–2.5 Å) and only two solvent molecules are bound simultaneously.

By excluding the bulk solvent from the calculation, the effect of microsolvation can be studied. As is expected from the excitation-induced CT (*vide infra*), hypsochromic shifts result each time when additional acetonitrile molecules are binding to the phenolate group (see Fig. 4). Salt bridges to the nitro group, in contrast, lead to bathochromic shifts. The picture

Table 1 SORCI S_1 excitation energies of *m*-nitrophenolate in acetonitrile^a

N_S	$N_{\text{CO}}^{\text{HB}}$	$N_{\text{NO}_2}^{\text{HB}}$	$E_{\text{bind}}^{\text{QM}}$ (kcal mol ⁻¹)	S_1 (eV)		VDE (eV)
				Vacuum	COSMO	
0	0	0	0.0	2.13	2.46	4.95
1	1	0	–0.9	2.15	2.30	5.01
2	2	0	–1.7	2.26	2.25	5.06
3	3	0	–2.3	2.37	2.15	5.13
4	3	1	–2.6	2.20	2.13	5.14
5	3	2	–2.9	2.05	2.15	5.15
6	4	2	–3.3	2.35	2.25	5.16
7	4	2	–3.9	2.37	2.23	5.40

^a Columns 1–3 contain the number of explicit solvent molecules, hydrogen bonds to the phenolate and to the nitro group. The bulk solvent is either excluded (vacuum) or represented by the COSMO model. All geometries were optimized in the presence of the COSMO reaction field. $E_{\text{bind}}^{\text{QM}}$ is the binding energy inside the COSMO medium (no BSSE correction), which would be zero if the solvent model was exact.

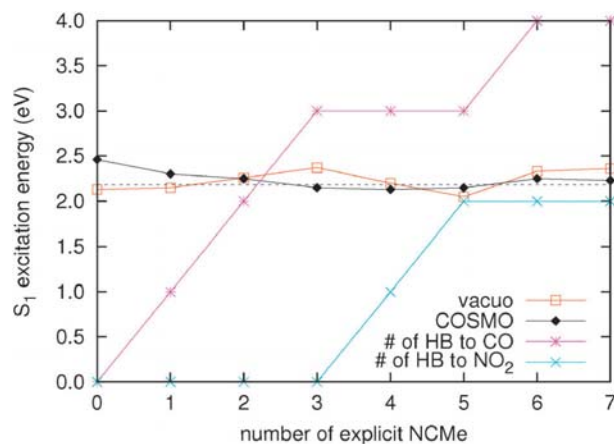


Fig. 4 SORCI S_1 excitation energies of *m*-nitrophenolate in acetonitrile: dependence on the number of explicit solvent molecules. The number of hydrogen bonds to the phenolate and nitro group are depicted. All geometries were optimized in the presence of the COSMO reaction field.

changes when the bulk solvent is included (COSMO). The S_1 energy converges rapidly to a value slightly above that obtained from the gas-phase calculation. Note that no explicit counter ion was included in the calculations. This procedure is justified by two observations. (1) In strongly polar solvents, the shift is widely independent from the exact position of the counter ion. (2) As reported previously,² the hypsochromic solvent shift of nitrophenolates in acetonitrile is grossly overestimated when including the counter ion explicitly but not any solvent molecules. Thus, including the counterion would not improve the convergence of the mixed QM/COSMO solvent model.

5 Discussion

5.1 Differences in the two gas-phase experiments

Different from the case of the *meta* isomer, the data from the ELISA and the Sep1 setups are consistent for *p*- and *o*-nitrophenolate, but the redshift in the Sep1 spectrum calls for an explanation and can be related to the different fragmentation processes and time windows monitored in the two setups.

The ELISA setup uses a weak laser field and measures neutrals produced essentially after 1-photon absorption, either due to slow fragmentation or electron autodetachment from the vibrationally hot ground state. The resulting spectrum may be quenched towards longer wavelengths if the the photon energy is insufficient to overcome the fragmentation barrier and the ionization threshold. For short wavelengths, *i.e.*, energies above the ionization threshold, fast electron detachment from excited resonance states may compete with internal conversion (IC) and quench the signal, because the neutrals would be produced before being deflected to the detection lap of the storage ring. The same applies to excited-state or fast ground-state fragmentation processes.

The Sep1 setup only detects fast dissociation channels, which result predominantly from the non-coherent absorption of two photons (Fig. S4 in ESI†), where the ns pulse duration allows for IC and vibrational energy redistribution, according

to mechanism (1). The Sep1 spectrum should therefore be associated with the convolution of the 1-photon cross-sections of the vibrationally hot and cold systems. This is not to be confused with coherent two-photon absorption processes where the photon energy is half the excitation energy.



Neither neutrals nor free electrons are detected in the Sep1 experiment. Therefore, the Sep1 spectrum may be quenched by electron detachment, even below the ionization threshold, owing to the excess energy of the two absorbed photons. The electron detachment can occur (a) from the vibrationally hot excited state ($A_v^{-*} \rightarrow A^0 + e^-$), competing with IC, or (b) as slow autodetachment from the vibrationally hot ground state ($A_{vv}^- \rightarrow A^0 + e^-$). Mechanism (b) has been suggested before to explain photodetachment spectra below the ionization threshold.¹⁸ Mechanism (a) might be relevant in the case of a resonance enhancement of the coupling between continuum and strongly allowed valence states, *e.g.*, when the VDE is close to the vertical excitation energy of the S_0 – S_1 transition, as is the case for *p*- and *o*-nitrophenolate (see Table 2). This has been suggested to explain sub-microsecond decay of photoexcited anions of a model chromophore (pCA^-) of the photoactive yellow protein (PYP).¹⁹ The PYP chromophore has quite similar electronic properties with its frontier π orbitals partially localized on the donor (phenolate) and acceptor (propenoic acid) groups. Pump-probe experiments on another model of the PYP chromophore found evidence for the competition between IC and electron detachment at the ps timescale for the decay of a resonant state near the ionization threshold.²⁰ On the other hand, IC was found after excitation into resonant states.²¹

The signal in the Sep1 experiment may also be quenched by electron detachment after single-photon absorption ($A^{-*} \rightarrow A^0 + e^-$). This process would be relevant for photon energies above the adiabatic detachment energy if IC is slow and the excited state is close to the continuum, which is the case for *p*- and *o*-nitrophenolate. This mechanism would best explain the observed quenching of the S_0 – S_1 absorption band towards shorter wavelengths (Fig. 1).

It is interesting to compare our results with another recent study on the methylated pCA^- model chromophore of PYP.²² Rocha-Rinza *et al.* measured the gas-phase absorption at ELISA using a different setup that allows illumination and neutral detection at the same lap of the ring, hence detecting neutrals from both electron detachment and fragmentation. The recorded spectra of different isomers show both valence and resonance states, but no additional features due to direct electron detachment, such as $A^- \xrightarrow{h\nu} A^0 + e^-$. In particular, their *meta* spectrum shows no absorptivity in the region of the VDE. This indicates that the direct ionization channel has a negligible cross-section compared with that of transitions into valence or resonance states.

5.2 Assignment of the S_1 state in *m*-nitrophenolate

When we associate the lowest band in the experimental solution spectrum with the band resolved in the Sep1 experiment, we obtain a hypsochromic solvent shift of +0.24 eV for acetonitrile. Our calculations predict a smaller shift of +0.05 eV, but this

error can easily be accounted for by the same effects that cause the shifts in the yield maxima between the two experimental setups (see Section 5.1) and by the expected errors of the computational model (basis-set superposition and size-consistency errors). In view of the agreement between the theoretical calculations, the Sep1 data, the experimental solution spectra, and the small predicted solvent effect, we conclude that the 532 nm (2.33 eV) absorption band in the Sep1 spectrum originates from the S_0 – S_1 transition, whereas the dominant feature in the ELISA spectrum must be of different origin.

Rigorous tests of the methodological approach support this conclusion. The differences in the ground-state geometry of the *meta* isomer, which will be discussed in the next section, are confirmed at the DFT and at the CASSCF level of theory (see ESI†). Spectra calculated at the SORCI level of theory corroborate the CC2 data, showing a constant redshift of the S_1 and higher-lying π – π^* states (see ESI†).

In none of the gas-phase spectra, the higher-lying bright resonant states are resolved that appear in the solution spectra and the theoretical data. Therefore, it must be explained why these bands do not appear in the gas-phase experiments with the *ortho* and *meta* isomers. The most likely reasons are rapid fragmentation and electron detachment, as discussed in Section 5.1. The hypothesis of electron detachment is supported by our calculations of the vertical detachment energies (Table 2), *e.g.*, 2.98 eV (416 nm) for the *ortho* isomer. As the experimental spectrum extends to at least 3.65 eV (340 nm), IC competes with autodetachment from the S_1 excited state in this energy region. The same situation has been observed in a recent study on the HBDI[−] chromophore of the green fluorescent protein.²³ Also in negatively charged DNA strands of adenine, IC was found after excitation above the VDE.²¹

In solution, the VDE is considerably higher, *e.g.*, for *m*-nitrophenolate in acetonitrile, employing the continuum-electrostatic COSMO model, PBE0 predicts a VDE of 4.95 eV (250 nm). Adding the six QM MeCN molecules that form salt-bridges to the chromophore, the VDE increases to 5.16 eV (240 nm). An additional MeCN molecule on top of the ring causes a further distinct blueshift. Completing the first solvation shell, the VDE can be expected to exceed 5.6 eV (220 nm), which is clearly above the intense bands in the near UV region of the solution spectrum.

In the absence of the bright resonant states and a clear S_1 absorption band, the ELISA spectrum of the *meta* isomer lacks any reference for the absolute absorptivity and the physical origin of the feature peaking at 363 nm (3.42 eV)

Table 2 Properties of the ground-state and the S_1 excitation of nitrophenolate isomers^a

	S_1 (eV)	f	$ \Delta\mu_{10} $ (D)	VDE (eV)	Q_{NPA}^{CO}	$Q_{NPA}^{CNO}^2$
<i>para</i>	3.21	0.53	5.2	3.33	0.25	0.61
<i>meta</i>	2.41	0.03	9.1	2.98	0.36	0.28
<i>ortho</i>	3.01	0.11	4.4	3.27	0.23	0.59
	(3.12)	(0.21)	(3.1)			

^a Excitation energies, oscillator strengths, and difference-dipole moments from CC2. VDE from CCSD(T)/aug-cc-pVDZ (see Section 3). NPA fragment charges (see text) from HF/TZVP. Values for the planar (transition state) geometry of *ortho* are given in parentheses.

remains unclear. Our CC2 calculations find a dipole-forbidden resonant transition at 3.84 eV and transitions into diffuse states that are strongly basis-set dependent (Fig. S8 in the ESI†), but any assignment to the feature peaking at 363 nm would be highly speculative.

Also the action spectroscopic study on the PYP model chromophore²² investigated the substitution effect. For the *meta* substitute, they find merely a weak and broad signal that they associate with the S_1 state, as predicted by their CC2 calculations. In contrast to our ELISA spectrum, they resolve higher-lying resonant states, which are also predicted by their CC2 calculations. Different from our ELISA spectrum, their *meta*-isomer spectrum does not show any absorbance in the region between S_1 and the resonant states, and therefore shows a good overall agreement with theory. As stated above, the main difference in their experimental setup is the detection of neutrals that are produced immediately after illumination, including neutrals produced by electron detachment.

5.3 Origin of the strong substitution effect in *m*-nitrophenolate

In the following, we develop a rationale for the anomalous properties of the S_1 state in the *meta* isomer and its relation to the topology of the molecule. The ground state of the *meta* isomer shows distinct differences in geometry (Fig. 5) and charge distribution, which can be understood when considering the canonical Lewis structures that dominate the ground-state wave function (Fig. 6). To analyze the charge distribution, Table 2 provides fragment charges obtained by summing the atomic charges of a natural population analysis²⁴ (NPA) of the HF wave function. The energy of the aromatic structure, which locates the excess charge on the phenolate oxygen, is essentially independent of the isomer, as both substituents form a single bond to the aromatic ring. The quinoid (or alternated) structure that assigns the formal charge to the nitro group features one additional bond and is thus more stable and dominates the wave function of the *para* and *ortho* isomers. Correspondingly, *ca.* 60% of the excess charge are located on the nitro group (Table 2), which forms a relatively strong C–N bond. For the topology of the *meta* isomer, this structure cannot be realized due to the even number of bonds between the substituents. The most stable alternated structures for *m*-nitrophenolate assign the formal charge on ring carbons and form the triple resonance indicated in Fig. 6. Structures with a negative nitro group require two radical centers in the ring and therefore hardly contribute. As a consequence, the NPA net charge in the nitro group is merely $-0.28 e$, whereas the charge on the ring and on

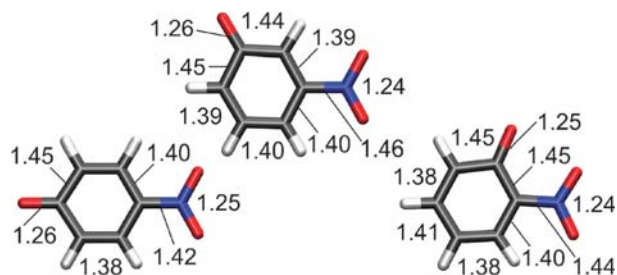


Fig. 5 Calculated MP2 ground-state geometries of nitrophenolate isomers.

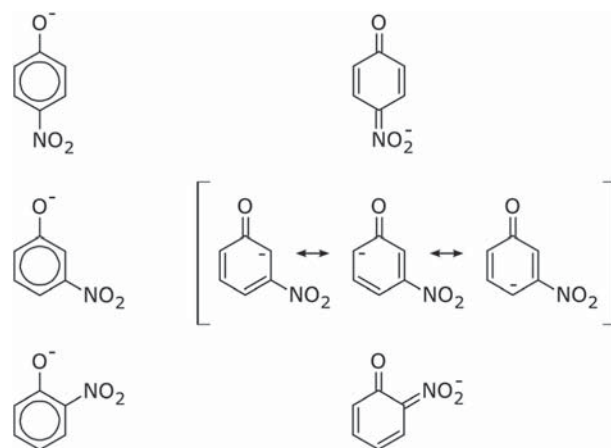


Fig. 6 Aromatic and quinoid/alternated Lewis structures dominating the ground state of nitrophenolates.

the phenolate oxygen is increased to 36% of the excess charge, each. The bond length alternation is reduced in the ring and enhanced in the nitro fragment.

The topology-related difference in the electronic structure is reflected in the frontier π molecular orbitals. As shown in Fig. 7, HOMO (LUMO) natural orbitals are more localized on the phenolate (nitro) fragment, respectively. Therefore, the S_0 – S_1 excitation in *m*-nitrophenolate has more CT character (see $|\Delta\mu_{10}|$ in Table 2) and a strongly reduced transition-dipole moment, compared to *p*- and *o*-nitrophenolate. The bathochromic shift in the *m*-nitrophenolate S_0 – S_1 excitation originates from the low energy of the “intrinsic” CT state corresponding to the phenolate–nitrobenzene donor–acceptor system. As a model, consider *p*-biphenolate (see ref. 2): when rotating the C–C bond connecting the nitrobenzene with the phenolate from the planar to the perpendicular orientation, donor and acceptor systems are fully separated. This shifts the CC2 S_1 excitation energy from 2.23 to 1.60 eV. The locally-excited states of nitrobenzene (phenolate) in contrast, are located at 4.5 (4.0) eV, respectively, employing the same level of theory.

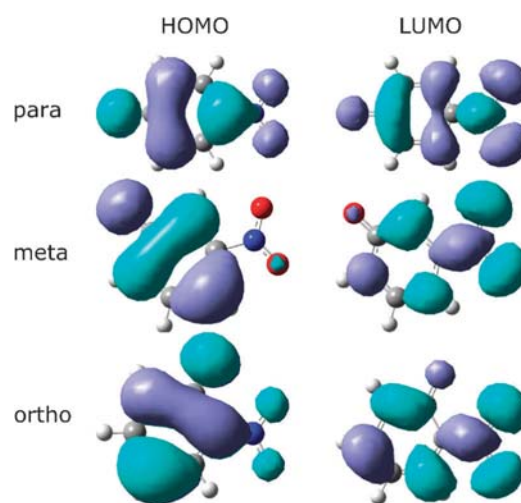


Fig. 7 Frontier natural orbitals from the state-averaged (S_0 and S_1) MR-DDCI2 density matrix. From top to bottom: *p*-, *m*-, *o*-nitrophenolate.

6 Conclusions

We studied the optical absorption properties of *p*-, *m*-, and *o*-nitrophenolate *in vacuo* and in bulk solution. Due to the different topology and the emerging resonance structures, the *meta* isomer features widely decoupled donor and acceptor regions, whereas the donor HOMO and acceptor LUMO are strongly mixed in the *para* and *ortho* isomers. As a consequence, the S_0 - S_1 excitation, which is characterized by a HOMO-LUMO π - π^* excitation in all three cases, is strongly red-shifted in the *meta* isomer, carries little oscillator strength, and has a strong CT character. Different from previously studied push-pull systems, like the anionic PYP chromophore pCA^- ,²² this does not necessarily lead to a strong solvent shift for the *meta* isomer, because donor and acceptor regions share the negative excess charge, which is stabilized by the solvent on both fragments. In acetonitrile, *e.g.*, the nitro group is better solvated than the phenolate group in the *para* and *ortho* isomers, leading to strong bathochromic shifts, whereas the opposite applies to the *meta* isomer, which shows a smaller hypsochromic shift.

Our comparison of data from two different experimental setups demonstrates the potential problems involved in photo-destruction spectroscopy with limitations in the energy- or time-window for detection of the fragmentation channels. In the case of the *meta*-isomer, the ELISA spectrum lacks the expected strong absorption bands of the resonant transitions and does not resolve the weak S_0 - S_1 band. This calls for further experiments to resolve the complete gas-phase UV-vis spectrum of *m*-nitrophenolate and accommodate the observed feature in the 363 nm region.

Acknowledgements

MW and AR acknowledge funding by the Spanish MICINN (“Juan de la Cierva”, FIS2010-65702-C02-01, PIB2010US-00652 and /CSD2010-00044/), “Grupos Consolidados UPV/EHU del Gobierno Vasco” (IT-319-07), European Research Council Advanced Grant DYNamo (ERC-2010-AdG No. 267374), and SGIker ARINA UPV/EHU). SBN acknowledges support from Lundbeckfonden and FNU.

References

- 1 M. J. Frisch, *et al.*, *Gaussian 03, Revision B.04*, Gaussian, Inc., Pittsburgh PA, 2003.
- 2 M.-B. Suhr Kirketerp, M. Åxman Petersen, M. Wanko, L. A. Espinosa Leal, H. Zettergren, F. M. Raymo, A. Rubio, M. Brøndsted Nielsen and S. Brøndsted Nielsen, *ChemPhysChem*, 2009, **10**, 1207–1209.
- 3 R. E. Martin and F. Diederich, *Angew. Chem., Int. Ed.*, 1999, **38**, 1350–1377.
- 4 K. Müllen, *Pure Appl. Chem.*, 1993, **65**, 89–96.
- 5 M. Brøndsted Nielsen and F. Diederich, *Chem. Rev.*, 2005, **105**, 1837–1867.
- 6 J. M. Tour, *Chem. Rev.*, 1996, **96**, 537–553.
- 7 G. Wegner and K. Müllen, *Electronic Materials: The Oligomer Approach*, Wiley-VCH, Weinheim, 1998.
- 8 J. U. Andersen, P. Hvelplund, S. Brøndsted Nielsen, S. Tomita, H. Wahlgreen, S. P. Møller, U. V. Pedersen, J. S. Forster and T. J. D. Jørgensen, *Rev. Sci. Instrum.*, 2002, **73**, 1284–1287.
- 9 S. P. Møller, *Nucl. Instrum. Methods Phys. Res., Sect. A*, 1997, **394**, 281–286.
- 10 A. Schäfer, H. Horn and R. Ahlrichs, *J. Chem. Phys.*, 1992, **97**, 2571–2577.
- 11 F. Weigend, M. Häser, H. Patzelt and R. Ahlrichs, *Chem. Phys. Lett.*, 1998, **294**, 143–152.
- 12 O. Christiansen, H. Koch and P. Jørgensen, *Chem. Phys. Lett.*, 1995, **243**, 409–418.
- 13 J. T. H. Dunning, *J. Chem. Phys.*, 1989, **90**, 1007.
- 14 TURBOMOLE V6.0 2009, a development of University of Karlsruhe and Forschungszentrum Karlsruhe GmbH, 1989–2007, TURBOMOLE GmbH, since 2007; available from <http://www.turbomole.com>.
- 15 F. Neese, *J. Chem. Phys.*, 2003, **119**, 9428–9443.
- 16 F. Neese, *ORCA—An Ab Initio, DFT and Semiempirical electronic structure package, Version 2.9*, MPI for Bioinorganic Chemistry, Mülheim/Ruhr, 2012.
- 17 C. Adamo and V. Barone, *J. Chem. Phys.*, 1999, **110**, 6158–6170.
- 18 E. A. Brinkman, E. Gunther, O. Schafer and J. I. Brauman, *J. Chem. Phys.*, 1994, **100**, 1840–1848.
- 19 I. B. Nielsen, S. Boye-Peronne, M. O. A. E. Ghazaly, M. B. Kristensen, S. Brøndsted Nielsen and L. H. Andersen, *Biophys. J.*, 2005, **89**, 2597–2604.
- 20 I.-R. Lee, W. Lee and A. H. Zewail, *PNAS*, 2006, **103**, 258–262.
- 21 L. Munksgaard Nielsen, S. Øvad Pedersen, M.-B. Suhr Kirketerp and S. Brøndsted Nielsen, *J. Chem. Phys.*, 2012, **136**, 064302.
- 22 T. Rocha-Rinza, O. Christiansen, D. B. Rahbek, B. Klaerke, L. H. Andersen, K. Lincke and M. Brøndsted Nielsen, *Chem.-Eur. J.*, 2010, **16**, 11977–11984.
- 23 M. W. Forbes and R. A. Jockusch, *J. Am. Chem. Soc.*, 2009, **131**, 17038–17039.
- 24 A. E. Reed, R. B. Weinstock and F. Weinhold, *J. Chem. Phys.*, 1985, **83**, 735–746.

On the Effect of a Single Solvent Molecule on the Charge-Transfer Band of a Donor–Acceptor Anion

Jørgen Houmøller,[†] Marius Wanko,[‡] Kristian Støchkel,[†] Angel Rubio,^{*,‡} and Steen Brøndsted Nielsen^{*,†}

[†]Department of Physics and Astronomy, Aarhus University, Ny Munkegade 120, DK-8000 Aarhus C, Denmark

[‡]Nano-Bio Spectroscopy Group and ETSF Scientific Development Centre, Departamento de Física de Materiales, Universidad del País Vasco/Euskal Herriko Unibertsitatea (UPV/EHU), Centro de Física de Materiales CSIC-UPV/EHU-MPC and DIPC, Av. Tolosa 72, E-20018 San Sebastian, Spain

S Supporting Information

ABSTRACT: Many biochromophore anions located within protein pockets display charge-transfer (CT) transitions that are perturbed by the nearby environment, such as water or amino acid residues. These anions often contain the phenolate moiety as the electron donor and an acceptor group that couples to the donor via a π -conjugated system. Here we show using action spectroscopy that single molecules of water, methanol, and acetonitrile cause blue shifts in the electronic transition energy of the bare *m*-nitrophenolate anion by 0.22, 0.22, and 0.12 eV, respectively (uncertainty of 0.05 eV). These shifts are similar to CC2-predicted ones and are in accordance with the weaker binding to the phenolate end of the ion by acetonitrile in comparison with water and methanol. The nitro acceptor group is almost decoupled from the phenolate donor, and this ion therefore represents a good model for CT excitations of an anion. We found that the shift caused by one acetonitrile molecule is almost half of that experienced in bulk acetonitrile solution, clearly emphasizing the important role played by the microenvironment. In protic solvents, the shifts are larger because of hydrogen bonds to the phenolate oxygen. Finally, but not least, we provide experimental data that serve to benchmark calculations of excited states of ion–solvent complexes.

Charge-transfer (CT) excitations play a significant role in chemistry and biology. For example, organic donor–acceptor compounds, which are characterized by CT excitations, have found use as nonlinear optical (NLO) chromophores.¹ Protein biochromophores such as the one from photoactive yellow protein (PYP) undergo CT excitations,² while the oxyluciferin anion responsible for light emission from fireflies and located within the luciferase enzyme may be formed biochemically in a CT excited state.³ In a CT excitation, an electron (or, more appropriately, charge density) moves from one part of the molecule (the donor) to another (the acceptor) or from one molecule to another. The energy of CT excitations strongly depends on the donor–acceptor coupling. At infinite separation, the excitation energy is simply the difference between the ionization energy of the donor and the electron affinity of the acceptor, which is typically smaller than the energy of local excitations on any of the moieties. Effective coupling via a π -

conjugated system allows the donor and acceptor states to delocalize and overlap, which reduces the gap between the local and CT excitations and gives oscillator strength to the latter. Such CT transitions can often be identified in the absorption spectrum from a strong dependence on solvent polarity. They are, however, hard to predict theoretically; in particular, time-dependent density functional theory (TDDFT) using local exchange–correlation functionals generally fails.^{4,5}

An important question up for debate is the spectral shift caused by a single solvent molecule or other hydrogen-bonding interactions on a molecular anion that displays a CT transition.^{2,6–8} The issue is of particular relevance for understanding the absorption by proteins in which a biochromophore is located in a binding pocket that provides shielding against bulk water. In this environment, specific interactions with immobile waters or charged or polar groups can widely tune the optical properties of the chromophore.⁹ Often there is limited access to water molecules, just one or two.¹⁰ The shift in absorption caused by a nearby water molecule depends on the character of the electronic transition (i.e., the degree of CT) and the geometry of the complex within the cavity. If a water molecule binds to the negative donor site, a blue shift is expected for a CT transition on the basis of simple electrostatic reasoning, since the interaction energy between the donor site and the water is lowered upon electron transfer to the acceptor site. The shift cannot be higher than the solvent binding energy unless the solvent molecule is unbound in the excited state. On the other hand, the polarizability is higher in the excited state than in the ground state, which reduces the blue shift. As the energy for binding to anions is larger than that to neutral chromophores, the microenvironment is expected to be of larger importance for anions, but the actual size of the induced shift by, say, a single water molecule still needs to be better established experimentally. This is the topic of the present work, in which we compared experimental results with theoretical ones.

A textbook example of a donor–acceptor chromophore anion is *m*-nitrophenolate (m^-), in which phenolate is the donor group and the nitro substituent is the acceptor group (Figure 1). Phenolate is a common motif among biochromophores and typically represents the donor state of these. In contrast to the other two isomers, ortho and para, the phenolate anionic group is widely decoupled from the nitro group in the meta isomer (see

Received: March 16, 2013

Published: April 23, 2013



Figure 1. (a) Structure of the *m*-nitrophenolate anion. (b) Frontier natural orbitals from the state-averaged (S_0 and S_1) MR-DDCI2 density matrix (data from ref 11).

the valence orbitals in Figure 1). For the ortho and para isomers, there exists an important resonance structure in which the negative charge is moved from the phenolate oxygen to the nitro group, and as a result of this strong coupling between the donor and acceptor states, the absorption is shifted much further to the blue than for the isolated meta ion, as recently reported.¹¹ Hence, m^- is an excellent and well-defined model system for testing the importance of microsolvation on the CT transition energy. Also the ion is small enough to allow for high-level quantum-chemical calculations and a benchmarking of these by comparison to experimental results. Here we report the results from a joint spectroscopic and theoretical characterization of *m*-nitrophenolate with a single water, methanol, or acetonitrile molecule attached. Water and methanol can make hydrogen bonds to the phenolate oxygen, while acetonitrile binds more as a dipole.

We note that gas-phase electronic absorption spectroscopy has earlier been done on several microsolvated protonated molecules such as amino acids, crystal violet, and polycyclic aromatic hydrocarbons¹² as well as metal cations and metal-ion complexes.¹³ Also the cross sections for photodetachment as functions of wavelength have been measured for anion complexes,¹⁴ as have photodestruction spectra of hydrated electron clusters.¹⁵

Action spectroscopy experiments were done in the present work with a home-built mass spectrometer.¹⁶ *m*-Nitrophenolate was purchased from Sigma-Aldrich, and ions were formed by electrospray ionization of the sample dissolved in acetonitrile. They were passed through an octopole transmission guide surrounded by a chamber with a gas inlet, where they were allowed to undergo ion–molecule reactions. The chamber was filled with water, methanol, or acetonitrile at a pressure of at least 0.01 mbar. All ions were collected in a 14-pole ion trap filled with helium buffer gas at room temperature. The trap was emptied with a repetition rate of 40 Hz, and the ion bunches were accelerated to kinetic energies of 50 keV. Those of interest according to m/z ratio were selected by a bending magnet, and every second ion bunch was photoexcited by light from an EKSPLA laser system operated at 20 Hz. In this laser system, the 1064 nm fundamental of an Nd:YAG laser was frequency-tripled to give 355 nm light, which was used to pump an optical parametric oscillator to produce visible light. Photofragment ions were selected by a hemispherical electrostatic analyzer (ESA) and counted by a channeltron detector. As the binding energies of the complexes are less than 1 eV (vide infra), the dissociation is expected to be complete before arrival at the analyzer (travel time of a couple of microseconds), avoiding kinetic shifts for which corrections must be made in cases where the dissociation time constant is long. Thus, even though the yield of complexes is low, the experiment benefits from complete photodissociation. We measured a low yield of fragment ions when the laser was off, which was due to collisions with residual gas in the beamline. This signal was proportional to the parent ion beam current but was too low to correct for ion-beam fluctuations. The experiment

was therefore repeated several times to average out these fluctuations. The “laser-off” signal was, however, subtracted from the “laser-on” signal to obtain a pure photoinduced yield of fragment ions. The laser wavelength was scanned from 420 to 700 nm. At each wavelength, the number of injections was at least 500.

Photodissociation of the bare m^- ion led to several fragment ions (Figure 2a) that were formed after the absorption of two

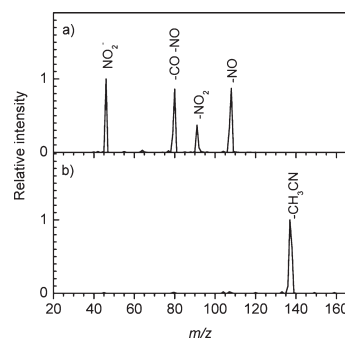


Figure 2. Photodissociation mass spectra of (a) bare m^- and (b) $m^-(\text{CH}_3\text{CN})$ obtained with 510 and 500 nm light, respectively.

photons. The dominant fragment ions were NO_2^- (m/z 46) and ions formed by the loss of NO (m/z 108), NO_2 (m/z 92), or CO and NO (m/z 80). Photodissociation mass spectra of the complexes of m^- with a solvent molecule [denoted as $m^-(\text{solvent})$] were also recorded to identify the fragment ions. The most dominant fragment was the bare ion (m/z 138) formed by evaporation of the solvent molecule [e.g., for $m^-(\text{CH}_3\text{CN})$, see Figure 2b]. Its yield increased linearly with laser power [see the Supporting Information (SI)], and one photon was therefore sufficient for the dissociation. This indicates that the dissociation energies are less than the photon energies (>2 eV). Indeed, the solvent binding energies calculated using DFT (PBE0 functional, aug-cc-pVDZ basis set; see Table S1 in the SI) were 0.64, 0.71, and 0.55 eV for water, methanol, and acetonitrile, respectively. These calculations were performed with TURBOMOLE.¹⁷ Similar binding energies were predicted by Zuev et al.⁶ for complexes of water with the PYP and green fluorescent protein (GFP) anions in their phenolate forms. When zero-point vibrational energy and corrections for the basis-set superposition error were included,¹⁸ we obtained binding energies of 0.54, 0.65, and 0.50 eV, respectively. For a simple dissociation process in which one bond is cleaved, the barrier for the reverse reaction is low or zero. Hence, the dissociation energy is similar to the activation energy, and the excess energy after photoexcitation is at least 1 eV (photon energy minus dissociation energy). It can therefore be assumed that all of the photoexcited ions dissociated within the experimental time window of a few microseconds. The action spectra of the complexes are therefore good representations of the corresponding gas-phase absorption spectra. Photoexcitation of $m^-(\text{CH}_3\text{OH})$ at high laser power also led to OH loss and dissociation of the nitrophenolate ion via two-photon processes.

The action spectra of the complexes are shown in Figure 3 together with the previously reported spectrum for the bare ion.¹¹ The band maxima and shifts relative to the bare ion are summarized in Table 1. The bare ion absorbs maximally at 2.34 eV (530 nm), and it is clearly evident that a single solvent molecule causes a blue shift in the absorption. It is worth

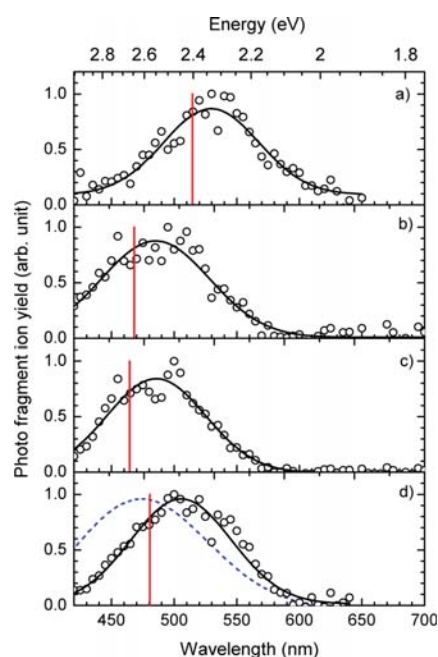


Figure 3. Action spectra of (a) bare m^- , (b) $m^-(\text{H}_2\text{O})$, (c) $m^-(\text{CH}_3\text{OH})$, and (d) $m^-(\text{CH}_3\text{CN})$. Gaussian curves are included to guide the eye. The red sticks show CC2-calculated values. The blue dashed curve in (d) is the spectrum in bulk acetonitrile solution.

Table 1. Absorption Band Maxima (λ_{max}) and Shifts from the Bare Ion (Δ)

ion	λ_{max} (nm) ^a	λ_{max} (eV) ^a	Δ (eV) ^a	λ_{max} (eV) ^b	Δ (eV) ^b
m^-	530	2.34		2.41	
$m^-(\text{H}_2\text{O})$	485	2.56	0.22	2.65	0.25
$m^-(\text{CH}_3\text{OH})$	485	2.56	0.22	2.67	0.26
$m^-(\text{CH}_3\text{CN})$	505	2.46	0.12	2.58	0.17

^aFrom experiment (Figure 3). ^bCC2-calculated.

emphasizing that the band shapes of the bare ion and the complexes are very similar and can be approximated by Gaussians with band widths of ~ 0.4 eV.

The shifts for water and methanol are the same [0.22 eV (45 nm)], and that for acetonitrile is about a factor of 2 smaller [0.12 eV (25 nm)]. In all three cases, the solvatochromic shift is merely a fraction of the solvent binding energy, with that of acetonitrile being the smallest (24%). Obviously, the strong hydrogen bonds formed with water and methanol (Figure 4) cause a stronger perturbation of the electronic structure of the chromophore than the interaction with acetonitrile. The latter still achieves a comparable binding energy, as it has the largest dipole moment

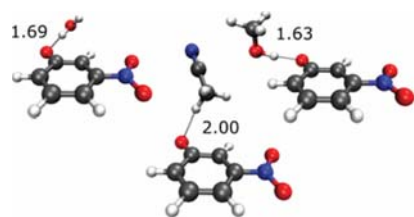


Figure 4. Minimum-energy structures of $m^-(\text{H}_2\text{O})$, $m^-(\text{CH}_3\text{OH})$, and $m^-(\text{CH}_3\text{CN})$ calculated at the MP2 level using the TZVPP basis set. Hydrogen-bond distances in Å are given.

and polarizability. Water has a slightly larger dipole moment than methanol, whereas methanol has a larger polarizability and forms a slightly stronger hydrogen bond (Figure 4), but the shifts are similar.

We also calculated vertical excitation energies at the CC2 level of theory using the optimized structures shown in Figure 4 (see Table 1). For the bare ion as well as the three complexes, the obtained values are ~ 0.1 eV higher in energy than the experimental absorption maxima, but the solvation shifts agree rather well (0.25, 0.26, and 0.17 eV for water, methanol, and acetonitrile, respectively). This result is satisfactory; the deviation of 0.1 eV is within the typical error of the CC2 method.¹⁹ Moreover, an inhomogeneous line broadening can be expected because of the orientational flexibility of the solvent molecule at room temperature, which is not taken into account by the calculations. We note that in the case of water binding to the PYP anion, Krylov and co-workers⁶ predicted a blue shift of 0.06 eV for the phenolate (electron donor) site and a red shift of 0.07 eV when water binds to the carboxyl group. When we placed the solvent molecule at the nitro group of m^- , we obtained red shifts of 0.27 and 0.25 eV for methanol and acetonitrile, respectively, demonstrating the strong CT character of the electronic transition in m^- compared with that in the PYP anion. Figure S4 in the SI shows that the density changes upon excitation are essentially localized on the phenolate oxygen and the nitro group. This is consistent with the observed strong perturbation due to hydrogen bonds.

In bulk acetonitrile solution, the absorption band maximum is at 2.62 eV (473 nm), which represents a blue shift of 0.28 eV relative to the bare ion. Interestingly, almost half of this shift is caused by a single solvent molecule, which clearly demonstrates the importance of the nearby environment on the electronic structure of the ions. In the protic solvents water and methanol, the band maxima are at 3.18 eV (390 nm) and 3.20 eV (387 nm), respectively. Hence, full completion of the solvation shell in these two solvents induces a larger blue shift than in acetonitrile. This is most likely linked to the fact that the phenolate oxygen can hydrogen-bond to two or three water or methanol molecules, rendering a CT excitation less favorable.

Finally, we did measurements on the bare m^- ion at another setup, the electrostatic ion storage ring in Aarhus (ELISA), where neutrals were measured instead of ionic fragments.²⁰ Ion bunches were stored in the ring for 24 ms before being irradiated with laser light. Neutrals produced within ~ 10 μs were counted by a secondary emission detector (SED). The obtained yield of photoneutrals as a function of wavelength is shown in Figure 5 together with the spectrum from Figure 3. The spectra follow each other nicely on the low-energy side from ~ 2.3 eV and down. In the 2.4–2.7 eV region, the yield of photoneutrals decreases with energy, but the relative yield is higher than in the photofragment ion experiment. At higher energies, the yield increases. A power dependence study at 2.95 eV (420 nm) revealed that the signal is mainly due to the absorption of two photons, though some contribution from one-photon absorption cannot be excluded (see the SI). We calculated the vertical detachment energy to be 2.98 eV, and we assign the signal to electron photodetachment of hot m^- anions, as this would account for the asymmetry of the absorption band and a skewing toward the blue. The band maximum from this experiment is at ~ 2.4 eV. Taken together, we estimate the experimental uncertainty in the band maximum to be 0.05 eV.

In conclusion, we have shown that the attachment of single solvent molecules of water, methanol, and acetonitrile causes

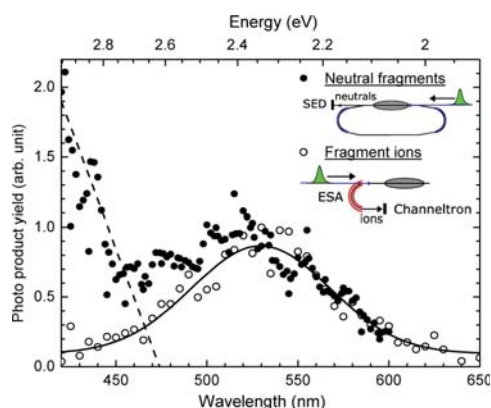


Figure 5. Action spectra of m^- recorded at two different setups. Solid circles: Photoneutrals were counted by an SED right after photoexcitation in a storage ring. A straight line fits the data at high energies. Open circles: Photodissociation followed by deflection of fragment ions in an ESA (same as Figure 3a).

blue shifts in the electronic absorption of m -nitrophenolate by 0.22, 0.22, and 0.12 eV, respectively (uncertainty of 0.05 eV). The CC2-calculated vertical excitation energies differ by ~ 0.1 eV from the experimental absorption maxima, but the predicted shifts for the complexes relative to the bare ion are nearly identical to the experimental ones. The smaller shift found for acetonitrile is ascribed to a weaker interaction with the electron-donating oxygen, which results in a smaller perturbation of the CT excitation energy. Interestingly, a single acetonitrile molecule provides nearly half of the solvent shift seen in bulk solution. Our data provide clear benchmarks for theoretical calculations of CT excitation energies of weakly bound ion–molecule complexes. This is highly relevant to shed light on the shifts induced by single water molecules or amino acid residues on biochromophore anions in protein pockets. Future work will address the role of stepwise solvation, which is an experimental challenge because of very low ion beam currents.

■ ASSOCIATED CONTENT

Supporting Information

Additional experimental and computational results. This material is available free of charge via the Internet at <http://pubs.acs.org>.

■ AUTHOR INFORMATION

Corresponding Author

angel.rubio@ehu.es; sbn@phys.au.dk

Notes

The authors declare no competing financial interest.

■ ACKNOWLEDGMENTS

S.B.N. acknowledges support from The Lundbeck Foundation and The Danish Council for Independent Research | Natural Sciences (10-082088). M.W. and A.R. acknowledge support from ERC Advanced Grant DYNamo (ERC-2010-AdG 267374), Spanish Grants (FIS2010-21282-C02-01 and PIB2010US-00652), Grupo Consolidado UPV/EHU del Gobierno Vasco (IT578-13), and European Commission Projects CRONOS (Grant 280879-2 CRONOS CP-FP7) and POCAONTAS (FP7-PEOPLE-2012-ITN, Project 316633). M.W. acknowledges support from the MICINN “Juan de la Cierva” Program.

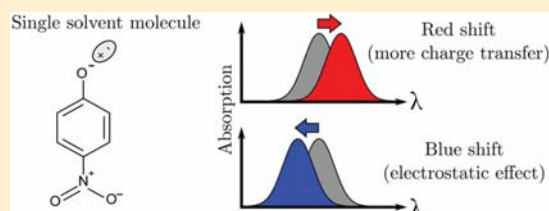
■ REFERENCES

- (1) (a) Cheng, L.-T.; Tam, W.; Marder, S. R.; Stiegman, A. E.; Rikken, G.; Spangler, C. W. *J. Phys. Chem.* **1991**, *95*, 10643. (b) Muthuraman, M.; Bagieu-Beucher, M.; Masse, R.; Nicoud, J.-F.; Desiraju, G. R. *J. Mater. Chem.* **1999**, *9*, 1471. (c) Muthuraman, M.; Nicoud, J.-F.; Masse, R.; Desiraju, G. R. *Mol. Cryst. Liq. Cryst.* **2001**, *356*, 1. (d) Boaz, B. M.; Das, S. J. *J. Cryst. Growth* **2005**, *279*, 383.
- (2) (a) Gromov, E. V.; Burghardt, I.; Köppel, H.; Cederbaum, L. S. *J. Am. Chem. Soc.* **2007**, *129*, 6798. (b) Gromov, E. V.; Burghardt, I.; Köppel, H.; Cederbaum, L. S. *J. Photochem. Photobiol., A* **2012**, *234*, 123.
- (3) (a) Navizet, I.; Liu, Y. J.; Ferré, N.; Xiao, H. Y.; Fang, W. H.; Lindh, R. *J. Am. Chem. Soc.* **2010**, *132*, 706. (b) Cai, D.; Marques, M. A. L.; Milne, B. F.; Nogueira, F. *J. Phys. Chem. Lett.* **2010**, *1*, 2781.
- (4) Tozer, D. J. *J. Chem. Phys.* **2003**, *119*, 12697.
- (5) Dreuw, A.; Weisman, J. L.; Head-Gordon, M. *J. Chem. Phys.* **2003**, *119*, 2943.
- (6) Zuev, D.; Bravaya, K. B.; Makarova, M. V.; Krylov, A. I. *J. Chem. Phys.* **2011**, *135*, No. 194304.
- (7) Rajput, J.; Rahbek, D. B.; Aravind, G.; Andersen, L. H. *Biophys. J.* **2010**, *98*, 488.
- (8) (a) Yagi, I.; Maeyama, T.; Fujii, A.; Mikami, N. *J. Phys. Chem. A* **2007**, *111*, 7646. (b) Maeyama, T.; Yagi, I.; Fujii, A.; Mikami, N. *Chem. Phys. Lett.* **2008**, *457*, 18.
- (9) (a) Hoffmann, M.; Wanko, M.; Strodel, P.; König, P. H.; Frauenheim, T.; Schulten, K.; Thiel, W.; Tajkhorshid, E.; Elstner, M. *J. Am. Chem. Soc.* **2006**, *128*, 10808. (b) Nakatani, N.; Hasegawa, J.; Nakatsuji, H. *J. Am. Chem. Soc.* **2007**, *129*, 8756. (c) Shu, X. K.; Shaner, N. C.; Yarbrough, C. A.; Tsien, R. Y.; Remington, S. J. *Biochemistry* **2006**, *45*, 9639. (d) Nienhaus, G.; Nienhaus, K.; Wiedenmann, J. *Springer Ser. Fluoresc.* **2012**, *11*, 241.
- (10) Nakatsu, T.; Ichiyama, S.; Hiratake, J.; Saldanha, A.; Kobashi, N.; Sakata, K.; Kato, H. *Nature* **2006**, *440*, 372.
- (11) Wanko, M.; Houmøller, J.; Stöckel, K.; Kirketerp, M.-B. S.; Petersen, M. Å.; Brøndsted Nielsen, M.; Brøndsted Nielsen, S.; Rubio, A. *Phys. Chem. Chem. Phys.* **2012**, *14*, 12905.
- (12) (a) Mercier, S. R.; Boyarkin, O. V.; Kamariotis, A.; Guglielmi, M.; Tavernelli, I.; Cascella, M.; Rothlisberger, U.; Rizzo, T. R. *J. Am. Chem. Soc.* **2006**, *128*, 16938. (b) Loison, C.; Antoine, R.; Broyer, M.; Dugourd, P.; Guthmuller, J.; Simon, D. *Chem.—Eur. J.* **2008**, *14*, 7351. (c) Alata, I.; Broquier, M.; Dedonder-Lardeux, C.; Jouvet, C.; Kim, M.; Sohn, W. Y.; Kim, S.; Kang, H.; Schütz, M.; Patzer, A.; Dopfer, O. *J. Chem. Phys.* **2011**, *134*, No. 074307.
- (13) (a) Liu, H.; Guo, W.; Yang, S. *J. Chem. Phys.* **2001**, *115*, 4612. (b) Faherty, K. P.; Thompson, C. J.; Aguirre, F.; Michne, J.; Metz, R. B. *J. Phys. Chem. A* **2001**, *105*, 10054. (c) Spence, T. G.; Trotter, B. T.; Posey, L. A. *J. Phys. Chem. A* **1998**, *102*, 7779. (d) Nonose, S.; Tanaka, H.; Okai, N.; Shibakusa, T.; Fuke, K. *Eur. Phys. J. D* **2002**, *20*, 619.
- (14) (a) Mihalick, J. E.; Gatev, G. G.; Brauman, J. I. *J. Am. Chem. Soc.* **1996**, *118*, 12424. (b) Serxner, D.; Dessent, C. E. H.; Johnson, M. A. *J. Chem. Phys.* **1996**, *105*, 7231.
- (15) Ayotte, P.; Johnson, M. A. *J. Chem. Phys.* **1997**, *106*, 811.
- (16) (a) Stöckel, K.; Milne, B. F.; Brøndsted Nielsen, S. *J. Phys. Chem. A* **2011**, *115*, 2155. (b) Wyer, J. A.; Brøndsted Nielsen, S. *Angew. Chem., Int. Ed.* **2012**, *51*, 10256.
- (17) TURBOMOLE V6.1 2009, a development of the University of Karlsruhe and Forschungszentrum Karlsruhe GmbH, 1989–2007, TURBOMOLE GmbH, since 2007; available from <http://www.turbomole.com>.
- (18) Boys, S.; Bernardi, F. *Mol. Phys.* **1970**, *19*, 553.
- (19) Schreiber, M.; Silva-Junior, M. R.; Sauer, S. P. A.; Thiel, W. *J. Chem. Phys.* **2008**, *128*, No. 134110.
- (20) (a) Andersen, J. U.; Hvelplund, P.; Brøndsted Nielsen, S.; Tomita, S.; Wahlgreen, H.; Møller, S. P.; Pedersen, U. V.; Forster, J. S.; Jørgensen, T. J. D. *Rev. Sci. Instrum.* **2002**, *73*, 1284. (b) Stöckel, K.; Kadhane, U.; Andersen, J. U.; Holm, A. I. S.; Hvelplund, P.; Kirketerp, M.-B. S.; Larsen, M. K.; Lykkegaard, M. K.; Brøndsted Nielsen, S.; Panja, S.; Zettergren, H. *Rev. Sci. Instrum.* **2008**, *79*, No. 023107. (c) Rajput, J.; Rahbek, D. B.; Aravind, G.; Andersen, L. H. *Biophys. J.* **2010**, *98*, 488.

Effect of a Single Water Molecule on the Electronic Absorption by *o*- and *p*-Nitrophenolate: A Shift to the Red or to the Blue?Jørgen Houmøller,[†] Marius Wanko,[‡] Angel Rubio,^{*,‡,§} and Steen Brøndsted Nielsen^{*,†}[†]Department of Physics and Astronomy, Aarhus University, DK-8000 Aarhus C, Denmark[‡]Nano-Bio Spectroscopy Group and ETSF, Dpto. Física de Materiales, Universidad del País Vasco, CFM CSIC-UPV/EHU-MPC & DIPC, 20018 San Sebastián, Spain[§]Max Planck Institute for the Structure and Dynamics of Matter and Center for Free-Electron Laser Science, Luruper Chaussee 149, 22761 Hamburg, Germany

Supporting Information

ABSTRACT: Many photoactive biomolecules are anions and exhibit $\pi\pi^*$ optical transitions but with a degree of charge transfer (CT) character determined by the local environment. The phenolate moiety is a common structural motif among biochromophores and luminophores, and nitrophenolates are good model systems because the nitro substituent allows for CT-like transitions. Here we report gas-phase absorption spectra of *o*- and *p*-nitrophenolate·H₂O complexes to decipher the effect of just one H₂O and compare them with ab initio calculations of vertical excitation energies. The experimental band maximum is at 3.01 and 3.00 eV for *ortho* and *para* isomers, respectively, and is red-shifted by 0.10 and 0.13 eV relative to the bare ions, respectively. These shifts indicate that the transition has become more CT-like because of localization of negative charge on the phenolate oxygen, i.e., diminished delocalization of the negative excess charge. However, the transition bears less CT than that of *m*-nitrophenolate·H₂O because this complex absorbs further to the red (2.56 eV). Our work emphasizes the importance of local perturbations: one water causes a larger shift than experienced in bulk for *para* isomer and almost the full shift for *ortho* isomer. Predicting microenvironmental effects in the boundary between CT and non-CT with high accuracy is nontrivial. However, in agreement with experiment, our calculations show a competition between the effects of electronic delocalization and electrostatic interaction with the solvent molecule. As a result, the excitation energy of *ortho* and *para* isomers is less sensitive to hydration than that of the *meta* isomer because donor and acceptor orbitals are only weakly coupled in the *meta* isomer.



INTRODUCTION

In freshman chemistry courses students are taught that an increase in electron delocalization within a molecule results in a lower gap between the highest occupied molecular orbital (HOMO) and the lowest unoccupied molecular orbital (LUMO); this is directly evident from molecular orbital diagrams or the simple electron-in-a-box model with increasing box lengths. These models nicely explain why the absorption band redshifts in the series ethylene, 1,3-butadiene, 1,3,5-hexatriene, etc. However, it is not always this simple: while the absorption by neutral polycyclic aromatic hydrocarbons (PAHs) duly redshifts with molecular size, a similar trend is not seen for the protonated linear analogues because those with an even number of aromatic rings display pronounced charge-transfer (CT) character (and therefore absorb further to the red than their size justifies), as beautifully demonstrated by Jouvett and co-workers.¹ Likewise, a decrease in delocalization due to, for example, microsolvation may actually lead to a lower excitation energy (red-shifted absorption band) if the electronic transition changes character and becomes CT-like (Figure 1).² Hence, a description of HOMO–LUMO gaps based only on electron delocalization is insufficient, and qualitative reasoning

is difficult because different effects can shift gap energies in opposite directions with unknown relative importance. Another issue to consider in the case of protonated species is internal proton transfer to the solvent molecules in the ground state when the solvent cluster is large enough.^{3,4} Altogether, it implies that it is in general nontrivial to predict the effect of microsolvation or other perturbations on transition energies.

The effect of a nearby environment is of particular importance for biochromophores located within protein pockets where there are a limited number of interactions with water molecules or amino acid residues. Examples include the chromophores of the green fluorescent protein (GFP) and the photoactive yellow protein (PYP)^{5–13} and the oxyluciferin luminophore located within the luciferase enzyme and responsible for light emission from fireflies;^{14–16} the phenolate moiety is a common structural motif for all three in their anionic forms.

Received: September 4, 2015

Revised: November 4, 2015

Published: November 9, 2015

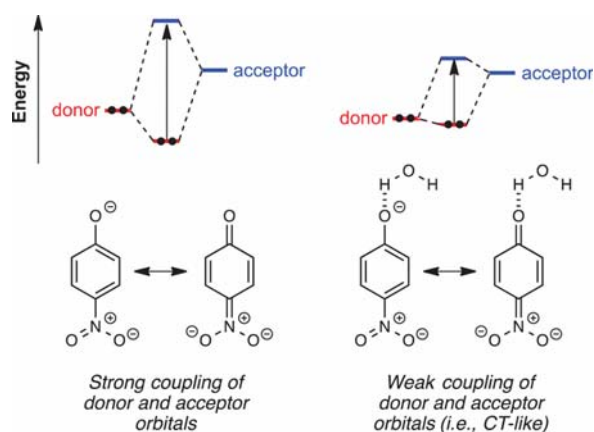


Figure 1. Left panel: HOMO and LUMO for *p*-nitrophenolate are linear combinations of orbitals located on a phenolate group (denoted donor) and a nitro group (acceptor) due to strong coupling (two important resonance forms). The electronic transition is $\pi\pi^*$ where the π and π^* states are fully delocalized. Right panel: A single water molecule may decouple the two groups such that the HOMO becomes more donor-like and the LUMO more acceptor-like, simply because the contribution of the resonance form with the electron on the NO_2 group, remotely located from the water, becomes insignificant. The $\pi\pi^*$ transition is now CT-like as electron density moves from one end of the molecule to the other.

As simple model systems for photoactive biomolecules we have studied *o*-, *m*-, and *p*-nitrophenolate isolated in vacuo using specialized mass spectroscopy equipment built in Aarhus.¹⁷ The HOMO and the LUMO are delocalized over the whole molecular anion in the former and latter cases (Figure 1) while the *meta* isomer displays CT-like excitation. This conclusion was reached from the *meta* isomer absorbing to the red of *ortho* (*o*) and *para* (*p*) isomers despite a lower electron delocalization (a resonance form where the electron is not allowed in the ground state for *meta* isomer); the redshift is 0.77 and 0.81 eV compared to *ortho* and *para* isomers, respectively. We also established that a single water molecule attached to the *meta* phenolate oxygen blueshifts the absorption by 0.22 eV, because upon excitation, the interaction between the water dipole and the center of excess charge is weakened as the latter moves from the phenolate toward the nitro group, i.e., away from the water.¹⁸

Now a compelling problem that remains to be resolved is whether a single water molecule attached to either *o* or *p* causes a redshift or a blueshift in the absorption. The water localizes the negative charge at the phenolate oxygen and thereby diminishes the importance of the Lewis resonance structure that assigns the negative charge to the nitro group (Figure 1). *Ortho* and *para* become *meta*-like so to speak, that is, decoupling is similar to the situation occurring naturally in the *meta* form, and a single water molecule should therefore give a redshift in the absorption, by as much as 0.8 eV (difference between bare *ortho* or *para* and bare *meta*). However, the price of moving the electron away from the phenolate oxygen and toward the nitro group also has to be paid, and based on results for the *meta* isomer, this electrostatic effect could be as much as 0.2 eV. Hence, we have two opposing effects on the transition energies, and the actual shift from the bare ion absorption is expected to be between -0.8 eV and $+0.2$ eV.

Here we address the effect of a single water molecule based on gas-phase ion spectroscopy of complexes between *o*- and *p*-nitrophenolate and water and theoretical calculations of excited states.

EXPERIMENTAL SECTION

It is difficult to measure the absorption spectrum of ions in vacuo because of a too low ion density for traditional light transmission experiments. Instead, the occurrence of light absorption is monitored from ion dissociation (action spectroscopy). The yield of fragment ions as a function of the wavelength of absorbed light is taken to represent the absorption spectrum under the assumption that photoexcitation leads to complete dissociation for all excitation energies within the time window of the experiment and that the quantum yield for light emission is independent of excitation energy. The former is most easily fulfilled for weakly bound complexes, such as those under study in this work.

The experimental setup (Figure 2) has been explained in detail elsewhere.^{19,20} Briefly, ions were produced by electro-

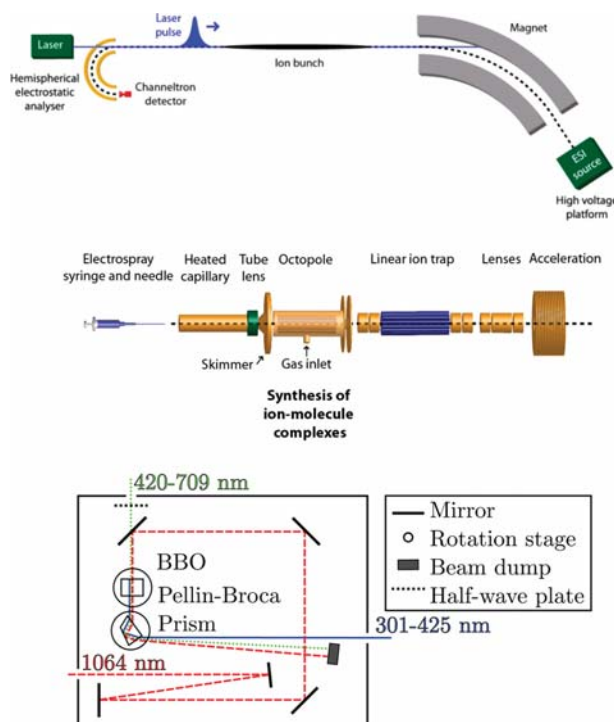


Figure 2. Top panel: Mass spectrometer setup (see text for details). Middle panel: The ion source. Water vapor is let into the octopole to produce ion–molecule complexes. Bottom panel: Illustration of the home-built sum-frequency generator, where IR and visible light are mixed in a BBO crystal to produce UV light. The delay line for the 1064 nm IR beam is for matching in time the visible beam from the OPO. A Pellin–Broca prism is used to separate the two pump beams from the generated beam.

spray ionization and subsequently trapped in an octopole for up to 25 ms by pulsing a lens directly after the octopole. Residual gas collisions cooled the ions to approximately room temperature. Water vapor was let into the octopole region to a pressure of 0.01–0.1 mbar to form ion–water complexes. All ions were then accelerated to a kinetic energy of 50 keV, and those of interest were selected according to their mass-to-

charge ratio by an electromagnet. These then traveled along a straight section where they interacted with a nanosecond-light pulse from a pulsed laser. Photoexcitation led to dissociation that was monitored by a hemispherical electrostatic analyzer (kinetic energy per charge selector). The yield of the selected fragment ion was counted by a channeltron detector. The time window for fragmentation is a few microseconds.

The results shown in this paper are combined measurements from two different wavelength regions. The main laser used is an EKSPLA Q-switched nanosecond pulsed laser, where the third harmonic of a Nd:YAG fundamental is used to pump an optical parametric oscillator (OPO). The output range of the OPO is 420–2300 nm. To produce light below 420 nm, we constructed a sum-frequency generator (Figure 2). This setup utilizes sum-frequency generation between the Nd:YAG infrared (IR) fundamental (1064 nm) and the visible light from the OPO, both originating from the same laser. The linear polarization of the visible light is changed by $\pi/2$ from passing through a half-wave plate to allow type-I phase matching in a barium borate (BBO) crystal. A Pellin–Broca prism is used for separation of the IR fundamental, the OPO light, and the sum-frequency light. Angle tuning of the BBO and the prism is achieved by two stepper-motor-rotation stages controlled by a LabView program. The output range of the sum-frequency generation is 301–425 nm. The output powers of the OPO and the sum-frequency setup are shown in Figure 3.

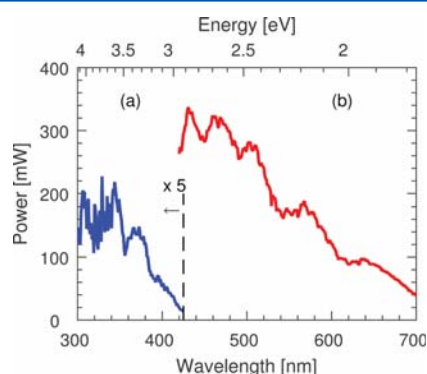


Figure 3. Laser power as a function of output wavelength. (a) Output from sum-frequency generation multiplied by a factor of 5. (b) Output from the EKSPLA OPO (visible region). The pulse energy is the power divided by the laser repetition rate (20 s^{-1}).

The repetition rates of the ion trap and the laser were 40 and 20 Hz, respectively. Hence, after each laser shot, we monitored the background dissociation due to residual gas collisions or unimolecular decay of metastable ions. This “laser-off” signal is proportional to the ion-beam current but was too low in these experiments to correct for fluctuations in ion current. Instead, the experiment was repeated a number of times to average out any such fluctuations. The laser-off signal was subtracted from the “laser-on” signal, and the resultant signal was corrected for the number of photons in the laser pulse.

COMPUTATIONAL DETAILS

If not indicated otherwise, geometries were optimized with the PBE0 functional and aug-cc-pVDZ basis set using the turbomole software.²¹ Vertical excitation energies (VEEs) were obtained with the CC2 coupled-cluster method,²² its spin-component-scaled version SCS-CC2, the second-order

algebraic diagrammatic construction method ADC(2)²³ (turbomole), SORCI,²⁴ and NEVPT2²⁵ (orca²⁶). For the latter two methods, a CASSCF(12,10) reference was used, which includes the entire π -system. The SORCI calculations start with the CASSCF orbitals and a MRDDCI2 step (thresholds: $T_{\text{pre}} = 10^{-3}$, $T_{\text{sel}} = 10^{-6}$) to produce approximate two-state averaged natural orbitals for the final MRDDCI3 calculation. All excited-state calculations were performed with the aug-cc-pVDZ basis. The models for bulk solution contained seven explicit water molecules, forming H-bonds with the solute, and the COSMO solvation model. The ADC(2)+COSMO excitation energies were calculated self-consistently using the cc2cosmo script and including off-diagonal contributions. Binding energies were calculated with CCSD(T) and the aug-cc-pVTZ basis, on SCS-MP2/aug-cc-pVDZ geometries and corrected for basis set superposition error (BSSE; same level of theory) and zero-point vibrational energy (ZPVE, from PBE0/aug-cc-pVTZ). Vertical detachment energies were calculated with CCSD(T), as in ref 17. Geometries and further results are provided in the Supporting Information.

RESULTS AND DISCUSSION

Photodissociation of the *o*-H₂O and *p*-H₂O complexes results in only one dominant fragment for each complex corresponding to loss of water (fragment ion $m/z = 138$, see the Supporting Information). The fragment ion yield increased linearly with laser power (see the Supporting Information), which indicates that dissociation is due to one-photon absorption and therefore that the binding energy of the complex is less than the photon energy ($>2.5 \text{ eV}$). For *p*-H₂O, we calculated binding energies of 0.41 eV (H-bond to phenolate) and 0.32 eV (H-bond to nitro group) (Figure 4).

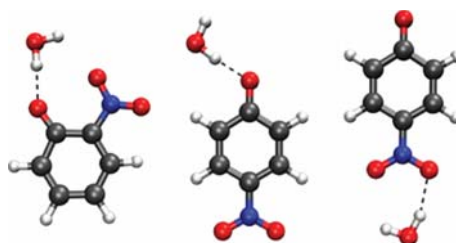


Figure 4. Calculated (PBE0/aug-cc-pVDZ) structures of *o*-H₂O, *p*-H₂O@PheO[−], and *p*-H₂O@NO₂.

At room temperature, we therefore expect the first isomer to strongly prevail in the ion beam (assuming that the limiting barrier for moving the water from one end to the other is low enough to allow for equilibrium to be established). Interestingly, the binding energy is lower than that previously calculated for the *meta* isomer (0.64 eV),⁸ which indicates that some of the negative charge in the *para* isomer is still on the nitro group (the donor and acceptor orbitals are not fully decoupled). This is in agreement with absorption spectra to be discussed later. For *o*-H₂O, the water binds to both groups but forms the stronger bond to the phenolate (Figure 4). Assuming that there is no barrier for the reverse reaction, the excess energy after photoexcitation is more than 2 eV (photon energy minus dissociation energy), and it is therefore reasonable to assume that the dissociation of the photoexcited ions occurs within the time window of the experiment (a few microseconds).

Action spectra of the complexes are shown in Figure 5. These were obtained as laser-on signal minus laser-off signal followed

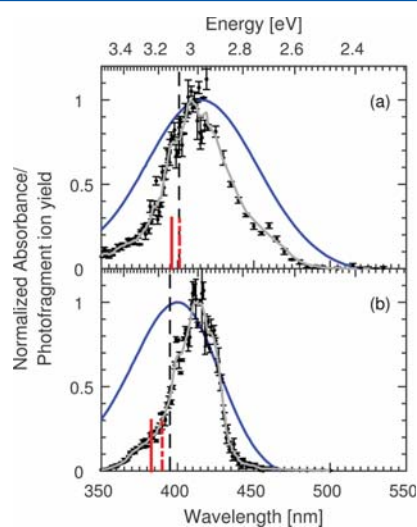


Figure 5. Action spectra of (a) *o*-H₂O and (b) *p*-H₂O. To help guide the eye, a five-point average curve (gray) is superimposed on the data. The blue curves are the absorbance spectra obtained in alkaline aqueous solution (pH 10) (the pK_a of both *o*-nitrophenol and *p*-nitrophenol is 7.2). The thick red vertical lines in the bottom of the spectra mark the CC2-calculated band maxima; the full lines are for the water complexes; and the broken lines are for the bare chromophores. The band maxima for the bare chromophores are marked by the broken vertical lines that span the whole height of the figures.

by a linear correction for the number of photons at each wavelength. The band maximum is at 3.01 eV (412 nm) for *o*-H₂O (Figure 5a) and at 3.00 eV (413 nm) for *p*-H₂O (Figure 5b).

It is evident that the water complexes absorb further to the red than the bare chromophores. The redshift for the *para* isomer [0.13 eV (17 nm)] is greater than that for the *ortho* isomer [0.10 eV (13 nm)]. The fact that a redshift is seen can be explained by the lesser degree of coupling between the donor and acceptor orbitals in the complexes. Judged by the calculated ground-state geometries (Figure 4), it is clear that the overall perturbing effect of the water molecule for the *ortho* isomer must be less than that for the *para* case because both the donor and acceptor groups are in close proximity to the water; this is in accordance with the measured redshifts.

For *o*-H₂O and *p*-H₂O, we calculated vertical detachment energies of 3.75 and 3.83 eV, respectively, which is ca. 0.5 eV higher than those reported for the bare anions.⁷ Importantly, these detachment energies are well above the absorption band maxima by more than 0.7 eV, and electron detachment is therefore not expected to be an important channel close to the band maxima.

In aqueous solution, the absorption band maxima of *o* and *p* are at 3.00 eV (415 nm, Figure 5a) and 3.11 eV (399 nm, Figure 5b), respectively. Interestingly, for *p* the shift by one single water molecule is larger than that after full hydration. Indeed, the absorption by the bare ion and *p*_(aq) is very similar; full hydration redshifts the band by only 0.03 eV (4 nm). This can easily be rationalized: in the fully hydrated ion, there are water molecules both at the phenolate oxygen and the nitro

group, and the donor and acceptor orbitals are therefore coupled, as they are in the bare ion. Interestingly, for the *ortho* isomer, the shift corresponding to bulk solution can be ascribed mainly to the effect from binding a single water molecule.

Furthermore, fully hydrated *o* absorbs to the red of *p*_(aq). A polarization effect can account for this: in general, an excited state is more polarizable than a ground state, and movement of electron density toward the water dipoles would bring down the excited-state energy of *o*_(aq) (the dipoles at the phenolate oxygen and the nitrogen group point in similar direction). A movement of electron density in the *para* isomer would be beneficial for some water molecules but not for others; the water dipole moments are pointing in different directions at the phenolate oxygen end and the nitro group end.

To see if theory can account for the observed hydration effects, we performed a series of quantum chemical calculations at various levels of theory. On the basis of the minimum-energy geometries, representing the anions and their microhydrated complexes at the 0 K limit (Figure 4), we calculated VEEs with the CC2, ADC(2), SORCI, and NEVPT2 methods (summarized in Table 1). The first three methods provide excitation

Table 1. Summary of Experimental Band Maxima and Calculated Vertical Excitation Energies (in Electronvolts)

	experimental λ_{\max}	CC2	ADC(2)	SORCI	NEVPT2
<i>o</i>	3.11	3.15	3.02	3.00	3.24
<i>o</i> -H ₂ O	3.01	3.20	3.06	3.05	3.29
<i>o</i> _(aq)	3.00		2.76	2.96	3.16
<i>p</i>	3.16	3.27	3.10	3.11	3.38
<i>p</i> -H ₂ O	3.00	3.33	3.16	3.23	3.50
<i>p</i> _(aq)	3.11		2.77	2.98	3.25

energies that maximally differ by 0.25 eV compared to experimental values, while the deviation is as much as 0.5 eV for NEVPT2. All methods consistently predict a small blueshift of both complexes compared to the solute in vacuo. Nevertheless, this shift is much smaller than that earlier reported for the *meta* isomer: 0.05 eV for *ortho*, 0.24 eV for *meta*, and 0.06 eV for *para* (CC2 method). Hence, theory is in accordance with a decoupling of donor and acceptor orbitals in *ortho* and *para* isomers upon water attachment, accounting for a shift that is smaller than that seen for the *meta* isomer. The relative importance between decoupling (giving a redshift) and loss of complex binding energy upon photoexcitation (electrostatic effect giving a blueshift) is, however, not correctly predicted.

Krylov and co-workers¹² reported on the effect of attachment of a single water molecule to the isolated chromophore anions of GFP and PYP proteins. They used as model systems deprotonated 4-hydroxybenzylidene-2,3-dimethylimidazolinone (HBDI) and deprotonated *para*-coumaric acid (pCA) to represent the chromophores in GFP and PYP, respectively. SOS-CIS(D)/cc-pVTZ-calculated VEEs for the HBDI anion and EOM-EE-CCSD/6-31+G(d,p) ones for the pCA anion revealed small blueshifts of 0.03 and 0.06 eV, respectively, due to the water (in both cases phenolate form of chromophore). These shifts are similar to what we calculate for *o* and *p*.

We also modeled the fully hydrated solute (see Computational Details). Full hydration yields a redshift relative to the bare ion, which varies with the quantum chemistry method, but in all cases is larger for *p* than for *o* (Table 1). As seen

experimentally, theory predicts the absorption by $\sigma_{(\text{aq})}$ to be to the red of $p_{(\text{aq})}$.

To investigate how the microhydration affects the CT character and energetics of the excitation, we consider the individual components of the solvent shift, i.e., (1) the change of the solute geometry, (2) the electrostatic interaction energy between the solvent and the polarized solute (V^{ES}), and (3) the electronic reorganization energy invested to polarize the solute (E^{ERO}). The geometry of the solute changes upon binding a water molecule because of the localization of the excess charge on the H-bond accepting group (Table 2). When the water in

Table 2. Calculated Bond Lengths (Angstroms) and SCS-CC2/aug-cc-pVDZ Vertical Excitation Energies (Electronvolts)^a

	C–O	C–N	complex	H ₂ O removed
σ	1.265	1.451	3.09 (3.9)	
σ -H ₂ O	1.271	1.452	3.13 (4.1)	3.09 (3.9)
p	1.268	1.425	3.18 (4.8)	
p -H ₂ O@Phe	1.280	1.434	3.24 (6.1)	3.17 (5.2)
p -H ₂ O@NO ₂	1.264	1.411	3.13 (3.0)	3.21 (4.0)

^aDifference in dipole moments between excited and ground states, $|\Delta\mu_{10}|$ (D), are given in parentheses. Geometries were optimized with SCS-MP2/aug-cc-pVDZ. Right column: bare solute with the same geometry as in the complex.

p -H₂O binds to the phenolate oxygen, the C–O and C–N bonds are stretched by 0.012 and 0.009 Å, respectively, which indicates that the first of the two resonance structures shown in Figure 1 gains weight. The excitation calculated for the bare solute with this displaced geometry shows a slightly increased charge transfer, as measured by the difference in dipole moment (last column in Table 2), but the expected redshift amounts to merely 0.01 eV. The opposite applies when the water binds to the nitro group. The difference in dipole moments is reduced, and we obtain a blueshift of 0.03 eV.

To calculate the exact contributions of components 2 and 3, we replace the water molecule by a set of point charges, as used in the TIP3P water model. This neglects the potential effect of charge transfer between solute and solvent but allows us to calculate V^{ES} exactly, based on the relaxed CC2 ground- and excited-state densities. If the water binds to the phenolate group, V^{ES} contributes a blueshift of 0.07 eV, whereas E^{ERO} is nearly the same for ground and excited states, contributing only –0.01 eV to the solvent shift. With the water binding to the nitro group, we obtain –0.03 and –0.01 eV for V^{ES} and E^{ERO} , respectively. An alternative decomposition that considers the polarization energy (Supporting Information, Table S2) yields the same trend. In summary, our calculations confirm a decoupling of donor and acceptor states in the p -H₂O complex, but the predicted effect on the absorption energy is rather small and overcompensated by the electrostatic interaction. The same trends were obtained with CC2 using PBE0 geometries (Table S1, Supporting Information).

CONCLUSIONS

We have shown that a single water molecule attached to σ - and p -nitrophenolate perturbs the electronic structure to produce a redshift in the electronic transition of 0.10 and 0.13 eV, respectively. This redshift is explained by a more CT-like transition in the chromophore when a water molecule is attached. Theory does not predict the correct direction of the

shift but does show that the electrostatic interaction between a water molecule and the ion competes with decoupling of acceptor and donor states, which is reflected in both bond lengths and enhanced CT. This is in contrast to the *meta* isomer where the addition of a water molecule hardly changes the coupling, and the electrostatic effect therefore dominates giving a large blueshift (according to both experiment and theory).

Our results have provided important insights into the effects of single water molecules or amino acid residues (serine or threonine OH groups) on the absorption by biochromophores containing the phenolate moiety. The next step would be to follow the stepwise effect of attachment of water molecules to p . The first few water molecules likely bind to the negative charge end, decoupling donor and acceptor groups and thereby causing gradual redshifts. As water starts to bind at the nitro group, the absorption moves back toward the blue as the coupling between the donor and acceptor groups is reestablished. Future experiments are planned to test this hypothesis but are difficult because of low ion beam currents.

ASSOCIATED CONTENT

Supporting Information

The Supporting Information is available free of charge on the ACS Publications website at DOI: 10.1021/acs.jpca.5b08634.

Calculated geometries and CC2 data using PBE0 geometries (PDF)

AUTHOR INFORMATION

Corresponding Authors

*E-mail: angel.rubio@ehu.es.

*E-mail: sbn@hphys.au.dk.

Notes

The authors declare no competing financial interest.

ACKNOWLEDGMENTS

S.B.N. acknowledges support from the Danish Council for Independent Research (Grant 4181-00048B). A.R. and M.W. acknowledge financial support from the European Research Council Advanced Grant DYnAmo (ERC-2010-AdG-267374), Spanish Grant (FIS2013-46159-C3-1-P), Grupos Consolidados UPV/EHU del Gobierno Vasco (IT578-13). Technical and human support provided by IZO-SGI (SGIker) of UPV/EHU.

ABBREVIATIONS

ADC(2), algebraic diagrammatic construction to second order; BBO, barium borate; BSSE, basis set superposition error; CC, coupled cluster; CT, charge transfer; EOM, equation-of-motion; GFP, green fluorescent protein; HBDI, 4-hydroxybenzylidene-2,3-dimethylimidazolinone; HOMO, highest occupied molecular orbital; IR, infrared; LUMO, lowest unoccupied molecular orbital; OPO, optical parametric oscillator; PAH, polycyclic aromatic hydrocarbon; pCA, *para*-coumaric acid; PYP, photoactive yellow protein; VEE, vertical excitation energy; ZPVE, zero-point vibrational energy

REFERENCES

- Alata, I.; Dedonder, C.; Broquier, M.; Marceca, E.; Juvet, C. Role of the Charge-Transfer State in the Electronic Absorption of Protonated Hydrocarbon Molecules. *J. Am. Chem. Soc.* **2010**, *132*, 17483–17489.

- (2) Brøndsted Nielsen, S.; Brøndsted Nielsen, M.; Rubio, A. Spectroscopy of Nitrophenolates in Vacuo: Effect of Spacer, Configuration, and Microsolvation on the Charge-Transfer Excitation Energy. *Acc. Chem. Res.* **2014**, *47*, 1417–1425.
- (3) Alata, I.; Broquier, M.; Dedonder-Lardeux, C.; Jouvet, C.; Kim, M.; Sohn, W. Y.; Kim, S.; Kang, H.; Schütz, M.; Patzer, A.; Dopfer, O. Microhydration Effects on the Electronic Spectra of Protonated Polycyclic Aromatic Hydrocarbons: [Naphthalene-(H₂O)_{n=1,2}]⁺H⁺. *J. Chem. Phys.* **2011**, *134*, 074307.
- (4) Dopfer, O.; Patzer, A.; Chakraborty, S.; Alata, I.; Omidyan, R.; Broquier, M.; Dedonder, C.; Jouvet, C. Electronic and Vibrational Spectra of Protonated Benzaldehyde-Water Clusters, [BZ-(H₂O)_(n≤5)]⁺H⁺: Evidence for Ground-State Proton Transfer to Solvent for $n \geq 3$. *J. Chem. Phys.* **2014**, *140*, 124314.
- (5) Niwa, H.; Inouye, S.; Hirano, T.; Matsuno, T.; Kojima, S.; Kubota, M.; Ohashi, M.; Tsuji, F. I. Chemical Nature of the Light Emitter of the Aequorea Green Fluorescent Protein. *Proc. Natl. Acad. Sci. U. S. A.* **1996**, *93*, 13617–13622.
- (6) Nielsen, S. B.; Lapierre, A.; Andersen, J. U.; Pedersen, U. V.; Tomita, S.; Andersen, L. H. Absorption Spectrum of the Green Fluorescent Protein Chromophore Anion in Vacuo. *Phys. Rev. Lett.* **2001**, *87*, 228102.
- (7) Sinicropi, A.; Andruniow, T.; Ferre, N.; Basosi, R.; Olivucci, M. Properties of the Emitting State of the Green Fluorescent Protein Resolved at the CASPT2//CASSCF/CHARMM Level. *J. Am. Chem. Soc.* **2005**, *127*, 11534–11535.
- (8) Bravaya, K.; Khrenova, M. G.; Grigorenko, B. L.; Nemukhin, A. V.; Krylov, A. I. Effect of Protein Environment on Electronically Excited and Ionized States of the Green Fluorescent Protein Chromophore. *J. Phys. Chem. B* **2011**, *125*, 8296–8303.
- (9) Gromov, E. V.; Burghardt, I.; Köppel, H.; Cederbaum, L. S. Electronic Structure of the PYP Chromophore in its Native Protein Environment. *J. Am. Chem. Soc.* **2007**, *129*, 6798–6806.
- (10) Gromov, E. V.; Burghardt, I.; Köppel, H.; Cederbaum, L. S. Native Hydrogen Bonding Network of the Photoactive Yellow Protein (PYP) Chromophore: Impact on the Electronic Structure and Photoinduced Isomerization. *J. Photochem. Photobiol., A* **2012**, *234*, 123–134.
- (11) de Groot, M.; Gromov, E. V.; Köppel, H.; Buma, W. J. High-Resolution Spectroscopy of Methyl 4-Hydroxycinnamate and its Hydrogen-Bonded Water Complex. *J. Phys. Chem. B* **2008**, *112*, 4427–4434.
- (12) Zuev, D.; Bravaya, K. B.; Makarova, M. V.; Krylov, A. I. Effect of Microhydration on the Electronic Structure of the Chromophores of the Photoactive Yellow and Green Fluorescent Proteins. *J. Chem. Phys.* **2011**, *135*, 194304.
- (13) Philip, A.; Eisenman, K.; Papadantonakis; Hoff, W. Functional Tuning of Photoactive Yellow Protein by Active Site Residue 46. *Biochemistry* **2008**, *47*, 13800–13810.
- (14) Navizet, I.; Liu, Y. J.; Ferré, N.; Xiao, H. Y.; Fang, W. H.; Lindh, R. Color-Tuning Mechanism of Firefly Investigated by Multi-Configurational Perturbation Method. *J. Am. Chem. Soc.* **2010**, *132*, 706–712.
- (15) Cai, D.; Marques, M. A. L.; Milne, B. F.; Nogueira, F. Bioheterojunction Effect on Fluorescence Origin and Efficiency Improvement of Firefly Chromophores. *J. Phys. Chem. Lett.* **2010**, *1*, 2781–2787.
- (16) Stöckel, K.; Hansen, C. N.; Houmøller, J.; Nielsen, L. M.; Anggara, K.; Linares, M.; Norman, P.; Nogueira, F.; Maltsev, O. V.; Hintermann, L.; Brøndsted Nielsen, S.; Naumov, P.; Milne, B. F. On the Influence of Water on the Electronic Structure of Firefly Oxyluciferin Anions from Absorption Spectroscopy of Bare and Monohydrated Ions in Vacuo. *J. Am. Chem. Soc.* **2013**, *135*, 6485–6493.
- (17) Wanko, M.; Houmøller, J.; Stöckel, K.; Kirketerp, M.-B. S.; Petersen, M. Å.; Brøndsted Nielsen, M.; Brøndsted Nielsen, S.; Rubio, A. Substitution Effects on the Absorption Spectra of Nitrophenolate Isomers. *Phys. Chem. Chem. Phys.* **2012**, *14*, 12905–12911.
- (18) Houmøller, J.; Wanko, M.; Stöckel, K.; Rubio, A.; Brøndsted Nielsen, S. On the Effect of a Single Solvent Molecule on the Charge-Transfer Band of a Donor-Acceptor Anion. *J. Am. Chem. Soc.* **2013**, *135*, 6818–6821.
- (19) Stöckel, K.; Milne, B. F.; Brøndsted Nielsen, S. Absorption Spectrum of the Firefly Luciferin Anion Isolated in Vacuo. *J. Phys. Chem. A* **2011**, *115*, 2155–2159.
- (20) Wyer, J. A.; Brøndsted Nielsen, S. Absorption by Isolated Ferric Heme Nitrosyl Cations In Vacuo. *Angew. Chem., Int. Ed.* **2012**, *51*, 10256–10260.
- (21) TURBOMOLE V7.0 2015, a development of University of Karlsruhe and Forschungszentrum Karlsruhe GmbH, 1989–2007; TURBOMOLE GmbH; Karlsruhe, Germany; since 2007.
- (22) Christiansen, O.; Koch, H.; Jørgensen, P. The 2nd-Order Approximate Coupled-Cluster Singles and Doubles Model CC2. *Chem. Phys. Lett.* **1995**, *243*, 409–418.
- (23) Schirmer, J. Beyond the Random-Phase Approximation - A New Approximation Scheme for the Polarization Propagator. *Phys. Rev. A: At., Mol., Opt. Phys.* **1982**, *26*, 2395–2416.
- (24) Neese, F. A Spectroscopy Oriented Configuration Interaction Procedure. *J. Chem. Phys.* **2003**, *119*, 9428–9443.
- (25) Angeli, C.; Cimiraglia, R.; Evangelisti, S.; Leininger, T.; Malrieu, J. P. Introduction of n-Electron Valence States for Multireference Perturbation Theory. *J. Chem. Phys.* **2001**, *114*, 10252–10264.
- (26) Neese, F. The ORCA program system. *WIREs Comput. Mol. Sci.* **2012**, *2*, 73–78.

On the Influence of Water on the Electronic Structure of Firefly Oxyluciferin Anions from Absorption Spectroscopy of Bare and Monohydrated Ions in Vacuo

Kristian Støchkel,[†] Christian Nygaard Hansen,[†] Jørgen Houmøller,[†] Lisbeth Munksgaard Nielsen,[†] Kelvin Anggara,[†] Mathieu Linares,[‡] Patrick Norman,[‡] Fernando Nogueira,[§] Oleg V. Maltsev,^{||} Lukas Hintermann,^{||} Steen Brøndsted Nielsen,^{*,†} Panče Naumov,^{*,†,#} and Bruce F. Milne^{*,§}

[†]Department of Physics and Astronomy, Aarhus University, Ny Munkegade, DK-8000 Aarhus C, Denmark

[‡]Division of Computational Physics, Department of Physics, Chemistry and Biology (IFM), Linköping University, SE-581 83 Linköping, Sweden

[§]Centre for Computational Physics, Department of Physics, University of Coimbra, Rua Larga, 3004-516 Coimbra, Portugal

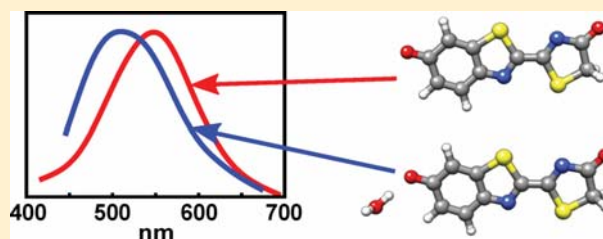
^{||}Department Chemie, Technische Universität München, Lichtenbergstrasse 4, 85748 Garching bei München, Germany

[‡]New York University Abu Dhabi, P.O. Box 129188, Abu Dhabi, United Arab Emirates

[#]Institute for Chemical Research and the Hakubi Center for Advanced Research, Kyoto University, Uji, Kyoto 611-0011, Japan

Supporting Information

ABSTRACT: A complete understanding of the physics underlying the varied colors of firefly bioluminescence remains elusive because it is difficult to disentangle different enzyme–lumophore interactions. Experiments on isolated ions are useful to establish a proper reference when there are no microenvironmental perturbations. Here, we use action spectroscopy to compare the absorption by the firefly oxyluciferin lumophore isolated in vacuo and complexed with a single water molecule. While the process relevant to bioluminescence within the luciferase cavity is light emission, the absorption data presented here provide a unique insight into how the electronic states of oxyluciferin are altered by microenvironmental perturbations. For the bare ion we observe broad absorption with a maximum at 548 ± 10 nm, and addition of a water molecule is found to blue-shift the absorption by approximately 50 nm (0.23 eV). Test calculations at various levels of theory uniformly predict a blue-shift in absorption caused by a single water molecule, but are only qualitatively in agreement with experiment highlighting limitations in what can be expected from methods commonly used in studies on oxyluciferin. Combined molecular dynamics simulations and time-dependent density functional theory calculations closely reproduce the broad experimental peaks and also indicate that the preferred binding site for the water molecule is the phenolate oxygen of the anion. Predicting the effects of microenvironmental interactions on the electronic structure of the oxyluciferin anion with high accuracy is a nontrivial task for theory, and our experimental results therefore serve as important benchmarks for future calculations.



INTRODUCTION

Bioluminescent organisms have developed mechanisms for catalytic production of cold light, which they utilize to communicate warning signals, or to attract prey or partners for mating. The core chemical event of bioluminescence (BL) is chemiexcitation, a sequence of chemical reactions, by which ground-state substrates (luciferins) in fireflies¹ and some coelenterates² are enzymatically converted by luciferase (Luc) to energy-rich intermediates. The intermediates, bearing a labile dioxetanone moiety in fireflies,³ decompose to produce the first excited state of the emitters, oxyluciferins, which relax to the ground state by emitting a photon of visible light.⁴ The one-to-one ratio of molecules of the intermediate and photons in this last step renders the BL reaction a very efficient process, with quantum yields that largely exceed those observed with non-

natural chemiluminescence reactions.⁴ The efficient BL emission can be utilized in microbiological analysis⁵ and is currently an indispensable tool in multicolor *in vivo* imaging.^{6–8} Recently, the potentials for applications involving secondary energy-transfer processes have been realized, including BRET in luciferase–protein dyads,⁹ FRET-based imaging with enzyme–quantum dot conjugates,^{10,11} and sequential energy transfer (BRET-FRET).¹²

The utility of BL as imaging tool triggered a great deal of research with the goal of developing an understanding of the underlying mechanisms. The dioxetanone intermediate in the firefly BL reaction sequence is an extremely unstable species

Received: November 20, 2012

Published: April 4, 2013

that remains synthetically inaccessible. Under controlled conditions, the lumophore (OxyLH_2) can be stabilized in the ground state for a reasonably long time, but the ground-state structure does not provide direct insight into the excited-state dynamics.^{13–15} A large number of theoretical studies have also been performed with the aim of elucidating details of the factors controlling BL (for recent reviews, see Navizet (2011),¹⁶ Hosseinkhani (2011),¹⁷ and da Silva (2011)¹⁸). These studies have increased in complexity since initial gas-phase calculations and now routinely include solvent effects, either implicitly through the use of continuum dielectric models, or by explicit inclusion of solvent molecules^{19,20} (the results of Min et al.²⁰ relate directly to the excited state of oxyluciferin) and even reduced models of the luciferase microenvironment,^{21–24} the spectrochemistry of OxyLH_2 has been experimentally established only in neat solutions.^{14,15} Most theoretical considerations of the effects of the luciferase framework are limited to the relevant amino acid residues from the crystal structures of luciferases from *Luciola cruciata*²⁵ or *Photinus pyralis*.²⁶ Recent results, however, suggest significant reorganization of the microenvironment during the lumophore deexcitation, thus questioning some earlier mechanistic inferences based on the ground-state structure of the luciferase–oxyluciferin complex, $[(\text{Luc})(\text{OxyLH}_2)]$.²⁴

Unlike fireflies (Lampyridae), which communicate the characteristic bursts of yellow-green light, and despite the fact that they utilize identical lumophore, some species of click beetles (Elateridae) emit orange light, while certain railroad worm species (Phengodidae) luminesce in the red region. These shifts in the emission color were successfully mimicked by deliberate point mutations in the Lampyridae luciferase family, and the wavelength of emission can be artificially tuned to values between 530 and 640 nm. As many as six mechanisms have been advanced to explain the molecular origin of this phenomenon, although without a consensus on its origin. The suggested mechanisms include keto–enol tautomerization, molecular twisting in excited state, effects of microenvironment (including deprotonation of the phenol functionality) and tautomerization/deprotonation of the hydroxythiazole fragment, stabilization by charge resonance, conformational changes in the active pocket, and concomitant modulation of polarity and covalency of an emitter–cation ion-pair. Experimental and theoretical contra-arguments have been subsequently advanced that discredit each of these mechanisms. Despite the numerous attempts and various experimental and theoretical approaches, due to lack of photophysical data on the excited lumophore free from environment effects, this conundrum remains unresolved.

A direct experimental spectrochemical benchmark of a single excited molecule (OxyLH_2)* in vacuo could end the long-term dispute. Indeed, the spectrochemical effects from the environment exerted by the amino acid residues or water molecules in the luciferase active pocket could be directly assessed against the spectral fingerprint of the bare ion if the latter were to be isolated in the absence of intermolecular interactions. This approach represents a simple, yet critically important starting point to understand the true reasons behind the color tuning and is the one we have taken here to shed light on this problem. Computational studies have previously highlighted the importance of water molecules in the firefly oxyluciferin system,^{23,27,28} and it was recently proposed¹⁴ that a single water molecule in the protein cavity could have a profound effect on the photophysical properties of the emitter and its

dynamics. Theoretical investigations of interactions between oxyluciferin and components of the luciferase active site in available crystal structures support the importance of water molecules in terms of their energetic effect on the emitter.^{18,27} To verify this hypothesis, using a special experimental setup, we utilize here action spectroscopy of the ionized firefly emitter OxyLH^- and its ion-complex $[(\text{OxyLH})(\text{H}_2\text{O})]^-$ to elucidate the spectrochemical consequences of a single water molecule on the isolated ion in vacuo. The 5,5-dimethyloxyluciferin anion (DMOxyL^-) was also included to provide a color-shift standard free of the potential variability of the gas phase $[(\text{OxyLH})(\text{H}_2\text{O})]^-$ complex. Finally, we note that recent theoretical work by Navizet et al.²⁹ supports the use of the isolated oxyluciferin anion as a model for the firefly lumophore because their results indicate that the light emitter is the same after chemical decomposition of firefly dioxetanone (either in vacuo or within the protein) to that obtained after photoexcitation of oxyluciferin.

In our experiment, we probe absorption and not light emission because the ion density is too low to result in enough emitted photons for detection. Indeed, the ion density is also insufficient for conventional light transmission experiments that are normally used to obtain absorption spectra, and this constitutes a significant barrier to the measurement of absorption by ions in vacuo. Instead, gas-phase ion spectroscopy relies on ionic dissociation driven by light absorption. In our setup, such action spectroscopy on macromolecular ions is realized by combining an electrospray ion source, electrostatic ion storage ring, and pulsed lasers. The setup has already provided valuable information on the light absorption by several chromophore ions, ionic GFP chromophore, protonated retinal Schiff bases, heme, porphyrin, and peptides,^{30–35} and the bioluminescence precursor, the D-(–)-luciferin anion, LH^- .³⁶ Recently, we have also modified an accelerator mass spectrometer (sector instrument) to perform gas-phase spectroscopy experiments. While delayed dissociation on time scales of hundreds of microseconds to tens of milliseconds is monitored in the ring experiment, fast dissociation occurring within a few microseconds is probed by the accelerator mass spectrometer. These complementary techniques were employed here to record the action spectra of isolated anions of OxyLH_2 and its complex with a single water molecule. These ground-state absorption data are indispensable direct benchmarks against which the theoretical models commonly used in studies of the excited-state structure of the firefly emitter can be assessed for the first time free from interferences by the complex structure of the luciferase active site. If such models can correctly predict the absorption by oxyluciferin and the influence of a microenvironment, they are likely also capable of providing useful information regarding microenvironmental effects in the emission spectra.

■ RESULTS AND DISCUSSION

Isolated OxyLH^- and DMOxyL^- Anions. First, we present the results from the storage ring experiments, where neutrals produced as a result of dissociation are monitored as a function of time. Time spectra obtained after photoexcitation in the ring of the OxyLH^- ion ($m/z = 249$) at 490, 530, and 580 nm, shown in Figure 1, confirm that the photoinduced dissociation is nearly complete after 400 μs . This time is much shorter than the storage time in the ring (~ 0.3 s). The revolution time of the ions is 64 μs . The neutrals that gave rise to the count rate were produced ~ 19 μs after the photo-

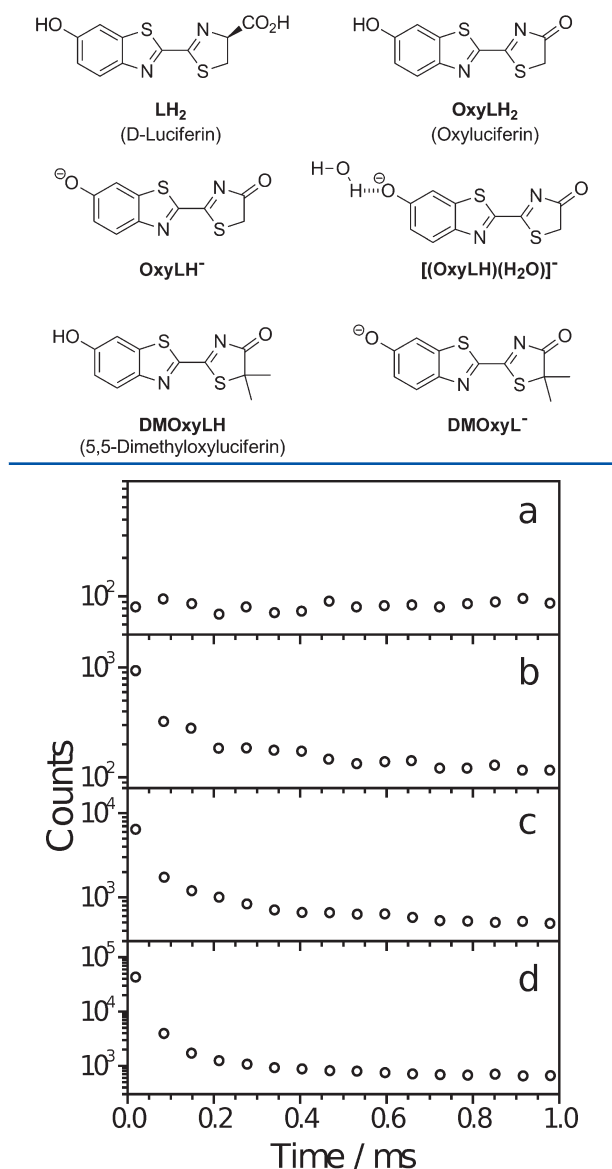


Figure 1. Time spectra of oxyluciferinate anions without laser irradiation (a), and after photoexcitation at 490 nm (b), 530 nm (c), and 580 nm (d). The spectrum in panel (a) is due to neutrals formed after collisions between the ions and the residual gas in the ring.

excitation in the first instance (first point in the time spectrum), and then after successive rotations in the ring. According to a power dependence study, the first point is due to neutrals formed from ions that have either absorbed one or two photons, whereas the following points are due to one-photon absorption. The contribution of the two-photon absorption to the first point increases with wavelength because lower excitation energies allow more ions to survive the travel from the laser-irradiated region to the opposite side of the ring where their decay is sampled. At high laser powers, the photoyield of neutrals saturates. To avoid such saturation effects and to minimize two-photon absorption, the power was attenuated during wavelength scans, and the first point was not included in the analysis. The subsequent five points were summed excluding the background of neutrals formed as a result of

collisions with residual gas in the ring (see Figure 1a). The yield of photoneutrals was then divided by the background count to correct for variations in the ion beam intensity and the number of photons in the laser pulse. This action signal is taken to represent the relative absorption cross section. Figure 2a shows the cross sections versus wavelength. The spectrum displays a broad band with λ_{max} between 535 and 555 nm with fwhm (full width at half maximum) of 95 nm.

Next, we consider the results from the single-pass experiments with the accelerator mass spectrometer. Here, ionic fragments formed up to 3 μs after photoexcitation were sampled, in contrast to the storage ring experiment where delayed dissociation was monitored on a much longer time scale. Photoexcitation leads to one dominant fragment anion at $m/z = 175$ and a minor one at $m/z = 206$ that correspond to loss of $\text{C}_2\text{H}_2\text{SO}$ (mass 74) and $\text{C}_2\text{H}_3\text{O}$ (mass 43), respectively. These are both formed as a result of two-photon absorption, in agreement with the time-spectra discussed above (the one-photon absorption is excluded in this experiment based on the narrow temporal window for dissociation). We assign the $m/z = 175$ fragment to deprotonated 2-cyano-6-hydroxybenzothiazole. Interestingly, this molecule is a breakdown product in the reactions between the oxyluciferin and water within the enzyme cavity required for repetitive flashing of the firefly emission.³⁷

The yields of each of the two fragment ions were measured as a function of the wavelength to give action spectra after correcting for ion beam fluctuations and number of photons in the laser pulses. The action spectrum based on the $m/z = 175$ fragment ion (Figure 2b) is similar to that obtained from the ring experiment: It displays a broad band with λ_{max} between 540 and 560 nm (Figure 2a). The spectrum based on the $m/z = 206$ ion (not shown) is similar but of worse quality due to much lower ion yields. Taken together, the results show that the bare oxyluciferinate anion **OxyLH⁻** absorbs maximally at 548 ± 10 nm, and that the absorption spectrum is broad (fwhm of 95 nm). We note that the absorption band of **OxyLH⁻** is only slightly red-shifted as compared to that of **LH⁻** (532 nm) reported earlier³⁶ despite the greater electron delocalization expected in the former. The excess electron density in **OxyLH⁻** can be located at either oxygen (two limiting resonance structures), while the carboxylate group in **LH⁻** is not conjugated with the ring π -electrons.

According to our calculations, the dominant tautomer of the oxyluciferinate ions isolated in our ion beam at room temperature is the keto form. As discussed later, the agreement between the predicted and the measured absorption bands is in strong support of this assignment. To ascertain the tautomer identity, the measurements were repeated with the 5,5-dimethylated oxyluciferinate anion (**DMOxyL⁻**, $m/z = 277$) where the molecule is locked as the keto tautomer by substitution. The action spectrum obtained based on the $m/z = 175$ fragment ion has a $\lambda_{\text{max}} = 540\text{--}570$ nm (Figure 2d), while the ring experiment provides $\lambda_{\text{max}} = 560\text{--}580$ nm (Figure 2c). Our estimate of the band maximum is 565 ± 10 nm. The red-shift of about 17 nm relative to **OxyLH⁻** is in accordance with the substitution effects observed in solution.¹⁴ The calculated spectra described below confirm that this spectral shift is due to substitution effects.

[(OxyLH)(H₂O)]⁻ Complex Anion. The impact of a single water molecule on the electronic structure of oxyluciferinate anions was measured with the accelerator mass spectrometer. While the photoinduced dissociation mass spectrum of bare **OxyLH⁻** was rather simple with two important fragment ions,

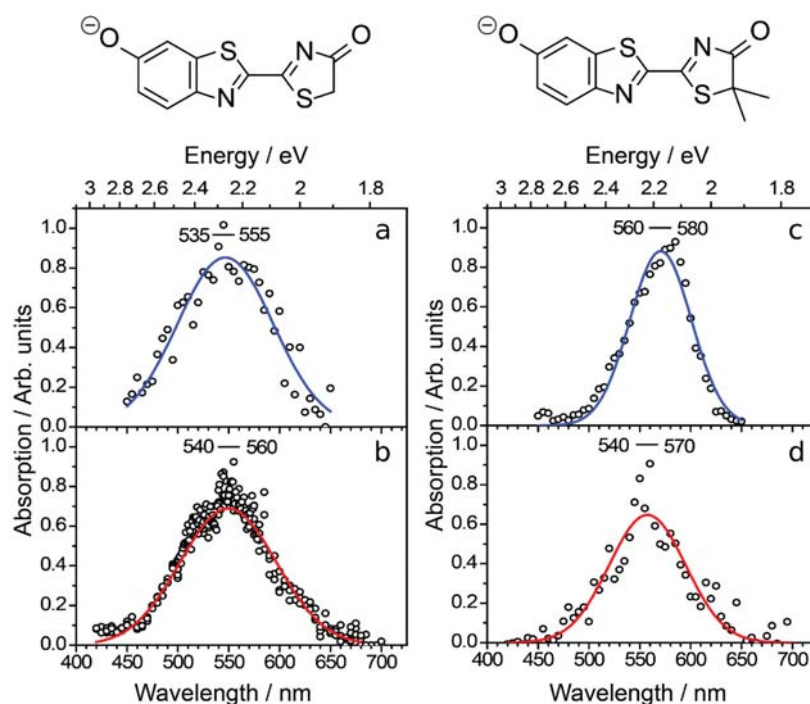


Figure 2. Action spectra of oxyLuciferinate and 5,5-dimethyloxyluciferinate anions obtained using two different instruments. **OxyLH⁻**: (a) ELISA, sampling of neutral fragments; (b) accelerator mass spectrometer, sampling of $m/z = 175$ fragment ions. **DMOxyL⁻**: (c) ELISA, sampling of neutral fragments; (d) accelerator mass spectrometer, sampling of $m/z = 175$ fragment ions. In the ELISA experiment, we detect neutrals traveling with high kinetic energies as they deposit energy in the detector, but we have no mass information. The curves are Gaussian fits to the data.

many more dissociation channels are available for the $[(\text{OxyLH})(\text{H}_2\text{O})]^-$ complex, including water loss, dissociation of the bridge between the two heterocycles, and decomposition of one of the rings. The water molecule remained bound to several fragment ions. The dominant fragment ion had $m/z = 150$ and is ascribed to separation of the two heterocyclic rings. The action spectra of each of the fragment ions are shown in Figure 3 (insufficient background counts from collision-induced dissociations prevented us from applying spectral corrections for ion beam fluctuations). The count rates of the photo-induced fragment ions were typically 1 s^{-1} , which placed a practical burden on this experiment. Nevertheless, the spectra are quite similar with $\lambda_{\text{max}} = 480\text{--}530 \text{ nm}$. The minor differences may be related to the different structures of the oxyLuciferinate–water complexes in the ion beam that could result in different dissociation pathways. Regardless of these small differences, the spectra are conclusive that a water molecule blue-shifts the absorption of the ion.

Theoretical Results. The optimized ground-state geometries used in all calculations are shown in Figure 4. Details of the optimization strategies and relative energies for different conformational and configurational properties are dealt with in the Methods section. These geometries were used for the evaluation of several common methods for the calculation of vertical electronic excitation energies.

The results of single-point EOM-CCSD and TDDFT electronic absorption calculations are given in Table 1. With the EOM-CCSD/Def2-TZVPPD method, a value of 481 nm was obtained for the **OxyLH⁻** excitation wavelength, as compared to the experimental wavelength of $548 \pm 10 \text{ nm}$. At the EOM-CCSD level with the smaller Def2-SVPD basis set,

these values were red-shifted by only $\sim 0.01 \text{ eV}$, indicating that the smaller basis set was capable of producing well-converged results.

The reduced excitation level (REL) diagnostic gives a measure of the character of a given excitation within the EOM-CC framework. Values close to unity indicate predominantly single-excitation character, while higher values indicate multiexcitation character. In all calculations performed in the present work, the excitations had REL values of 1.1 ± 0.02 . Therefore, the excitations observed in the oxyLuciferin systems possess predominantly single-excitation character, and all of the relevant physics should be described accurately even with the truncation of the coupled-cluster expansion at second order.³⁸ Greater multielectron character, on the other hand, would have required inclusion of triples excitations, e.g., using EOM-CCSD(T).

Excellent agreement with the high-level EOM-CCSD result came from the two hybrid functionals, B3LYP and CAM-B3LYP, which also showed minimal changes on going from the Def2-SVPD basis set to the much larger Def2-TZVPPD set. However, the pure DFT functionals SVWN and BLYP were found to provide excitation energies that were lower than that obtained with EOM-CCSD and that in fact were in very good agreement with experiment, giving errors for both functionals relative to experiment of less than 10 nm. The fact that the EOM-CCSD and hybrid TDDFT methods gave values that were significantly blue-shifted relative to the experimental **OxyLH⁻** value suggested that the approximations used in the calculations were neglecting some effects (e.g., vibronic effects) that were important in the **OxyLH⁻** system. The apparently superior performance of the pure DFT functionals was most

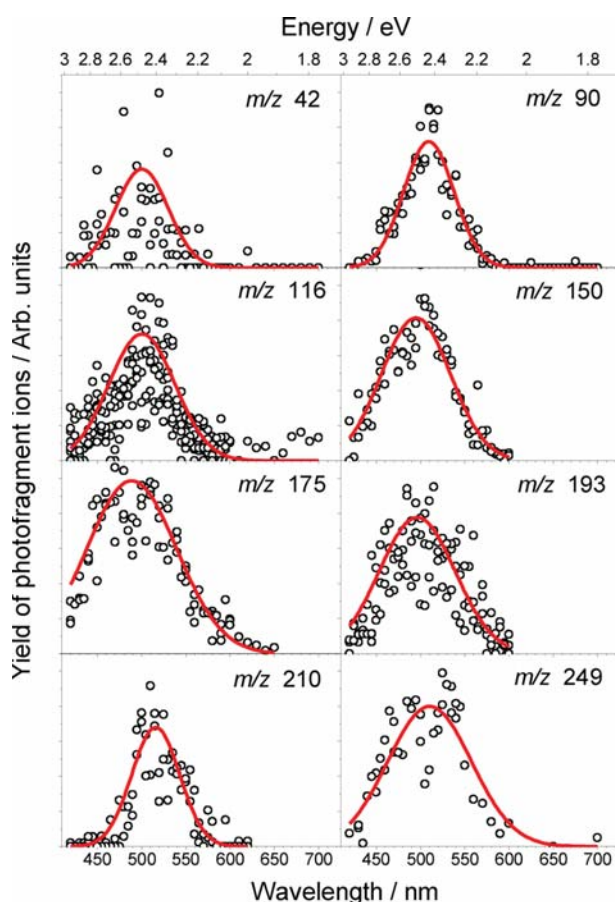


Figure 3. Action spectra of oxyluciferin–water complexes obtained using the accelerator mass spectrometer. The fragment ion masses are indicated on each panel. The red curves are Gaussian fits to the data.

likely an example of fortuitous cancellation of errors in these formally less sophisticated methods.

In relation to theoretical predictions of color-tuning effects in BL, a more important set of results were the calculated shifts relative to OxyLH^- for the $[(\text{OxyLH})(\text{H}_2\text{O})]^-$ and DMOxyL^- systems (Table 1). The EOM-CCSD/Def2-TZVPPD method yielded a blue-shift of 10 nm for the $[(\text{OxyLH})(\text{H}_2\text{O})]^-$ complex and a red-shift of 3 nm for the DMOxyL^- anion, which, although providing qualitatively correct predictions, were approximately one-fifth of the size of the shifts observed in the experimental spectra in both cases. Despite the large split between the performance of the pure and hybrid functionals seen in the TDDFT results for OxyLH^- , there was very little difference in the predicted spectral shifts obtained from the four functionals. All of the TDDFT-predicted shifts for DMOxyL^- were ± 2 nm relative to EOM-CCSD, while the $[(\text{OxyLH})(\text{H}_2\text{O})]^-$ EOM-CCSD shift was underestimated by all of the functionals except CAM-B3LYP, with BLYP performing worst. That all of the methods used here were able to correctly predict the sign of the spectral shift in these systems but failed to deliver the correct magnitude is most likely an indication that the sources of error mentioned above for OxyLH^- may become even more critical in these systems due to the complexed water molecule in $[(\text{OxyLH})(\text{H}_2\text{O})]^-$ and the addition of two methyl groups in DMOxyL^- .

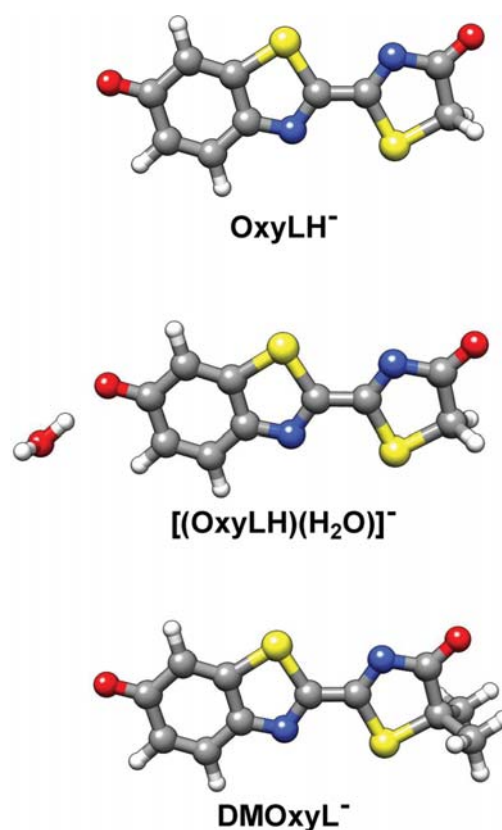


Figure 4. B3LYP/Def2-SVPD optimized structures of the three systems studied.

Table 1. Calculated Absorption Energies for OxyLH^- , $[(\text{OxyLH})(\text{H}_2\text{O})]^-$, and DMOxyL^- ^a

	$\lambda_{\text{abs}} (S_1 \leftarrow S_0)/\text{nm}$	
	Def2-SVPD	Def2-TZVPPD
OxyLH⁻		
EOM-CCSD	478	477
SVWN	545	546
BLYP	540	542
B3LYP	490	491
CAM-B3LYP	464	466
[(OxyLH)(H₂O)]⁻		
EOM-CCSD	470 (−8)	467 (−10)
SVWN	541 (−4)	542 (−4)
BLYP	538 (−2)	539 (−3)
B3LYP	485 (−5)	487 (−4)
CAM-B3LYP	455 (−9)	458 (−8)
DMOxyL⁻		
EOM-CCSD	481 (+3)	480 (+3)
SVWN	549 (+4)	550 (+4)
BLYP	544 (+4)	546 (+4)
B3LYP	493 (+3)	495 (+4)
CAM-B3LYP	466 (+2)	469 (+3)

^aWavelength shifts relative to isolated OxyLH^- given in parentheses.

It is of interest to note that Min et al. performed calculations to investigate the effect of explicit waters on the electronic structure of oxyluciferin anion at the TD-B3LYP/6-31+G(d,p)//B3LYP/6-31+G(d,p) level where they found that one water molecule hydrogen-bonded to the phenolate oxygen

(similar to $[(\text{OxyLH})(\text{H}_2\text{O})]^-$ in the present work (Figure 4)) caused a blue-shift of 2 nm in the predicted absorption.²⁰ The small difference between their blue-shift and our value of 5 nm can be rationalized by the slightly different basis sets used in the geometry optimizations and subsequent excitation calculations. Min et al. included diffuse functions only on non-hydrogens during the geometry optimizations and in the excitation calculations (6-31+G(d,p)), whereas our basis set contained diffuse functions on all atoms (Def2-SVPD).

Min et al. found that when the water molecule was located at the opposite (keto) end of the anion this was found to produce a 4 nm red-shift in the absorption. Thus, longitudinal polarization of the anion in opposite directions was seen to be capable of producing shifts either to higher or to lower energy in the spectrum. This polarization effect was systematically investigated by the incremental application of electric fields during real-space/time TDDFT calculations on the oxyluciferin anion by Cai et al., who also found that the absorption peak could be shifted either to higher or lower energies by the polarizing field.³⁹ The redistribution of charge density in the anion due to the electron-withdrawing inductive ($-I$) effect associated with the methyl groups attached to the thiazolone ring in DMOxyL^- might be expected to be qualitatively similar to the effect of a water molecule hydrogen-bonded to the keto oxygen, which is in keeping with both our experimental and our theoretical data.

A further feature of the experimental spectra that was of interest in terms of the performance of simulation techniques was the significant peak-broadening. In an attempt to extend the single-point static calculations in a way that might shed more light on the origins of this broadening, molecular dynamics (MD) simulations were performed for the three oxyluciferin systems. The resulting composite spectra obtained from TDDFT calculations on the sampled MD trajectories are shown in Figure 5. Both the LDA (SVWN) and the CAM-B3LYP functionals were used, representing the simplest and most complex functionals employed in this study. Although the single-point TD-LDA result for OxyLH^- was closest to experiment, this was probably due to cancellation of errors at the equilibrium geometry, which might not be the case for the distorted geometries obtained from the MD run. TD-CAM-B3LYP performed well relative to the EOM-CCSD data, and its better treatment of charge-transfer type excitations might be important in the distorted geometries.

The spectral profiles obtained from the MD-averaged TD-LDA calculations were found to fit well the degree of band broadening observed experimentally. Differential changes in the band maxima for the three systems enhanced the calculated color shift by 2 nm for both $[(\text{OxyLH})(\text{H}_2\text{O})]^-$ and DMOxyL^- leading to shifts of -6 and $+6$ nm, respectively, relative to OxyLH^- .

The composite peaks obtained with the CAM-B3LYP functional were slightly less broad than those obtained with LDA. This may be due to a greater sensitivity to geometrical distortion with the LDA functional leading to a greater spread of the excitation energies. The individual excitations are shown in Figure 5 as crosses, and tighter clustering of those obtained with CAM-B3LYP is evident. The peak maxima in the CAM-B3LYP case yielded a blue-shift of 7 nm for $[(\text{OxyLH})(\text{H}_2\text{O})]^-$ relative to OxyLH^- , but only a 1 nm red-shift for the DMOxyL^- anion. These shifts relative to one another are in better proportion for CAM-B3LYP (as compared to the experimental shifts) than with LDA.

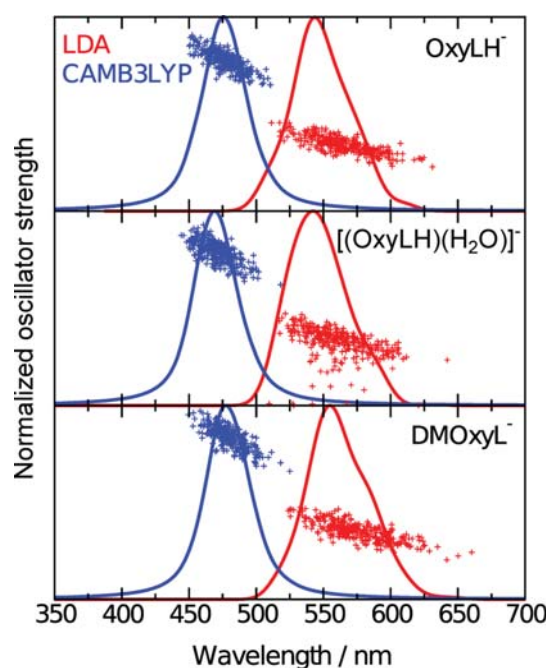


Figure 5. Composite TD-DFT spectra obtained from 300 ps molecular dynamics simulations. Results obtained with the LDA (SVWN) functional are shown in red, and those obtained with the CAM-B3LYP functional are shown in blue. Spectral profiles were obtained from sums of Lorentzian functions fit to individual excitations (+), which were then normalized to put them on the same scale as the single excitations.

It is interesting to note that during the MD simulations the maximum deviation from planarity of the oxyluciferins was of the order of $10\text{--}20^\circ$ in agreement with the DFT calculations and confirming the quality of the force field parametrization (a plot of the energy of rotation about the inter-ring carbon-carbon bond in OxyLH^- is shown in Figure S2). These data provided further evidence that only the low energy trans-form should be populated at room temperature, in agreement with the Boltzmann factor ratio given below (Methods section). During the simulation started with the water molecule located at the phenolate end of oxyluciferin, the water was seen to migrate to the benzothiazole nitrogen in $\sim 10\%$ of the snapshots where the absorption was red-shifted to ~ 590 nm. However, the small percentage of snapshots where this occurred combined with the fact that the oscillator strengths for the excitation were lower than the average during the simulation meant that this had a small effect on the overall spectrum. Repeat simulations with the water molecule located initially at the midpoint of the oxyluciferin or bound to the keto oxygen were run, but in these cases the water rapidly migrated to the phenolate group and remained there as was seen in the first simulation.

Relation of Gas-Phase Data to Firefly Bioluminescence. All Lampyridae species naturally emit green-yellow light, although at slightly different wavelengths. A consistent property of the spatial disposition of the amino acids in the active pocket of their luciferases is a “barrel” of low polarity, which wraps the substrate/product, with the two termini being exposed to polar environments. This provides a central microenvironment with properties more comparable to the gas phase than to bulk (aqueous) solvent. *Photuris pennsylvanica*

fireflies emit green light with a maximum at $\lambda_{\text{max}}^{\text{em}} = 538$ nm, while the North American fireflies *Photinus pyralis* produce yellow-green light at $\lambda_{\text{max}}^{\text{em}} = 562$ nm. Although they share a significant portion of the **Luc** amino acid sequence with fireflies, the railroad worms *Phrixotrix hirtus* produce red light with $\lambda_{\text{max}}^{\text{em}} = 623$ nm. For the bare ion, we observe broad absorption with a maximum at $\lambda_{\text{max}}^{\text{abs}} = 548 \pm 10$ nm. The typical Stokes shifts of oxyluciferin in nonaqueous diluted solutions, as a very crude estimate for the respective gas-phase values, range between 69 and 96 nm, with the values in solvents of low polarity being at the higher end of this range.¹⁴ As the absorption sets a lower limit for the wavelength of emitted light, the estimated emission of the bare ion at 617–644 nm (orange or red) necessitates inclusion of microenvironment effects to account for the natural emission at lower wavelengths (green). Indeed, the action spectra recorded here evidenced that addition of a single water molecule blue-shifts the absorption by about 50 nm. A single water molecule could blue-shift the Stokes-shifted emission of the ion in vacuo to about 567–594 nm (i.e., green to yellow). The results of the present study suggest that such a dynamic water molecule could make a significant contribution to shifting the emission color of the oxyluciferin ion between green and red. Further support for this suggestion can be found in the results of molecular dynamics simulations of oxyluciferin in which the importance of water molecules in modulating electronic structure in the ground and excited states in the enzyme active site was highlighted.^{28,29}

The crystal structure of the complex of *Luciola cruciata* luciferase with oxyluciferin does not contain a water molecule bound to the phenoxyl group of the lumophore.²⁵ Several waters are located nearby, but these are presumably strongly constrained in the electrostatic environment of the pair of arginine residues at the benzothiazole end of the active site. However, the benzothiazole hydroxyl group in structures of both wild-type and mutant luciferases in a complex with a molecule that represents a model for the unstable intermediate in the bioluminescence reaction is bound to a water molecule at 2.7 Å from the oxygen atom.²⁵ Combined with the molecular dynamics results mentioned above^{28,29} and the results of the present work, this observation appears to support our proposal that a dynamic water molecule could interact significantly with the benzothiazole oxygen of oxyluciferin and may play an important role in the color tuning of the firefly emission.

Another issue to consider is that the most favorable location of the water may be different in the excited state than in the ground state of the oxyluciferin anion. Because, in the biological setting, the oxyluciferin anion is formed in its excited state, it is possible that the water is located in a way that it stabilizes the excited state more than the ground state. As a result, the water molecule would then cause a red-shifted emission. In accordance with this, Ai-min and co-workers²⁰ predicted a 3 nm blue-shift in the emission upon binding of a single water molecule to the benzothiazole oxygen, while the emission red-shifted by 8 nm for water binding to the thiazole oxygen. In other work,²⁸ Song and Rhee calculated the average emission energies (RI-CIS(D) without EOM-CCSD corrections) for solvated oxyluciferin ion configurations that had one more water on the thiazole oxygen than on the benzothiazole oxygen (1.419 eV), the same number on both oxygens (1.429 eV), and one more on the benzothiazole oxygen than on the thiazole oxygen (1.449 eV). Even though the trends from these two works are in accordance with our reasoning, the shifts are small. Song and Rhee instead ascribed color modulation to nearby

charges, for example, the positively charged ammonium of a protonated lysine residue or the negatively charged AMP.

An analysis of energetic interactions within the luciferase active site by Milne et al. using the fragment molecular orbital method supports the importance of both the charged species and the active site water molecules in terms of their (de)stabilizing effects on the oxyluciferin anion in the ground state.²⁷ However, because the theoretical models commonly employed in this field of research in general appear to underestimate the blue-shift in absorption by a single water molecule, the influence on emission may also be underestimated. More work is clearly needed to fully address the role of the nearby environment in fine-tuning the details of the electronic transition between the ground and excited states of this system.

CONCLUSION

The action spectra reported here provide the first experimental evidence on the absorption by the singly charged oxyluciferin anion and its complex with water isolated in vacuo and demonstrated a strong perturbation of the electronic structure by a single water molecule. A range of calculations using methods of varying theoretical complexity uniformly support the experimental data and were found to provide reliable predictions of color-shifts in the $[(\text{OxyLH})(\text{H}_2\text{O})]^-$ and DMOxyL^- systems, although the magnitude of the shifts was underestimated. We cannot from our absorption experiments tell the exact role of a water molecule on the emission but only speculate that its influence is large enough for color modulation because it significantly perturbs the difference in energy levels between ground and excited states when it binds to the ground-state geometry. Obtaining quantitative agreement with experiment from calculations on these ions is nontrivial, and more work is needed to improve the theoretical description. Importantly, for a theoretical model to be used to shed light on microenvironmental effects in firefly luminescence, it is required to provide the experimentally measured energy difference between the ground and excited states of the bare oxyluciferin anion and the perturbation caused by a water molecule bound to the ground-state geometry.

METHODS

Experimental Details. The setups used for gas-phase spectroscopy have been described in detail elsewhere,^{30–36,40,41} and only a brief description is given below. Oxyluciferin and 5,5-dimethyloxyluciferin, prepared as described before,¹⁴ were dissolved in methanol and electrosprayed. Ions were accumulated in a multipole ion trap in which they experienced collisions with helium buffer gas kept at room temperature.

In the ELISA experiments, an ion bunch was accelerated to kinetic energy of 22 keV, and the ions of interest were selected with a bending magnet. These were injected into the ring that is based on purely electrostatic deflectors and focusing elements. The ions circulated until they changed their mass-to-charge ratio as a result of either collisions with residual gas in the ring (pressure of about 10^{-10} mbar) or photoexcitation. Neutrals produced on the injection side of the ring were not influenced by the electric fields and hit a microchannel plate detector located at the end of the straight section. The rate of neutrals hitting the detector was a measure of the number of ions circulating in the ring. OxyLH^- ions were photoexcited after about 45 ms. The third harmonic (355 nm) from a Nd:YAG laser was used to pump an optical parametric oscillator (OPO) (EKSPLA laser system). Neutral density filters were used to attenuate the laser power. The repetition rate of the experiment was 10 Hz.

For experiments using the accelerator mass spectrometer, an ion bunch was accelerated to energy of 50 keV, and appropriate ions were again selected with a bending magnet. These were photoexcited by light from a laser system similar to that used with ELISA in a merged beam configuration. An electrostatic analyzer allowed particular fragment ions to reach a channeltron detector where they were counted. The yield of fragment ions as a function of excitation wavelength was monitored up to 3 μ s after photoexcitation. The experiment was performed at a repetition rate of 40 Hz. The laser was run at 20 Hz; thus only every second ion bunch was irradiated to obtain the real laser-induced signal. Also, laser-off spectra were used to correct for ion beam fluctuations from the yield of fragment ions produced as a result of collisions with the residual gas. Hydrated ions were generated by introducing water vapor in an octopole transmission guide located before the multipole trap. The kinetic energies of the ions in the ion source were retained as low as possible to prevent collision-induced water loss from the fragile molecular complexes. The ion beam signal of the complexes was insufficient for meaningful corrections for ion beam fluctuations; instead, the experiment was repeated multiple times to compensate for such variations.

Theoretical Methods. All electronic structure calculations were performed using GAMESS-US (1 October 2010 (R1) release).⁴²

Geometries were optimized at the B3LYP⁴³ level with the diffuse-augmented polarized double- ζ basis set Def2-SVPD.⁴⁴ The isolated anion was optimized in both the cis and the trans conformations because both might be populated in the experiment. An energy difference of 23.6 kJ mol⁻¹ was found, indicating a Boltzmann factor ratio of 1: 5.14 \times 10⁻⁵ in favor of the trans-form at 300 K, and so the cis-form was neglected thereafter. That the trans-enol form of OxyLH⁻ might be important was also considered, but this geometry was found to lie 47.4 kJ mol⁻¹ higher than the trans-keto form (Boltzmann ratio of 1:5.97 \times 10⁻⁹ in favor of the keto-form). *trans*-DMOxyL⁻ was optimized at the same level.

Geometry optimizations for the [(OxyLH)(H₂O)]⁻ complex were performed with water hydrogen-bonded to either the benzothiazole or the thiazolone end of the trans-keto anion. The thiazolone-bound configuration lay 10.5 kJ mol⁻¹ higher in energy with a corresponding Boltzmann factor ratio of 1:1.48 \times 10⁻² favoring the benzothiazole complex at 300 K and indicating an insignificant contribution from the thiazolone configuration.

To obtain a computational benchmark for the electronic excitations in these systems, calculations were performed with equation-of-motion coupled cluster theory including single and double excitations (EOM-CCSD).^{38,45-48} The inclusion of triples excitations for molecules of this size was too demanding, and therefore the calculations were truncated at the EOM-CCSD level. However, the results obtained showed that the excitations were predominantly single-electron in character meaning that the physics required to accurately describe these excitations was already contained in the EOM-CCSD method.³⁸ Both the Def2-SVPD and the large Def2-TZVPPD basis sets were used. To minimize the computational effort involved in these calculations in terms of memory- and disk-usage, the reduced virtual space method⁴⁹ was employed. A cutoff of 50 eV above the HOMO level was found to give results that changed by less than 2 nm when the cutoff was increased to 60 eV and by less than 1 nm when increased to 70 eV. These changes were not consistently positive or negative, due to the nonvariational nature of the calculations, and so negligible net change was seen beyond the 50 eV cutoff.

TDDFT⁵⁰ calculations used a series of four functional forms of increasing formal complexity representing different rungs on the Jacob's ladder of (TD)DFT approximations.⁵¹⁻⁵³ The SVWN (local density approximation) and BLYP (generalized gradient approximation) functionals were selected to investigate the performance of pure DFT in this system.⁵⁴⁻⁵⁶ The commonly used hybrid functional B3LYP (20% Hartree-Fock (HF) exchange) was also included. For excitations with significant nonlocal character, TDDFT methods can produce large errors due to an incomplete treatment of long-range interactions.^{57,58} The range-separated hybrid CAM-B3LYP functional, designed to provide a more balanced description of excitation

processes with, for example, charge-transfer character,⁵⁹ was therefore also included. TDDFT calculations were performed with the Def2-SVPD basis set and repeated with the much more flexible Def2-TZVPPD basis.⁴⁴ Minor changes (\sim 0.01 eV) indicated that the Def2-SVPD results were well converged.

Molecular dynamics simulations were performed with Tinker v6.1.⁶⁰ OxyLH⁻ parameters²⁴ were converted to fit the Tinker CHARMM22^{61,62} functional form. Torsional parameters relating to the bond bridging the two heterocyclic substructures were adjusted for a better fit of the torsion profile calculated with DFT (see the Supporting Information). Additional parameters required for DMOxyL⁻ and [(OxyLH)(H₂O)]⁻ were taken from the CHARMM22 set. Atomic partial charges were calculated using the CHELPG approach (charges from electrostatic potentials using a grid-based method)⁶³ at the B3LYP/Def2-SVPD level with Orca v2.9.0.⁶⁴ 300 ps in vacuo simulations were run at 300 K in the NVE ensemble. Sampling at 1 ps intervals gave 300 input structures for subsequent TDDFT/Def2-SVPD calculations using the LDA (SVWN) and CAM-B3LYP functionals. The dominant first excitations and oscillator strengths from each calculation were collected, and a Lorentzian broadening function with a half-width of 10 nm was applied using the Gabedit v2.4.0 package.⁶⁵ The resulting composite peaks were then renormalized so as to fit them onto the same scale as the individual excitations.

■ ASSOCIATED CONTENT

● Supporting Information

Force field parameters used in molecular dynamics simulations of the oxyluciferinate and 5,5-dimethyloxyluciferinate anions. B3LYP/Def2-SVPD optimized geometries (and total energies) used in EOM-CCSD and TDDFT single-point calculations. This material is available free of charge via the Internet at <http://pubs.acs.org>.

■ AUTHOR INFORMATION

Corresponding Author

sbn@phys.au.dk; pance.naumov@nyu.edu; bruce@teor.fis.uc.pt

Notes

The authors declare no competing financial interest.

■ ACKNOWLEDGMENTS

S.B.N. gratefully acknowledges support from Lundbeckfonden. P.N. thanks the Human Frontier Science Project (grant RGY0081/2011) and the Kyoto University's Hakubi Project for funding. B.F.M. thanks the Portuguese Foundation for Science and Technology for funding (PTDC/FIS/103587/2008) and the Laboratory for Advanced Computation of the University of Coimbra for the provision of computer resources, technical support, and assistance. P.N. acknowledges financial support from the Swedish Research Council (Grant No. 621-2010-5014). M.L. thanks SERC (Swedish e-Science Research Center) for funding and SNIC for providing computer resources.

■ REFERENCES

- (1) Shimomura, O. *Bioluminescence: Chemical Principles and Methods*; World Scientific: NJ, 2006.
- (2) Cormier, M. J.; Hori, K.; Anderson, J. M. *Biochim. Biophys. Acta* **1974**, *346*, 137-164.
- (3) Liu, F.; Liu, Y.; De Vico, L.; Lindh, R. *J. Am. Chem. Soc.* **2009**, *131*, 6181-6188.
- (4) Ando, Y.; Niwa, K.; Yamada, N.; Enomoto, T.; Irie, T.; Kubota, H.; Ohmiya, Y.; Akiyama, H. *Nat. Photonics* **2008**, *2*, 44-47.
- (5) Kricka, L. J. *Biolumin. Chemilumin., Part C: Methods Enzymol.* **2000**, *305*, 333-345.
- (6) Greer, L. F.; Szalay, A. A. *Luminescence* **2002**, *17*, 43-74.

- (7) Mezzanotte, L.; Que, I.; Kaijzel, E.; Branchini, B.; Roda, A.; Löwik, C. *PLoS One* **2011**, *6*, e19277.
- (8) Foucault, M.-L.; Thomas, L.; Goussard, S.; Branchini, B. R.; Grillot-Courvalin, C. *Appl. Environ. Microbiol.* **2010**, *76*, 264–274.
- (9) Takakura, H.; Sasakura, K.; Ueno, T.; Urano, Y.; Terai, T.; Hanaoka, K.; Tsuboi, T.; Nagano, T. *Chem.-Asian J.* **2010**, *5*, 2053–2061.
- (10) So, M.-K.; Xu, C.; Loening, A. M.; Gambhir, S. S.; Rao, J. *Nat. Biotechnol.* **2006**, *24*, 339–343.
- (11) Ma, N.; Marshall, A. F.; Rao, J. *J. Am. Chem. Soc.* **2010**, *132*, 6884–6885.
- (12) Branchini, B. R.; Rosenberg, J. C.; Ablamsky, D. M.; Taylor, K. P.; Southworth, T. L.; Linder, S. J. *Anal. Biochem.* **2011**, *414*, 239–245.
- (13) Solntsev, K. M.; Laptinok, S. P.; Naumov, P. *J. Am. Chem. Soc.* **2012**, *134*, 16452–16455.
- (14) Naumov, P.; Ozawa, Y.; Ohkubo, K.; Fukuzumi, S. *J. Am. Chem. Soc.* **2009**, *131*, 11590–11605.
- (15) Naumov, P.; Kochunnonny, M. *J. Am. Chem. Soc.* **2010**, *132*, 11566–11579.
- (16) Navizet, I.; Liu, Y.-J.; Ferré, N.; Roca-Sanjuán, D.; Lindh, R. *ChemPhysChem* **2011**, *12*, 3064–3076.
- (17) Hosseinkhani, S. *Cell. Mol. Life Sci.* **2011**, *68*, 1167–1182.
- (18) Pinto da Silva, L.; Esteves da Silva, J. C. G. *ChemPhysChem* **2011**, *12*, 3002–3008.
- (19) Ren, A.; Goddard, J. D. *J. Photochem. Photobiol., B* **2005**, *81*, 163–170.
- (20) Min, C.; Zou, L.; Sun, Y.; Guo, J.; Ren, A.-M.; Goddard, J. D. *Chin. J. Chem.* **2011**, *29*, 2301–2307.
- (21) Orlova, G.; Goddard, J. D.; Brovko, L. Y. *J. Am. Chem. Soc.* **2003**, *125*, 6962–6971.
- (22) Nakatani, N.; Hasegawa, J. Y.; Nakatsuji, H. *J. Am. Chem. Soc.* **2007**, *129*, 8756–8765.
- (23) Navizet, I.; Liu, Y.-J.; Ferré, N.; Xiao, H.-Y.; Fang, W.-H.; Lindh, R. *J. Am. Chem. Soc.* **2010**, *132*, 706–712.
- (24) Song, C.-I.; Rhee, Y. M. *Int. J. Quantum Chem.* **2011**, *111*, 4091–4105.
- (25) Nakatsu, T.; Ichiyama, S.; Hiratake, J.; Saldanha, A.; Kobashi, N.; Sakata, K.; Kato, H. *Nature* **2006**, *440*, 372–376.
- (26) Conti, E.; Franks, N.; Brick, P. *Structure* **1996**, *4*, 287–298.
- (27) Milne, B. F.; Marques, M. A. L.; Nogueira, F. *Phys. Chem. Chem. Phys.* **2010**, *12*, 14285.
- (28) Song, C.-I.; Rhee, Y. M. *J. Am. Chem. Soc.* **2011**, *133*, 12040–12049.
- (29) Navizet, I.; Roca-Sanjuán, D.; Yue, L.; Liu, Y.-J.; Ferré, N.; Lindh, R. *Photochem. Photobiol.* **2012**, *89*, 319–3125.
- (30) Brøndsted Nielsen, S.; Lapiere, A.; Andersen, J. U.; Pedersen, U. V.; Tomita, S.; Andersen, L. H. *Phys. Rev. Lett.* **2001**, *87*, 228102.
- (31) Rajput, J.; Rahbek, D.; Andersen, L.; Hirshfeld, A.; Sheves, M.; Altoè, P.; Orlandi, G.; Garavelli, M. *Angew. Chem., Int. Ed.* **2010**, *49*, 1790–1793.
- (32) Lykkegaard, M. K.; Ehlerding, A.; Hvelplund, P.; Kadhane, U.; Kirketerp, M.-B. S.; Brøndsted Nielsen, S.; Panja, S.; Wyer, J. A.; Zettergren, H. *J. Am. Chem. Soc.* **2008**, *130*, 11856–11857.
- (33) Wyer, J. A.; Brøndsted Nielsen, S. *J. Chem. Phys.* **2010**, *133*, 084306.
- (34) Wyer, J. A.; Ehlerding, A.; Zettergren, H.; Kirketerp, M.-B. S.; Brøndsted Nielsen, S. *J. Phys. Chem. A* **2009**, *113*, 9277–9285.
- (35) Wyer, J. A.; Jensen, C. S.; Brøndsted Nielsen, S. *Int. J. Mass Spectrom.* **2011**, *308*, 126–132.
- (36) Stöckel, K.; Milne, B. F.; Brøndsted Nielsen, S. *J. Phys. Chem. A* **2011**, *115*, 2155–2159.
- (37) Gomi, K.; Kajiyama, N. *J. Biol. Chem.* **2001**, *276*, 36508–36513.
- (38) Bartlett, R. J. *Wiley Interdiscip. Rev. : Comput. Mol. Sci.* **2012**, *2*, 126–138.
- (39) Cai, D.; Marques, M. A. L.; Nogueira, F. *J. Phys. Chem. B* **2011**, *115*, 329–332.
- (40) Stöckel, K.; Kadhane, U.; Andersen, J. U.; Holm, A. I. S.; Hvelplund, P.; Kirketerp, M.-B. S.; Larsen, M. K.; Lykkegaard, M. K.; Nielsen, S. B.; Panja, S.; Zettergren, H. *Rev. Sci. Instrum.* **2008**, *79*, 023107–023107-6.
- (41) Andersen, J. U.; Hvelplund, P.; Nielsen, S. B.; Tomita, S.; Wahlgreen, H.; Møller, S. P.; Pedersen, U. V.; Forster, J. S.; Jørgensen, T. J. D. *Rev. Sci. Instrum.* **2002**, *73*, 1284.
- (42) Schmidt, M. W.; Baldrige, K. K.; Boatz, J. A.; Elbert, S. T.; Gordon, M. S.; Jensen, J. H.; Koseki, S.; Matsunaga, N.; Nguyen, K. A.; Su, S. J.; Windus, T. L.; Dupuis, M.; Montgomery, J. A. *J. Comput. Chem.* **1993**, *14*, 1347–1363.
- (43) Stephens, P. J.; Devlin, F. J.; Chabalowski, C. F.; Frisch, M. J. *J. Phys. Chem.* **1994**, *98*, 11623–11627.
- (44) Rappoport, D.; Furche, F. *J. Chem. Phys.* **2010**, *133*, 134105.
- (45) Stanton, J. F.; Bartlett, R. J. *J. Chem. Phys.* **1993**, *98*, 7029–7039.
- (46) Piecuch, P.; Kucharski, S. A.; Kowalski, K.; Musial, M. *Comput. Phys. Commun.* **2002**, *149*, 71–96.
- (47) Kowalski, K.; Piecuch, P. *J. Chem. Phys.* **2004**, *120*, 1715–1738.
- (48) Wloch, M.; Gour, J. R.; Kowalski, K.; Piecuch, P. *J. Chem. Phys.* **2005**, *122*, 214107.
- (49) Send, R.; Kaila, V. R. I.; Sundholm, D. *J. Chem. Phys.* **2011**, *134*, 214114.
- (50) Runge, E.; Gross, E. K. U. *Phys. Rev. Lett.* **1984**, *52*, 997.
- (51) Perdew, J. P.; Schmidt, K. *AIP Conf. Proc.* **2001**, *577*, 1–20.
- (52) Perdew, J. P.; Ruzsinszky, A.; Constantin, L. A.; Sun, J.; Csonka, G. I. *J. Chem. Theory Comput.* **2009**, *5*, 902–908.
- (53) Casida, M. E. *J. Mol. Struct. (THEOCHEM)* **2009**, *914*, 3–18.
- (54) Vosko, S.; Wilk, L.; Nusair, M. *Can. J. Phys.* **1980**, *58*, 1200–1211.
- (55) Becke, A. *Phys. Rev. A* **1988**, *38*, 3098–3100.
- (56) Lee, C.; Yang, W.; Parr, R. *Phys. Rev. B* **1988**, *37*, 785–789.
- (57) Peach, M. J. G.; Benfield, P.; Helgaker, T.; Tozer, D. J. *J. Chem. Phys.* **2008**, *128*, 044118.
- (58) Peach, M. J. G.; Le Sueur, C. R.; Ruud, K.; Guillaume, M.; Tozer, D. J. *Phys. Chem. Chem. Phys.* **2009**, *11*, 4465–4470.
- (59) Yanai, T.; Tew, D. P.; Handy, N. C. *Chem. Phys. Lett.* **2004**, *393*, 51–57.
- (60) Ponder, J. W.; Richards, F. M. J. *Comput. Chem.* **1987**, *8*, 1016–1024.
- (61) MacKerell, A. D.; et al. *J. Phys. Chem. B* **1998**, *102*, 3586–3616.
- (62) Foloppe, N.; MacKerell, A. D., Jr. *J. Comput. Chem.* **2000**, *21*, 86–104.
- (63) Breneman, C. M.; Wiberg, K. B. *J. Comput. Chem.* **1990**, *11*, 361–373.
- (64) Neese, F. *ORCA, an ab initio, Density Functional and Semiempirical program package*; University of Bonn: Germany, 2006.
- (65) Allouche, A.-R. *J. Comput. Chem.* **2011**, *32*, 174–182.

DOI: 10.1002/cphc.201300019

On the Photoabsorption by Permanganate Ions in Vacuo and the Role of a Single Water Molecule. New Experimental Benchmarks for Electronic Structure Theory

Jørgen Houmøller,^[a] Sydney H. Kaufman,^[b] Kristian Støchkel,^[a] Lokesh C. Tribedi,^[c] Steen Brøndsted Nielsen,^{*[a]} and J. Mathias Weber^{*[b]}

We report electronic spectra of mass-selected MnO_4^- and $\text{MnO}_4^-\cdot\text{H}_2\text{O}$ using electronic photodissociation spectroscopy. Bare MnO_4^- fragments by formation of MnO_3^- and MnO_2^- , while the hydrated complex predominantly decays by loss of the water molecule. The band in the visible spectral region shows a well-resolved vibrational progression consistent with the excitation of a Mn–O stretching mode. The presence of a single water molecule does not significantly perturb the

spectrum of MnO_4^- . Comparison with the UV/Vis absorption spectrum of permanganate in aqueous solution shows that complete hydration causes a small blueshift, while theoretical models including a dielectric medium have predicted a redshift. The experimental data can be used as benchmarks for electronic structure theory methods, which usually predict electronic spectra in the absence of a chemical environment.

1. Introduction

Permanganate, MnO_4^- , is one of the most prominent oxidation reagents in chemistry, its distinctive violet colour being known to every freshman chemistry student. It is a tetroxo d^0 transition-metal complex with a tetrahedral (T_d) ground-state geometry. Its beautiful electronic spectrum exhibits a clear vibronic structure even in room-temperature aqueous solutions. First spectra of MnO_4^- embedded in crystal lattices were reported by Teltow^[1] in 1938–39 but with limited resolution. A well-resolved spectrum at low temperatures was later published by Holt and Ballhausen^[2] in 1967. It has become a prototype spectrum for the spectroscopy of transition-metal ion complexes and spurred large interest among quantum chemists for several decades.^[2–6]

Electronic excitations of MnO_4^- result in geometry changes to lower symmetries (C_{3v} , C_{2v} and D_{2d}) due to Jahn–Teller distortion.^[4,5] As a result, the electronic spectrum of permanganate is exceptionally difficult to describe theoretically and as such stands out among the tetroxo complexes, despite the modest size of MnO_4^- and its d^0 electron configuration. Indeed, the ion

is not only of significant interest in inorganic chemistry but has become a benchmark system to test and develop advanced electronic structure models.^[4–6] Until now, calculated excitation energies have been compared to the absorption spectrum of permanganate in aqueous solution or to that of KMnO_4 diluted in KClO_4 crystals at cryogenic temperatures. The overall band shapes, including intricate vibronic structures, are relatively well recovered, but the calculated spectra are significantly shifted from experimental spectra by as much as 1 eV, even for modern approaches based on time-dependent density functional theory.^[4,5]

Since quantum chemistry calculations on MnO_4^- are usually carried out for isolated ions in the absence of a surrounding medium, certainly a more proper reference is the spectrum of permanganate in vacuo. In the present work, we address whether the differences between experimental and calculated spectra are due to limitations of the theoretical models or owed to environmental perturbations. We report here on the intrinsic absorption by MnO_4^- ions from 1.77 to 4.46 eV (700–278 nm) and for $\text{MnO}_4^-\cdot\text{H}_2\text{O}$ ions from 1.77 to 2.95 eV (700–420 nm) in the absence of an environment, based on action spectroscopy experiments using three different experimental setups in Aarhus and Boulder. The results for the water complex allow us to directly probe the role of a single water molecule on the electronic structure of permanganate; in contrast to the bare and the fully solvated ion, this is an inherently asymmetric system.

The number of gas-phase experimental studies on permanganate ions by mass spectrometry and laser spectroscopy is limited. The ion can easily be brought into the gas phase with electrospray ionization as first shown by Lau et al.^[7] Low-energy collision-induced dissociation (CID) experiments revealed that the lowest-energy dissociation channels are loss of

[a] J. Houmøller, Dr. K. Støchkel, Prof. S. Brøndsted Nielsen
Department of Physics and Astronomy, Aarhus University
Ny Munkegade 120, 8000 Aarhus C (Denmark)
E-mail: sbn@phys.au.dk

[b] S. H. Kaufman, Prof. J. M. Weber
JILA and Department of Chemistry & Biochemistry
University of Colorado
440 UCB, Boulder, CO 80309-0440 (USA)
E-mail: weberjm@jila.colorado.edu

[c] Prof. L. C. Tribedi
Department of Nuclear and Atomic Physics
Tata Institute of Fundamental Research Colaba
Mumbai 400005 (India)

Supporting information for this article is available on the WWW under <http://dx.doi.org/10.1002/cphc.201300019>.

oxygen or dioxygen from MnO_4^- . Wang and co-workers^[8] measured its photoelectron spectrum using 194 nm photons and determined the vertical and adiabatic detachment energies to be 4.91 and 4.80 eV. These are much higher than the first few electronic excitation energies. Hence, electron detachment does not need to be considered in our experiments where we use visible and UV light with photon energies less than 4.5 eV.

2. Results and Discussion

We first present the results from the Aarhus experiments where photo-excitation was carried out within the first intense electronic band. This band has been assigned to a transition characterized mainly as a HOMO→LUMO ($1t_1 \rightarrow 2e$) type belonging to the 1^1T_2 state.^[4] It gives permanganate solutions their characteristic colour.

To verify that the ions with $m/z = 119$ u/e produced by electro-spray ionization were indeed MnO_4^- , high-energy (50 keV in laboratory frame) CID and charge reversal (CR) experiments were done. Air was used as the collision gas. The CID spectra had peaks at $m/z = 103$ and 87 u/e that can be assigned to MnO_3^- and MnO_2^- , while CR resulted in peaks at $m/z = 27.5$, 55, 71, 87 and 103 u/e corresponding to Mn^{2+} , Mn^+ , MnO^+ , MnO_2^+ and MnO_3^+ formed after the detachment of at least two electrons (see the Supporting Information). There were no indications of impurities in the ion beam with $m/z = 119$ u/e.

The dominant fragment ions of MnO_4^- after irradiation at 540 nm (2.3 eV) are MnO_3^- and MnO_2^- , formed after loss of either one or two oxygen atoms, with a branching ratio of 0.95:1 (see the Supporting Information). The fluence dependences of both processes show that two photons are needed for dissociation (see the Supporting Information). Storage-ring experiments revealed that dissociation occurs rapidly since no dissociation events were registered after more than half a revolution in the ring (21 μs , Figure 1). This is reasonable since MnO_4^- has only nine vibrational degrees of freedom and the excess energy available for simple bond cleavage after two-photon absorption is at least 1 eV. Assuming that the electronic excitation energy is converted into vibrational energy on the electronic ground-state surface, dissociation of a hot ion should therefore be fast. Finally, we note that photodecomposition of permanganate in solution mainly leads to evolution of O_2 , not production of O .^[9] This suggests that solvent caging effects prevent the loss of atomic oxygen.

The $\text{MnO}_4^- \cdot \text{H}_2\text{O}$ complex dissociates almost exclusively to MnO_4^- and H_2O after the absorption of a single 540 nm photon. This is not surprising as typical binding energies of water–anion complexes are of the order of 0.5 eV. Again, full dissociation is expected within the time window for sampling fragmentation (a few microseconds).

To obtain action spectra we measured the yields of MnO_3^- and MnO_2^- ions from MnO_4^- , and MnO_4^- from $\text{MnO}_4^- \cdot \text{H}_2\text{O}$. The MnO_3^- fragment action spectrum of MnO_4^- (Figure 2a) shows a vibrational progression with an average spacing of $(740 \pm 50) \text{ cm}^{-1}$, which is mainly due to the Mn–O stretching vibration in the 1^1T_2 excited state. This value is in excellent agreement with the values of approximately 770 cm^{-1} reported by

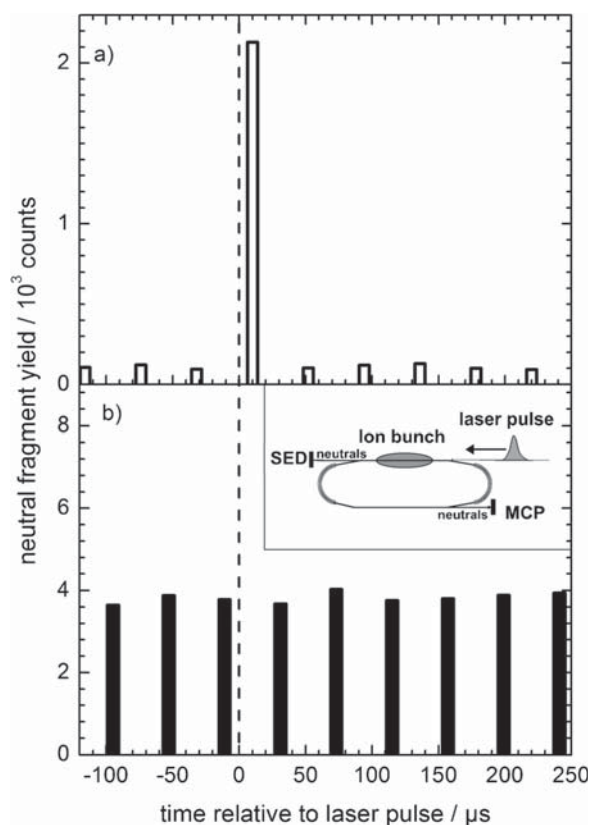


Figure 1. Yield of neutrals from MnO_4^- ions circulating in an electrostatic ion-storage ring. Neutral atoms or molecules are formed either from collisions between the ions and residual gas in the ring (pressure of 10^{-10} mbar) or as a result of 540 nm photodissociation. The time for the laser pulse is set to zero. Neutrals were detected by a secondary emission detector (SED) on the side where photoexcitation was performed (a) and by a microchannel plate (MCP) detector located on the opposite side (b). No delayed photodissociation was observed. Data were acquired during approximately two hours.

Holt and Ballhausen.^[2] The lowest-energy peak is observed at 16850 cm^{-1} (2.09 eV). Sampling MnO_2^- fragment ions instead gives an action spectrum (Figure 2b) that has the same peaks but a distribution that favours peaks to the blue and suppresses the lowest-energy peak. This is simply due to the higher threshold energy required to lose O_2 compared to O . To obtain the total photodissociation action spectrum, we added the two spectra together (see curve in Figure 2c). Peak positions are summarized in Table 1. The maximum cross section is

Table 1. Summary of in vacuo spectroscopic data (peaks 1–7) for MnO_4^- and $\text{MnO}_4^- \cdot \text{H}_2\text{O}$. All energies are in cm^{-1} . The uncertainty is about 50 cm^{-1} . Average spacings are 740 cm^{-1} for MnO_4^- and 725 cm^{-1} for $\text{MnO}_4^- \cdot \text{H}_2\text{O}$.

ion	1 ^[a]	2 ^[b]	3 ^[b]	4 ^[b]	5 ^[b]	6 ^[b]	7 ^[b]
MnO_4^-	16850	730	770	720	760	710	740
$\text{MnO}_4^- \cdot \text{H}_2\text{O}$	16920	730	770	700	770	640	740

[a] Lowest-energy transition. [b] Peak n is given as the shift relative to peak $n-1$.

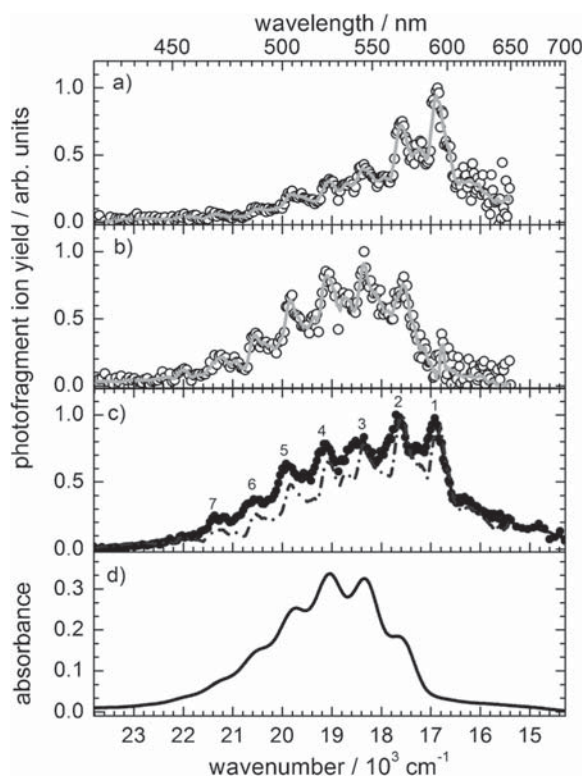


Figure 2. Action spectra of MnO_4^- sampling a) MnO_3^- and b) MnO_2^- fragment ions. The solid curves are based on a Savitzky–Golay smoothing filter using five and three successive data points. c) Action spectrum of $\text{MnO}_4^- \cdot \text{H}_2\text{O}$ sampling MnO_4^- fragment ions. The sum of the two solid curves from (a) and (b) is included (---). Peaks are numbered 1–7, and their associated energies are listed in Table 1. d) Absorption spectrum of an aqueous solution of KMnO_4 (100 μM concentration). We note that the photofragment yield for bare MnO_4^- below approximately 15 400 cm^{-1} was too low to be reported due to relatively low laser pulse energy and the two-photon nature of the photodissociation process.

found for the two lowest-energy components (i.e. the $v''=0$ to $v'=0$ and $v''=0$ to $v'=1$ transitions). We note that there is considerable spectral congestion in the gas-phase spectra, probably due to the fact that the ions are prepared at room temperature which leads to hot bands. As a consequence, we cannot resolve the vibrational progressions in the bending and wagging modes, which have lower vibrational energies.^[2,4] Interestingly, weak signatures roughly halfway between the main progressions can be seen, which are consistent with progressions in the Mn–O stretching modes building on the $v=1$ hot band in the ground-state bending or wagging modes.^[4]

The photodissociation spectrum of $\text{MnO}_4^- \cdot \text{H}_2\text{O}$ is shown in Figure 2c. It is surprisingly similar to that of MnO_4^- , both in respect to peak positions and the overall band shape. The vibronic peaks are shifted towards higher energies by less than 100 cm^{-1} (12 meV). The spectral data are summarized in Table 1. It is evident that the water binds to the electronic ground state with almost equal strength as to the first excited state. This is a surprising result since a single water molecule or hydrogen bond interaction often causes significant blueshifts in electronic bands.^[10] However, it is in line with the exceptional stability of the permanganate ion described in a com-

bined photoelectron spectroscopy and quantum chemical study.^[8] It is also consistent with the observation by Sam and Simmons,^[11] who showed that KMnO_4 can be dissolved in benzene by complexing with dicyclohexyl-18-crown-6 and that the absorption spectrum is very similar to that of permanganate ions in aqueous solution, even though nuclear magnetic resonance indicated an ion pair in benzene and a less symmetric permanganate ion. The spectrum of the water complex serves as an interesting benchmark system for quantum chemistry since methods have to be able to deal with perturbations caused by the water both in the ground state and the electronically excited state.

The absorption spectrum of MnO_4^- in aqueous solution is also shown in Figure 2. We note that the band contours of the isolated ions are different from those in the condensed phase. The $v''=0 \rightarrow v'=2$ and $v''=0 \rightarrow v'=1$ peaks represent the maximum of the band contours for aqueous solutions and low-temperature diluted crystals,^[2] while we find that the $v''=0 \rightarrow v'=0$ and $v''=0 \rightarrow v'=1$ are of similar intensity for the isolated ions, indicating a noticeable change in the excited-state surface along the Mn–O stretching coordinate upon full solvation. There is a solvatochromic shift of 1220 cm^{-1} (0.15 eV) towards the blue for the diluted crystal spectrum (800 cm^{-1} in aqueous solution). This shift can be caused, for example, by breaking of the symmetry of the solute ion in interactions with the solvent. If this were so, then attachment of a single water molecule would introduce a large fraction of the solvatochromic shift. The spectrum of $\text{MnO}_4^- \cdot \text{H}_2\text{O}$ shown in Figure 2c implies that this is not the case, which indicates that differential stabilization of the ground and excited state upon more complete solvation is a more likely source of the solvatochromic shift observed.

Based on time-dependent density functional calculations Neugebauer et al.^[5] and Jose et al.^[4] were able to simulate the vibronic structure of the experimental spectra from low-temperature crystalline solutions, making important band assignments possible. Comprehensive discussions on previous theoretical work are given in these two very informative papers. However, the calculated spectra were shifted by more than 0.5 eV towards the red to match the condensed phase spectra. With the gas-phase spectrum of MnO_4^- at hand, we can conclude that the predictions of absolute energies are actually off by more than 0.7 eV including the 0.15 eV blueshift seen between bare ions and ions in diluted crystals. We note that the inclusion of dielectric environmental effects in the form of the COSMO solvation model led to predicted redshifts in the excitation energies^[6] and not the experimentally observed blueshifts. This highlights the fact that permanganate is certainly still a challenge for electronic structure theory.

Our spectra display absorption to the red of the first peak extending all the way down to 14 300 cm^{-1} for $\text{MnO}_4^- \cdot \text{H}_2\text{O}$. Similar features are observed in absorption spectra of aqueous solutions and in diluted crystals at room temperature,^[1] while Holt and Ballhausen did not find absorption below the lowest-energy vibronic band.^[2] The origin of this absorption is unclear. The highest energy part of it may be caused by hot bands, but they cannot account for the low-energy onset of the band.

Triplet states could be responsible for the low-lying excitations, and their energies as calculated by Dickson and Ziegler^[6] are compatible with the experimentally observed position of this low-energy band. Irrespective of the actual assignment, our work clearly verifies that this band is due to MnO_4^- and not another solute species in solution.

Next we consider the results from the Boulder experiments where photoexcitation was performed in the UV. Absorption of UV radiation by MnO_4^- leads to the loss of one oxygen atom upon absorption of a single photon as revealed by the fluence dependence (see the Supporting Information) of the photodissociation signal at 3.75 eV photon energy (331 nm). Weak signals corresponding to the loss of dioxygen were also observed, but they were insufficient to record useful photodissociation spectra.

The second and third absorption bands exhibit much less vibronic structure than the first. The data obtained in vacuo (Figure 3) show more details than spectra taken in aqueous

in a Mn–O stretching vibration, similar to the vibronic signatures observed in the first electronic band. Electronic structure calculations predict vertical transition energies for the second and third electronic bands which are too high by 0.6 and 1.2 eV.^[4]

3. Conclusions

We measured the electronic spectra of isolated permanganate ions and their complexes with one water molecule attached. The lowest-energy bands are almost identical except for a tiny blueshift of 12 meV caused by the presence of a single water molecule. We established that complete hydration gives rise to a blueshift of about 0.1 eV and a crystalline KClO_4 environment leads to a blueshift of 0.15 eV. For the second and third electronic bands we observed blueshifts upon full solvation of the ion. Interestingly, the trend of solvatochromic shifts from the bare ion to an aqueous solution to the diluted crystal (Table 2)

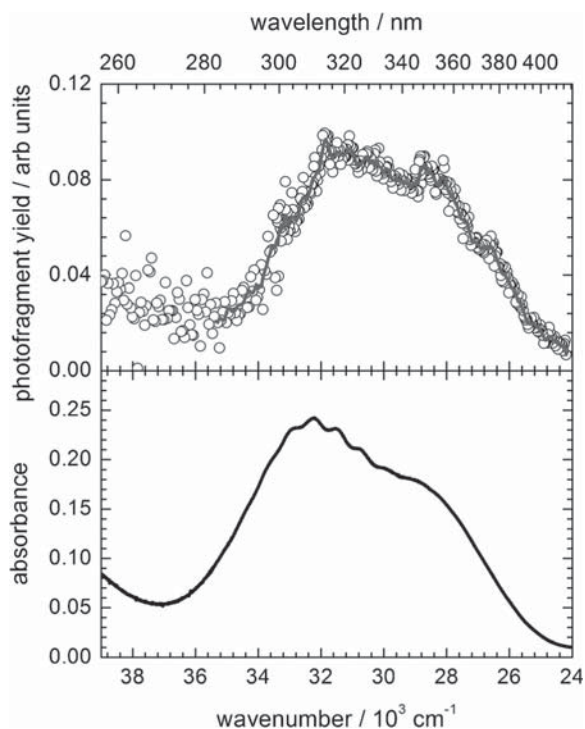


Figure 3. a) UV photofragment action spectrum of MnO_4^- monitoring MnO_3^- . The solid line shown in the regions of the second and third electronic bands is a smoothed curve using seven-point adjacent averaging. b) Absorption spectrum of an aqueous solution of KMnO_4 (100 μM concentration).

solutions, but fewer than those obtained in crystals at low temperatures.^[2] The second band, which marks the transition from the ground state to the 2^1T_2 state,^[4] shows an onset at 24 000 cm^{-1} . The first discernible structure is a shoulder at 26 700 cm^{-1} , red-shifted by approximately 740 cm^{-1} from the first observable shoulder in the crystal spectrum by Holt and Ballhausen.^[2] A weak intensity modulation with irregular spacing can be observed in both the second and the third electronic band, which is compatible with a vibrational progression

Band	1st	2nd	3rd
aqueous solution	800	N/A	400
diluted crystal	1220	740	1280

shows that the chemical environment in crystal experiments that have been mostly used to benchmark calculations up to now is more perturbative than an aqueous solution. This is consistent with the observation that the overall in vacuo band contours and relative intensities in the UV are closer to aqueous-solution data than to crystal spectra, highlighting that the environment of an ion is important for its electronic properties. The spectra provide new and much-needed benchmarks for sophisticated electronic structure calculations on this highly important metal ion complex. Last but not least, our data allow theorists to test the role of a single water molecule on the electronic states of permanganate. Future experiments using cryogenically cooled ions may be a good way to obtain an even better benchmark for this system.

Experimental Section

Altogether three experimental approaches for molecular beam photodissociation spectroscopy were used in this work, an accelerator mass spectrometer and the electrostatic storage ring ELISA, both in Aarhus, and a reflectron time-of-flight mass spectrometer in Boulder. The setups have been described in detail elsewhere,^[12,13] and only a brief description is given below. In all experiments, KMnO_4 was dissolved in acetonitrile and electrosprayed. The internal vibrational energy in both experiments corresponds to room temperature.

Aarhus Experiments

Ions were passed through a heated capillary and tube-lens/skimmer region into an octopole that is operated as a trap by proper pulsing of the lens directly following it. There, ions were in some experiments allowed to react with H₂O for 25 ms at a pressure of about 0.1 mbar. Ions were accelerated to 50 keV kinetic energies, and those of interest were selected by an electromagnet and subsequently irradiated with light (420–700 nm) from an optical parametric oscillator pumped by the third harmonic of a Nd:YAG laser with a repetition rate of 20 Hz. Ion bunches were about 5 μs long and laser pulses shorter than 10 ns. An electrostatic analyzer was scanned to identify the fragment ions; these were counted by a channeltron detector. Since the ion source was running at 40 Hz, only every second ion bunch was irradiated to obtain the laser-induced signal. The formation of fragments with the laser off was due to either dissociation of metastable ions or to collisions with residual gas in the beam line. For high count rates, this yield was used to correct for small fluctuations in the intensity of the parent ions. The photo-induced yield of fragment ions was measured as a function of wavelength. Yields were corrected for photon flux to obtain action spectra and several spectra were taken on different days and averaged. As fragmentation is a result of absorption, these spectra were taken to represent absorption by the ions.

In other experiments, MnO₄⁻ ions were photo-excited by 540 nm light in a storage ring after 15 ms of storage. Dissociation was monitored as a function of time by detecting neutral fragments formed either on the side where irradiation was done or on the other side of the instrument using a secondary emission detector (SED) and a microchannel plate (MCP) detector (Figure 1). The ion revolution time was 42 μs.

Boulder Experiments

After passing through a desolvation capillary, electrosprayed ions were accumulated in a linear hexapole ion trap. Subsequently, they were extracted from the trap, focused using ion optics and injected into the acceleration region of a Wiley–McLaren time-of-flight mass spectrometer. Ions of interest were irradiated at the first space focus of the mass spectrometer by the output of a nanosecond-pulsed optical parametric converter. Using a two-stage reflectron, fragment ions were mass-separated from remaining, undissociated parent ions. Ions were detected on a microchannel plate detector at the second space focus of the mass spectrometer. Photo-dissociation action spectra were obtained by monitoring the fragment ion intensity as a function of photon energy and corrected for laser fluence. Signals due to unimolecular decay of metastable (hot) parent ions or collisions with residual gas were subtracted by running the laser at 20 Hz and the ion source at 40 Hz, subtracting the ion signals without irradiation from those obtained with irradiation. Several spectra were taken on different days and averaged.

The UV/Vis absorption spectrum of KMnO₄ dissolved in water at 100 μM concentration was acquired using a Varian Cary 500 Scan UV-visible-NIR spectrometer (version 8.01) with 10 mm path length, 10 cm⁻¹ step size, 2 nm resolution and an integration time of 0.1 s.

Acknowledgements

This work was supported by Lundbeckfonden, FNU, and by the National Science Foundation (CHE-0845618 and PHY-1125844). S.H.K. is a NSF Graduate Research Fellow (DGE-1144083). L.C.T. and J.M.W. gratefully acknowledge support from Guest Professorships at Aarhus University.

Keywords: gas-phase spectroscopy · mass spectrometry · permanganate · quantum chemistry · single water complex

- [1] a) J. Teltow, *Z. Phys. Chem. Abt. A* **1938**, *40*, 397–430; b) J. Teltow, *Z. Phys. Chem. Abt. A* **1939**, *43*, 198–212.
[2] S. L. Holt, C. J. Ballhausen, *Theor. Chim. Acta* **1967**, *7*, 313–320.
[3] a) M. Wolfsberg, L. Helmholtz, *J. Chem. Phys.* **1952**, *20*, 837–843; b) C. J. Ballhausen, A. D. Liehr, *J. Mol. Spectrosc.* **1958**, *2*, 342–360; c) C. J. Ballhausen, *Theor. Chim. Acta* **1963**, *1*, 285–293; d) A. Viste, H. B. Gray, *Inorg. Chem.* **1964**, *3*, 1113–1123.
[4] L. Jose, M. Seth, T. Ziegler, *J. Phys. Chem. A* **2012**, *116*, 1864–1876.
[5] J. Neugebauer, E. J. Baerends, M. Nooijen, *J. Phys. Chem. A* **2005**, *109*, 1168–1179.
[6] a) H. Hsu, C. Peterson, R. M. Pitzer, *J. Chem. Phys.* **1976**, *64*, 791–795; b) H. Johansen, S. Rettrup, *Chem. Phys.* **1983**, *74*, 77–81; c) H. Nakai, Y. Ohmori, H. Nakatsuji, *J. Chem. Phys.* **1991**, *95*, 8287–8291; d) M. Nooijen, *J. Chem. Phys.* **1999**, *111*, 10815–10826; e) K. H. Johnson, F. C. Smith, Jr., *Chem. Phys. Lett.* **1971**, *10*, 219–223; f) S. J. A. van Gisbergen, J. A. Groeneveld, A. Rosa, J. G. Snijders, E. J. Baerends, *J. Phys. Chem. A* **1999**, *103*, 6835–6844; g) P. Boulet, H. Chermette, C. A. Daul, F. Gilardoni, J. Weber, G. Zuber, *J. Phys. Chem. A* **2001**, *105*, 885–894; h) G. Menconi, N. Kaltsoyannis, *Chem. Phys. Lett.* **2005**, *415*, 64–68; i) M. Buijse, E. J. Baerends, *J. Chem. Phys.* **1990**, *93*, 4129–4141; j) R. M. Dickson, T. Ziegler, *Int. J. Quantum Chem.* **1996**, *58*, 681–687; k) A. J. Bridgeman, G. Cavigliasso, *Polyhedron* **2001**, *20*, 2269–2277; l) M. Seth, T. Ziegler, A. Banerjee, J. Autschbach, S. J. A. van Gisbergen, E. J. Baerends, *J. Chem. Phys.* **2004**, *120*, 10942–10954.
[7] T. C. Lau, J. Y. Wang, K. W. M. Siu, R. Guevremont, *J. Chem. Soc. Chem. Commun.* **1994**, 1487–1488.
[8] G. L. Gutsev, B. K. Rao, P. Jena, X. B. Wang, L. S. Wang, *Chem. Phys. Lett.* **1999**, *312*, 598–605.
[9] H. Nakai, Y. Ohmori, H. Nakatsuji, *J. Phys. Chem.* **1995**, *99*, 8550–8555, and references therein.
[10] a) D. Zuev, K. B. Bravaya, M. V. Makarova, A. I. Krylov, *J. Chem. Phys.* **2011**, *135*, 194304; b) E. V. Gromov, I. Burghardt, H. Koppel, L. S. Cedersbaum, *J. Am. Chem. Soc.* **2007**, *129*, 6798–6806.
[11] D. J. Sam, H. F. Simmons, *J. Am. Chem. Soc.* **1972**, *94*, 4024–4025.
[12] a) K. Stöckel, B. F. Milne, S. Brøndsted Nielsen, *J. Phys. Chem. A* **2011**, *115*, 2155–2159; b) J. A. Wyer, S. Brøndsted Nielsen, *Angew. Chem.* **2012**, *124*, 10402–10406; *Angew. Chem. Int. Ed.* **2012**, *51*, 10256–10260; c) J. U. Andersen, P. Hvelplund, S. Brøndsted Nielsen, S. Tomita, H. Wahlgreen, S. P. Møller, U. V. Pedersen, J. S. Forster, T. J. D. Jørgensen, *Rev. Sci. Instrum.* **2002**, *73*, 1284–1287; d) K. Stöckel, U. Kadhane, J. U. Andersen, A. I. S. Holm, P. Hvelplund, M.-B. S. Kirketerp, M. K. Larsen, M. K. Lykkegaard, S. Brøndsted Nielsen, S. Panja, H. Zettergren, *Rev. Sci. Instrum.* **2008**, *79*, 023107; e) J. Rajput, D. B. Rahbek, G. Aravind, L. H. Andersen, *Biophys. J.* **2010**, *98*, 488–492.
[13] J. C. Marcum, A. Halevi, J. M. Weber, *Phys. Chem. Chem. Phys.* **2009**, *11*, 1740–1751.

Received: January 9, 2013

Published online on February 1, 2013



Cite this: *Phys. Chem. Chem. Phys.*,
2015, 17, 25793

The Soret absorption band of isolated chlorophyll *a* and *b* tagged with quaternary ammonium ions†

Mark H. Stockett,^a Lihi Musbat,^b Christina Kjær,^a Jørgen Houmøller,^a Yoni Toker,^b Angel Rubio,^{c,d} Bruce F. Milne*^{d,e} and Steen Brøndsted Nielsen*^a

We have performed gas-phase absorption spectroscopy in the Soret-band region of chlorophyll (Chl) *a* and *b* tagged by quaternary ammonium ions together with time-dependent density functional theory (TD-DFT) calculations. This band is the strongest in the visible region of metalloporphyrins and an important reporter on the microenvironment. The cationic charge tags were tetramethylammonium, tetrabutylammonium, and acetylcholine, and the dominant dissociation channel in all cases was breakage of the complex to give neutral Chl and the charge tag as determined by photoinduced dissociation mass spectroscopy. Two photons were required to induce fragmentation on the time scale of the experiment (microseconds). Action spectra were recorded where the yield of the tag as a function of excitation wavelength was sampled. These spectra are taken to represent the corresponding absorption spectra. In the case of Chl *a* we find that the tag hardly influences the band maximum which for all three tags is at 403 ± 5 nm. A smaller band with maximum at 365 ± 10 nm was also measured for all three complexes. The spectral quality is worse in the case of Chl *b* due to lower ion beam currents; however, there is clear evidence for the absorption being to the red of that of Chl *a* (most intense peak at 409 ± 5 nm) and also a more split band. Our results demonstrate that the change in the Soret-band spectrum when one peripheral substituent (CH_3) is replaced by another (CHO) is an intrinsic effect. First principles TD-DFT calculations agree with our experiments, supporting the intrinsic nature of the difference between Chl *a* and *b* and also displaying minimal spectral changes when different charge tags are employed. The deviations between theory and experiment have allowed us to estimate that the Soret-band absorption maxima *in vacuo* for the neutral Chl *a* and Chl *b* should occur at 405 nm and 413 nm, respectively. Importantly, the Soret bands of the isolated species are significantly blueshifted compared to those of solvated Chl and Chl–proteins. The protein microenvironment is certainly not innocent of perturbing the electronic structure of Chls.

Received 14th March 2015,
Accepted 9th April 2015

DOI: 10.1039/c5cp01513h

www.rsc.org/pccp

Introduction

Chlorophyll (Chl) *a* and *b* are the light-absorbers of plants and are composed of a porphyrin macrocycle with a divalent magnesium ion in the centre. The $\pi\pi^*$ transitions in the macrocycle are responsible for the strong absorption of these molecules which

spans most of the visible spectrum except for the green region (which is the reason for the green colour of plants). There are two main absorption bands denoted the Soret and the Q bands, the latter covering the absorption by proteins in the red region while the former is in the blue. The only difference between Chl *a* and Chl *b* is one of the peripheral substituents that in Chl *a* is a formyl group (CHO) and in Chl *b* a methyl group (CH_3). Just this small difference causes the Soret band of Chl *b* to be redshifted compared to that of Chl *a* while the opposite is true for the Q bands.^{1,2} Hence by using two different chlorophylls instead of one, plants absorb over a broader region and thereby better take advantage of the solar spectrum.

It is nontrivial to predict the absorption spectra of Chl *a* and *b* and what effect the protein environment has.³ Axial ligation, nonspecific interactions with nearby amino acid residues, and exciton coupling between two or more Chls can all be expected to contribute to modulation of the absorption.⁴ Similarly, solution-phase absorption spectra will display a significant dependence

^a Department of Physics and Astronomy, Aarhus University, Ny Munkegade 120, DK-8000 Aarhus C, Denmark. E-mail: sbn@phys.au.dk

^b Institute of Nanotechnology and Advanced Materials, Bar-Ilan University, Ramat-Gan 290002, Israel

^c Max Planck Institute for the Structure and Dynamics of Matter and Center for Free-Electron Laser Science, Luruper Chaussee 149, 22761 Hamburg, Germany

^d Nano-Bio Spectroscopy Group and ETSF, Dpto. Física de Materiales, Universidad del País Vasco, CFM CSIC-UPV/EHU-MPC & DIPC, 20018 San Sebastián, Spain

^e Centre for Computational Physics, Department of Physics, University of Coimbra, Rua Larga, 3004-516 Coimbra, Portugal. E-mail: bruce@teor.fis.uc.pt

† Electronic supplementary information (ESI) available: Ion bunch profiles; action spectra at 25 kV and 50 kV ion kinetic energies; orbital contributions to calculated TD-CAM-B3LYP/Def2-SVP excitations. See DOI: 10.1039/c5cp01513h

on the solvent used. To disentangle different effects it is desirable (or even necessary) to possess accurate knowledge of the absorption characteristics of isolated Chls *in vacuo*, the simplest of all situations. In our previous work we recorded gas-phase absorption spectra in the Q-band region and found that the isolated molecules displayed significantly blueshifted absorption spectra compared to their protein analogues, by as much as 70 nm.⁵ Interestingly, we found the difference between Chl *a* and Chl *b* Q-bands to be an intrinsic effect which does not necessarily involve microenvironmental interactions with the carbonyl group of Chl *b*. The absorption was obtained indirectly from action spectroscopy where the yield of a fragment ion was monitored as a function of excitation wavelength using a mass spectrometer. However, as Chl is a neutral molecule not amenable to conventional mass spectroscopy, we tagged the molecules with quaternary ammonium ions, namely tetramethylammonium (1⁺), tetrabutylammonium (2⁺), or acetylcholine (3⁺). These charge tags have no mobile protons so we know with certainty where the charge is located. Spectra were found to be surprisingly independent of the charge tag which indicated that it was remote from the π electron cloud. Density Functional Theory (DFT) calculations fully supported this idea. While theory also showed very little dependence on the charge tag, the computed vertical excitation energies were systematically blueshifted by 0.11 eV for Chl *a* and on average 0.15 eV for Chl *b* relative to experimental band maxima. This deviation, however, allowed us to calibrate calculated values for bare molecules with no charge tags and obtain best estimates of the lowest-energy Q_y(0–0) band (642 nm for Chl *a* and 626 nm for Chl *b*).

Previous work was also done by Saito *et al.*⁶ on deprotonated Chl *a* and Chl *b*; however, the absorption is significantly different to those of the neutral chromophores as the conjugated network is changed upon deprotonation.

Here our focus is on the Soret-band absorption, and we make use of the same charge-tagging method introduced above. In the previous work we could only conclude that the band maximum was below 420 nm, the lower end of the visible output from the optical parametric oscillator (OPO) that was used for the experiments.

Experimental

To produce light below 420 nm with enough intensity for the current experiments, we constructed a new laser module mixing the fundamental output from a Nd:YAG laser (1064 nm) with the visible output from the OPO (to be described elsewhere). Due to technical limitations of this new laser system, our spectra are of lower quality than those in the Q-band region, but are still good enough to make firm conclusions.

Experiments were done with a home-built sector instrument equipped with an electrospray ion source and a tuneable laser system described in detail elsewhere.^{7,8} All compounds, Chl *a*, Chl *b*, both from spinach, salts of tetramethylammonium, tetrabutylammonium, and acetylcholine were obtained from Sigma-Aldrich. Methanol solutions of chlorophyll *a* and *b* and

the charge tag were made and electrosprayed. All ions were accumulated in an octopole trap that was emptied every 25 ms (40 Hz repetition rate) to produce 10 μ s long ion bunches. Acceleration to 50 keV energies was followed by selection of ions of interest according to mass-to-charge ratio by a bending magnet. These were then irradiated by light from a pulsed laser system: The fundamental from a Nd:YAG laser (EKSPILA) was frequency tripled to 355 nm ultraviolet light that was split into a visible photon (420–720 tuneable range) and an infrared idler photon in an optical parametric oscillator (OPO). The 1064 nm fundamental was mixed with the visible OPO output in the home-made laser module to produce light in the 301–425 nm range. The length of the laser pulses was a few nanoseconds with a 20 Hz firing rate. Hence only every second ion bunch was irradiated which allowed us to obtain the pure photoinduced signal as 'laser on' minus 'laser off'. Fragment ions formed were analysed by a hemispherical electrostatic analyser (ESA) (according to kinetic energy per charge) and counted by a channeltron detector. A LabView program was used to synchronise the laser triggering and the ion trap emptying time. Three different experiments were done: (1) photoinduced dissociation mass spectroscopy: The ESA was scanned at a fixed laser wavelength. (2) Power dependence: the yield of a fragment ion was monitored as a function of laser power to determine the number of photons required for its formation on the time scale of the experiment (up to 20 microseconds). Neutral density filters were used to attenuate the laser beam. (3) Action spectroscopy: the photo-induced yield of a fragment ion *versus* excitation wavelength was recorded.

Computational details

The geometries of all compounds/complexes were optimised at the DFT level using the gradient-corrected PBE functional^{9,10} and the Def2-SVP^{11,12} polarised split-valence basis set. The Orca software package was used for all geometry optimisations.¹³ Default cut-off criteria for convergence of the self-consistent field and nuclear gradient calculations were employed. Previously it was found that the complexation of acetylcholine cation to Chl did not involve interaction with the Mg²⁺ ion and so this binding mode was again excluded for the present work.

Excitation energies were calculated using time-dependent DFT¹⁴ with the GAMESS-US software (1st October 2010 (R1) release).¹⁵ The range-separated CAM-B3LYP functional^{16,17} was selected as this had previously been shown to provide good results for the gas-phase Q-band spectra of Chl *a* and *b* and similar to those obtained with the computationally demanding equation of motion coupled-cluster level of theory.^{18,19} Similarly, the Def2-SVP basis set was selected for these calculations because previous work had shown that it provided results in good agreement with experiment.¹⁹ Several extremely weak excitations with oscillator strengths approaching zero were found lying between the Q and Soret bands, and for this reason it was necessary to include the first 15 excited states of the Chl systems in order to capture the excitations corresponding to the Soret band.

Results and discussion

Experimental results

Photoexcitation of complexes between Chl *a/b* and a quaternary ammonium tag led in all cases to separation of the complex. A representative example is shown in Fig. 1 for Chl *a*-1⁺ where the wavelength of light is 360 nm, and the dominant fragment ion is 1⁺ (*m/z* 74). Fig. 2 shows the production of this fragment ion as a function of laser power. Clearly more than one photon is needed to cause dissociation within the instrumental time for sampling dissociation (up to about 20 microseconds, see ion bunch profile in ESI[†]). A quadratic fit seems to account nicely for the data, which indicates that two photons are required. The data points at maximum laser power were not included as saturation occurred corresponding to photoexcitation of all ions in the interaction volume (a two-photon Poisson fit including saturation fully accounts for all points, see ESI[†]). To obtain action spectra, the photoinduced signal should therefore be divided by the number of photons raised to the power of two.

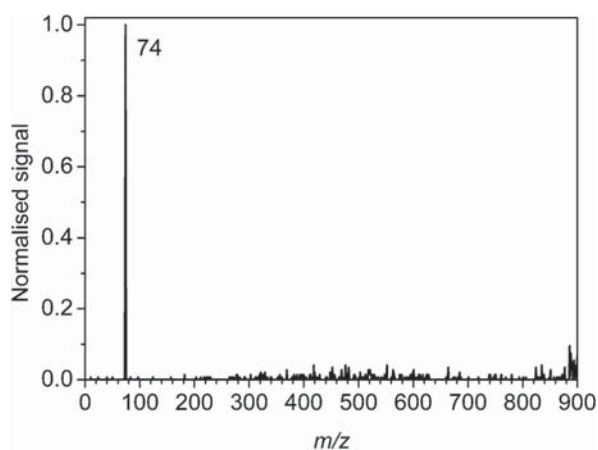


Fig. 1 Photoinduced dissociation (PID) mass spectrum of Chl *a*-1⁺. $\lambda = 360$ nm. The dominant fragment ion is the charge tag with mass 74.

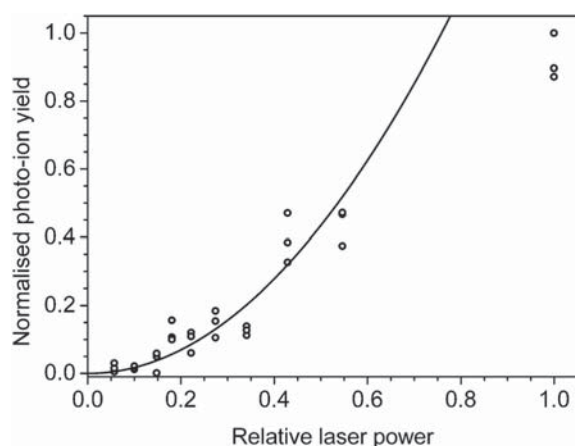


Fig. 2 Power dependence for the formation of 1⁺ from Chl *a*-1⁺. $\lambda = 360$ nm. An ax^2 function was fit to the data neglecting the highest laser power where saturation occurred.

These action spectra are taken to represent the absorption spectra of the ions. This is valid when the fluorescence is insignificant or the fluorescence quantum yields do not depend on the excitation wavelength. Quantum yields have not been measured for gas-phase molecules but are 0.25 for solvated Chl *a* independent of solvent and excitation wavelength and 0.11 and 0.06 for Chl *b* in ether and methanol solutions, respectively.²⁰

Action spectra of Chl *a*-3⁺ and Chl *b*-3⁺ recorded by sampling the yield of 3⁺ as a function of wavelength are shown in Fig. 3. They were obtained after averaging of six and five scans, respectively, taken with 1 nm steps, and smoothing by 12-point sliding averages (raw spectra are shown in the ESI[†]). The laser beam overlap with the ion beam oscillates slightly due to the finite step size by which we can move the prism in the laser module, which is needed to separate the generated photon from the 1064 nm and visible photon. This means that we have to be cautious in over-interpreting the band shapes. However, both ions reveal absorption below 425 nm, and the major band for Chl *a* is blueshifted relative to that for Chl *b*. Hence the observation in proteins and in solutions that the Soret band of Chl *a* is to the blue of that of Chl *b* is obtained also for the gas-phase complexes. Hence this shift is an intrinsic effect originating from the methyl and formyl ring substituents being different. A similar conclusion was drawn for the Q band that was found to be further to the red for Chl *a* than for Chl *b*.⁵ The band maximum is at 404 ± 5 nm for Chl *a*-3⁺ while the maximum is at 409 ± 5 nm for Chl *b*-3⁺ but with a shoulder at 422 nm. Also a shoulder at about 440 nm was earlier seen for Chl *b*. The Soret band is broad or split (in the case of Chl *b*) which is due to the asymmetry of the Chl molecule which gives rise to different transition dipoles along the *x*- and *y*-axes of the porphyrin ring as well as vibronic coupling. There is also absorption occurring at wavelengths below 380 nm, with maxima at about 365 nm and 340 nm.

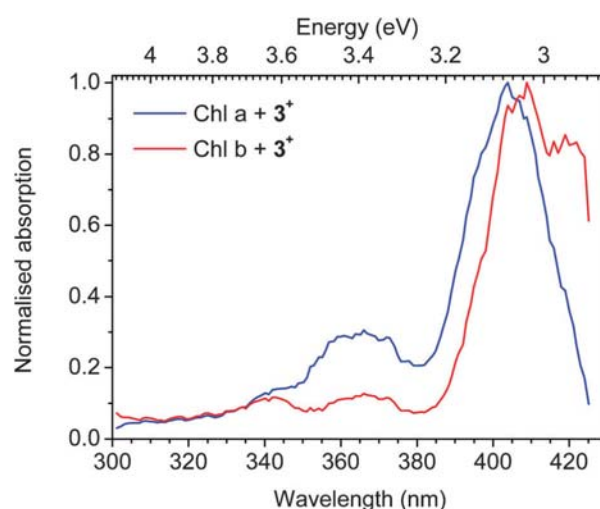


Fig. 3 Action spectra of Chl *a*-3⁺ and Chl *b*-3⁺. These are taken to represent the absorption by the ion-molecule complexes. The maximum of the band is set to 1.

We note that we have tested for reproducibility by repeating the experiment for Chl *a*-3⁺ two months later than the first measurements and also with a lower acceleration voltage of 25 kV (see ESI[†]). At 25 kV acceleration the time for dissociation is on average longer than at 50 kV acceleration but there was no significant difference between the action spectra. Hence we assume that most ions that have absorbed two photons dissociate before reaching the ESA over the whole wavelength region.

The dependence on the charge tag of the absorption by Chl *a* is evident from Fig. 4. The band width for Chl *a*-2⁺ seems a bit narrower than those of the two others but otherwise the spectra are quite similar. The band maxima are at 403 ± 5 nm, 404 ± 5 nm, and 404 ± 5 nm for Chl *a* tagged with 1⁺, 2⁺, and 3⁺. Hence as for the Q-band region, the charge tag plays a minor role for the Soret-band absorption in accordance with its location far away from the π electron cloud and attached to the carbonyl oxygens of the sidechains. A similar conclusion is reached from comparison of Chl *b*-1⁺ with Chl *b*-3⁺. Band maxima are summarised in Table 1 and compared with values obtained from the theoretical calculations.

In Fig. 5 we show the full spectra of Chl *a*-3⁺ and Chl *b*-3⁺ covering both the Soret-band and Q-band regions, the latter based on previously published spectra.⁵ As mentioned before the Soret band is blue-shifted for Chl *a* compared to Chl *b* while the opposite is true for the Q band. It seems that the relative

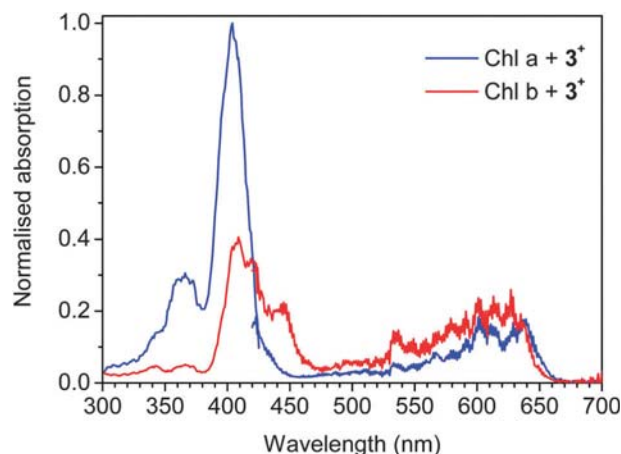


Fig. 5 Action spectra of Chl *a*-3⁺ and Chl *b*-3⁺ in the Soret and Q-band regions. The total spectra are made by combining spectra taken from 300 nm to 425 nm (present work) with spectra from 420 nm to 700 nm (previous work).⁵

strength between the Soret band and the Q band is higher for Chl *a* than for Chl *b*. However, it should be noticed that spectra were combined based on the overlap in the relatively small region of 420–425 nm where the absorption by Chl *a* is changing rapidly.

Theoretical results and comparison with experimental data

Details of the geometries and binding of the charge tags to the Chl molecules have been given previously and will not be discussed further here.⁵

The TD-CAM-B3LYP calculated excitations energies for the variously tagged Chls along with those of the bare neutral Chl *a* and *b* are shown in Tables 1 and 2. An arbitrary oscillator strength cut-off of 0.1 was used to eliminate unimportant excitations in the regions of interest and improve the clarity of the tabulated data. Details of the electronic transitions and their orbital components contributing to the individual excitations underlying the bands observed in the experimental spectra are provided in Tables S1 and S2 in the ESI.[†]

For the isolated Chl *a* and *b* it was found that the Soret-band region was composed of three excitations with a separation between the highest and lowest energy excitations of approximately 2 eV. When the charge tags were present, the excitation of intermediate energy was suppressed and no longer contributed significantly to the band; however, the other two

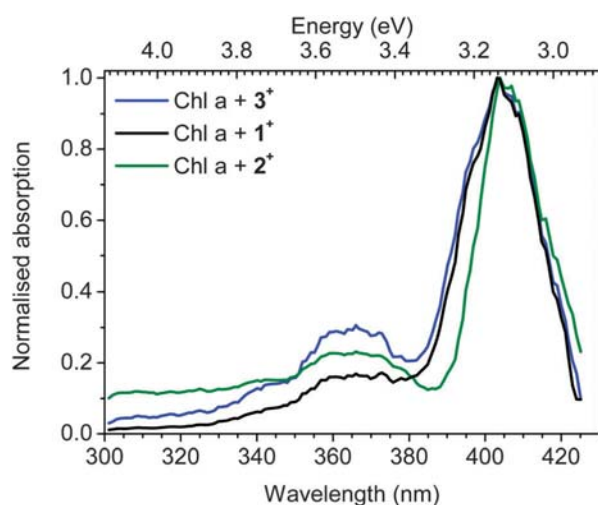


Fig. 4 Action spectra of Chl *a* with the three different charge tags. The spectra are taken to represent the absorption by the ion–molecule complexes.

Table 1 Summary of experimental band maxima and vertical transition energies (in eV) for the Soret band^a

	1 ⁺	2 ⁺	3 ⁺	No tag	Diethyl-ether
Exp. Chl <i>a</i>	3.08 (403)	3.07 (404)	3.07 (404)	3.06 (405) ^b	2.90 (428)
Theory Chl <i>a</i>	3.54 (350)	3.51 (354)	3.48 (356)	3.47 (358)	
Exp. Chl <i>b</i>	3.03 (409)		3.03 (409)	3.00 (413) ^b	2.73 (453)
Theory Chl <i>b</i>	3.34 (371)	3.32 (374)	3.29 (377)	3.28 (378)	

^a Corresponding absorption wavelengths are provided in parenthesis (in nm). ^b Estimated values based on deviation between theory and experiment for tagged Chls.

Table 2 TD-CAM-B3LYP/Def2-SVP transition energies contributing to the Soret band and secondary minor peak. Values in eV with oscillator strengths in parentheses

	1 ⁺	2 ⁺	3 ⁺	No tag
Chl <i>a</i>				
Soret	3.42 (0.91) 3.67 (0.81)	3.38 (0.87) 3.64 (0.79)	3.36 (0.78) 3.60 (0.73)	3.34 (0.65) 3.45 (0.41) 3.61 (0.90)
Minor peak	3.99 (0.11) 4.07 (0.25)	4.07 (0.24)	3.92 (0.29) 4.08 (0.23) 4.14 (0.15) 4.17 (0.19)	4.00 (0.17)
Chl <i>b</i>				
Soret	3.25 (1.00) 3.43 (0.72)	3.23 (0.939) 3.41 (0.747)	3.20 (0.86) 3.38 (0.75)	3.16 (0.68) 3.32 (0.83) 3.37 (0.39)
Minor peak	4.02 (0.11) 4.13 (0.28)	4.14 (0.297)	3.93 (0.20) 4.11 (0.13) 4.13 (0.23) 4.14 (0.15)	4.21 (0.12)

excitations remained at more or less the same energy as in the bare-chromophore cases.

Regardless of the nature (or absence) of the charge tag a redshift of around 0.1 to 0.2 eV was noted in the Soret-band excitations of Chl *b* relative to those of Chl *a*, in good agreement with experiment (see Fig. 3–5).

The geometrical means of the contributing calculated excitations were used for comparison with the Soret-band maxima recorded experimentally (Table 1). This permitted the calculation of the average deviations between theory and experiment which were found to be +0.44 eV for Chl *a* and +0.29 eV for Chl *b*. By subtracting these figures from the Soret-band averages calculated for the bare neutral Chls it was possible to estimate values for the isolated chlorophyll Soret band *in vacuo* of 3.06 eV (405 nm) for Chl *a* and 3.00 eV (413 nm) for Chl *b*.

The weaker, higher-energy band observed in the experimental spectra was also reproduced well by the TD-CAM-B3LYP calculations. Experimentally this band was observed to lie approximately 0.3 eV higher in energy than the Soret band at 365 ± 10 nm whilst in the calculated spectra this blueshift was around 0.5 eV. The relative intensities of the Soret band and this minor band were also well reproduced with the minor band's excitations possessing oscillator strengths around one quarter of those of the Soret-band excitations (compare tabulated values in Table 2 with spectra in Fig. 3 and 4).

Comparison with solvated-Chl and pigment-protein spectra

In diethyl ether Chl *a* has band maxima at 428 nm, 409 nm, 379 nm, and 326 nm while the lowest energy maximum is at 418 nm in methanol.¹⁹ Chl *b* has band maxima at 453 nm and 429 nm in diethyl ether. Hence solvation causes significant redshifts of the Soret band for both Chl *a* and Chl *b*. As the resolution of our gas-phase spectra is poor, we can only say that the shift of the most intense peak of the Soret band is <23 nm for Chl *a* and <30 nm for Chl *b*.

In leaves all Chl pigment molecules are linked to proteins and display different absorption:²¹ light-harvesting Chl *a,b*-protein

complexes have band maxima at 437 nm and 472 nm and the Chl *a* of photosystem II reaction centers at 437 nm. Hence the nearby protein environment causes larger shifts than those upon solvation. The shifts are likely due to either axial ligation or exciton coupling or a combination hereof. Heimdal *et al.*⁴ calculated shifts due to axial ligation between 3 and 35 nm, the largest effect being for negatively charged ligands. More work to decipher the effect of axial ligation on the absorption by the gas-phase complexes would be needed to address this issue in more detail and to verify the calculations.

Conclusions

We have provided a detailed experimental and theoretical study of the Soret absorption band of isolated chlorophyll *a* and *b* in the presence of quaternary ammonium ions (charge tags). Good agreement between experimental and theoretical (TD-DFT) data on the ion-molecule complexes allowed us to calibrate calculated values for bare Chl *a* and Chl *b*; our best estimates of the Soret-band maxima *in vacuo* are 405 nm and 413 nm. The absorption by Chl *a* is blueshifted relative to Chl *b* as also seen for solvated Chl *a* and *b* and when the two pigments are situated in proteins. Our work shows this to be an intrinsic effect that does not necessarily involve microenvironmental perturbations with the formyl group of Chl *b*. Still the gas-phase absorption spectra are significantly blueshifted compared to protein spectra, which emphasises the strong effect of the microenvironment on the overall transition energies. Particularly axial ligation to the magnesium centre is expected to play a role, which is to be explored more in the future.

Acknowledgements

SBN and MHS acknowledge Lundbeckfonden and Villumfonden for support. BFM thanks the Donostia International Physics centre and the Centre de Física de Materiales, University of the Basque Country for financial support. BFM also thanks the Laboratory for Advanced Computing of the University of Coimbra, Portugal for the provision of computer resources, technical support and assistance. AR acknowledges financial support from the European Research Council Advanced Grant DYNamo (ERC-2010- AdG-267374), Spanish Grant (FIS2013-46159-C3-1-P), Grupos Consolidados UPV/EHU del Gobierno Vasco (IT578-13) and European Community FP7 project CRONOS (Grant number 280879-2) and COST Actions CM1204 (XLIC) and MP1306 (EUSpec). LM and YT acknowledge Cost Action CM1204 (XLIC) for support (ECOST-STSM-CM1204-301114-047659).

Notes and references

- 1 J. Gross, *Pigments in vegetables: chlorophylls and carotenoids*, Springer, New York, 1991.
- 2 G. C. Papageorgiou, Fluorescence of Photosynthetic Pigments *in Vitro* and *in Vivo*, in *Chlorophyll *a* Fluorescence. A Signature of Photosynthesis*, ed. G. C. Papageorgiou and Govindjee,

- Advances in Photosynthesis and Respiration Springer, Dordrecht, 2004, vol. 19.
- 3 J. Linnanto and J. Korppi-Tommola, *Phys. Chem. Chem. Phys.*, 2006, **8**, 663.
 - 4 J. Heimdahl, K. P. Jensen, A. Devarajan and U. Ryde, *JBIC, J. Biol. Inorg. Chem.*, 2007, **12**, 49.
 - 5 B. F. Milne, Y. Toker, A. Rubio and S. Brøndsted Nielsen, *Angew. Chem., Int. Ed.*, 2015, **54**, 2170.
 - 6 M. Saito, T. Tanabe, K. Noda and M. Lintuluoto, *Phys. Rev. A: At., Mol., Opt. Phys.*, 2013, **87**, 033403.
 - 7 K. Støchkel, B. F. Milne and S. Brøndsted Nielsen, *J. Phys. Chem. A*, 2011, **115**, 2155.
 - 8 J. A. Wyer and S. Brøndsted Nielsen, *Angew. Chem., Int. Ed.*, 2012, **51**, 10256.
 - 9 J. Perdew, M. Ernzerhof and K. Burke, *J. Chem. Phys.*, 1996, **105**, 9982.
 - 10 J. P. Perdew, K. Burke and M. Ernzerhof, *Phys. Rev. Lett.*, 1996, **77**, 3865; J. P. Perdew, K. Burke and M. Ernzerhof, *Phys. Rev. Lett.*, 1997, **78**, 1396.
 - 11 A. Schäfer, H. Horn and R. Ahlrichs, *J. Chem. Phys.*, 1992, **97**, 2571.
 - 12 F. Weigend and R. Ahlrichs, *Phys. Chem. Chem. Phys.*, 2005, **7**, 3297.
 - 13 F. Neese, *Wiley Interdiscip. Rev.: Comput. Mol. Sci.*, 2012, **2**, 73.
 - 14 E. Runge and E. K. U. Gross, *Phys. Rev. Lett.*, 1984, **52**, 997.
 - 15 M. W. Schmidt, K. K. Baldrige, J. A. Boatz, S. T. Elbert, M. S. Gordon, J. H. Jensen, S. Koseki, N. Matsunaga, K. A. Nguyen, S. J. Su, T. L. Windus, M. Dupuis and J. A. Montgomery, *J. Comput. Chem.*, 1993, **14**, 1347.
 - 16 M. J. G. Peach, P. Benfield, T. Helgaker and D. J. Tozer, *J. Chem. Phys.*, 2008, **128**, 044118.
 - 17 M. J. G. Peach, C. R. L. Sueur, K. Ruud, M. Guillaume and D. J. Tozer, *Phys. Chem. Chem. Phys.*, 2009, **11**, 4465.
 - 18 K. Støchkel, C. N. Hansen, J. Houmøller, L. M. Nielsen, K. Anggara, M. Linares, P. Norman, F. Nogueira, O. V. Maltsev, L. Hintermann, S. Nielsen Brøndsted, P. Naumov and B. F. Milne, *J. Am. Chem. Soc.*, 2013, **135**, 6485.
 - 19 H. Du, R.-C. A. Fuh, J. Li, L. A. Corkan and J. S. Lindsey, *Photochem. Photobiol.*, 1998, **68**, 141; J. M. Dixon, M. Taniguchi and J. S. Lindsey, *Photochem. Photobiol.*, 2005, **81**, 212.
 - 20 L. S. Forster and R. Livingston, *J. Chem. Phys.*, 1952, **20**, 1315.
 - 21 J. R. Evans and J. M. Anderson, *Biochim. Biophys. Acta*, 1987, **892**, 75.

Chlorophyll

International Edition: DOI: 10.1002/anie.201601979

German Edition: DOI: 10.1002/ange.201601979

On the Exciton Coupling between Two Chlorophyll Pigments in the Absence of a Protein Environment: Intrinsic Effects Revealed by Theory and Experiment

Bruce F. Milne,* Christina Kjær, Jørgen Houmøller, Mark H. Stockett, Yoni Toker, Angel Rubio, and Steen Brøndsted Nielsen*

Abstract: Exciton coupling between two or more chlorophyll (Chl) pigments is a key mechanism associated with the color tuning of photosynthetic proteins but it is difficult to disentangle this effect from shifts that are due to the protein microenvironment. Herein, we report the formation of the simplest coupled system, the Chl a dimer, tagged with a quaternary ammonium ion by electrospray ionization. Based on action spectroscopic studies in vacuo, the dimer complexes were found to absorb 50–70 meV to the red of the monomers under the same conditions. First-principles calculations predict shifts that somewhat depend on the relative orientation of the two Chl units, namely 50 and 30 meV for structures where the Chl rings are stacked and unstacked, respectively. Our work demonstrates that Chl association alone can produce a large portion of the color shift observed in photosynthetic macromolecular assemblies.

The absorption wavelengths of chlorophyll (Chl) molecules are modulated by the microenvironment surrounding each pigment molecule. In this way, nature has evolved a method by which the coverage of the optical spectrum and the subsequent transfer of the absorbed energy is optimized,^[1,2]

leading to photon energy conversion efficiencies of 95% in photosynthetic systems.^[3] The harvesting of light energy in photosynthesis is therefore far more efficient than anything thus far developed by our most cutting-edge scientific and technological efforts. Furthermore, small modifications to the basic Chl structure, for example, the replacement of a methyl group in Chl a with a formyl group in Chl b, also lead to some fine-tuning of the absorption spectra.^[4]

For decades a great deal of research activity has been directed at understanding precisely how natural systems modulate the absorption energies of Chl species. The highly complex nature of the macromolecular systems involved has, however, always served to complicate such attempts. In recent years, experimental approaches have been joined by theoretical/computational methods, and this has permitted studies at levels of detail that were previously unattainable.^[5–12]

Experimental methods have also continued to develop, and recently it has become possible to study absorption processes in Chl molecules free of solvent and other micro-environmental effects. In pioneering experiments, Shafizadeh et al.^[13] utilized two-color pump-probe spectroscopy to measure the lowest energy absorption band of neutral Chl a evaporated from spinach leaves. They found the origin band of the Q_y transition to be at 647 nm. Recent action spectroscopy experiments on Chl a tagged with quaternary ammonium cations, in combination with theory, provided an absorption band maximum of similar value (642 nm).^[14,15] In this case, the absorption was obtained from the dissociation of the complex, and a calibrated value was determined for the neutral molecule based on the deviation between theory and experiment. Using this same technique, Q-band maxima were obtained for Chl b,^[14] and the Soret band was measured for both Chl a and Chl b.^[15] Importantly, the large difference in the absorption spectra of Chl a and Chl b was concluded to be an intrinsic effect and not due to local hydrogen-bond interactions with the formyl group of Chl b, for example, clearly demonstrating the advantage of looking at isolated molecules. Compared to literature values for Chl in a variety of natural protein complexes, absorption in vacuo was found to be blue-shifted by 50 nm.^[16–19]

With the absorption spectra of bare Chl now well established, we can begin to ask the question of whether shifts that are due to interactions with the protein environment are more or less important than those that are due to excitonic coupling between two or more pigments. This issue was very recently discussed by Baghbanzadeh and Kassal.^[20] The interactions basically govern the mechanism for energy

[*] Dr. B. F. Milne

CFisUC, Department of Physics, University of Coimbra
Rua Larga, 3004-516 Coimbra (Portugal)
E-mail: bfmilne@uc.pt

C. Kjær, J. Houmøller, Dr. M. H. Stockett, Prof. S. B. Nielsen
Department of Physics and Astronomy, Aarhus University
Ny Munkegade, DK-8000 Aarhus C (Denmark)
E-mail: sbn@phys.au.dk

Dr. Y. Toker
Institute of Nanotechnology and Advanced Materials
Bar-Ilan University, Ramat-Gan 5290002 (Israel)

Prof. A. Rubio
Max Planck Institute for the Structure and Dynamics of Matter
Luruper Chaussee 149, 22761 Hamburg (Germany)

Prof. A. Rubio
Nano-Bio Spectroscopy Group and ETSF
Universidad del País Vasco
CFM CSIC-UPV/EHU-MPC & DIPC, 20018 San Sebastián (Spain)

Supporting information and the ORCID identification number(s) for the author(s) of this article can be found under <http://dx.doi.org/10.1002/anie.201601979>.

© 2016 The Authors. Published by Wiley-VCH Verlag GmbH & Co. KGaA. This is an open access article under the terms of the Creative Commons Attribution Non-Commercial License, which permits use, distribution and reproduction in any medium, provided the original work is properly cited, and is not used for commercial purposes.

transfer to the reaction center: For funneling via localized states on the potential energy surface, the protein environment is most important whereas supertransfer requires fully delocalized states where all pigments are electronically coupled. In naturally occurring photosynthetic complexes, there can be significant uninterrupted interfacial regions between Chl molecules, and these presumably play an important part in facilitating energy transfer between pigments. Herein, we have applied the action spectroscopy method used previously on individual Chl pigments to the study of Chl a dimers in vacuo to evaluate the extent to which the close association of chromophores contributes to the spectral shift of Chl in photosynthetic systems.

To study photoabsorption with our approach it is necessary for the chromophore to be charged; however, the direct ionization of a molecule such as Chl in order to produce a charged ion would yield the absorption energies for the anion/cation instead of the neutral molecule. To get around this problem, we have employed our previously developed technique of non-covalently tagging the chromophore with charged species to produce a complex ion.^[14,15]

The experimental setup has been described in detail elsewhere.^[21,22] Chl a (provided by Sigma–Aldrich) was dissolved in methanol, and salts of either tetramethylammonium (1^+) or acetylcholine (3^+) were added (see Figure 1). These solutions were electrosprayed to produce complexes consisting of chlorophylls and one charge tag. All ions were accumulated in an octopole ion trap for 25 ms. Following extraction from the trap, the ions were accelerated to 40 keV. The charge-tagged complexes were then selected according to their mass-to-charge ratios by an electromagnet and photoexcited by a laser pulse (few nanoseconds long). Photoexcitation led to dissociation of the complex, and the daughter ions were separated according to their kinetic energies (proportional to m/z) using an electrostatic analyzer and counted with a channeltron detector. The light source used was the visible output (420–700 nm) of an optical parametric oscillator (OPO) pumped by a frequency-tripled, Q-switched Nd:YAG laser (EKSPILA). The repetition rate of the laser was 20 Hz, and only every second ion bunch was irradiated. The real photoinduced signal was obtained as the difference

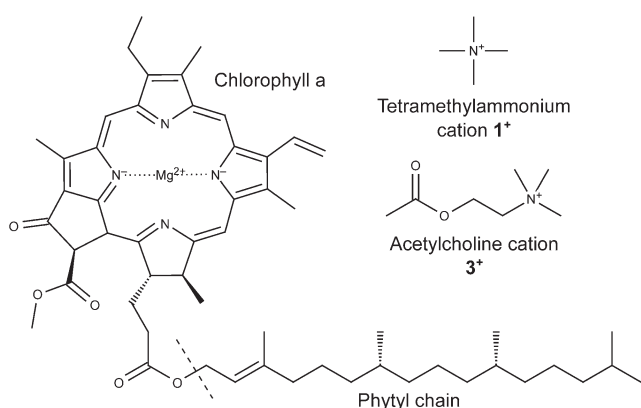


Figure 1. Structures of molecular species employed in the present work. Numbering of the cationic tags chosen to be consistent with our previous related work on Chl spectra.^[14,15]

between the “laser on” and “laser off” signals. Each ion bunch contained about one hundred charge-tagged Chl dimer complexes.

Collision-induced dissociation (CID) experiments were also performed by leaking atmospheric air into the beam line after the mass-selection step and again scanning the electrostatic analyzer (ESA) for daughter ion mass spectrometry. These experiments were done to confirm the identity of the complex, and the corresponding spectra can be found in the Supporting Information.

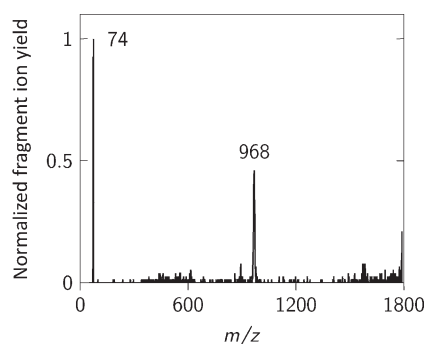


Figure 2. PID mass spectrum of the dimer complex $(\text{Chl a})_2\text{-}1^+$ normalized to the highest fragment ion yield. The spectrum was obtained with $\lambda = 420$ nm. Two fragment ions are observed: the charge tag 1^+ (m/z 74) and the monomer complex $\text{Chl a-}1^+$ (m/z 968).

Photoexcitation of the dimer cation complexes led to loss of either one Chl a or both Chl a (see Figure 2). Power dependence experiments revealed that at least two photons were needed for dissociation to occur within the instrumental time window of approximately 10 μs . While the complexes are weakly bound, they have many degrees of freedom accounting for dissociation not being a simple one-photon process.

To correct for the variation in laser power across the spectral region, the photoinduced signal was divided by the number of photons at each wavelength, that is, the laser pulse energy was divided by the photon energy, raised to the power of 2.3 (according to the power-dependence measurements, see the Supporting Information). The resulting action spectra associated with each fragment ion are very similar (Supporting Information) and were combined to give a total action spectrum for each charge-tagged dimer (Figure 3). The band maximum occurs at 652 ± 5 nm (1.902 ± 0.015 eV) for both dimer complexes. The spectra shown here were recorded with lower resolution than those in our previous work on Chl monomers^[14,15] as the experiment was more difficult owing to much lower ion currents. It is important to note that although the overall band shape slightly depends on the power correction, the band maximum does not within the experimental uncertainty. Hence, our data show that the interaction between two Chl pigments causes a red shift in the absorption band maximum of about 15–25 nm (or 50–70 meV) relative to the monomer charge-tag complexes. There is a second band in the dimer spectrum at higher energy that may be due to the higher-lying exciton state but more work is needed to establish this with certainty.

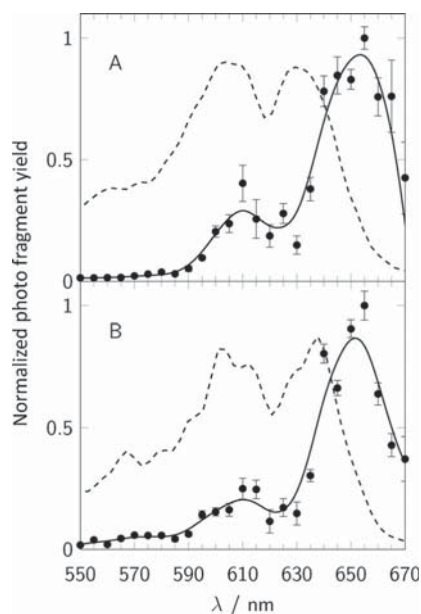


Figure 3. Total 2.3-photon-corrected action spectra for the dimer complexes compared to the monomer complexes (dashed lines). A) Complexes with charge tag 1^+ . B) Complexes with charge tag 3^+ . Line smoothing using spline functions was performed because of the low resolution of the dimer spectra. For the purpose of consistency between data sets, the same smoothing was applied to the monomer spectra.

It is also evident from our spectra that the absorption covers a broad region from 550 nm to 675 nm. This is expected owing to vibronic coupling and the asymmetry of the chromophores (different transition dipoles along each diagonal). Aside from the spectral shift, we observed that the double-maximum character of the monomer spectrum (which is due to vibronic coupling) was lost in the case of the dimer. For now, the origin of this effect remains unclear and requires further study. The band maxima will be compared to the theoretical vertical excitation energies in the following.

The first excitation energies in vacuo for Chl a dimers complexed with a single 1^+ charge tag in two different optimized ground-state geometries were calculated using time-dependent density functional theory (TD-DFT; Figure 4).^[23] The range-separated CAM-B3LYP functional^[24,25] has been found^[26] to provide results similar to those obtained with the computationally demanding equation-of-motion coupled-cluster level of theory, and its use ensured consistency with our previous work. The difference in the first excitation energies of chlorophyll (for both the a and b forms) using the charge tags 1^+ and 3^+ was previously found to be less than 0.03 eV, and it was for this reason that in the present work only the simpler 1^+ was employed in the theoretical calculations.^[14]

The TD-DFT excitation energies together with the experimental band maxima are given in Table 1. Values for both dimer configurations are given because the energy difference between them was only 0.018 eV at the DFT/CAM-B3LYP/Def2-SVP level of theory, and so both can be expected to be significantly populated at 298 K. The distances between the two magnesium centers are 5.05 Å (stacked

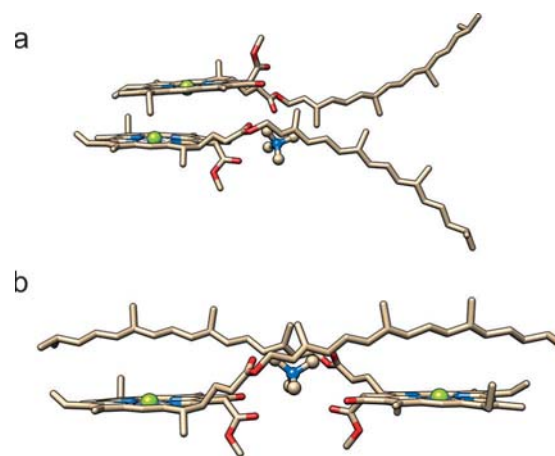


Figure 4. DFT/PBE/Def2-SVP-optimized geometries of the Chl a dimer tagged with 1^+ in stacked (a) and linear (b) configurations. Chl a displayed in stick format, charge tag displayed in ball-and-stick format. Hydrogen atoms omitted for clarity.

configuration) and 19.04 Å (linear configuration). For comparison, the experimental and calculated excitation energies for the monomeric Chl a- 1^+ complex from our previous work are also shown.^[14] The predicted red shift for the two dimer structures relative to the monomer structure is 30–50 meV, which is close to the measured value of 50–70 meV considering an uncertainty of 15 meV in the experimental data.

The main $Q_y(0,0)$ absorption band in Chl-containing proteins is found between 660 nm and 680 nm but absorption at even longer wavelengths (701–710 nm) is also seen for Chl units in photosystem I.^[16–19,27] It is easy to account for absorption in the 660–680 nm region because 1) isolated neutral Chl a and Chl b that are free of charge tags absorb maximally at 642 nm and 626 nm, respectively, according to our previous work, 2) axial ligation has been predicted to give a red shift of 9–19 nm,^[28] and 3) the shift that is due to exciton coupling according to our present results is 15–25 nm. The maximum shift would therefore be about 680 nm. However, to account for the absorption at 701–710 nm, it seems that either the two Chl units have to be closer to each other than is the case here (forced together by the protein environment) to increase the coupling—although this seems unlikely as the stacked dimer configuration found in the present work is already close to the lower limit for the intermolecular approach—or in addition to the environmental effect of the protein surroundings, more than two Chl units couple. This is supported by the crystal structures of systems such as the major light harvesting complex (LHC-II) and photosystem I

Table 1: Energies of the experimental band maxima and vertical transition energies for the Chl a dimer. Values in eV with the corresponding absorption wavelengths in nm in parentheses.

	(Chl a) ₂ - 1^+	Chl a- 1^+ ^[a]	Δ^{Dimer}
exp.	1.90 (652)	1.97 (629)	−0.07 (+23)
theory (stacked)	2.028 (611)	2.081 (596) ^[b]	−0.053 (+15)
theory (linear)	2.050 (605)	2.081 (596) ^[b]	−0.031 (+9)

[a] Values from previous work.^[14] [b] Single value for the unique Chl a monomer complex configuration.

from green plants in which close proximity between more than two Chl pigments occurs frequently.^[29,30] We aim to investigate the influence of larger pigment assemblies within these protein–Chl complexes in the future by looking at trimers or larger clusters of Chl molecules.

Acknowledgements

B.F.M. acknowledges funding from the Portuguese Foundation for Science and Technology (CONT_DOUT/11/UC/405/10150/18/2008) and thanks the DIPC and CFM (UPV/EHU) and the Laboratory for Advanced Computation (University of Coimbra) for support. S.B.N. acknowledges support from the Danish Council for Independent Research (4181-00048B) and the Villum Foundation. A.R. acknowledges financial support from the European Research Council (ERC-2010-AdG-267374), a Spanish grant (FIS2013-46159-C3-1-P), Grupos Consolidados (IT578-13), AFOSR (FA2386-15-1-0006), AOARD (144088), the H2020-NMP-2014 project MOSTOPHOS (SEP-210187476), and COST Action (MP1306, “EUSpec”).

Keywords: absorption spectroscopy · chlorophyll · density functional calculations · mass spectrometry · photosynthesis

How to cite: *Angew. Chem. Int. Ed.* **2016**, *55*, 6248–6251
Angew. Chem. **2016**, *128*, 6356–6359

- [1] G. D. Scholes, T. Mirkovic, D. B. Turner, F. Fassiolli, A. Buchleitner, *Energy Environ. Sci.* **2012**, *5*, 9374–9393.
- [2] G. R. Fleming, G. S. Schlau-Cohen, K. Amarnath, J. Zaks, *Faraday Discuss.* **2012**, *155*, 27–41.
- [3] Y. C. Cheng, G. R. Fleming, *Annu. Rev. Phys. Chem.* **2009**, *60*, 241–262.
- [4] J. Gross, *Pigments in vegetables: chlorophylls and carotenoids*, Springer, New York, **1991**.
- [5] J. Jornet-Somoza, J. Alberdi-Rodriguez, B. F. Milne, X. Andrade, M. A. L. Marques, F. Nogueira, M. J. T. Oliveira, J. J. P. Stewart, A. Rubio, *Phys. Chem. Chem. Phys.* **2015**, *17*, 26599.
- [6] L. Joly, R. Antione, A. R. Alloche, M. Broyer, J. Lemoine, P. Dugourd, *J. Am. Chem. Soc.* **2007**, *129*, 8428–8429.
- [7] G. Féraud, C. Dedonder, C. Jouvét, Y. Inokuchi, T. Haino, R. Sekiya, T. Ebata, *J. Phys. Chem. Lett.* **2014**, *5*, 1236–1240.
- [8] J. Rajput, D. B. Rabek, L. H. Andersen, A. Hirshfeld, M. Sheves, P. Altoe, G. Orlandi, M. Garavelli, *Angew. Chem. Int. Ed.* **2010**, *49*, 1790–1793; *Angew. Chem.* **2010**, *122*, 1834–1837.
- [9] S. Xu, S. Gozem, A. I. Krylov, C. R. Christopher, J. M. Weber, *Phys. Chem. Chem. Phys.* **2015**, *17*, 31938–31946.
- [10] J. F. Greisch, M. E. Harding, M. Kordel, W. Klopffer, M. M. Kappes, D. Schoos, *Phys. Chem. Chem. Phys.* **2013**, *15*, 8162–8170.
- [11] S. M. J. Wellman, R. A. Jockusch, *J. Phys. Chem. A* **2015**, *119*, 6333–6338.
- [12] N. J. A. Coughlan, B. D. Adamson, L. Gamon, K. Catani, E. J. Bieske, *Phys. Chem. Chem. Phys.* **2015**, *17*, 22623–22631.
- [13] N. Shafizadeh, M. H. Ha-Thi, B. Soep, M. A. Gaveau, F. Piuze, C. Pothier, *J. Chem. Phys.* **2011**, *135*, 114303.
- [14] B. F. Milne, Y. Toker, A. Rubio, S. B. Nielsen, *Angew. Chem. Int. Ed.* **2015**, *54*, 2170–2173; *Angew. Chem.* **2015**, *127*, 2198–2201.
- [15] M. H. Stockett, L. Musbat, C. Kjør, J. Houmøller, Y. Toker, A. Rubio, B. F. Milne, S. B. Nielsen, *Phys. Chem. Chem. Phys.* **2015**, *17*, 25793–25798.
- [16] E. L. Smith, *J. Gen. Physiol.* **1941**, *24*, 565–582.
- [17] N. W. Withers, R. S. Alberte, R. A. Lewin, J. P. Thornber, G. Britton, T. W. Goodwin, *Proc. Natl. Acad. Sci. USA* **1978**, *75*, 2301–2305.
- [18] J. A. Guikema, L. A. Sherman, *Arch. Biochem. Biophys.* **1983**, *220*, 155–166.
- [19] J. C. Waldron, J. M. Anderson, *Eur. J. Biochem.* **1979**, *102*, 357–362.
- [20] S. Baghbazadeh, I. Kassal, *Phys. Chem. Chem. Phys.* **2016**, *18*, 7459–7467.
- [21] K. Støchkel, B. F. Milne, S. B. Nielsen, *J. Phys. Chem. A* **2011**, *115*, 2155–2159.
- [22] J. A. Wyer, S. B. Nielsen, *Angew. Chem. Int. Ed.* **2012**, *51*, 10256–10260; *Angew. Chem.* **2012**, *124*, 10402–10406.
- [23] E. Runge, E. K. U. Gross, *Phys. Rev. Lett.* **1984**, *52*, 997.
- [24] M. J. G. Peach, P. Benfield, T. Helgaker, D. J. Tozer, *J. Chem. Phys.* **2008**, *128*, 044118.
- [25] M. J. G. Peach, C. R. Le Sueur, K. Ruud, M. Guillaume, D. J. Tozer, *Phys. Chem. Chem. Phys.* **2009**, *11*, 4465–4470.
- [26] K. Støchkel, C. N. Hansen, J. Houmøller, L. M. Nielsen, K. Anggara, M. Linares, P. Norman, F. Nogueira, O. V. Maltsev, L. Hintermann, S. B. Nielsen, P. Naumov, B. F. Milne, *J. Am. Chem. Soc.* **2013**, *135*, 6485–6493.
- [27] J. E. Mullet, J. J. Burke, C. J. Arntzen, *Plant Physiol.* **1980**, *65*, 814–822.
- [28] J. Heimdal, K. P. Jensen, A. Devarajan, *J. Biol. Inorg. Chem.* **2007**, *12*, 49–61.
- [29] Z. Liu, H. Yan, K. Wang, T. Kuang, J. Zhang, L. Gui, *Nature* **2004**, *428*, 287–292.
- [30] A. Ben-Shem, F. Frolov, N. Nelson, *Nature* **2003**, *426*, 630–635.

Received: February 25, 2016

Published online: April 13, 2016

A cylindrical quadrupole ion trap in combination with an electrospray ion source for gas-phase luminescence and absorption spectroscopy

Mark H. Stockett,^{a)} Jørgen Houmøller, Kristian Støchkel, Annette Svendsen, and Steen Brøndsted Nielsen

Department of Physics and Astronomy, Aarhus University, Aarhus, Denmark

(Received 5 February 2016; accepted 16 April 2016; published online 3 May 2016)

A relatively simple setup for collection and detection of light emitted from isolated photo-excited molecular ions has been constructed. It benefits from a high collection efficiency of photons, which is accomplished by using a cylindrical ion trap where one end-cap electrode is a mesh grid combined with an aspheric condenser lens. The geometry permits nearly 10% of the emitted light to be collected and, after transmission losses, approximately 5% to be delivered to the entrance of a grating spectrometer equipped with a detector array. The high collection efficiency enables the use of pulsed tunable lasers with low repetition rates (e.g., 20 Hz) instead of continuous wave (cw) lasers or very high repetition rate (e.g., MHz) lasers that are typically used as light sources for gas-phase fluorescence experiments on molecular ions. A hole has been drilled in the cylinder electrode so that a light pulse can interact with the ion cloud in the center of the trap. Simulations indicate that these modifications to the trap do not significantly affect the storage capability and the overall shape of the ion cloud. The overlap between the ion cloud and the laser light is basically 100%, and experimentally >50% of negatively charged chromophore ions are routinely photodepleted. The performance of the setup is illustrated based on fluorescence spectra of several laser dyes, and the quality of these spectra is comparable to those reported by other groups. Finally, by replacing the optical system with a channeltron detector, we demonstrate that the setup can also be used for gas-phase action spectroscopy where either depletion or fragmentation is monitored to provide an indirect measurement on the absorption spectrum of the ion. *Published by AIP Publishing.* [<http://dx.doi.org/10.1063/1.4948316>]

I. INTRODUCTION

Spectroscopy of (bio)molecular chromophore ions isolated *in vacuo* is a field of intense research with the goal to reveal their intrinsic electronic structure in the absence of perturbations from a solvent or protein micro-environment.^{1–7} These large and fragile chromophore ions are typically produced by electrospray ionization (ESI) to guarantee a soft transfer to the gas phase. Comparisons of gas-phase spectra to those measured when the chromophore is fully solvated or within a protein pocket provide information on, e.g., the effect of nearby water molecules or amino acid residues. Most work has focused on absorption spectroscopy where absorption is identified indirectly from either ion dissociation or electron detachment, so-called action spectroscopy. This is because the ion density is too low for a traditional transmission experiment where the attenuation of light passing through a sample is measured. Instead, specialized mass spectroscopy equipment is required to identify the fate of the ion after light absorption. Only a few experimental groups have measured the light emitted from mass-selected photoexcited ions. Here we present a new setup to measure luminescence from ions produced by ESI, but first we discuss some of the difficulties associated with such experiments.

In most luminescence spectroscopy experiments on molecular ions produced by ESI, the ions are trapped in either

a linear quadrupole trap, a Paul trap (i.e., a 3-D quadrupole trap), or a Penning trap.^{8–16} The experiments are non-trivial, not only because of the inherently low ion density but also because photons are emitted in all directions, and the collection of the emitted photons is limited by poor optical access to the trapped ions. Sensitive light detectors are needed to detect each of the rare events. Detection efficiencies are typically much less than 1% of the total emitted photons. As an added complication, light scattered from the laser or ambient light is also detected, which reduces the signal-to-noise ratio, or even causes saturation of the detector if one is not careful enough. The same ions are irradiated multiple times with the use of either high repetition rate (e.g., 80 MHz) pulsed lasers or continuous wave (cw) lasers. This approach necessitates collisional (or radiative) cooling of the excited ions between each excitation event. The pressure of the helium buffer gas used to facilitate the trapping of the ions, together with the applied laser power, are therefore highly important adjustable parameters. The rate of collisions at typical buffer gas densities (10^{14} cm^{-3}) is $\sim 10^5 \text{ s}^{-1}$ while the time between two laser pulses from an 80 MHz laser is only 12.5 ns. For a pulsed laser experiment, the number of photons in each pulse has to be kept low to avoid two-photon absorption, which is the reason for the use of high repetition rate lasers. The optimal solution is to produce a high number of photons broadly distributed over time to maximize the number of excitation events, each associated with emitted photons from the ions being hit. A cw laser is as such the best choice but the wavelength tunability is poor compared to that of a pulsed laser. An alternative

^{a)}Electronic mail: stockett@phys.au.dk

approach, described here, utilizes a laser with a low repetition rate (20 Hz), and where the ion trap is emptied and refilled following every laser shot.

While measuring the spectrum of light emitted (i.e., dispersed fluorescence) from isolated ions is difficult for the above-mentioned reasons, it has some advantages over gas-phase absorption spectroscopy. Unlike action spectroscopy, where the absorption of multiple photons is often required to induce measurable fragmentation, fluorescence can be observed following the absorption of just a single photon. This is particularly important for large molecular ions that are not easily dissociated, and where kinetic shifts can skew the spectrum obtained from an absorption experiment. Indeed, beautiful fluorescence spectra of ionic laser dyes have been reported, and even time-resolved light emission has been followed on the nanosecond time scale.^{8,17–19} Spectra have also been published of biomolecular ions, e.g., xanthene-based rhodamine dyes,^{11,12,15,19} fluorescein and derivatives,^{20,21} and non-covalent host-guest complexes.¹⁷ Finally, Förster Resonance Energy Transfer (FRET) experiments on gas-phase biomolecular ions have been performed^{22–31} to monitor the separation of double-stranded oligonucleotide anions (i.e., duplex melting) or conformations of peptides and proteins and noncovalent complexes.

To study molecular ions that are produced by low-current ion sources (e.g., ESI) and that have low fluorescence quantum yields, setups with high collection efficiencies are desirable. Further, such setups are crucial if laser systems with low repetition rates are to be employed. Here we describe a homebuilt setup that is based on a Paul trap with a cylindrical geometry following the design of Wells *et al.*³² The advantage of using a Paul trap instead of, e.g., a linear quadrupole trap is the confinement of ions to the center, and the light emitted after photo-excitation is almost originating from a point source. The cylindrical variant is much easier to construct and modify than the traditional version which utilizes hyperbolic electrodes. In our design, a hole in the cylindrical electrode permits laser irradiation of the trapped ions and one end-cap electrode is a wire mesh grid. A condenser lens is mounted as close as possible to the grid electrode allowing light collection from a greater solid angle than in other existing setups. We have performed detailed numerical simulations which show that, despite all the modifications, the electric field near the center of our trap is close to that of an ideal quadrupole trap. The idea behind this design is based on a setup made by O'Keefe and co-workers^{33–36} to measure light-induced fluorescence spectra of small molecular cations (e.g., CD^+ , N_2^+ , and BrCN^+) produced directly in a quadrupole ion trap by electron ionization.

Applying this approach to larger molecular ions was suggested by Parks and co-workers over a decade ago,⁹ but never implemented until now.

We demonstrate that our setup provides high quality dispersed fluorescence spectra of ions produced by ESI even when a 20 Hz laser is used as the excitation source. In contrast to other ESI-trap fluorescence experiments, the ions are only irradiated once before the trap is emptied, and there are therefore no issues with thermalization of photo-excited ions or photodissociation (the latter of course depletes the population of ions stored in the trap and thus lowers the fluorescence signal but the fragment ions do not otherwise disturb the experiment); we will discuss this issue later in this article. The setup can also be used for absorption spectroscopy (based on dissociation and electron detachment) from a simple replacement of the light collection optics with a channeltron detector. Finally, we discuss the potential use of such a setup for detection of light emission from cryogenically cooled ions.

II. DESIGN

The electrospray ion source and cylindrical quadrupole ion trap, shown together in Fig. 1, are similar to those previously used on the ELISA (Electrostatic Ion Storage Ring, Aarhus) electrostatic storage ring.³⁷ All components were manufactured in-house. Ions formed by electrospray ionization enter the first vacuum chamber through a heated capillary. A tube lens focuses the ions through a skimmer into a second chamber. The ions are guided through this chamber, which serves mainly as a differential pumping stage, by an octopole ion guide. A lens packet focuses the ions through a small aperture at the exit of the ion guide into a third chamber where the ion trap is mounted. An Einzel lens focuses the ion beam into the entrance aperture of the trap.

The cylindrical ion trap, shown in Fig. 2, was built using the optimized geometry determined by Wells *et al.*³² The cylindrical geometry combines ease of manufacture with adequate performance in mass-selective operation. The inner radius of the cylinder is $r_1 = 10$ mm and the axial distance from the center of the trap to the end-cap electrode is $z_1 = 9$ mm, and there is a gap of $D = 1$ mm between the cylinder electrode and the end-caps. A radio frequency (RF) potential of frequency $\Omega/2\pi = 770$ kHz and amplitude up to $V = 1.5$ kV (0-peak) is applied to the cylinder using a home built power supply to create an approximate quadrupolar potential for ion trapping. Additional DC voltages ± 15 V are applied to the end-caps. A $L = 4$ mm hole through the side of the cylinder electrode permits laser excitation of the trapped ions. The laser pulse

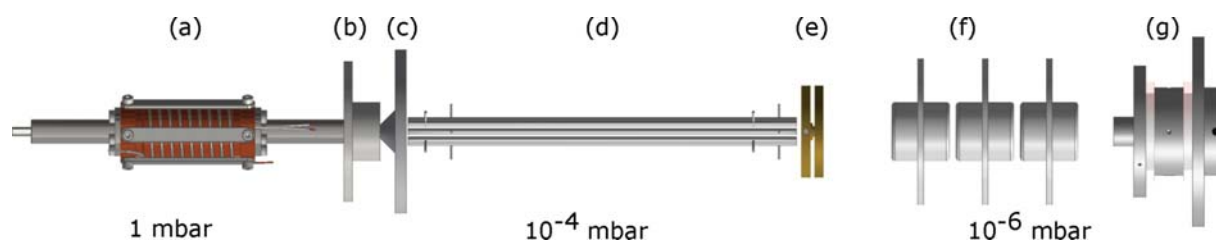


FIG. 1. Schematic of electrospray ion source and cylindrical ion trap. Shown are the (a) heated capillary, (b) tube lens, (c) skimmer, (d) octopole ion guide, (e) lens packet, (f) Einzel lens, and (g) cylindrical ion trap.

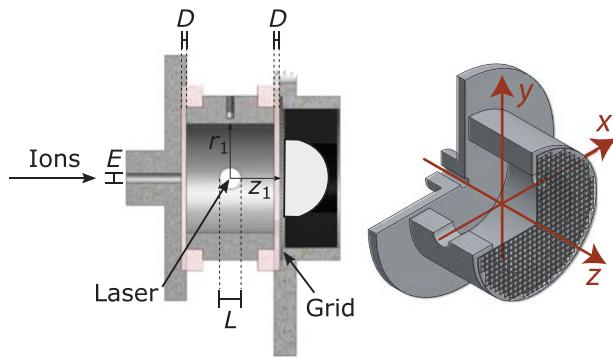


FIG. 2. Cutaway views of the cylindrical ion trap with modified end-cap for fluorescence experiments. A wire mesh grid electrode permits more emitted radiation to be collected by the aspheric condenser lens directly behind the grid. The hole in the cylinder (diameter $L = 4$ mm) allows laser access. Ions enter the trap through a hole of diameter $E = 2$ mm. Also indicated are the trap dimensions $r_1 = 10$ mm, $z_1 = 9$ mm, and the gap between the cylinder and end-cap electrodes $D = 1$ mm. The axes used in our numerical simulations are defined in the right-hand view, where the lens and its mounting have been removed to reveal the grid.

(beam diameter ~ 3 mm) enters and exits the vacuum chamber containing the trap through anti-reflection coated fused silica windows oriented perpendicular to the beam. No baffles are used to reduce scattered laser light; a simple iris outside the chamber is used to define the beam diameter.

For use in fluorescence experiments, one of the end-caps has been replaced with a wire mesh grid electrode to permit more light to be collected. A schematic of the optical system is shown in Fig. 3. An aspheric condenser lens (Thorlabs, 18 mm diameter) is mounted inside the modified end-cap with the optical surface as close to the grid as possible to maximize the solid angle for light collection. The focal length of the lens (15 mm) is chosen such that the ion cloud sits slightly inside the focal distance. This yields a well-collimated beam of collected radiation which is coupled out of the vacuum chamber through an anti-reflection coated window. The high numerical aperture of the aspheric lens (0.57) corresponds to a solid angle of 1.1 sr, meaning that nearly 10% of the light emitted by the ions falls within the cone of angles collected by the lens. Outside the vacuum chamber, notch filters (Thorlabs) used to reduce scattered laser light and an achromatic focusing lens (Thorlabs, focal length 10 cm) are mounted on a rail

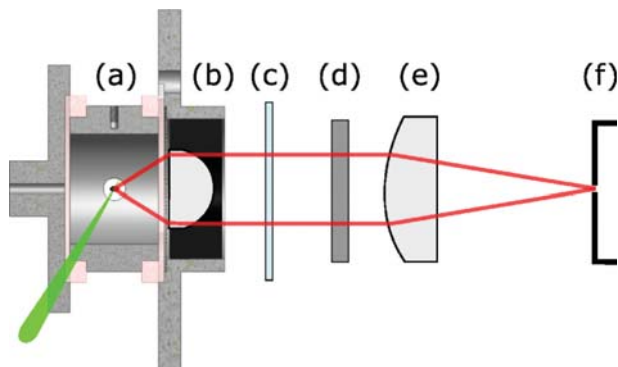


FIG. 3. Schematic optical layout showing (a) trap, (b) condenser lens, (c) chamber window, (d) notch filter, (e) collector lens, and (f) spectrometer entrance slit.

system co-axial with the ion trap. The achromatic lens focuses the collected radiation onto the entrance slit of a grating spectrometer (Andor Shamrock 303i, 303 mm focal length) equipped with an electron multiplying CCD camera (Andor Newton model DU970P-BVF, 1600×200 $16 \mu\text{m} \times 16 \mu\text{m}$ pixels). Taking into account transmission losses from the grid electrode and all optical elements, we estimate that approximately 5% of the emitted radiation is delivered to the spectrometer entrance slit. This high collection efficiency distinguishes our apparatus from those developed by other groups.

For all fluorescence spectra presented in this article, the 1 MHz readout mode of the CCD camera was used, with a pre-amplifier gain of 4 and an electron multiplication gain of 255. A 50 kHz readout mode was not found to meaningfully improve the signal-to-noise ratio in our experiments. A 300 lines/mm grating (500 nm blaze) and a 1.5-2.0 mm slit width on the spectrometer provided adequate resolution. The triggering of the laser, camera, and trap are controlled using a simple LabVIEW program and a TTL pulse generator.

III. NUMERICAL SIMULATIONS

To investigate the properties of the cylindrical ion trap with the mesh grid electrode and to estimate the size of the ion cloud, numerical simulations were performed using the SIMION 8.0 software. The program was used to solve the Laplace equation for the chosen trap geometry on a grid with a spatial resolution of 0.1 mm. For the cloud simulations, 1000 ions of mass 163 amu (or 479 amu) and charge $-1e$ (or $+1e$) were initialized in the center of the trap with a kinetic energy of 0.2 eV and a corresponding velocity vector uniformly distributed in all directions. Ion trajectories were computed by numerical integration of the equations of motion while at the same time taking into account collisions between the ion and the He buffer gas. The collisions happened at random times, but such that the average distance travelled by the ions between collisions was equal to the mean free path (assuming a collisional cross section of $\sigma = 2.3 \times 10^{-18} \text{ m}^2$) at a buffer gas pressure of 5×10^{-3} mbar. The collisions were modelled as hard-sphere elastic collisions in which the He atom was generated with a random velocity drawn from a Maxwell-Boltzmann velocity distribution with a temperature of $T = 300$ K (see Ref. 38 for details). Each ion was propagated for a time span of 4000 μs , and its position was logged at a time interval of 10 μs , but only during the last 1000 μs of the simulation to ensure that the ion ensemble was equilibrated. To simulate the stability region, the buffer gas collisions were turned off, and the ions were initialized slightly outside the trap center with a kinetic energy of 2 meV with a spatially isotropic velocity distribution. The RF amplitude (0-peak), V , and DC offset, U , were varied, and a point in (V, U) space was defined as stable if the ions were still trapped after a propagation time of 1 ms.

Fig. 4 shows the ion column density for two of the ions presented later in this work, simulated under typical experimental conditions. Also indicated is the area accessible to the laser light. The FWHM (Full Width at Half Maximum) of the distributions in the radial and axial directions is

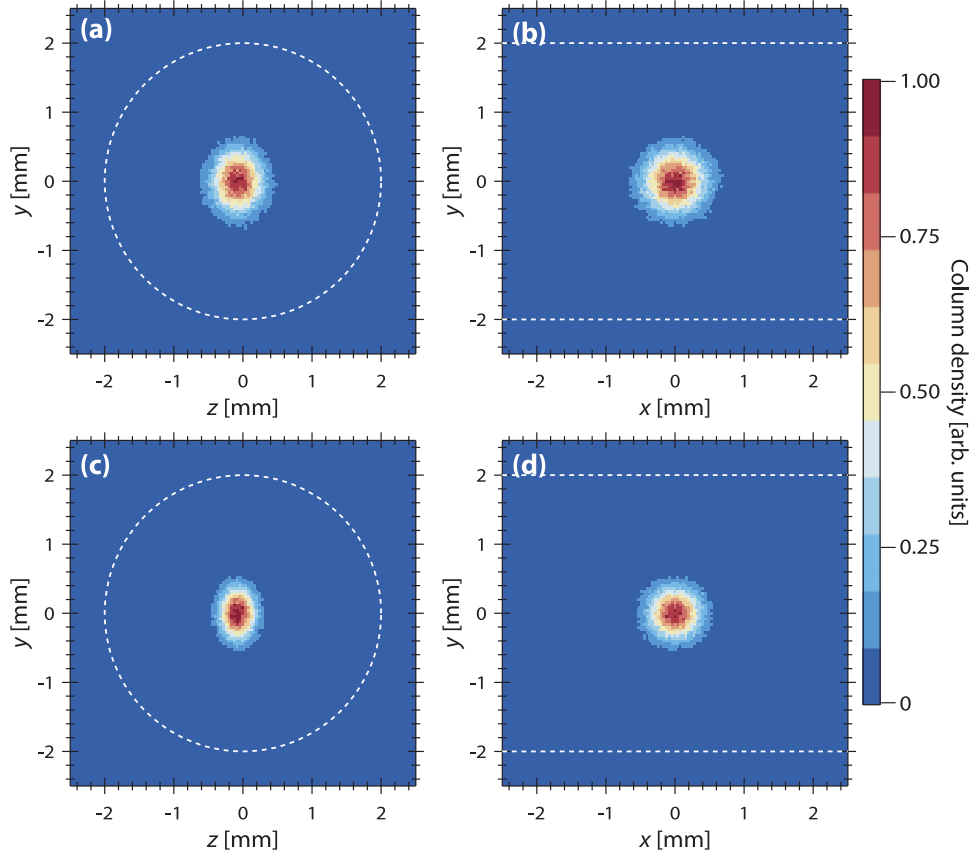


FIG. 4. Simulated column densities of ions in cylindrical trap at a buffer gas pressure of 5×10^{-3} mbar at a temperature of $T = 300$ K. Panels (a) and (b) are for ions of mass 163 amu and charge $q = -1e$ trapped at an RF amplitude of $V = 450$ V and an RF frequency of $\Omega/2\pi = 770$ kHz, and with end-cap potentials of +15 V. The ion cloud is viewed along the x (a) and z (b) axes. Panels (c) and (d) are for ions of mass 479 amu and charge $q = +1e$ trapped at an RF amplitude of $V = 1000$ V and an RF frequency of $\Omega/2\pi = 770$ kHz, and with end-cap potentials of -15 V. The ion cloud is viewed along the x (c) and z (d) axes. The areas bounded by the white dashed curves indicate the areas accessible to the laser light.

0.7 mm and 0.5 mm for ions of mass 163 amu and 479 amu respectively. Hence, both ion clouds occupy a small volume compared to that accessible to the laser light thus ensuring a good overlap between the two.

In Fig. 5, we show the equipotential curves calculated using SIMION for the cylindrical ion trap (full lines). From these simulations, it is clear that the wire mesh grid electrode causes only minor distortions of the field, and only very close

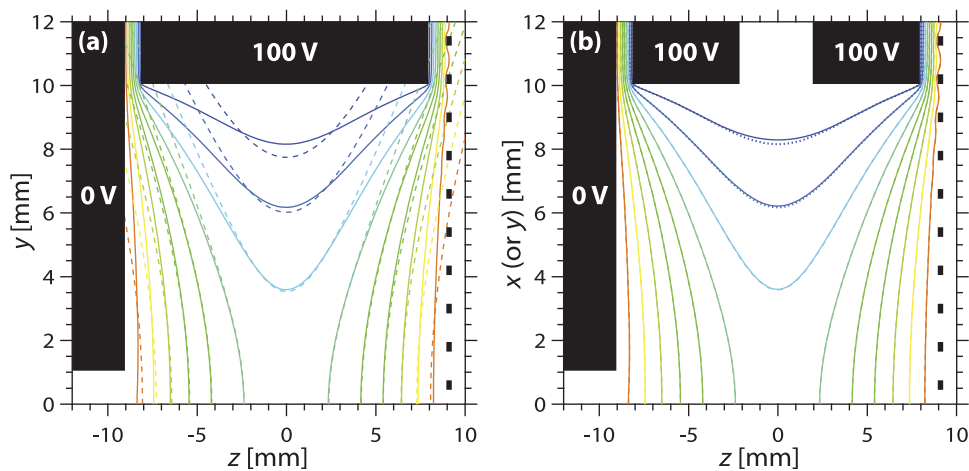


FIG. 5. Calculated equipotential curves of the cylindrical ion trap with a RF potential of 100 V applied to the ring electrode while both end cap electrodes are kept at ground potential. (a) Equipotential curves in the (z, y) plane. The full lines display the equipotential curves in steps of 10 V from 0 V to 100 V. The dashed lines represent the corresponding equipotential curves of the pure quadrupolar potential that provides the best description of the cylindrical trap potential. (b) Equipotential curves in the (z, x) plane. The full lines display the equipotential curves in steps of 10 V from 0 V to 100 V. For comparison, the dotted lines represent the corresponding equipotential curves in the (z, y) plane also shown in (a).

to the grid itself. In Fig. 5(a), an ideal quadrupolar field (dashed lines) is shown for comparison. Although the field in our cylindrical trap deviates from the ideal case close to the electrodes, it is very similar near the center of the trap (recall that the ion cloud diameter is less than 1 mm). In Fig. 5(b), the (very small) effect of the laser access holes can be seen by comparing the equipotential curves in the (z, x) (solid lines, see Fig. 2 for axes) to those in the (z, y) plane (dotted lines, same as solid lines in Fig. 5(a)). Taken together, these simulations demonstrate that our modified cylindrical ion trap should function in much the same way as a traditional Paul trap.

For future experiments, we intend to operate the trap in a mass-selective mode by adding a DC offset U to the RF potential applied to the cylinder electrode, using the octopole as a pre-trap. We have therefore simulated, and present here, the stability diagram for our cylindrical trap, including the effects of the grid electrode and laser access holes. These calculations are also important for establishing the low-mass cutoff in RF-only mode. The stability region of an ideal three-dimensional quadrupole ion trap is described in terms of the a and q parameters defined as³⁹

$$a_z = -2a_r = \frac{-16qeU_0}{m(r_0^2 + 2z_0^2)\Omega^2}, \quad (1)$$

$$q_z = -2q_r = \frac{8qeV}{m(r_0^2 + 2z_0^2)\Omega^2}. \quad (2)$$

Here, m and qe are the ion mass and charge, Ω and V the angular frequency and amplitude of the RF potential, while $U_0 = U - U_{\text{end}}$ is the difference between the static potential applied to the ring electrode, U , and that applied to the end cap electrodes, U_{end} . The parameters, r_0 and z_0 , describe the trap geometry such that $2r_0$ is the innermost diameter of the ring electrode while $2z_0$ is the smallest distance between the end cap electrodes (in analogy with our definition of r_1 and z_1 for the cylindrical ion trap in Fig. 2). In order to apply the well-established theory for ideal quadrupole ion traps to our cylindrical ion trap, a pure quadrupolar potential is fitted to the potential created by the current trap geometry (Fig. 5) which yields the values $r_0 = 9.2$ mm and $z_0 = 8.8$ mm as compared to $r_1 = 10$ mm and $z_1 = 9$ mm. Fig. 6 displays the simulated stability region for two different potentials applied to the end cap electrodes and the theoretical stability regions obtained using the ordinary Mathieu stability diagram with the a and q parameters described above. As can be seen, the theoretical curves provide a very good description of the simulated stability regions. It is also clear that the potential applied to the end cap electrodes must be taken into consideration in mass-selection mode, as this potential offsets the entire stability region. Based on our calculated stability region parameters and the operating range of our RF power supply, we should be able to mass-selectively store ions with masses from about 80 to 270 amu. With no mass-selection, there is in principle no upper limit to the mass of the ion which can be stored.

IV. RESULTS

The fluorescence spectra of three different cations from the family of Rhodamine laser dyes (Rhodamine 6G

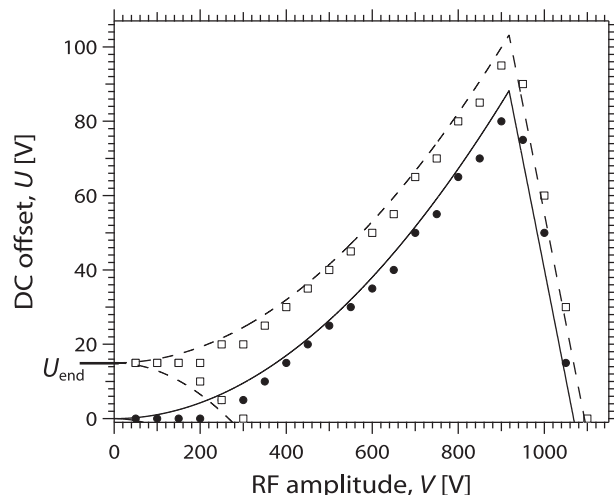


FIG. 6. Simulated stability region for an ion of mass 163 amu in the cylindrical ion trap. The filled circles and open squares represent the simulated stability region with the end cap electrodes kept at ground potential or at +15 V, respectively. Also shown are the two theoretical stability regions determined by use of Eq. (1).

(479 amu), Rhodamine B (479 amu), and Sulphorhodamine B (559 amu)) recorded with our apparatus are shown in Fig. 7. An optical parametric oscillator pumped with a 20 Hz, frequency-tripled, Q-switched Nd:YAG laser (EKSPLA) produced <10-ns pulses which were overlapped with the stored ion cloud. The linewidth of the laser is <5 cm^{-1} , and approximately 0.1 mJ/pulse was delivered to the trap. The ions are accumulated in the trap for approximately 50 ms (one laser cycle time) and then irradiated with a single laser pulse, with the resulting emission being out-coupled and detected as described above. We note that no DC offset was applied to the cylinder electrode ($U = 0$), and thus all ions produced in the ESI source with masses greater than the low mass cutoff (about 160 amu for the RF amplitude used, $V = 1000$ V) were stored. The trap is then emptied by switching off the RF trapping voltage and raising the entrance end-cap voltage

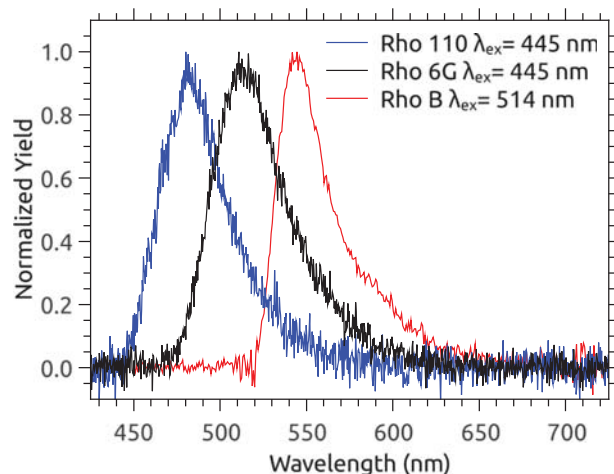


FIG. 7. Dispersed fluorescence spectra of trapped Rhodamine 110, Rhodamine 6G, and Rhodamine B cations excited by a ns-pulsed laser at the indicated wavelengths. Notch filters at corresponding wavelengths were used to reduce scattered laser light.

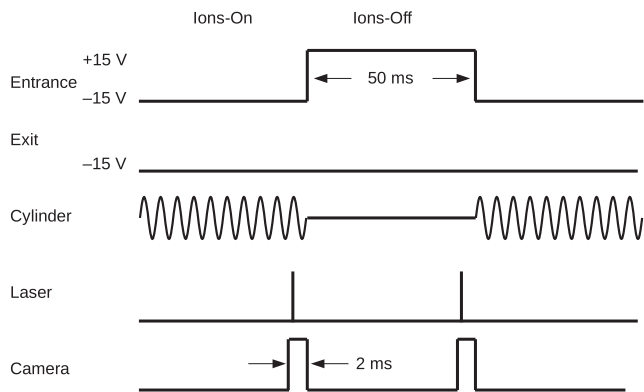


FIG. 8. Timing diagram for measuring fluorescence spectra of positive ions with a 20 Hz ns-pulsed laser.

to +15 V. Another spectrum is then acquired after the next laser shot with no ions in the trap (laser-on, ions-off). The +15 V entrance end-cap voltage prevents ions from entering the trap during the ions-off acquisition. A schematic timing diagram for one such cycle is shown in Fig. 8. This cycle is repeated with alternating acquisitions of ions-on and ions-off spectra to improve signal-to-noise. The spectra in Fig. 7 are the difference between the ions-on and ions-off signals accumulated over 10 000 cycles (about 15 min).

Dispersed fluorescence spectra of Rhodamine B cations were measured with different helium buffer gas pressures in the trap, varying by more than an order of magnitude (Fig. 9). The pressure is not measured directly in the trap for technical reasons, and the gauge reading is therefore a lower bound on the actual trap pressure. Further, these values have not been corrected for gas species. The lowest value was 0.5×10^{-4} mbar and the highest 8.0×10^{-4} mbar. While the total fluorescence signal not surprisingly depends on pressure as there is an optimum pressure for ion trapping, the normalized dispersed fluorescence spectra do not. This clearly shows the advantage of replacing ions between each laser irradiation event. We do not rely on collisional cooling of hot ions, which is needed when the same ions are irradiated (quasi-)continuously.^{10,12}

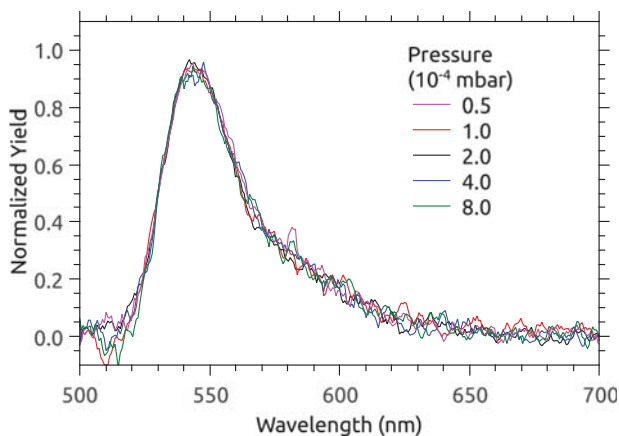


FIG. 9. Dispersed fluorescence spectra of Rhodamine B cations ($\lambda_{ex} = 514$ nm, $250 \mu\text{J}/\text{pulse}$) recorded at different buffer gas pressures (measured outside the trap).

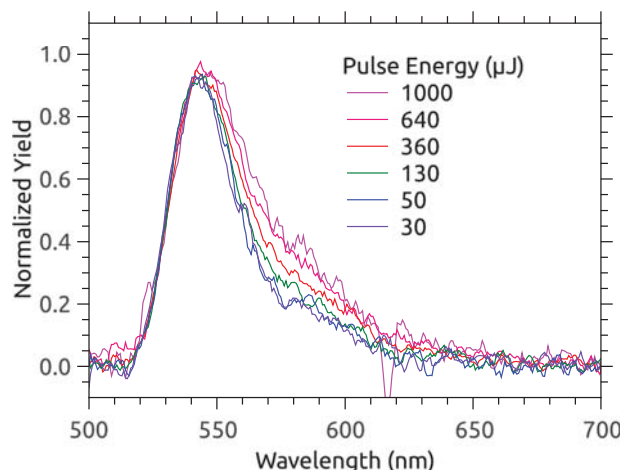


FIG. 10. Dispersed fluorescence spectra of Rhodamine B cations ($\lambda_{ex} = 514$ nm) recorded at different laser intensities (measured following the trap).

It should be noted that by using a high-intensity pulsed laser, multiple photon absorption is possible within a single pulse. This distorts the shape of the fluorescence band, as shown in Fig. 10. Use of high laser pulse energies (measured using a power meter placed after the trap) introduces a shoulder to the red, but the band maximum remains unchanged.

We have also used our setup to measure the fluorescence spectra of ions excited with a continuous wave (cw) laser. In Fig. 11, we show the results of one such experiment, where Rhodamine 110 cations were excited using a blue (405 nm) laser pointer. For these measurements, the camera exposure time was increased to 40 ms, but all other timing parameters (Fig. 8) were kept the same. This measurement demonstrates the sensitivity and flexibility of our apparatus.

To obtain reasonable signal-to-noise ratios for the fluorescence spectra of laser dyes using our pulsed laser, acquisition times of minutes are needed. Hence it takes at least an order of magnitude longer time to record a spectrum with a 20-Hz laser than it does when much higher repetition rate lasers or cw lasers are used. However, our approach has several advantages: (1) The photon collection efficiency is higher than that for other

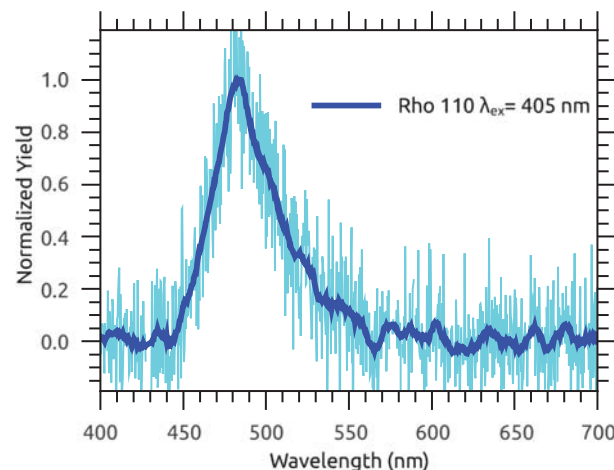


FIG. 11. Dispersed fluorescence spectrum of trapped Rhodamine 110 cations excited with a 5 mW, 405 nm cw laser.

setups where fluorescence is measured from ions produced by ESI. (2) Fluorescence spectra are independent of helium buffer gas pressure as discussed above. (3) The number of photons emitted is directly related to the fluorescence quantum yield and does not change between each laser shot. Hence the time it takes to record a given number of photons emitted from a cloud of trapped ions is linearly proportional to the fluorescence quantum yield. If we assume 100% fluorescence quantum yields for the laser dyes studied, it would take 100 times longer to detect the same number of photons from ions that have a quantum yield of say only 1%. This is a doable experiment. (4) If electron detachment or prompt dissociation occur with a certain probability (P_{loss}), the number of ions, $N(n)$, in a multiple irradiation experiment quickly decreases with the number of laser shots (n): $N(n) = N_0(1 - P_{\text{loss}} \cdot P_{\text{abs}})^n$. Here, N_0 is the initial number of ions in the trap, and P_{abs} is the probability with which the ion absorbs a photon, which depends on the laser power and can be as high as 50% in our experiments (see Section V). Even if $P_{\text{loss}} \cdot P_{\text{abs}}$ is only 1%, N is reduced by more than four orders of magnitudes after $n = 1000$ laser shots, that is after only about 10 μs using a 80 MHz laser. This issue is irrelevant with our setup as long as the fluorescence quantum yield is non-zero. (5) The replacement of ions between each laser shot could be

important for further development of a setup for detecting fluorescence from cryogenically cooled ions. Here cooling times between irradiation events become more crucial, which is an issue that is avoided with a low repetition rate. In such experiments, the octupole ion guide in our ESI source could be used as a pre-trap to maximize the cooling time in the Paul trap, an approach that has been demonstrated previously.⁴⁰

V. DEPLETION MEASUREMENTS

In order to optimize the trapping parameters and laser-ion overlap, we performed photo-depletion measurements on several molecular anions. These experiments also demonstrate the possibilities for utilizing our apparatus for absorption action spectroscopy. For these measurements, the condenser lens and optical assembly is removed and a channeltron detector placed outside the trap facing the grid electrode. While being continuously filled with ions from the electrospray source, the trap is emptied at a repetition rate of 40 Hz. This is accomplished by switching off the RF voltage ($1/e$ fall-time $\sim 3 \mu\text{s}$) and swapping the polarity of the DC voltage on the entrance end-cap from +15 V to -15 V (for negative ions) while keeping the exit end-cap at +15 V. Prior to every

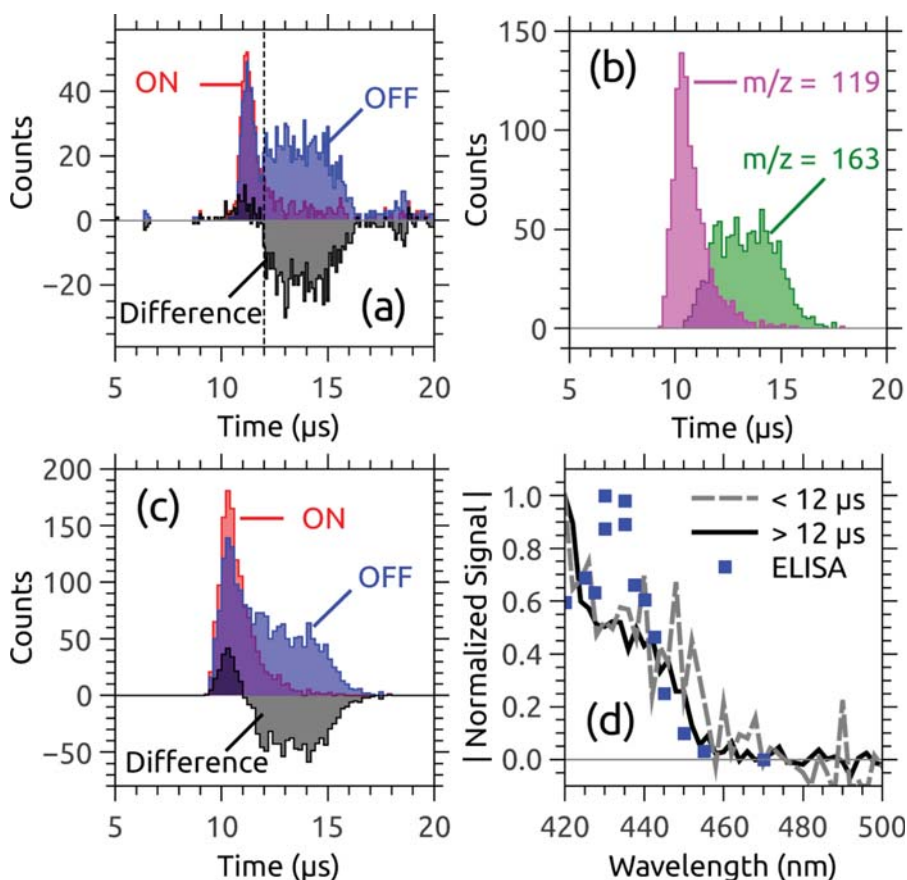


FIG. 12. Action spectroscopy of pCA^- ions stored in the trap. Panel (a) shows the time profiles of the ion bunches ejected from the trap with (ON, red) and without (OFF, blue) laser irradiation, and the difference between the ON and OFF signals (Difference, black) showing clear evidence for photodepletion of the stored pCA^- ions. For times $>12 \mu\text{s}$ the difference signal is negative indicating electron detachment, whereas for times $<12 \mu\text{s}$ the difference signal is positive, suggesting fragmentation of the pCA^- ions. Panel (b) shows simulated time profiles for 1000 ions of mass 163 amu (pCA^- , green) and 119 amu ($[\text{pCA-CO}_2]^-$, pink) stored in the trap using the same parameters as the experiment. Panel (c) are hypothetical ON, OFF and difference profiles (same labelling as (a)) based on the simulated time profiles in (b). Panel (d) shows the normalized magnitude of the experimental difference signal as a function of excitation wavelength for times $>12 \mu\text{s}$ (black) and $<12 \mu\text{s}$ (gray). Also shown are action spectra recorded at the ELISA storage ring.⁴²

second emptying, the ion cloud is irradiated with a single laser pulse. The neutralization of the stored anions, whether by direct electron detachment or delayed emission, gives rise to a difference in the number of ions counted by the channeltron between the laser-on and laser-off measurements.

This difference signal can be clearly seen in Fig. 12(a), where we show the ion bunch profiles for deprotonated *trans-p*-coumaric acid (pCA^-) ejected from the trap with and without 422 nm laser excitation prior to extraction. The difference signal is negative for times (measured from when the trigger signal to empty the trap is sent) greater than 12 μs , due to photodepletion of the pCA^- ions. The depletion at this wavelength is greater than 50% of the stored ion population, implying excellent overlap of the laser beam with the ion cloud. The large peak in the time profile between 10 and 12 μs is presumably due to the presence in the trap of ions other than pCA^- (no mass-selection was applied in these experiments) which are not depleted by irradiation at these wavelengths. Indeed, the difference signal for times $<12 \mu\text{s}$ is slightly positive, suggesting that these co-stored ions could be charged fragments of pCA^- . Time-resolved photodissociation experiments⁴¹ have found that 70% of photo-excited pCA^- ions (mass 163 amu) decay by vibrational auto-detachment, with the rest undergoing dissociation, losing a CO_2 group and yielding a fragment with a mass of 119 amu. In Fig. 12(b), we show time profiles simulated in SIMION using the same trapping parameters as in the experiment, but assuming that only ions of mass 163 or 119 amu were stored. Fig. 12(c) shows hypothetical laser-on, laser-off, and difference signals assuming equal initial populations of mass 163 and 119, 100% depletion of mass 163 with 30% fragmentation to mass 119. The agreement with the measured time profiles is striking, and strongly suggests that the difference in time profiles can be viewed as a crude time-of-flight mass spectrum. Fig. 12(d) shows the magnitude of the pCA^- depletion signal (for times $>12 \mu\text{s}$) and the positive difference signal (formation of fragments with mass 119 amu, times $<12 \mu\text{s}$) as functions of the laser wavelength, corrected for laser power and normalized to the signal at 420 nm. The spectra are identical, and in good agreement with earlier gas-phase absorption spectra measured using the electrostatic storage ring ELISA.⁴² While far from definitive, these preliminary results point to exciting possibilities for combining photo-induced dissociation mass spectroscopy experiments with fluorescence measurements using this apparatus.

Another example demonstrating the versatility of our apparatus is shown in Fig. 13, where we show action spectra for deprotonated *trans*-thiophenyl-*p*-coumarate (pCT^-) ions. In this case, photo-excitation has been shown to lead to the fast (100 ns timescale) loss of the thiophenyl group with a high Kinetic Energy Release (KER).⁴¹ In our experiments, this high KER causes the fragments to no longer be stored. These fragments are ejected from the trap shortly after the laser pulse in characteristic microbunches in phase with the RF voltage, as shown in the inset of Fig. 13. The two action spectra, measured by monitoring the depletion of the stored pCT^- ions and the ejection of fragment ions, are both in good agreement with previous measurements at ELISA.⁴²

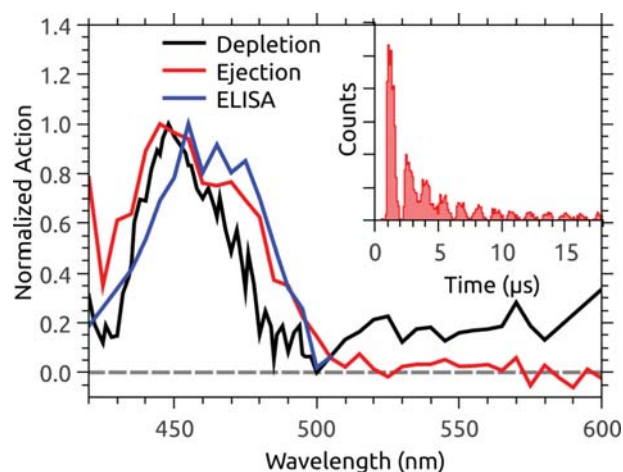


FIG. 13. Action spectra for the pCT^- ion stored in the trap. The action spectrum recorded at the ELISA storage ring is also shown for comparison. The inset shows the ejection of high kinetic energy fragments from the trap in phase with the RF trapping voltage.

VI. CONCLUSION

We have presented a thorough description of our home-built apparatus for measuring luminescence spectra of trapped molecular ions produced by electrospray ionization (ESI). Our design is based on a modified Paul trap with a cylindrical geometry and a specially designed end-cap for efficient light collection using a condenser lens mounted as close as possible to the emitting ions. The high collection efficiency of our setup permits the use of a low repetition rate (20 Hz) laser for excitation, allowing the trap to be emptied and refilled between each laser shot. In this way, the ions are only irradiated once, eliminating the considerations surrounding the cooling ions between excitation events and the buildup of photoproducts that can occur under continuous irradiation. We have furthermore demonstrated that our setup can be used to measure the absorption spectra of trapped ions. We refer to the apparatus as LUNA, or luminescence instrument in Aarhus, after the latin name for the Moon, which lights up the night sky.

ACKNOWLEDGMENTS

We gratefully acknowledge support from the Carlsberg Foundation (Grant No. 2013_01_0180), the Villum Foundation, the Danish Council for Independent Research (Grant No. 4181-000488), and the Lundbeck Foundation. The authors also thank Henrik B. Pedersen for technical support in connection with our numerical simulations.

¹S. Brøndsted Nielsen and J. A. Wyer, *Photophysics of Ionic Biochromophores* (Springer, 2013).

²S. M. Wellman and R. A. Jockusch, *J. Phys. Chem. A* **119**, 6333 (2015).

³G. Féraud, M. Berdakin, C. Dedonder, C. Juvet, and G. A. Pino, *J. Phys. Chem. B* **119**, 2219 (2014).

⁴F. Rosu, V. Gabelica, E. De Pauw, R. Antoine, M. Broyer, and P. Dugourd, *J. Phys. Chem. A* **116**, 5383 (2012).

⁵J. C. Marcum, A. Halevi, and J. M. Weber, *Phys. Chem. Chem. Phys.* **11**, 1740 (2009).

⁶J. Rajput, D. B. Rahbek, L. H. Andersen, A. Hirshfeld, M. Sheves, P. Altoè, G. Orlandi, and M. Garavelli, *Angew. Chem., Int. Ed.* **49**, 1790 (2010).

- ⁷S. Brøndsted Nielsen, M. Brøndsted Nielsen, and A. Rubio, *Acc. Chem. Res.* **47**, 1417 (2014).
- ⁸J. Friedrich, J. Fu, C. L. Hendrickson, A. G. Marshall, and Y.-S. Wang, *Rev. Sci. Instrum.* **75**, 4511 (2004).
- ⁹J. T. Khoury, S. E. Rodriguez-Cruz, and J. H. Parks, *J. Am. Soc. Mass Spectrom.* **13**, 696 (2002).
- ¹⁰N. A. Sassin, S. C. Everhart, B. B. Dangi, K. M. Ervin, and J. I. Cline, *J. Am. Soc. Mass Spectrom.* **20**, 96 (2009).
- ¹¹M. W. Forbes and R. A. Jockusch, *J. Am. Soc. Mass Spectrom.* **22**, 93 (2011).
- ¹²Q. Bian, M. W. Forbes, F. O. Talbot, and R. A. Jockusch, *Phys. Chem. Chem. Phys.* **12**, 2590 (2010).
- ¹³M. Kordel, D. Schooss, C. Neiss, L. Walter, and M. M. Kappes, *J. Phys. Chem. A* **114**, 5509 (2010).
- ¹⁴J.-F. Greisch, M. E. Harding, M. Kordel, W. Klopper, M. M. Kappes, and D. Schooss, *Phys. Chem. Chem. Phys.* **15**, 8162 (2013).
- ¹⁵K. Chingin, R. M. Balabin, V. Frankevich, H. Chen, K. Barylyuk, R. Nieckarz, A. Fedorov, and R. Zenobi, *Phys. Chem. Chem. Phys.* **12**, 14121 (2010).
- ¹⁶K. Chingin, H. Chen, G. Gamez, and R. Zenobi, *J. Am. Soc. Mass Spectrom.* **20**, 1731 (2009).
- ¹⁷M. F. Czar and R. A. Jockusch, *ChemPhysChem* **14**, 1138 (2013).
- ¹⁸A. M. Nagy, F. O. Talbot, M. F. Czar, and R. A. Jockusch, *J. Photochem. Photobiol., A* **244**, 47 (2012).
- ¹⁹S. K. Sahoo and R. A. Jockusch, *J. Photochem. Photobiol., A* **220**, 173 (2011).
- ²⁰P. D. McQueen, S. Sahoo, H. Yao, and R. A. Jockusch, *Angew. Chem., Int. Ed.* **49**, 9193 (2010).
- ²¹H. Yao and R. A. Jockusch, *J. Phys. Chem. A* **117**, 1351 (2013).
- ²²A. S. Danell and J. H. Parks, *Int. J. Mass Spectrom.* **229**, 35 (2003).
- ²³M. Dashtiev, V. Azov, V. Frankevich, L. Scharfenberg, and R. Zenobi, *J. Am. Soc. Mass Spectrom.* **16**, 1481 (2005).
- ²⁴F. O. Talbot, A. Rullo, H. Yao, and R. A. Jockusch, *J. Am. Chem. Soc.* **132**, 16156 (2010).
- ²⁵A. T. Iavarone and J. H. Parks, *J. Am. Chem. Soc.* **127**, 8606 (2005).
- ²⁶A. T. Iavarone, A. Patriksson, D. van der Spoel, and J. H. Parks, *J. Am. Chem. Soc.* **129**, 6726 (2007).
- ²⁷A. T. Iavarone, D. Duft, and J. H. Parks, *J. Phys. Chem. A* **110**, 12714 (2006).
- ²⁸A. T. Iavarone, J. Meinen, S. Schulze, and J. H. Parks, *Int. J. Mass Spectrom.* **253**, 172 (2006).
- ²⁹X. Shi and J. H. Parks, *J. Am. Soc. Mass Spectrom.* **21**, 707 (2010).
- ³⁰X. Shi, D. Duft, and J. H. Parks, *J. Phys. Chem. B* **112**, 12801 (2008).
- ³¹M. F. Czar, F. Zosel, I. König, D. Nettels, B. Wunderlich, B. Schuler, A. Zarrine-Afsar, and R. A. Jockusch, *Anal. Chem.* **87**, 7559 (2015).
- ³²J. M. Wells, E. R. Badman, and R. G. Cooks, *Anal. Chem.* **70**, 438 (1998).
- ³³F. J. Grieman, B. H. Mahan, and A. O'Keefe, *J. Chem. Phys.* **72**, 4246 (1980).
- ³⁴F. J. Grieman, B. H. Mahan, A. O'Keefe, and J. S. Winn, *Faraday Discuss.* **71**, 191 (1981).
- ³⁵B. H. Mahan and A. O'Keefe, *J. Chem. Phys.* **74**, 5606 (1981).
- ³⁶F. J. Grieman, B. H. Mahan, and A. O'Keefe, *J. Chem. Phys.* **74**, 857 (1981).
- ³⁷J. U. Andersen, P. Hvelplund, S. Brøndsted Nielsen, S. Tomita, H. Wahlgreen, S. P. Møller, U. V. Pedersen, J. S. Forster, and T. J. D. Jørgensen, *Rev. Sci. Instrum.* **73**, 1284 (2002).
- ³⁸A. D. Appelhans and D. A. Dahl, *Int. J. Mass Spectrom.* **216**, 269 (2002).
- ³⁹R. E. March and J. F. Todd, *Quadrupole Ion Trap Mass Spectrometry* (John Wiley & Sons, 2005), Vol. 165.
- ⁴⁰J. A. Wyer and S. Brøndsted Nielsen, *Angew. Chem., Int. Ed.* **51**, 10256 (2012).
- ⁴¹L. Lammich, J. Rajput, and L. H. Andersen, *Phys. Rev. E* **78**, 051916 (2008).
- ⁴²I. B. Nielsen, S. Boyé-Péronne, M. O. A. El Ghazaly, M. B. Kristensen, S. Brøndsted Nielsen, and L. Andersen, *Biophys. J.* **89**, 2597 (2005).

Nile blue shows its true colors in gas-phase absorption and luminescence ion spectroscopy

M. H. Stockett,^{a)} J. Houmøller, and S. Brøndsted Nielsen
Department of Physics and Astronomy, Aarhus University, Aarhus, Denmark

(Received 15 July 2016; accepted 26 August 2016; published online 9 September 2016)

Nile blue is used extensively in biology as a histological stain and fluorescent probe. Its absorption and emission spectra are strongly solvent dependent, with variations larger than 100 nm. The molecule is charged due to an iminium group, and it is therefore an obvious target for gas-phase ion spectroscopy. Here we report the absorption and emission spectra of the mass-selected bare ions isolated *in vacuo*, and based on our results we revisit the interpretation of solution-phase spectra. An accelerator mass spectrometer was used for absorption spectroscopy where the absorption is represented by the yield of photofragment ions versus excitation wavelength (action spectroscopy). The luminescence experiments were done with a newly built ion trap setup equipped with an electrospray ion source, and some details on the mass selection technique will be given which have not been described before. *In vacuo*, the absorption and emission maxima are at 580 ± 10 nm and 628 ± 1 nm. These values are somewhat blue-shifted relative to those obtained in most solvents; however, they are much further to the red than those in some of the most non-polar solvents. Furthermore, the Stokes shift in the gas phase (1300 cm^{-1}) is much smaller than that in these non-polar solvents but similar to that in polar ones. An explanation based on charge localization by solvent dipoles, or by counterions in some non-polar solvents, can fully account for these findings. Hence in the case of ions, it is nontrivial to establish intrinsic electronic transition energies from solvatochromic shifts alone. *Published by AIP Publishing.* [<http://dx.doi.org/10.1063/1.4962364>]

I. INTRODUCTION

Nile blue (NB) is a histological stain that has found wide applications as a fluorescent probe¹ and in cell biology.² It is a phenoxazinium and carries one positive charge that is delocalized over the whole molecule; two important resonance formulas are shown in Fig. 1 where either the diethylamino substituent or the amino substituent is an iminium. The heterocyclic oxygen bridges the conjugation and is also partly positively charged. This electronic delocalization gives rise to strong absorption in the visible region and thus intensely colored solutions. NB is soluble in polar solvents like water, largely because of the positive charge, which can be important for some biotechnological applications.

The spectroscopic properties of Nile blue, the structurally similar (but neutral) Nile red, and their derivatives have been investigated in great detail.^{3–8} The electronic transition energies of NB decrease as the solvent polarity increases, e.g., absorption (emission) band maxima are 473 nm (546 nm) in *n*-hexane and 635 nm (674 nm) in water.⁸ The fluorescence quantum yield is also solvent dependent, with measured values ranging from 0.01 in water⁹ to 0.27 in methanol and 0.50 in 1,2-dichloroethane.¹⁰ However, these effects do not have a simple dependence on solvent polarity, which has led to considerable disagreement over the character of the transition. This matter is complicated by the possibility, recognized by several authors,^{5,7} that

heterogeneous ion-counterion pairs may be formed in some non-polar solvents; this issue will be addressed further here.

Gas-phase ion spectroscopy is necessary to firmly establish the intrinsic spectroscopic properties of NB in the absence of environmental perturbations induced by solvent molecules or counter-anions. Experimental gas-phase data are also useful to benchmark quantum chemical calculations of the NB optical properties.^{3,6} In this work, we have studied the absorption by NB isolated *in vacuo* using Photo-Induced Dissociation (PID) action spectroscopy as well as its luminescence spectrum after photo-excitation utilizing a new instrument in which a quadrupole ion trap is coupled to an optical spectrometer.¹¹ We note that earlier gas-phase spectroscopy of NB is limited to the infrared multiple photon dissociation (IRMPD) spectrum revealing vibrational frequencies.⁴

II. EXPERIMENTAL DETAILS

In the study of complex molecules in the gas-phase, the density of ions *in vacuo* is too low for traditional transmission experiments employing Beer's law. Instead, action spectroscopy is performed using specially designed mass spectrometers. Photon absorption is identified indirectly from the production of ion fragments, neutrals, or electrons whose yields are monitored versus excitation wavelength. Such a spectrum is taken to represent the electronic absorption spectrum.

^{a)} Author to whom correspondence should be addressed. Electronic mail: stockett@phys.au.dk

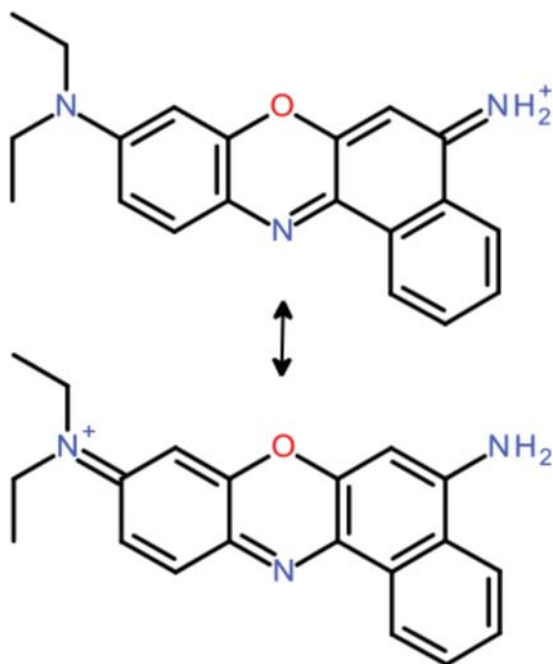


FIG. 1. Dominant resonance formulas of Nile blue.

The accelerator mass spectrometer instrument for gas-phase ion absorption spectroscopy has been described in detail previously.^{12,13} Briefly, NB was produced in gas phase by electrospray ionization (ESI) of NB dissolved in methanol. Ions were accumulated in an octopole ion trap that was emptied every 25 ms. Ions were accelerated to 50 keV kinetic energies, and those of interest were selected by a bending magnet by their mass to charge ratio ($m/z = 318$ amu for NB). Every second ion bunch was irradiated with visible light from a 20 Hz laser system (EKSPLA). The fundamental from an Nd:YAG laser was frequency tripled to 355 nm, which was used to pump an optical parametric oscillator (OPO) to produce visible light. Neutral density filters were used to reduce laser power when needed. Fragment ions produced were separated by a hemispherical electrostatic analyzer and counted by a channeltron detector. Synchronization and timing were controlled by a LabView program.

In the case of luminescence spectroscopy, photons emitted by laser-excited ions are collected and detected. This is nontrivial due again to the low number of ions but also due to limited optical access to the ions in the radio-frequency (RF)

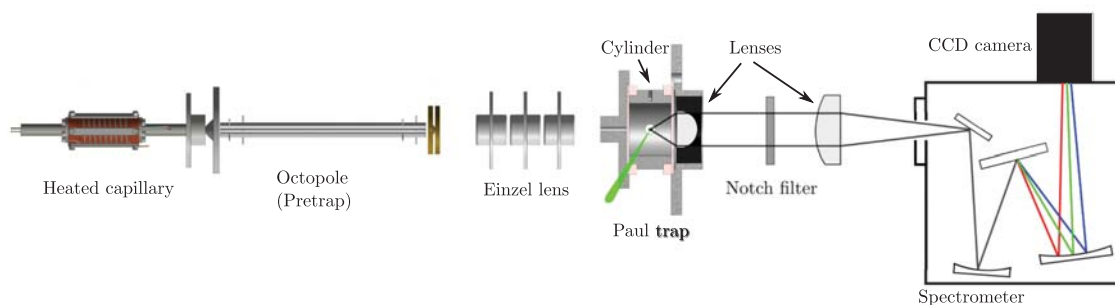
ion traps typically used in these experiments.^{14,15} It is crucial to diminish the scattered light to an absolute minimum.¹⁶ Our setup for luminescence experiments (LUNA) has also been described previously.¹¹ The heart of this instrument, shown schematically in Fig. 2, is a custom-made cylindrical Paul trap with integrated optics and a large light-collection solid angle. We have implemented a new scheme for mass selection of trapped ions prior laser irradiation which is suitable for use with low repetition rate pulsed lasers such as that employed here (20 Hz). In contrast to other researchers using cw or MHz repetition rate lasers,^{14,17} the ions in our trap are irradiated by a single laser shot before the trap is emptied and refilled. This eliminates problems like photobleaching and the need for fine-tuning of the laser power and buffer gas pressure.¹⁸ The details of this scheme are found in the [supplementary material](#).

Ions produced by ESI are accumulated in an octopole for 50 ms. The ion bunch is then transferred to the Paul trap, where the ions are cooled to the center in collisions with helium buffer gas. After a certain storage time (~ 1 ms), the DC voltage on the cylinder electrode is changed to mass select the ions of interest (see the [supplementary material](#)). Next follows the laser excitation pulse (from the same 20 Hz repetition rate laser system described above) and the detection of fluorescence. To correct for scattered laser light and other background sources, the experiment is repeated in alternating sets of 100 cycles with ions in the trap followed by 100 cycles with no ions (the trap RF voltage is switched off). The difference between the “ions on” and “ions off” acquisitions is the fluorescence signal.

III. RESULTS AND DISCUSSION

A. Photo-induced dissociation action spectroscopy

Excitation of Nile blue at 560 nm leads to one dominant fragment ion ($m/z = 274$ amu), formed after loss of C_3H_8 (44 amu) from the parent ion (318 amu) via a 1,2-elimination process within the diethylamino group. This dissociation channel was also seen to dominate after absorption of multiple IR photons.⁴ Minor fragment ions are at $m/z = 303$ [0.08]: loss of CH_3 , 289 [0.08]: loss of CH_3CH_2 , 260 [0.03]: loss of two CH_3CH_2 , and 246 [0.05]: loss of $N(CH_2CH_3)_2$, with their yields given relative to $m/z = 274$ amu in brackets. The mass resolution is low and the given masses could be off by 1 amu. Laser power dependence experiments were

FIG. 2. The luminescence in Aarhus instrument, LUNA.¹¹

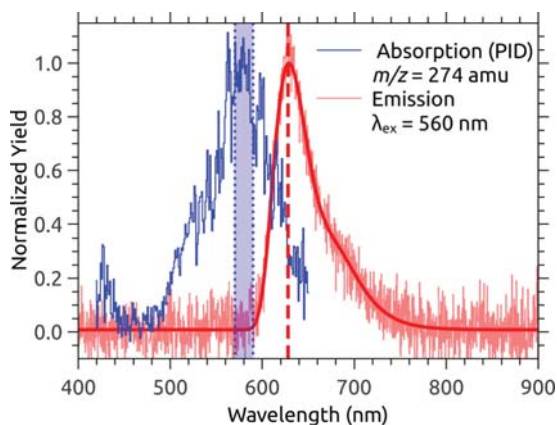


FIG. 3. Absorption (blue) and emission (red) spectra of NB *in vacuo*. The solid red line is a fit to the emission data. The vertical lines indicate the absorption and emission band maxima and their uncertainties.

performed to establish the number of photons absorbed by the parent ions in order to form each fragment within the instrumental time scale of 20 μ s. For $m/z = 274$ and 303 amu, the yield increased quadratically with the laser power (shown for $m/z = 274$ in Fig. S3 of the [supplementary material](#)), indicating a 2-photon process. At high laser power, some saturation occurred. All other fragments appeared to result from the absorption of 3 or more photons. For the wavelength scan experiments, neutral density filters were therefore used to reduce laser power where needed in the spectrum. Several scans (more than ten) were combined to give the action spectrum for the formation of $m/z = 274$ in Fig. 3; each data point is obtained after subtraction of “laser off” signal from “laser on” signal divided by the number of photons in the pulse raised to second order (to account for the 2-photon power dependence and the variation of the laser power across the tuning range). It is evident that absorption occurs over a broad region from 480 nm to 650 nm. Similar action spectra were obtained for the other fragment ions (not shown). The absorption band maximum is at about 580 nm with an uncertainty of ± 10 nm, as indicated by the blue shaded area in Fig. 3.

Time-Dependent Density Functional Theory (TD-DFT) calculations predict a gas-phase absorption band maximum of 512 nm for NB cations,⁶ while the dynamic approach taken by Marazzi *et al.* predicts 545 or 585 nm, depending on the functional used. The rather large differences between theoretical methods and between theory and experiment illustrate the importance of performing such experiments in the gas-phase.

B. Luminescence spectroscopy of Nile blue cations *in vacuo*

NB ions were mass-selected and stored in the Paul trap, followed by irradiation with laser light. Two excitation wavelengths were used, 560 nm and 515 nm, within the absorption band of the ions (*vide supra*). The luminescence spectrum after 560 nm excitation is shown in Fig. 3. The solid line is a fit to the data using a sum of two extreme value functions,

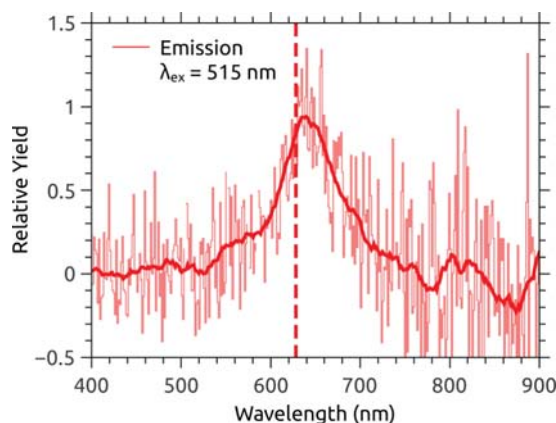


FIG. 4. Emission from NB ions *in vacuo* with $\lambda_{\text{ex}} = 515$ nm. The solid line is a 50-point Savitzky-Golay smoothing. The vertical line indicates the emission band maximum obtained from the $\lambda_{\text{ex}} = 560$ nm spectrum (Fig. 3).

$$y = A \times \exp[-\exp((x - x_0)/w) - (x - x_0)/(w)] \quad (1)$$

as recommended by Greisch *et al.*¹⁹ The position of the band maximum obtained from this fit is 628 ± 1 nm. There is a small shoulder at 668 nm due to a vibronic transition with a vibrational frequency of about 1400 cm^{-1} . This shoulder is also reflected in the absorption spectrum at around 536 nm. The spectrum obtained after 515 nm excitation (Fig. 4) is similar but of lower quality as this wavelength is in the tail of the absorption band.

Comparing the maxima of the gas-phase absorption and emission spectra (Fig. 3), the Stokes shift is about $1300 \pm 300 \text{ cm}^{-1}$. This is significantly greater than that seen in other gas-phase ion experiments, e.g., $< 500 \text{ cm}^{-1}$ for rhodamine cations.²⁰ According to resonance Raman spectroscopy of NB in solution, a 590 cm^{-1} vibrational mode is strongly coupled with the electronic transition.²¹ A simple scheme can therefore account for the shift: absorption involves the 590 cm^{-1} mode with $v' - v = +1$ (v' and v are excited state and ground state vibrational quantum numbers) followed by internal vibrational redistribution (IVR) and $\Delta v' = -1$. According to the mirror-image rule, the emission will then be associated with $v' - v = -1$. As a result, the difference between absorption and emission is two quanta of 590 cm^{-1} , i.e., 1180 cm^{-1} . This number is close to the measured shift of 1300 cm^{-1} , noting that the frequency may be different for the gas-phase ion than in solution.

C. Comparison with spectroscopic data for Nile blue in solution

Dutt *et al.*,²² Krihak *et al.*,²³ Jose and Burgess,⁸ and Gilani *et al.*⁵ give values for the absorption and emission band maxima of NB in different solvents, mostly with chloride or perchlorate counter-anions. In Fig. 5 we have plotted these values versus the normalized solvent polarity, E_T^N . This scale is based on the $E_T(30)$ scale but normalized so that tetramethylsilane has a polarity of 0 and water 1.²⁴ The $E_T(30)$ values refer to excitation energies of propidium phenol betaine in different solvents.²⁵ This indicator molecule is a neutral zwitterion which experiences a significant decrease in

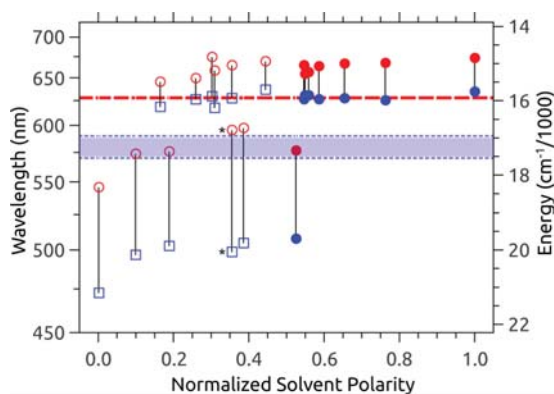


FIG. 5. Absorption (blue) and emission (red) maxima of NB in various solvents. Filled symbols indicate protic solvents. The horizontal lines indicate the gas phase values and their uncertainties.

dipole moment upon excitation (charge transfer (CT)). In the figure, horizontal lines indicate the absorption and emission maxima measured *in vacuo*. The E_T^N value for vacuum should be close to zero. In cases where multiple authors report values for a common solvent, the average has been plotted. In the case of acetone, Jose *et al.* give significantly different values than the other authors (the counterion is not given in this case); these are denoted with asterisks.

We make the following observations:

1. The solution-phase data fall in two groups: one group of solutions display absorption at about 625 nm and emission at about 660 nm, while a group of (mostly) non-polar solvents has larger variations in the band maxima which are much further to the blue. 1-decanol is the only protic solvent, and the only one with $E_T^N > 0.5$, to fall into this latter “blue” group.
2. The Stokes shifts are significantly larger for solvents in the blue group than in the red group (2800 cm^{-1} compared to 780 cm^{-1}); this does not depend on whether the solvent is protic or aprotic.
3. The gas-phase band maxima are in between the two groups and display a Stokes shift of 1300 cm^{-1} , closer to that seen for the red group than to the blue group.

In general,²⁶ one expects the absorption and emission of solvated molecules to be red-shifted relative to their gas-phase values. This is because the excited state is usually more stabilized by the instantaneously polarizable medium. Following absorption, the excited state energy may be further reduced (and the ground state energy raised) by the re-orientation of the solvent molecules. This increases the Stokes shift, an effect that increases with increasing solvent polarity. It is thus highly unusual that a non-polar solvent such as *n*-hexane ($E_T^N = 0.009$) should give transitions which are strongly *blue-shifted*, and with much larger Stokes shifts, compared to the gas phase and to more polar solvents. These measurements indicate that NB does not exist as a solvated ion in this solvent, or in the other non-polar solvents in the blue group. Indeed, the data are easily understood in terms of heterogeneous ion-counterion pair formation for solvents in this group, which would account both for blue-shifted absorption and a large Stokes

shift. A similar argument can also explain the red-shifted absorption in the other solvents relative to the gas-phase data.

There are two opposing effects on transition energies due to specific interactions with a nearby counter-ion or a single solvent dipole. In both cases, the charge is localized in favor of one of the resonance formulas in Fig. 1, which results in a charge-transfer-like transition as negative charge density moves towards the positive end upon excitation. Charge-transfer (CT) transitions are normally to the red of transitions that are delocalized over the whole molecule before and after. For example, the CT transition of the *meta*-nitrophenolate anion absorbs 6500 cm^{-1} to the red of the *para*- isomer (which has no CT character) *in vacuo*.²⁷

On the other hand, the electrostatic interaction energy between the ion and the counter-ion/dipole is diminished in the excited state, which causes a blue-shift. For the ion pair, the lowering of the interaction energy between the charge site and the counter-anion can easily be more important than the redshift due to a CT-like transition. For example, the Coulomb energy between an iminium group and a nearby chloride ion at a distance of 3 \AA is nearly 40000 cm^{-1} . Even a partial loss of this energy upon a CT-like excitation would cause a significant blue-shift compared to gas phase. Furthermore, the less-positive charge on the iminium would cause partial separation of the ion pair in the excited state. This would lead to a large Stokes shift as the geometry would be wrong for the ground state ion pair complex (the excited energy state is lowered while the ground state energy is increased).

The situation in a polar solvent is more subtle. The electrostatic interaction energy due to specific interactions with a solvent dipole is weaker than in the counterion case, and the competition with the effect of charge localization transition energies is more closely balanced. In the nitrophenolate example, addition of a single water molecule to the *meta*-nitrophenolate anion blue-shifts the CT band by 1800 cm^{-1} , while *para*-nitrophenolate is *red-shifted* by 1050 cm^{-1} .^{28,29} In some cases where the ion has no permanent dipole moment, binding of a single solvent dipole has no effect on the absorption band.^{30,31} Furthermore, in a bulk solvent, there will be favorable interactions between the positive charge that is generated by the CT transition and nearby solvent dipoles, which may reduce or eliminate the loss of electrostatic interaction upon excitation. Taken together, the effect of specific interactions with a nearby solvent molecule can be expected to give an overall red-shift.

The Stokes shift in the polar solvents is slightly smaller than in gas phase which implies that there is little or no reorientation of the solvent dipoles for these solvents. This contrasts with the interpretation of Gilani *et al.* where solvent reorientation is considered important due to a large apparent increase in dipole moment in the excited state compared to the ground state.⁵ The ground and excited state dipole moments were obtained from the solvatochromic methods but with large uncertainties. Dutt *et al.* also find a large increase in dipole moment using solvatochromic methods.²² On the other hand, recent calculations by Marazzi *et al.* using a polarizable continuum model for the solvent find that

the dipole moment of NB *decreases* in the excited state.³ While they do not explicitly calculate excited state dipole moments, Fleming *et al.* find a high degree of orbital overlap between the ground and excited states of NB (again using a continuum model), indicating little change in dipole moment.⁶ This suggests that charge localization by specific interactions with nearby solvent molecules may play an important role.

Excluding the solvents where ion-counterion pair formation is suspected based on comparison to gas-phase data, NB appears to be only weakly solvatochromic. The average red-shift in the absorption band maximum in solution is about 1300 cm⁻¹. This is close to the red-shift of the (non-CT) transition in *para*-nitrophenolate given by the addition of a single solvent molecule. More gas-phase experiments are needed to determine the effect of specific interactions with solvent molecules on complex ions like Nile blue.

IV. CONCLUSION

It can be difficult to interpret and model the effect of solvation on the optical properties of a complex molecule. This is especially true in the case of ions, where interactions with counter-ions and solvent dipoles are strong and can perturb the ion's energy structure in ways that are difficult to predict quantitatively. Gas-phase ion spectroscopy can be used to determine intrinsic absorption and luminescence spectra in the absence of these perturbations. The continued development of gas-phase ion spectroscopy techniques is increasing the quality and availability of these spectra, which serve as a baseline for comparison to solution and even more complex situations like biological media.³² Furthermore, theoretical calculations of complex ions are much more straightforward to carry out without considering a solvent environment, and gas-phase experiments are crucial benchmarks for such calculations. In the case of Nile blue, differing interpretations have been applied to the available experimental and theoretical data.^{3,5,6,8} Our new gas-phase spectra allow us to re-evaluate these interpretations and place all the available data in a self-consistent framework which can explain many of the unusual characteristics of Nile blue.

SUPPLEMENTARY MATERIAL

See [supplementary material](#) for a detailed description of the mass selection scheme developed for use with low repetition rate pulsed lasers, as well as photo-induced dissociation laser power dependence measurements.

ACKNOWLEDGMENTS

S.B.N. acknowledges support from the Danish Council for Independent Research (Grant No. 4181-00048B), the Villum Foundation, and the Carlsberg Foundation.

- ¹X.-D. Liu, C. Fan, R. Sun, Y.-J. Xu, and J.-F. Ge, *Anal. Bioanal. Chem.* **406**, 7059 (2014).
- ²H. Ju, Y. Ye, and Y. Zhu, *Electrochim. Acta* **50**, 1361 (2005).
- ³M. Marazzi, H. Gattuso, and A. Monari, *Theor. Chem. Acc.* **135**, 57 (2016).
- ⁴R. J. Nieckarz, J. Oomens, G. Berden, P. Sagulenko, and R. Zenobi, *Phys. Chem. Chem. Phys.* **15**, 5049 (2013).
- ⁵A. G. Gilani, S. Hosseini, M. Moghadam, and E. Alizadeh, *Spectrochim. Acta, Part A* **89**, 231 (2012).
- ⁶S. Fleming, A. Mills, and T. Tuttle, *Beilstein J. Org. Chem.* **7**, 432 (2011).
- ⁷J. Jose, Y. Ueno, and K. Burgess, *Chem. - Eur. J.* **15**, 418 (2009).
- ⁸J. Jose and K. Burgess, *Tetrahedron* **62**, 11021 (2006).
- ⁹H. Oliveira, A. Camargo, L. Macedo, M. Gehlen, and A. Da Silva, *Spectrochim. Acta, Part A* **58**, 3103 (2002).
- ¹⁰R. Sens and K. H. Drexhage, *J. Lumin.* **24**, 709 (1981).
- ¹¹M. H. Stockett, J. Houmøller, K. Støchkel, A. Svendsen, and S. Brøndsted Nielsen, *Rev. Sci. Instrum.* **87**, 053103 (2016).
- ¹²K. Støchkel, B. F. Milne, and S. Brøndsted Nielsen, *J. Phys. Chem. A* **115**, 2155 (2011).
- ¹³J. A. Wyer and S. Brøndsted Nielsen, *Angew. Chem., Int. Ed.* **124**, 10402 (2012).
- ¹⁴Q. Bian, M. W. Forbes, F. O. Talbot, and R. A. Jockusch, *Phys. Chem. Chem. Phys.* **12**, 2590 (2010).
- ¹⁵N. A. Sassin, S. C. Everhart, B. B. Dangi, K. M. Ervin, and J. I. Cline, *J. Am. Soc. Mass Spectrom.* **20**, 96 (2009).
- ¹⁶J. T. Khoury, S. E. Rodriguez-Cruz, and J. H. Parks, *J. Am. Soc. Mass Spectrom.* **13**, 696 (2002).
- ¹⁷M. Kordel, D. Schooss, C. Neiss, L. Walter, and M. M. Kappes, *J. Phys. Chem. A* **114**, 5509 (2010).
- ¹⁸V. Frankevich, X. Guan, M. Dashtiev, and R. Zenobi, *Eur. J. Mass Spectrom.* **11**, 475 (2005).
- ¹⁹J.-F. Greisch, M. E. Harding, W. Klopper, M. M. Kappes, and D. Schooss, *J. Phys. Chem. A* **118**, 3787 (2014).
- ²⁰M. W. Forbes and R. A. Jockusch, *J. Am. Soc. Mass Spectrom.* **22**, 93 (2011).
- ²¹M. K. Lawless and R. A. Mathies, *J. Chem. Phys.* **96**, 8037 (1992).
- ²²G. B. Dutt, S. Doraiswamy, N. Periasamy, and B. Venkataraman, *J. Chem. Phys.* **93**, 8498 (1990).
- ²³M. Krihak, M. Murtagh, and M. Shahriari, *J. Sol-Gel Sci. Technol.* **10**, 153 (1997).
- ²⁴C. Reichardt and T. Welton, *Solvents and Solvent Effects in Organic Chemistry* (John Wiley & Sons, 2011).
- ²⁵C. Reichardt, *Chem. Rev.* **94**, 2319 (1994).
- ²⁶J. R. Lakowitz, *Principles of Fluorescence Spectroscopy* (Kluwer Academic/Plenum Publishers, 1999).
- ²⁷M. Wanko, J. Houmøller, K. Støchkel, M.-B. Suhr Kirketerp, M. Å. Petersen, M. Brøndsted Nielsen, S. Brøndsted Nielsen, and A. Rubio, *Phys. Chem. Chem. Phys.* **14**, 12905 (2012).
- ²⁸J. Houmøller, M. Wanko, A. Rubio, and S. Brøndsted Nielsen, *J. Phys. Chem. A* **119**, 11498 (2015).
- ²⁹J. Houmøller, M. Wanko, K. Støchkel, A. Rubio, and S. Brøndsted Nielsen, *J. Am. Chem. Soc.* **135**, 6818 (2013).
- ³⁰M. H. Stockett and S. Brøndsted Nielsen, *J. Chem. Phys.* **142**, 171102 (2015).
- ³¹M. H. Stockett and S. Brøndsted Nielsen, *Phys. Chem. Chem. Phys.* **18**, 6996 (2016).
- ³²M. H. Stockett, L. Musbat, C. Kjær, J. Houmøller, Y. Toker, A. Rubio, B. F. Milne, and S. Brøndsted Nielsen, *Phys. Chem. Chem. Phys.* **17**, 25793 (2015).